



HAL
open science

Novel fabrication of Alloy 625 and MCrAlY bond coat by laser powder bed fusion and microstructure control

Jiwon Lee

► **To cite this version:**

Jiwon Lee. Novel fabrication of Alloy 625 and MCrAlY bond coat by laser powder bed fusion and microstructure control. Materials. Ecole des Mines d'Albi-Carmaux; Changwon National University, 2020. English. NNT : 2020EMAC0008 . tel-03070795

HAL Id: tel-03070795

<https://theses.hal.science/tel-03070795>

Submitted on 16 Dec 2020

HAL is a multi-disciplinary open access archive for the deposit and dissemination of scientific research documents, whether they are published or not. The documents may come from teaching and research institutions in France or abroad, or from public or private research centers.

L'archive ouverte pluridisciplinaire **HAL**, est destinée au dépôt et à la diffusion de documents scientifiques de niveau recherche, publiés ou non, émanant des établissements d'enseignement et de recherche français ou étrangers, des laboratoires publics ou privés.

Université Fédérale



Toulouse Midi-Pyrénées

THÈSE

En vue de l'obtention du

DOCTORAT DE L'UNIVERSITÉ DE TOULOUSE

délivré par

IMT – École Nationale Supérieure des Mines d'Albi-Carmaux

Cotutelle internationale avec Changwon National University, République de Corée

présentée et soutenue par

Jiwon LEE

le 17 juin 2020

Titre :

**Novel fabrication of Alloy 625 and MCrAlY bond coat
by laser powder bed fusion and microstructure control**

École doctorale et discipline ou spécialité :

AA : Génie mécanique, mécanique des matériaux

Unité de recherche :

Institut Clément Ader, UMR CNRS 5312, IMT Mines Albi

Directeurs de thèse :

Philippe LOURS, Professeur, IMT Mines Albi

Hyun-Uk HONG, Professeur, Changwon National University, République de Corée

Autres membres du jury :

Heon-Young HA, Chargé de Recherche, Korea Institute of Materials Science, Rapporteur

Sophie COSTIL, Professeur, Univ. de Technologie de Belfort-Montbéliard, Rapporteur

Je-Hyun LEE, Professeur, Changwon National University, Président

Mustapha JOUIAD, Professeur, Université de Picardie Jules Vernes, Examineur

Étienne COPIN, Maître-assistant, IMT Mines Albi, Examineur

Mathieu TERNER, Professeur assistant, Changwon National University, Examineur



Thesis for the Degree of *Doctor of Philosophy*

**Novel Fabrication of Alloy 625 and
MCrAlY Bond Coat by Laser Powder Bed
Fusion and Microstructure Control**

June 2020

**Graduate School of Changwon National University
Department of Metallurgy & Advanced Materials
Engineering**

IMT Mines Albi - Aéronautique, Astronautique

Jiwon Lee

Thesis for the Degree of *Doctor of Philosophy*

**Novel Fabrication of Alloy 625 and
MCrAlY Bond Coat by Laser Powder Bed
Fusion and Microstructure Control**

Thesis Supervisor: *Philippe Lours & Hyun-Uk Hong*

**A Thesis submitted to the graduated school of
Changwon National University & IMT Mines Albi in
partial fulfillment of the requirements for the degree
of *Doctor of Philosophy***

June 2020

**Graduate School of Changwon National University
Department of Metallurgy & Advanced Materials
Engineering**

IMT Mines Albi - Aéronautique, Astronautique

Jiwon Lee

This thesis, written by *Jiwon Lee*,
has been approved as a thesis for the degree of
Doctor of Philosophy

Prof. Hong HyunUk (Changwon National University), Director

Prof. Lours Philippe (IMT Mines Albi), Director

Dr. Ha HeonYoung (Korean Institute of Materials Science), reviewer

Prof. Costil Sophie (UTBM), reviewer

Prof. Jouiad Mustapha (Université de Picardie), examiner

Prof. Lee JeHyun (Changwon National University), examiner

Dr. Copin Etienne (IMT Mines Albi), examiner

Dr. Terner Mathieu (Changwon National University) examiner

June 2020

Graduate School of Changwon National University
& IMT Mines Albi

Table of Contents

I.	Résumé long en français.....	1
II.	Introduction	1 5
III.	Literature review	1 9
3.1	Additive manufacturing	1 9
3.1.1	Families of additive manufacturing technologies	2 1
3.1.2	Additive manufacturing for metallic components.....	2 2
3.2	Materials	2 6
3.2.1	Introduction of Ni-based superalloys	2 6
3.2.2	Strengthening mechanisms of Ni-based superalloys.....	2 8
3.2.3	Introduction of Alloy 625.....	3 4
3.2.4	Precipitation formation of Alloy 625	3 6
3.2.5	L-PBF manufacturing of Alloy 625	3 7
3.3	Introduction of coatings on superalloys	4 0
3.3.1	Introduction of MCrAlY coatings	4 1
3.4	Grain boundary strengthening of γ matrix	4 5
3.4.1	Improvement of GB cohesion strength in Ni-based superalloy	4 6
3.4.2	GB serration.....	4 7
IV.	Methodology	5 0
4.1	Alloy 625 and MCrAlY powders.....	5 0

4.2	Additive manufacturing	5	1
4.3	Microstructure analysis	5	2
4.4	Observation	5	3
4.5	Experiments	5	3
V.	Publications and scientific contribution	5	5
5.1	Focus of research	5	5
5.2	Graphical abstract	6	0
5.3	Introduction of articles	6	1
VI.	Conclusions	8	6
VII.	References	9	0
VIII.	Annex	1	0 2
Résumé	1	6 1

I. Résumé long en français

Le superalliage 625 à base de Ni a été largement utilisé pour les applications sous-marines, aérospatiales et turbines à gaz en raison de sa bonne résistance à haute température, de sa résistance au fluage, de sa résistance à la corrosion et de son excellente soudabilité. Cependant, ses bonnes propriétés mécaniques contribuent à des difficultés d'usinage, qui ont conduit à l'intérêt pour l'application de cet alliage dans le domaine de la fabrication additive (FA). La technologie AM présente de nombreux avantages. Le plus grand avantage est qu'il peut être utilisé pour fabriquer des formes complexes sans outillage; conception pour la fabrication additive (DfAM) ce qui signifie qu'il n'y a aucune contrainte dans la conception des pièces Cette caractéristique de la FA est intéressante principalement dans le domaine aérospatial car elle peut réduire le poids des pièces du moteur en éliminant les matériaux inutiles à certains endroits, ce qui serait nécessaire pour une fabrication facile par un outillage conventionnel et réduit également les dommages d'usure dus au contact des pièces. En plus du domaine aérospatial, l'application de la technologie AM s'est étendue à d'autres industries et l'intérêt pour cette technologie augmente. L'étude de base des compétences de fabrication s'est poursuivie, mais essayer d'appliquer la technologie AM dans de nouveaux contextes devient de plus en plus courant, comme le traitement de multi-matériaux, comme les alliages acier / cuivre.

La présente étude a évalué la faisabilité de l'application de l'alliage 625 à base de nickel fabriqué par AM, en particulier par fusion sur lit de poudre laser (L-PBF), dans des conditions industrielles réelles en appliquant un traitement post-thermique et en développant de nouveaux multi-matériaux à base d'alliage 625. Premièrement, en ce qui concerne les propriétés mécaniques, les propriétés de traction à température ambiante et à haute température ont été évaluées, et divers traitements thermiques ont

été suggérés pour améliorer les propriétés de l'alliage. Il a été vérifié que l'échantillon tel que construit en L-PBF avait une résistance suffisamment élevée; cependant, il avait le potentiel d'être fracturé plus rapidement que souhaité en raison de la faible ténacité et des défauts dus à un refroidissement non homogène. Par conséquent, divers traitements post-thermiques ont été appliqués pour améliorer ses propriétés mécaniques à température ambiante et à haute température. Avec tous ces traitements thermiques, il était possible de produire des échantillons fabriqués par L-PBF qui avaient des microstructures similaires à celles d'un ouvragé, qui est la microstructure préférée, composée de grains polycristallins et de précipités. Ils ont montré une ductilité améliorée et ont maintenu une résistance raisonnable. Bien que la microstructure traitée thermiquement ressemblait beaucoup à la microstructure forgée, ses joints de grains (GB) étaient généralement plus faibles à des températures plus élevées. Par conséquent, un traitement thermique par dentelure aux limites des grains (GBS) a été suggéré.

Le GBS est une réaction spontanée dans laquelle des GB ondulés sont formés; la réaction peut être déclenchée par des traitements thermiques spécialement conçus. Il a été démontré qu'il est efficace pour inhiber la propagation des fissures, en particulier lors du fluage des superalliages à base de Ni principalement solides renforcés en solution. Un traitement thermique spécifique, comprenant un refroidissement lent entre la solution et les températures de vieillissement, a conduit avec succès au SGB dans les études précédentes. De plus, le mécanisme du GBS a été étudié pour le comprendre en profondeur afin qu'il puisse être appliqué à d'autres systèmes d'alliages. Sur la base de cette étude, l'introduction du GBS dans l'alliage corroyé 625 a été réalisée. L'alliage forgé dentelé GB 625 a montré des motifs en zigzag de GB avec des carbures M₂₃C₆ et NbC au niveau des GB. Dans une étude plus approfondie, ce traitement thermique a été appliqué à l'alliage 625 produit au L-PBF. Le traitement thermique a été adapté pour être appliqué à l'alliage L-PBF 625 compte tenu de sa microstructure particulière. En tenant compte du rôle prédominant de la microstructure,

les propriétés de traction à température ambiante et à haute température des échantillons produits par chaque traitement thermique ont été comparées.

Une autre méthode a été suggérée pour améliorer les propriétés des superalliages et augmenter leurs températures de fonctionnement. Les revêtements de surface ont été développés pour protéger les substrats de l'oxydation, de la corrosion et des dommages thermiques à haute température afin que leurs propriétés mécaniques puissent être maintenues pendant un fonctionnement plus long. En règle générale, les revêtements de barrière thermique (TBC) ont un effet isolant, qui diminue la température à laquelle un superalliage est réellement soumis, ce qui permet au superalliage de résister à un fonctionnement à des températures d'environ 150 ° C au-dessus de leur limite supérieure habituelle. Ces TBC consistent généralement en une couche de finition externe en céramique (TC) pour l'isolation thermique et une couche intermédiaire de liaison métallique MCrAlY (BC, où généralement M = Ni, Co, Fe ou une combinaison de ceux-ci) pour tenir compte de la différence entre les coefficients de expansion entre le TC et le substrat en superalliage, et pour faire croître une couche d'oxyde protecteur mince, compacte et adhérente favorisant une résistance optimisée à la corrosion à chaud. L'alliage MCrAlY peut être utilisé comme matériau de revêtement de liaison et comme matériau de revêtement de recouvrement lui-même. L'épaisseur du revêtement de recouvrement MCrAlY est illimitée, sa résistance à l'oxydation / corrosion est proportionnelle à son épaisseur. Ainsi, un matériau MCrAlY est généralement requis sur un substrat en superalliage exposé à des environnements difficiles pour les deux raisons.

Le processus de revêtement est totalement différent de celui de la production de substrat en superalliage; les couches de revêtement sont généralement appliquées sur le substrat par projection d'air ou de plasma sous vide (APS / VPS), dépôt physique en phase vapeur par faisceau d'électrons (EB-PVD) et placage aux ions d'arc (AIP). Les processus séparés de fabrication d'alliages revêtus nécessitent une main-d'œuvre, un coût et du temps considérables. Pour ces considérations, le L-PBF d'une couche de

liaison NiCrAlY sur un substrat en alliage 625, lui-même produit par le L-PBF, est également considéré. Bien qu'il y ait eu quelques études sur la fabrication multi-matériaux par la technologie AM, c'est la première fois, à notre connaissance, que le L-PBF est utilisé pour produire à la fois un substrat en superalliage et une couche de liaison MCrAlY. Nous pensons que cette méthode peut améliorer la liaison entre le substrat et le revêtement en raison de la nature du processus L-PBF, qui implique la refusion typique des couches sous-jacentes. La production finale de géométries enrobées complexes, telles que des lames, est un défi car les technologies PBF nécessitent le dépôt d'une couche entière de poudre, limitant ainsi le dépôt sur des surfaces planes. Cependant, on pense que ce problème pourrait être résolu prochainement en améliorant la partie de la machine comme la liberté de mouvement de balayage laser, en utilisant un réservoir à poudre multiple, etc. Dans ce travail, l'optimisation des paramètres de processus L-PBF pour MCrAlY est décrite sur la base de plusieurs critères, et les matériaux tels que produits sont minutieusement analysés. De plus, les propriétés d'oxydation de l'alliage 625 revêtu de MCrAlY de manière optimale ont été évaluées par analyse gravimétrique thermique (TGA). En outre, les propriétés de résistance thermique, en particulier la résistance à la dilatation et à la contraction thermiques rapides, ont été évaluées par des essais de choc thermique. Les résultats ont démontré la faisabilité du revêtement MCrAlY sur le substrat de superalliage au moyen de L-PBF, et sa fonction s'est avérée raisonnable.

Par conséquent, nous concluons que le traitement post-thermique et le revêtement MCrAlY fabriqué au L-PBF améliorent les propriétés mécaniques de l'alliage 625 fabriqué par L-PBF à des températures de fonctionnement réelles (~ 982 °C) au lieu de l'alliage 625 conventionnel. Les effets de ces procédures ont été démontrés sur la base de la microstructure et des aspects fonctionnels des échantillons fabriqués.

Publications et contribution scientifique

Objet de la recherche

- Fabrication d'un système bi-matière en alliage 625 revêtu de NiCrAlY par L-PBF.
 - ⇒ Chaque propriété du substrat et de l'alliage revêtu uniquement doit être évaluée et améliorée pour être certifiée pour la commercialisation / l'application.
- La microstructure de divers alliages L-PBF traités thermiquement 625 a été étudiée et leurs propriétés de traction ont été comparées à température ambiante.
 - ⇒ Pour considérer les conditions de fonctionnement réelles de l'alliage, une étude des propriétés à haute température a été envisagée. En outre, le GBS a été choisi comme un moyen d'améliorer les propriétés mécaniques à haute température. Par conséquent, le mécanisme de GBS doit être étudié pour la première étape à appliquer pour la première fois au superalliage à base de Nb ajouté (alliage 625).
- Le mécanisme GBS a été compris pour la première fois avec un modèle en alliage.
 - ⇒ L'étape suivante consiste à appliquer le GBS à l'alliage corroyé 625, l'alliage standard.
- L'application de GBS à l'alliage corroyé 625 a été réussie.
 - ⇒ Enfin, il était prêt à appliquer le GBS au L-PBF Alloy 625.
- Le GBS a été induit avec succès dans l'alliage L-PBF 625 et ses propriétés de traction à haute température ont été évaluées avec du L-PBF recristallisé, du L-PBF tel que construit et de l'alliage 625 forgé. ductilité que le L-PBF Comme

construit à haute température. En particulier, l'échantillon induit par GBS a une résistance à l'occurrence de DSA.

⇒ Une étude plus approfondie de la résistance à l'oxydation et au choc thermique de l'alliage revêtu de L-PBF NiCrAlY est nécessaire.

- Un test TGA pour l'alliage 625 en vrac, l'alliage 625 revêtu de NiCrAlY en vrac et NiCrAlY, tous fabriqués par L-PBF, a été réalisé et l'échantillon revêtu a montré une résistance à l'oxydation intermédiaire entre deux échantillons en vrac. Par conséquent, la fabrication de composants revêtus par L-PBF n'est pas anodine.
- Le test de choc thermique a été testé pour un échantillon revêtu d'As-NiCrAlY avec et sans couche de finition. De plus, un échantillon revêtu d'As-NiCrAlY traité thermiquement avec une couche de finition a également été appliqué. Il n'y avait pas de délaminage entre le substrat et la couche de revêtement de liaison NiCrAlY, ce qui signifie que sa propriété de dilatation / contraction thermique est stable même dans les conditions de refroidissement / chauffage rapide.

1. A novel approach to the production of NiCrAlY bond coat onto IN625 superalloy by selective laser melting

Cette étude portait sur la faisabilité de produire un matériau de couche de liaison NiCrAlY directement sur un substrat en alliage 625 produit par L-PBF. Dans la présente étude, le L-PBF a été utilisé pour fabriquer à la fois le substrat de superalliage à base de Ni et la couche de liaison NiCrAlY, ce qui est la première fois que cela a été étudié, au meilleur de nos connaissances, en relation avec la fabrication AM. Quinze paramètres de traitement différents ont été testés, et tous les cas ont montré une dilution substantielle entre NiCrAlY et le substrat de superalliage en raison de la

caractéristique de refusion typique du processus L-PBF, assurant une excellente liaison métallurgique. Les paramètres optimaux du procédé, épaisseur de couche $t = 50 \mu\text{m}$, espacement des hachures $h = 120 \mu\text{m}$, puissance laser $P = 250 \text{ W}$ et vitesse de balayage laser $v = 800 \text{ mm / s}$, ont été sélectionnés en fonction de plusieurs critères. Un revêtement NiCrAlY d'environ $250 \mu\text{m}$ d'épaisseur a été obtenu avec une très faible porosité résiduelle $\leq 0,1\%$, comprenant une zone de dilution $\sim 35\%$, un profil de dureté lisse entre 275 et 305 Hv, de faibles niveaux de contraintes résiduelles et une distribution progressive de la concentration en Al . Ces résultats ont confirmé la faisabilité du L-PBF comme méthode alternative pour le dépôt de revêtements dans les systèmes TBC ou le revêtement MCrAlY lui-même.

2. Influence of heat treatments on microstructure evolution and mechanical properties of Inconel 625 processed by laser powder bed fusion

Cette étude portait sur le comportement mécanique à température ambiante et la microstructure d'échantillons d'alliage 625 tels que construits et traités thermiquement fabriqués par L-PBF. Contrairement au reste du travail, dans ce cas, les échantillons ont été réalisés avec des machines différentes (machine EOSINT M270 Dual Mode, qui est équipée d'un laser à fibre Yb 200W avec un diamètre de spot de $100 \mu\text{m}$) avec de la poudre (distribution de taille entre d_{30} de $16 \mu\text{m}$ et d_{90} de $48 \mu\text{m}$) à partir d'une source différente (puissance laser de 195 W , vitesse de balayage de 1200 mm / s , distance d'éclosion de $0,09 \text{ mm}$ et épaisseur de couche de $0,02 \text{ mm}$) dans le cadre d'une étude menée en collaboration avec Politecnico di Torino en Italie . Bien que l'échantillon de L-PBF fabriqué tel quel a montré de bonnes propriétés de traction, un traitement post-thermique est recommandé pour obtenir des propriétés mécaniques spécifiques afin de satisfaire les exigences industrielles. Différents types de traitements thermiques ont été effectués pour produire chaque microstructure et ont sélectionné chaque traitement thermique représentatif par comparaison de la dureté

Brinell. Les carbures γ'' et M23C6 à grains recristallisés sont apparus dans l'échantillon traité par vieillissement direct (DA) (700 ° C / 24 h), produit à partir de la microstructure telle que construite, qui présentait des structures colonnaires à haute densité de dislocation et des carbures NbC. Un traitement en solution (S) (1150 ° C / 2 h) a donné à l'échantillon une structure de grains austénitiques équiaxes recristallisés avec des carbures MC primaires et secondaires. En outre, l'échantillon traité par solution / vieillissement (SA) (1150 ° C / 2 h - 700 ° C 24 h) a montré la même microstructure que celle de l'échantillon S, mais avec des carbures γ'' et M23C6. La température optimale pour les traitements thermiques a été choisie en comparant les valeurs de dureté Brinell et l'observation de la microstructure. Quatre types d'échantillons ont été soumis à des essais de traction à température ambiante avec l'échantillon tel que construit comme contrepartie. L'échantillon tel que construit a montré des valeurs de limite d'élasticité (YS) et de résistance à la traction ultime (UTS) de 783 MPa et 1041 MPa respectivement, avec une ductilité de 33%. L'échantillon DA présentait des valeurs YS et UTS de 1 012 MPa et 1 222 MPa, avec la ductilité la plus faible de 23%. L'échantillon S a montré les valeurs YS et UTS les plus basses de 396 MPa et 883 MPa avec l'incrément de ductilité le plus élevé de 55%. L'échantillon SA a montré une augmentation significative de la résistance: YS = 722 MPa, UTS = 1 116 MPa et une ductilité corrélée de 35%. Selon les résultats de traction, le traitement en solution contribue à l'augmentation de ductilité et le traitement de vieillissement améliore la résistance. Par conséquent, il a été démontré que l'évolution de la microstructure de l'alliage L-PBF 625 sous divers traitements thermiques offre un large spectre de propriétés mécaniques possibles.

3. A new observation of strain-induced grain boundary serration and its underlying mechanism in a Ni–20Cr binary model alloy

Dans cette étude, dans le cadre du renforcement GB à haute température, le

mécanisme du GBS a été étudié à travers un alliage modèle binaire Ni-20Cr pour préparer l'application à l'alliage 625 fabriqué par additif dans l'étude ultérieure. Un alliage entièrement traité en solution solide a été traité thermiquement sur la base de l'étude précédente adaptée pour un alliage à matrice Ni – Cr. Selon l'hypothèse du mécanisme de GBS, il n'y a eu aucun cas de GBS comme prévu. Cependant, le signe de GBS s'est produit en donnant une déformation de 5% pendant le processus de vieillissement direct / refroidissement lent dans lequel le GBS a eu lieu, qui a été conduit après le processus de solution solide. La microstructure de l'échantillon dans lequel le SGB s'est produit a été analysée par TEM et la méthode 3D-APT. Il y avait une densité élevée de dislocations autour des GB en raison d'une contrainte de 5% pendant le processus de vieillissement / refroidissement lent, ce qui a favorisé l'enrichissement en Cr près et au niveau des GB. Pour que l'échantillon présente le même comportement juste par traitement thermique, la température de dissolution a été augmentée pour induire un enrichissement en Cr près et au niveau des GB avec le concept de diffusion assistée par vide, et cela a bien fonctionné. L'analyse 3D-APT approfondie a montré que les échantillons dentelés présentaient un large enrichissement en Cr au niveau des GB dentelés. La caractéristique commune des deux échantillons était l'enrichissement en Cr, et la tension sur les GB était considérée comme le déclencheur du SGB. La déformation par calcul du premier principe était d'environ 0,97 kJ / mol. Ainsi, il a été démontré que le minimum de 0,97 kJ / mol de déformation peut conduire au SGB par les atomes interstitiels au niveau des GB.

4. First evidence of grain boundary serration in a specifically heat treated wrought Alloy 625 Ni-based superalloy

Récemment, l'introduction du GBS a été étudiée principalement pour les superalliages à base de Ni renforcés en solution solide à faible fraction volumique γ' , tels que l'alliage 230 et l'alliage 617. Le présent travail a étudié l'induction du GBS

dans superalliage à base de Ni renforcé en solution ayant une minorité de caractérisation de renforcement par précipitation par le carbure MC et γ'' . Le traitement thermique spécialement conçu (1250 ° C / 30 min - 5 ° C / min de refroidissement lent - 800 ° C / 0-1000 h) a été appliqué à l'alliage corroyé 625 sur la base des travaux précédents, et une dentelure significative a été observée pour la première fois. Des carbures M₂₃C₆ ainsi qu'une quantité significative de carbures MC ont été observés aux GB, alors qu'il n'y avait aucun signe de précipitation γ'' . Le traitement de refroidissement lent s'est avéré favoriser efficacement la formation de joints de grains dentelés, même en l'absence de vieillissement. Pendant ce temps, à mesure que le temps de vieillissement augmente, la précipitation de la phase δ était évidente.

5. Heat treatment design for superior high-temperature tensile properties of Alloy 625 produced by SLM

L'alliage 625 fabriqué au L-PBF a été soumis à des essais de traction à haute température. Compte tenu de l'étude récente qui décrit un essai de traction réalisé à température ambiante avec du L-PBF tel que construit et divers échantillons traités thermiquement, un traitement thermique GBS modifié (augmentation de la température de la solution solide de 1250 → 1300 ° C) a été appliqué à l'alliage L-PBF 625 (échantillon 'GBS HT'). Ce traitement thermique a été développé pour améliorer le renforcement GB qui se produit généralement à haute température avec des conditions de faible contrainte. Grâce à ce traitement thermique, la structure colonnaire de l'échantillon construit en As a été détruite et tous les grains ont été équiaxés. De plus, des GB dentelés ont été produits avec succès et la plupart des GB ont été décorés avec des carbures NbC. En outre, un traitement thermique de recristallisation (RX HT) a également été effectué pour induire la recristallisation et un état de solution solide approprié ayant une valeur de dureté élevée. Ces deux

échantillons traités thermiquement ont été soumis à des essais de traction à haute température avec des échantillons de L-PBF tel que construit (AB) et d'alliage corroyé 625. Les essais de traction ont été réalisés à température ambiante, 500 ° C, 600 ° C et 700 ° C dans les mêmes conditions dans l'air. Un essai de traction à température ambiante a été effectué pour vérifier la fiabilité de chaque échantillon et ses résultats peuvent être comparés à l'étude précédente de en ce qui concerne les conditions de fabrication de l'échantillon. Les graphiques de traction des deux échantillons traités thermiquement étaient situés entre ceux des échantillons AB et ouvrés. Ainsi, leurs forces étaient plus élevées que celles de l'échantillon forgé, et ils avaient des valeurs de ductilité plus élevées que l'échantillon AB. Ces résultats peuvent être attribués aux différences de savoir si la microstructure initiale est colonnaire ou équiaxe, s'il y a des GB droits ou des GB dentelés, et s'il y a ou non des précipitations. Comme dans une étude précédente dans laquelle des essais de traction ont été effectués à température ambiante, les trois échantillons (forgé, RX HT, GBS HT) ayant une structure de grains équiaxes ont montré une ductilité améliorée. D'autre part, les trois autres échantillons (AB, RX HT, GBS HT) ayant des précipités ont montré des valeurs de résistance améliorées. Bien que les traitements thermiques n'aient pas pu améliorer la ductilité autant que l'échantillon forgé, le phénomène DSA, qui montre une propriété de traction inattendue à une vitesse de déformation et une température typiques, a rarement été observé dans l'échantillon de GBS HT. Par conséquent, l'échantillon de GBS HT semble avoir un bon effet sur une partie de l'alliage 625 fabriqué au L-PBF.

6. Oxidation of NiCrAlY coating deposited by selective laser melting for thermal barrier coating application

La fabrication du L-PBF est considérée comme particulièrement appropriée pour les pièces à géométrie complexe avec une microstructure multicouche, y compris des systèmes de barrière thermique et / ou de revêtement environnemental, pour satisfaire

à la fois les spécifications structurelles et environnementales. Du point de vue des spécifications environnementales, l'oxydation à haute température de NiCrAlY entièrement traité au L-PBF par les conditions de paramètres optimales précédemment testées et réussies ($P = 250 \text{ W}$, $v = 800 \text{ mm / s}$) recouvrant le substrat en alliage 625 les pièces ont été étudiées à des températures comprises entre $800 \text{ }^\circ \text{C}$ et $1000 \text{ }^\circ \text{C}$. NiCrAlY, alliage 625 et bi-matériaux autoportants en vrac ont été fabriqués en utilisant la méthode L-PBF. Pour être représentatif des composants revêtus, deux couches minces (environ $100 \text{ }\mu\text{m}$) de poudre NiCrAlY ont été balayées au laser à la surface de l'alliage 625 pour former le multi-matériau. Les échantillons revêtus ont ensuite été extraits en utilisant une technique de polissage mécanique douce pour assurer une épaisseur et une finition de surface répétables de l'échantillon. Il convient de noter que la fabrication du L-PBF NiCrAlY était particulièrement difficile et a entraîné des macro-fissures dans les échantillons de NiCrAlY en vrac en raison de la forte contrainte résiduelle volumétrique, alors que la raison pour laquelle des micro-fissures sont observées au niveau de la perle laser pour le revêtement est prédite par fissuration retardée. Cependant, il n'a pas été suffisamment endommagé pour empêcher la réalisation de l'étude. Comme prévu, le NiCrAlY en vrac et les bi-matériaux ont démontré un comportement d'oxydation amélioré par rapport à l'alliage 625. En effet, l'oxydation de NiCrAlY autoportant volumineux a donné une couche d' Al_2O_3 dense et continue dans cette plage de température, ce qui était attendu pour cette composition de NiCrAlY. Cela signifie qu'aucun effet d'évaporation de l'Al n'a été observé (un problème parfois observé dans le L-PBF). Cependant, la formation d'oxydes à la surface du matériau bicouche diffèrait de celle du NiCrAlY autoportant volumineux. A titre de comparaison, l'oxydation du matériau bicouche a conduit à des régions à couche d' Al_2O_3 dense et continue ainsi qu'à des régions composées d'un mélange de Cr_2O_3 externe et d' Al_2O_3 interne. Des cartes EDS étendues à la surface du bi-matériau ont mis en évidence la distribution hétérogène des éléments constitutifs du revêtement NiCrAlY, entraînant certaines régions avec une activité Al inférieure à celle requise pour la formation d'une couche continue et dense d' Al_2O_3 . Les régions à

faible activité en Al et à haute activité en Al étaient liées à la topographie de la surface du L-PBF et correspondaient aux régions de pic et de vallée, respectivement d'où il provient de l'épaisseur homogène de la couche de poudre déposée. De plus, les fissures ont été principalement trouvées dans les régions à haute activité Al et elles ont pu être atténuées en appliquant un traitement thermique de détente ou la diffusion. La fabrication de composants revêtus mais petits avec un revêtement cassant par L-PBF n'est pas anodine et nécessite une étude plus approfondie.

7. Thermal shock resistance of the NiCrAlY coated Alloy 625 multi material manufactured by L-PBF (paper in preparation)

C'est la première fois à notre connaissance qu'un système de superalliage + couche de liaison est produit à la fois par L-PBF. L'étude du comportement d'oxydation, précédemment rapportée, a mis en évidence la fiabilité du bi-matériau. Ce bi-matériau est destiné à être utilisé dans des conditions d'exposition à haute température telles que les applications de turbines à gaz de moteurs d'avion. Pour cette raison, la résistance aux chocs thermiques (cycles rapides de chauffage et de refroidissement) est également critique. Un grément de brûleur approchant les conditions sévères qui pourraient être rencontrées pendant le fonctionnement imposant un chauffage et un refroidissement très rapides a été utilisé. Cette étude a été menée en collaboration avec nos collègues italiens du Département des sciences appliquées et de la technologie du Politecnico di Torino. Le Burner Rig in Politecnico di Torino (Fig. 18) est un appareil sur mesure spécialement conçu pour reproduire les conditions de température sévères rencontrées dans un moteur à turbine à gaz. La machine est équipée notamment d'une chambre de combustion constituée d'une plaque en céramique résistante à la chaleur usinée pour accueillir jusqu'à 10 échantillons, 20 tubes de trempe à l'air pour un refroidissement rapide de la surface supérieure et / ou inférieure de chaque échantillon, 20 thermocouples pour des mesures précises de la surface supérieure et inférieure de

chaque spécimen. Sur le dessus de la plaque, un brûleur délivre une flamme réelle en brûlant soit du méthane, soit un mélange de méthane régulé + carburant. Seul le méthane a été utilisé dans la présente étude. Un système de vannes manuelles avec manomètre permet la régulation du débit d'air pour la trempe. Le Burner Rig est contrôlé manuellement au moyen d'un logiciel qui permet de réguler le débit de méthane et le rapport air / méthane, déclencher la trempe de l'air et surveiller / contrôler les températures. La température maximale prévue est de 1300 ° C. Dans la présente étude, le débit de méthane a été réglé à 1 m³ / h, le rapport air / méthane a été fixé à 1,2, la température maximale a été fixée à 950 ° C et la température de trempe a été fixée à 300 ° C. Tous les essais expérimentaux ont été réalisés dans le cadre d'une campagne d'essais de deux mois à Turin. Fait également partie de la collaboration internationale créée autour du présent doctorat. thèse, la caractérisation des matériaux a fait l'objet d'un programme de stage de 4 mois. Un étudiant d'IMT Mines-Albi, sous la direction du présent auteur Jiwon Lee, était responsable de la caractérisation.

II. Introduction

Ni-based superalloy 625 has been widely used for submarine, aerospace, and gas turbine applications because of its good high-temperature strength, creep resistance, corrosion resistance, and excellent weldability. However, its good mechanical properties contribute to difficulties in machining, which have led to the interest in application of this alloy in the additive manufacturing (AM) field. AM technology has many advantages. The greatest advantage is that it can be used to manufacture complex shapes without tooling; design for additive manufacturing (DfAM) which means there are no constraints in designing of parts. This characteristic of AM is attractive mostly in the aerospace field because it can reduce the weight of engine parts by eliminating unnecessary materials in some locations, that would be required for easy fabrication by conventional tooling and also reduce wear damage due to part contact. In addition to the aerospace field, the application of AM technology has spread to other industries, and interest in this technology is increasing. The basic study of fabrication skills has continued, but trying to applying AM technology in new contexts is becoming more common now, such as the processing of multi-materials, like steel/copper alloys [1–3].

The present study assessed the feasibility of applying AM-fabricated, especially laser powder bed fusion (L-PBF), Ni-based Alloy 625 under real industrial conditions by applying post-heat treatment and to develop Alloy 625-based novel multi-materials. First, with respect to the mechanical properties, the ambient and high-temperature tensile properties were evaluated, and various heat treatments were suggested to improve the alloy's properties. The L-PBF fabricated as-built sample was verified to have sufficiently high strength; however, it had the potential to be fractured more quickly than being desired due to the low toughness and defects due to non-homogeneous cooling. Therefore, various post-heat treatments were applied to improve its room-temperature and high-temperature mechanical properties. With all of these heat treatments, it was possible to produce samples fabricated by L-PBF that had

microstructures similar to that of a wrought one, which is the preferred microstructure, composed of polycrystalline grains and precipitates. They showed improved ductility and maintained reasonable strength. Although the heat-treated microstructure was much like the wrought microstructure, its grain boundaries (GBs) were typically weaker at higher temperatures. Therefore grain boundary serration (GBS) heat treatment was suggested.

GBS is a spontaneous reaction in which wavy GBs are formed; the reaction can be triggered by specifically designed heat treatments. It has been demonstrated that it is effective in inhibiting crack propagation, especially during creep of primarily solid solution-strengthened Ni-based superalloys. A specific heat treatment, including slow cooling between solution and aging temperatures successfully led to GBS in previous studies [4, 5]. In addition, the mechanism of GBS was studied to understand it in depth so that it could be applied to other alloy systems. Based on this study, the introduction of GBS in wrought Alloy 625 was achieved. GB serrated wrought Alloy 625 showed zigzag patterns of GBs with $M_{23}C_6$ and NbC carbides at the GBs. In further study, this heat treatment was applied to L-PBF produced Alloy 625. The heat treatment was adapted for application to the L-PBF Alloy 625 considering its peculiar microstructure. Taking the predominant role of microstructure into account, the room-temperature as well as high-temperature tensile properties of samples produced by each heat treatment were compared.

Another method has been suggested to enhance the properties of superalloys and increase their operating temperatures. Surface coatings have been developed to protect substrates from oxidation, corrosion, and thermal damages at high temperature so that their mechanical properties can be maintained for longer operation [6–9]. Typically, thermal barrier coatings (TBC) have an insulation effect, which decreases the temperature that a superalloy is actually subjected to, which permits the superalloy to withstand operation at temperatures about 150 °C above their usual upper limit [10–14]. These TBCs commonly consist of an external ceramic top coat (TC) for thermal

insulation and an intermediate MCrAlY metallic bond coat (BC, where typically M = Ni, Co, Fe or a combination of those) to accommodate the difference between the coefficients of thermal expansion between TC and superalloy substrate, and to grow a thin, compact, and adherent protective oxide scale promoting optimized hot corrosion resistance [10–15]. The MCrAlY alloy can be used as a bond coat material and as an overlay coating material itself. The thickness of MCrAlY overlay coating is unlimited, its resistance to oxidation/corrosion is proportional to its thickness. Thus, MCrAlY material is generally required on a superalloy substrate being exposed to harsh environments for both reasons.

The coating process is totally different from that of superalloy substrate production; the coating layers are generally coated on the substrate by air or vacuum plasma spray (APS/VPS), electron beam-physical vapor deposition (EB-PVD), and arc ion plating (AIP) [11, 12]. The separate processes of coated alloy manufacturing require considerable manpower, cost, and time. For these considerations, L-PBF of an NiCrAlY bond coat on an Alloy 625 substrate, itself produced by L-PBF, is considered as well. Although there have been some studies on multi-material manufacturing by AM technology, this is the first time, to the best of our knowledge, that L-PBF has been used to produce both a superalloy substrate and an MCrAlY bond coat. We believe that this method can improve the bonding between the substrate and coating due to the nature of the L-PBF process, which involves the typical remelting of underlying layers. The ultimate production of complex coated geometries, such as blades, is challenging because PBF technologies require the deposition of an entire layer of powder, thus limiting deposition on flat surfaces. However, it is believed that this issue could be addressed soon by improving the machine part like the freedom of laser scanning motion, using multiple-powder tank, etc. In this work, the optimization of the L-PBF process parameters for MCrAlY is described on the basis of several criteria, and the as-produced materials are thoroughly analyzed. Additionally, the oxidation properties of the optimally MCrAlY-coated Alloy 625 were assessed by

thermal gravimetric analysis (TGA). Furthermore thermal resistance properties, especially resistance to rapid thermal expansion and contraction, were assessed by thermal shock testing. The results demonstrated the feasibility of MCrAlY coating on the superalloy substrate by means of L-PBF, and its function was found to be reasonable.

Therefore, we conclude that post-heat treatment and L-PBF manufactured MCrAlY coating improve the mechanical properties of Alloy 625 manufactured by L-PBF at real operating temperatures (~982 °C) as an alternative to conventional Alloy 625. Furthermore, the positive effects of these procedures were demonstrated based on the microstructure and functional aspects of the fabricated samples.

III. Literature review

3.1 Additive manufacturing

AM is “a process of joining materials to make objects from 3-dimensional (3D) model data, usually layer upon layer, as opposed to subtractive manufacturing methodologies” [16], which means it can be used for all kinds of production, maintaining and conserving its required properties. Moreover, AM can achieve the manufacture of complex and near net shape without tooling. This advantage would lead to saving of material and reduction of the product weight. Hence, this technology is identified as a key factor leading the 4th industrial revolution. On the other hand, it also has some disadvantages, such as high investment costs (for metals), low volume production rate, expensive raw materials, and post-processing. Despite these problems, the revenues generated by the AM technique are growing every year. According to one report [17], the global AM market is expected to reach 41.59 billion dollars or more by 2027.

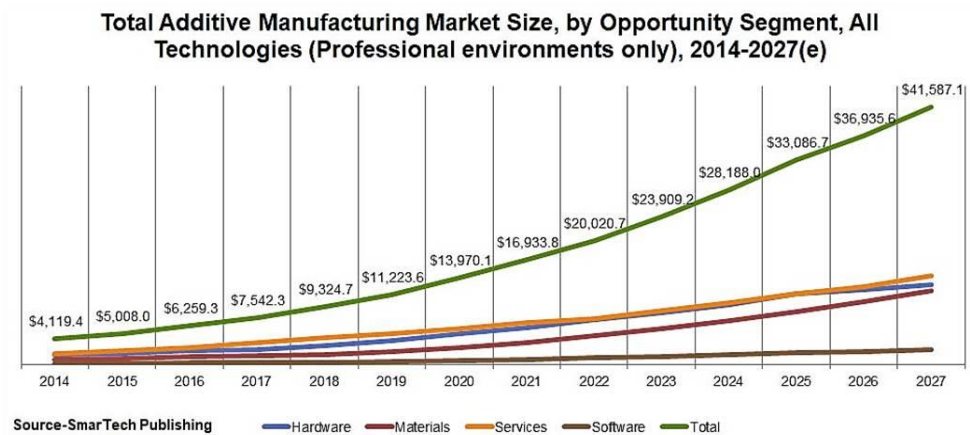


Figure 1. Total additive manufacturing market size (billion \$) by opportunity segment and its prospect by 2027 [17].

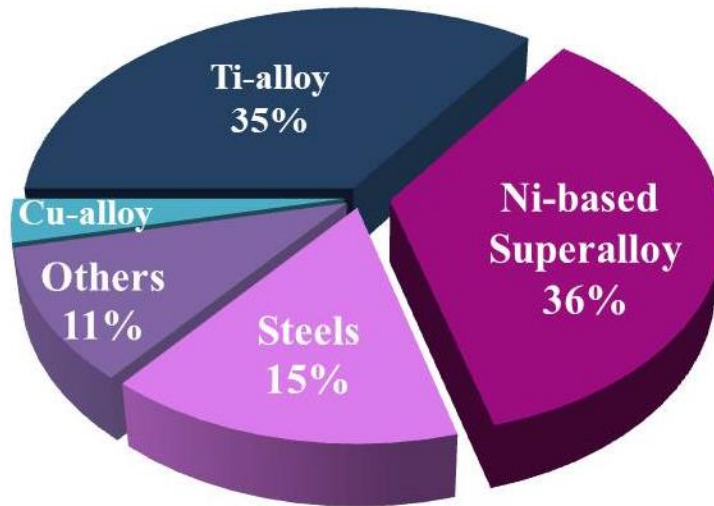


Figure 2. Pie-chart of generally used AM materials (searched in google scholar, total 100 papers).

As seen in Figure 1, the AM market will continue to grow and, accordingly, prospects for its growth are evident in the material sector as well as in services related to AM. Ti-alloys have been the most studied materials used in AM, as seen in Figure 2, along with Ni-based superalloys especially Alloy 718 and 625 due to their excellent weldability. Although nickel-based superalloys are known to be widely used for high-temperature applications due to their excellent high-temperature mechanical properties, literature reviews have shown that AM-fabricated Ni-based superalloys are mainly based on microstructure analysis or research on room-temperature mechanical properties according to parameter condition differences (Fig. 3). Therefore, it is believed that more AM research cases are needed for the real application of these alloys.

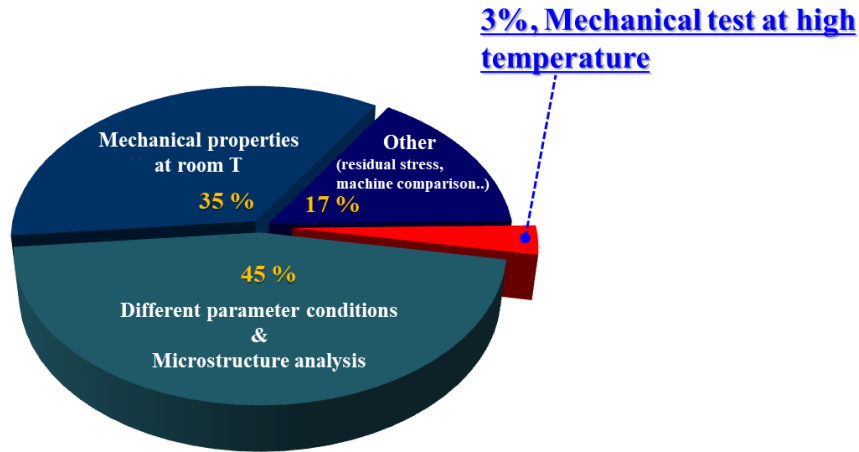


Figure 3. Pie-chart of study fields in AM related to Ni-based superalloy

3.1.1 Families of additive manufacturing technologies

AM technologies are broadly divided into seven families (Fig.4). These families use different manufacturing methods or heat sources. In the binder jetting method, an inkjet printer head is used to spread selectively a liquid binder onto a powder bed to glue particles together and create the desired geometry layer by layer; subsequently, heat treatment is applied to remove binder and to sinter the particles together the particles together [18]. Direct energy deposition (DED) is a method in which melt metal feedstock (either powder or a wire) is projected with directed continuous coaxial nozzles to the melt pool created on the part by the beam of a high energy source (laser or electron beam) [19]. Material extrusion additive manufacturing, whose representative method is fused deposition modeling (FDM), uses a continuous filament of a thermoplastic material as a base material. A coil feeds the filament via a heated moving extruder head, and the molten material is deposited onto a platform [20]. Material jetting is a process in which layers of a photopolymer or a wax are selectively deposited using either a continuous or drop on demand (DOD) approach onto a build platform via inkjet printer heads. It allows forms to be manufactured with

different materials within the same part [20, 21]. The PBF method employs high-power laser/electron beams focused on a metal powder bed [20, 22]. Sheet lamination uses welded, glued, or assembled sheets of a material that are cut away to form the desired object using a digitally guided laser [22]. In vat polymerization, a vat of liquid photopolymer is used to constructs a model layer by layer through a curing process by ultraviolet (UV) light [22]. Among various AM methods, PBF and DED are usually employed in industry where deal with metallic materials because of their suitability for processing metallic materials, in the form of powder [23].

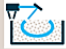






TECHNOLOGY		MATERIALS	TYPICAL MARKETS	RELEVANCE FOR METAL	AM technologies for metal objects
	Powder bed fusion – Thermal energy selectively fuses regions of a powder bed	Metals, polymers	Prototyping, direct part	●	
	Directed energy deposition – Focused thermal energy is used to fuse materials by melting as the material is deposited	Metals	Direct part, repair	◐	
	Sheet lamination – Sheets of material are bonded to form an object	Metals, paper	Prototyping, direct part	◑	
	Binder jetting – Liquid bonding agent is selectively deposited to join powder material	Metals, polymers, foundry sand	Prototyping, direct part, casting molds	◑	
	Material jetting – Droplets of build material are selectively deposited	Polymers, waxes	Prototyping, casting patterns	○	
	Material extrusion – Material are selectively dispensed through a nozzle or orifice	Polymers	Prototyping	○	
	Vat photopolymerization – Liquid photopolymer in a vat is selectively cured by light-activated polymerization	Photopolymers	Prototyping	○	

Figure 4. Various AM methods and their available materials [24].

3.1.2 Additive manufacturing for metallic components

The DED technique, also referred to as laser-engineered net shaping (LENS), direct laser metal deposition (DLMD), and laser cladding is carried out by feeding the metal powder into coaxially operating nozzles with a laser beam directed onto the part surface [25] as shown in Fig. 5. It has the advantage that it can be employed for diverse material processing activities, such as metallic coating, high-value component repair, prototyping, and even low-volume manufacturing with a closed-loop control

system to maintain dimensional accuracy and material integrity. Moreover, it can be used to quickly create large parts [27, 28]. This method can be used for repairing and coating due to the nature of the technique; a flat starting base plate is not necessary [18]. Bi-material manufacturing by DED has been already studied in relation to two different kinds of Ti alloys (TC11/Ti2AlNb) [29], pure copper (Cu), stainless steel 304L [30], molybdenum alloy [31], and other materials. However, it has significant disadvantage of a rough surface finish, due to the large width of the deposited bead. Powder DED results in a better surface finish than the wire DED technique, with typical XY resolutions of 100 to 1,000 μm and 2,000 to 50,000 μm , respectively [32].

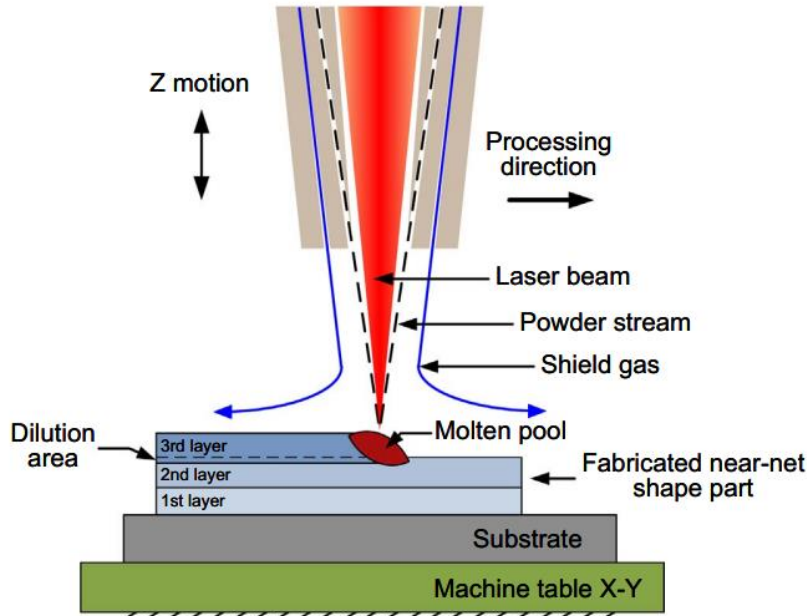


Figure 5. Schematic diagram of DED process [26].

On the other hand, the PBF process produces a much better surface finish (higher resolution) than the DED method, with a resolution of 20 to 200 μm [32]. This technology uses a small-diameter of heat source as laser or electron beam [33] to

selectively melt thin layers of powders (L-PBF: 20 μm - 100 μm , EBM: 50 μm - 200 μm). It can build parts with complex geometries but not as large as those that can be built by DED. Generally, the recoating system is spreading over a thin layer of metallic powder, which is commonly made up of the same material as that of the powder bed, and selected areas are fused together layer by layer [18]. There are three representative PBF- type techniques, selective laser sintering (SLS), electron beam melting (EBM), and laser powder bed fusion (L-PBF,) roughly depending on their type of beam used, the power of the beam, and the melting ratio, as shown in the Table 1.

Table 1. Comparison of characteristics of SLS, EBM and L-PBF [34].

	SLS	EBM	L-PBF
Type of Beam	Laser beam	Electron beam	Laser beam
Melting Ratio	Partial	Full	Full
Material	All (especially for polymers)	All (especially for Ti-alloy)	All

The SLS differs from EBM and L-PBF in that this method is used for rapid-prototyping due to low volume density of parts produced. Moreover, metallic powder is not commonly used in SLS currently [35]. The major difference between EBM and L-PBF is the heat source; power is supplied by transferring kinetic energy (electron beam) and photon absorption (laser), respectively [18]. The power of the energy source of EBM can be about 10 times higher than L-PBF [36]. Because of the high power input to the thin metallic powder bed, the officially known cooling rate is up to 10^6 K in both cases (or higher in L-PBF since it does not have a pre-scanning system). This rapid cooling rate can raise the residual stresses in the part interior, causing detachment from the base plate or cracking at the edge side. To reduce the cooling rate, heating of the powder bed is conducted as follows. The temperature should be kept higher than 600 $^{\circ}\text{C}$ in EBM by pre-scanning of every layer prior to melting. In L-PBF,

the sole base plate is heated up to 200–500 °C [37] accordingly, the supporters connecting the base plate and the part surface, which is expected to be subject to high stress, are heated together. Furthermore, the beam power difference requires the appropriate adjustment of the powder size to be melted well, thus minimizing the porosity of the volume under the given power of the scan. The powder should be in the size range of 15–45 µm and 45–105 µm in L-PBF and EBM, respectively [18]. In L-PBF, the powder directly absorbs the heat energy from the laser and melts, whereas in EBM, the powder is penetrated by an electron beam that produces heat energy from the kinetic energy transfer, causing the particles to melt and adhere to each other [38]. Because the large beam spot size requires a larger powder size, it can produce larger layer thickness resulting in higher production rate than L-PBF while it has a rougher surface finish. The characterization results obtained for samples produced by the two methods are presented in Table 2. Schematics of both methods are shown in Fig. 6.

Table 2. Comparison of manufacturing conditions of EBM and L-PBF

	EBM	L-PBF
Beam source	Electron beam	Laser
Atmosphere	Vacuum	Ar atmosphere (<oxygen 0.1 %)
Preheating	>600 °C	200–500 °C
Powder size	45–105 µm	15–45 µm
Average powder layer thickness	20–100 µm	50–200 µm
Beam scan speed	0.3-1.0 m/s	>1000 m/s

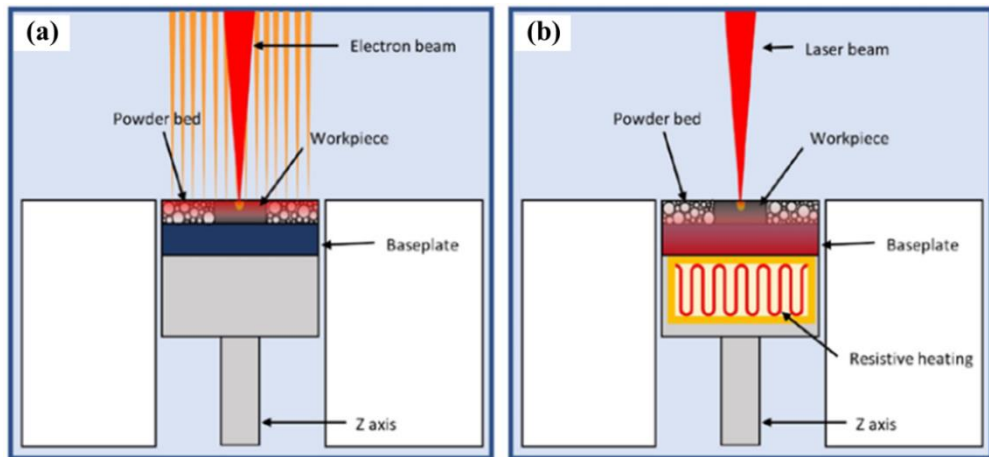


Figure 6. Schematic comparison of pre-scanning heated EBM and L-PBF with preheated base plate [39].

3.2 Materials

3.2.1 Introduction of Ni-based superalloys

A superalloy is an alloy that can withstand operating temperatures usually over 500 °C. Such an alloy retains good mechanical properties at a high temperature that is over 70% of their melting temperature compared to conventional structural alloys [40, 41]. These superalloys are made of group VIII B elements of the periodic table with relatively low reaction rates for mechanical strength and oxidative improvement [42]. Therefore, most superalloys are employed for power generation, aero-engines, exhaust valves, steam turbines, and so forth. Superalloys are classified as Fe-based, Ni-based, and Co-based depending on their base metal, and Ni-based superalloys are the most often used.

Fe-based alloys are widely applied in discs and rotors with relatively low operating temperatures for economic reasons, although they have lower mechanical properties at

temperatures higher than 750 °C. Co-based superalloys are used at extremely high temperatures above 1000 °C, but they have the disadvantage of relative high cost of cobalt. Finally, Ni-based superalloys use nickel as a base metal in combination with other elements, such as Cr, Co, Al, Ta, W, Re, Mo, and C to improve their high-temperature mechanical properties [43]. Table 3 show typical wrought Ni-base superalloy compositions. Ni-based superalloys have become more prominent in recent years due to the limitations of Fe- and Co-based superalloys. In particular, they are used in the main engines of aircraft and gas turbines for power generation, where high-temperature corrosion and oxidation resistance is required. Ni-based superalloys are divided into 'wrought alloys', 'powder metallurgy (PM) alloys' and 'cast alloys' according to the method of manufacture. They are usually manufactured by PM or the casting method if cold working or hot working (e.g. forging, rolling, etc.) is difficult, which is the case if the ratio of gamma prime reinforcement (see section 2.2.2) is between 30% and 40%. Meanwhile, the gamma prime phase increases the creep strength as the fraction increases.

The wrought alloys can be divided into 'solid solution-strengthened alloys', which show high-temperature strength by solutionizing added elements, and 'precipitation-strengthened alloys', which show greatly increased strength due to precipitation by aging treatment.

Table 3. Compositions of typical wrought Ni-based superalloys

	C	Cr	Ni	Mn	Si	Mo	W	Co	Al	Ti	Nb	Cu	Ta	Fe	
Hastelloy X	0.15	22.0	Bal	0.6	0.5	9.0	0.6	1.5						18.5	Solid solution hardening type
Alloy 600	0.04	15.4	Ba.	0.2	0.1									9.7	
Alloy 601	0.03	21.9	Ba.	0.2	0.2	0.1			1.4	0.3	0.1			14.5	
Alloy 617	0.08	21.6	Ba.	0.1	0.1	9.5	0.9	12.5	1.2	0.3					
Alloy 625	0.05	21.5	Ba.	0.3	0.3	9.0	0.9	0.5	0.4	0.4	2.0		1.7		
Haynes 230	0.11	21.7	Bal	0.5	0.4	1.4	1.4		0.3				1.2		
IN718	0.08	20	54	0.1	0.1	2.9			0.5	1.0	5			Bal	Precipitation hardening type (10~50% γ')
Alloy 263	0.06	20	Bal	0.6	0.4	6		20	0.6	2.4		0.2		0.7	
IN740	0.03	25	Ba.	1.2	0.5	0.5		20	0.9	1.8	2			0.7	
Waspaloy	0.03	19	Bal	0.2	0.2	4		13	1.5	3.0		0.2		0.7	

3.2.2 Strengthening mechanisms of Ni-based superalloys

The main strengthening mechanisms for Ni-based superalloys are the solid-solution strengthening effect achieved by the addition of substitute solute atoms, such as Cr, Mo, W, and Co to the FCC- γ Ni matrix, and precipitation strengthening by combining Ni atoms having an FCC structure, which is stable at high temperature, with Al, Ti, and Nb to induce γ' [$\text{Ni}_3(\text{Al}, \text{Ti})$] (ordered fcc structure $L1_2$), γ'' [Ni_3Nb] (bct structure DO_{22}). In both cases, C, B, and Zr can also be added to increase grain boundary strengthening. As the result of adding solute atoms to Ni-based superalloys, various other phases and precipitates can appear depending on the composition, as illustrate in Fig. 7 [44].

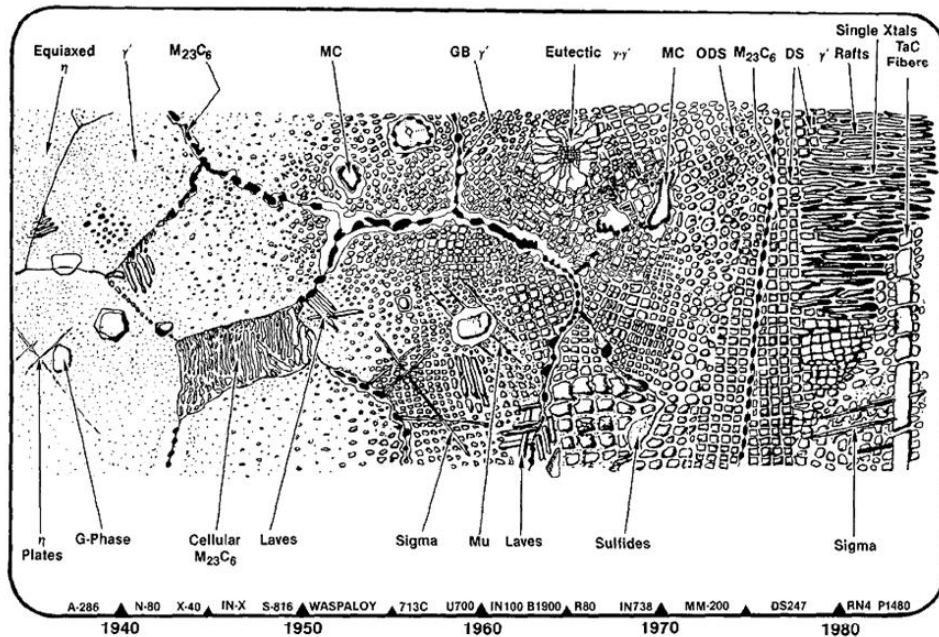


Figure 7. Schematic diagram showing various microstructures with historic development of Ni-based superalloy [42].

Solid-solution strengthening is generally induced by the addition of solute atoms, such as Co, Cr, Mo, and W. Several conditions are required for the achievement of effective solid-solution strengthening, namely, large lattice incoherence with the matrix, low stacking fault energy, and the addition of an element that has a high melting point. Moreover, the lower the diffusion coefficient after solution in matrix the element has, the greater the solid-solution strengthening effect is. Therefore, the elements with BCC structure and the VIB series can lead to effective solid-solution strengthening. Co strengthens the material by lowering the stacking fault energy and making cross slip difficult. Cr contributes to solid-solution strengthening and oxidation resistance by forming Cr_2O_3 on the surface. Furthermore, to improve the mechanical properties as well as the corrosion and oxidation resistance, C and B are added. C forms carbides combined with reactive elements in the amount of 0.05–0.2 wt% in superalloys. Ti, Ta, Nb, W, and Hf form MC-type carbides which decompose

into $M_{23}C_6$ and M_6C at the grain boundaries during operation or heat treatment. Although these carbides are not known to have a significant impact on the mechanical property due to their low volume fraction, they affect the creep property and fracture property when they are precipitated at the grain boundaries. B reacts with Zr and Hf to form an M_3B_2 -type boride, which strengthens the grain boundary system. The role of each solute element added to Ni-based superalloys is presented in Table 4.

Table 4. Roles of alloying elements in the Ni-base superalloys [42, 44].

Phase relation / property	Roles
Solid solutions strengthening of γ	W, Mo, Ti, Al, Cr, Re strengthen Fe, Co, Cu Strengthen slightly
Solid solution strengthening of γ'	Mo, W, Ti, Cr strengthen V, Co weaken Mn, Fe, Cu strengthen slightly
Mole fraction of γ'	Cr, Ti, Al, Nb, Mo, Co, Ta, V, Fe increase
Anti-phase boundary energy	Ti, Co, Mo, Fe increase Al, Cr decrease
γ - γ' lattice mismatch	Ta, Nb, C, Ti increase Cr, Mo, W, Si, V, Cu, Mn decrease Al, Fe, Co, negligible effect
Coarsening rate of γ'	Ti, Mo, Nb, Co, Fe decrease Cr increase B, Zr no effect
Oxidation and hot corrosion resistance	Cr, Hf, Si, Y, La, Pt improve other element variable

Precipitation strengthening of a Ni-based superalloy means strengthening by precipitation of γ' and γ'' phases. Here, γ' is an A_3B -type intermetallic compound having an ordered FCC structure ($L1_2$), which is coherent with the matrix. In an A_3B -type compound, A is mainly composed of electronegative elements, such as Ni and Co, and B is composed of electropositive elements, such as Al, Ti, Nb, Hf, and Ta. Elements like Cr, Mo, W, and Fe can be substituted for either A or B. Accordingly, the general chemical formula of γ' is $(Ni, Co)_3(Al, Ti)$ [45]. The γ' phase is an $L1_2$ -ordered structure in which the Ni atom is located at the center of the crystal, and the Al

atoms are located at each vertex.

There are two main mechanisms of strengthening in a precipitation-strengthened Ni-based superalloy. First, when the γ' phase is precipitated, dislocations movement is hindered, and they stack upon each other due to a coherence difference from the matrix. Secondly, if a dislocation goes into the γ' phase, it shows an anti-phase boundary (APB) and is separated into partial dislocations. The formation of an APB or a stacking fault (SF) between two partial dislocations hinders dislocation's motion, which means that the structure is 'strengthened'.

The precipitation strengthening mechanism is divided into two, 'Orowan bypassing' and 'shearing' depending on interaction between precipitates and dislocations. Shearing mechanism usually occurs when size of the coherent precipitate with matrix is small. The APB and SF take place during dislocation shearing. However incoherent parts are rather subject to bow-out by the Orowan mechanism as size of precipitates increase, dislocations left rings around a precipitate since it is difficult for a dislocation to overcome [46, 47]. Each precipitation contributing to alloy strengthening has critical size (r_0) where the mechanism changes from shearing to Orowan bypassing as indicated in Figure 8.

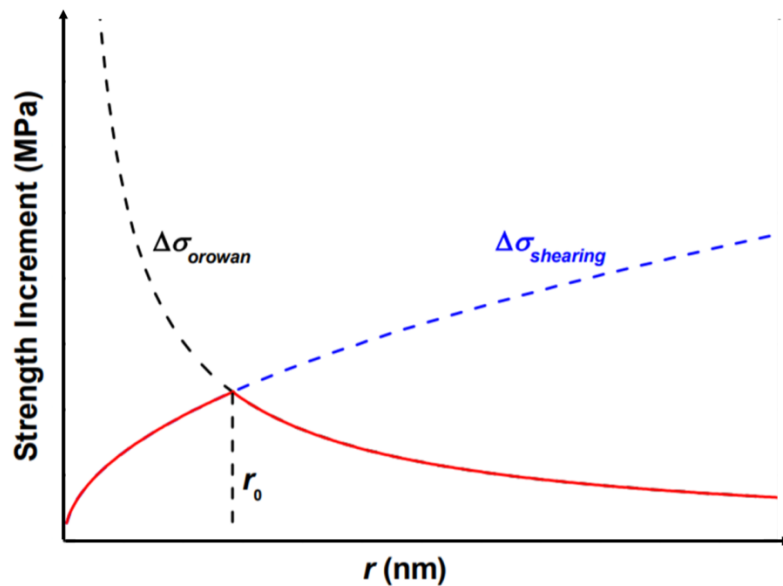
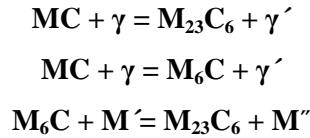


Figure 8. The variation of strength increment with the particle size. The strengthening mechanism is changed by critical size (r_0) of a precipitate [46, 47].

In the case of γ' [Ni_3Nb] phase, it is generated if there are sufficient amounts of Nb and Ta elements in the matrix, and strengthening mechanism is similar to that of the γ' phase. However, it has an ordered BCT (DO_{22}) structure in comparison to the γ' phase. It is characterized by an elliptical shape aligning along the $\langle 110 \rangle$ direction of the matrix. In addition, because it is a metastable phase, if it is exposed for a long time at the temperature of 650 °C or higher, the phase transforms to an acicular δ -phase [Ni_3Nb] with an orthorhombic DO_a structure [48–50].

Large amounts of solute elements are added to improve the high-temperature mechanical properties of Ni-based superalloys, which are combined with the C. The carbides present in Ni-based superalloys are mainly observed at the grain boundaries; these include MC, M_{23}C_6 , and M_6C . MC carbide is generated at high temperature combining Ti, Ta, Nb, W, Co, Cr, and Hf with C, which is produced in the form of a blocky and script shape during solidification. The M_{23}C_6 carbides are produced in the temperature range of 790 to 816 °C, especially when Cr binds to C, which is deposited

in the grain boundaries and improves creep resistance. M_6C carbides are produced in a temperature range of 816 to 982 °C in alloys containing large amounts of Mo and W, and they have excellent high-temperature stability. As shown above, these carbides have a stable temperature range and react with different phases to form other types of precipitates. They undergo the following reactions [51]:



Here M' is gamma phase depleted in certain alloying elements and M'' gamma phase of slightly different composition

The other phases which can be found in Ni superalloys are topological close packed (TCP) phases, and they include laves phases, μ , η , and σ . They are precipitated as plate or acicular shapes in Ni-based superalloys. They are brittle, so when they are subjected to stress, they are susceptible to cracking around them and their morphology make them preferential crack initiation sites. Therefore, TCP phases should be suppressed as much as possible. In particular, the σ phase, which is a metallic compound formed in the range of 650 to 925 °C, is the most problematic one. It is characterized by a structure similar to $M_{23}C_6$ carbide. Hence, it is mainly nucleated in $M_{23}C_6$ carbide, and its formation rate increases when the material is stressed [52]. Table 5 summarizes the composition and crystal structure of the above-described phases and some other phases that may be formed in Ni-based superalloys.

Table 5. Summary of composition and crystal structure for the various phase in Ni-based superalloys [42-44].

Phase	Chemical formula	Ti	Nb	Mo	Cr	Fe	Lattice	Lattice parameters (Å)
-------	------------------	----	----	----	----	----	---------	------------------------

γ -matrix	-	-	-	-	-	-	fcc	a=3.58-3.62
γ'	Ni ₃ (Al, Ti)	-	-	-	-	-	fcc-ordered	a=3.58-3.62
γ'' -MN ₃	Ni ₃ Nb						bct-ordered	a=3.62, c=7.41
δ -MN ₃	Ni ₃ Nb	4.5	19	1	4	2	orthorhombic ordered	a=5.14, b=4.25, c=4.53
Laves, MN ₂	(Nb, Ti)(Fe, Ni, Cr) ₂	1-3	26- 29	2-4	13-15	11-12	hexagonal	a=4.74, c=7.72
M ₃ B ₂ boride	(Nb, Ti, Cr) ₃ B ₂	1-3	37- 44	10- 35	22-27	3-5	tetragonal	a=5.78, c=3.16
MgO				91Mg			cubic	a=4.21
MNP phosphide	Nb(Ni,Fe,Cr)P	2	45	4	14	7	hexagonal	a=6.11, c=7.09
(Ti,Nb)CS		50	43		2		hexagonal	a=3.21, c=11.20
η -phase	Ni ₃ (Ti,Nb)	-	-	-	-	-	hcp	a=5.10, c=8.31
σ -phase	CrFeMoNi	-	-	-	-	-	tetragonal	a=8.80, c=7.70
M ₆ C	Fe ₃ Nb ₃ C	-	-	-	-	-	fcc	a=10.85- 11.75
M ₇ C ₃	Cr ₇ C ₃	-	-	-	-	-	hexagonal	a=13.98, c=4.52
M ₂₃ C ₆	Cr ₂₃ C ₆	-	-	-	-	-	fcc	a=10.56- 10.65
MC	TiC, NbC	8-8.5	15- 84	<3	<6	<1	cubic	a=4.47
M(C,N) carbonitride	(Nb,Ti,Zr)C,N	-	-	-	-	-	cubic	a=4.24-4.47

3.2.3 Introduction of Alloy 625

Alloy 625 was invented around 1964 for application in high-pressure steam lines in power plants, and its application in industry was gradually broadened due to its robustness in harsh environments. As presented in Figure 9, this alloy was originally developed from Alloy 600 to improve the corrosion properties; it can endure highly acidic environments, marine conditions, and high temperature conditions (from cryogenic to 980 °C in theory) [53].

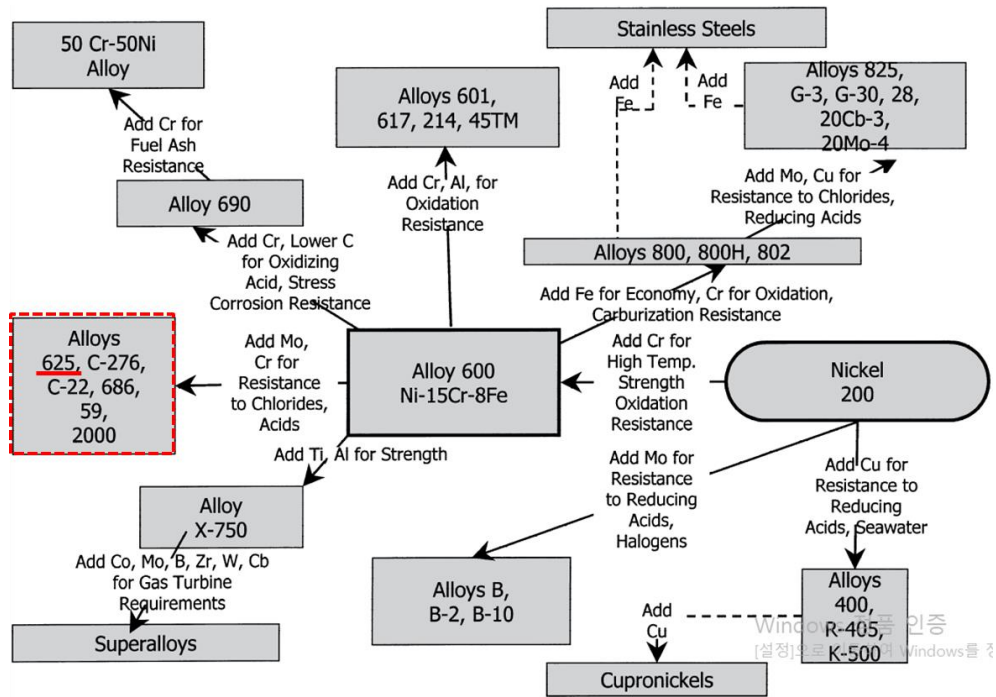


Figure 9. Block diagram of Ni-based superalloy development [54].

In addition to these properties, highly alloyed Alloy 625 can provide high strength in harsh environments. Its nominal composition is presented in Table 6. Mo has the solid-solution-strengthening effect on its matrix with Fe and Nb. In addition, it contributes to the good corrosion resistance together with high level of Cr content. Al and Ti are added in small amounts mainly for refining purposes to enhance weldability by suppression of the γ' phase in comparison to other alloys, such as Alloy 718, while a sufficient Nb+Ti+Al content has a positive effect on precipitation hardening owing to the presence of the γ'' phase [55].

On the other hand, large amounts of alloy elements do not always have good effects. When this alloy is solidified from the liquid state, the dominating solidification reaction is the enrichment of the remaining interdendritic liquid in Nb, and the

consequent formation of Nb-rich laves phase and/or Nb carbide during the final stages of solidification. The phase formation during solidification is governed by the C/Nb ratio; the formation of γ +NbC occurs with no laves phase at a high C/Nb ratio. First γ +NbC is formed, followed by laves phase formation at the end of solidification at an intermediate C/Nb ratio; γ +laves is formed with no NbC at a low C/Nb ratio. The primary NbC carbide that appears when it is solidified is normally very large, and it can be serve as a crack initiation site in the presence of an external load. Thus, it is preferable that this compound be dissolved during the solid-solution process to the greatest extent possible.

Table 6. Element composition of Alloy 625

Ni	Cr	Fe	Mo	Nb	C	Mn	Si	P	S	Al	Ti
Bal.	20-23	5.0*	8.0-10.0	3.15-4.15	0.1*	0.50*	0.50*	0.015*	0.015*	0.40*	0.40*

* means maximum value

3.2.4 Precipitation formation of Alloy 625

Three different types of carbides, namely, MC, M₆C, and M₂₃C₆ as well as intermetallic phases, such as γ'' and δ can precipitate in Alloy 625 as indicated in Figure 10. Each precipitate is formed during heat treatment depending on the precipitation temperature and duration. Three kinds of carbides are usually precipitated at the grain boundaries. The MC carbide (M is Nb and Ti) is precipitated as thin grain boundary films at the temperature range from 871 to 1037 °C, but it is usually present during solidification as a large primary carbide. The primary MC carbide consumes a large amount of Nb, which is one of the main elements for strengthening; hence, homogenization and solid-solution treatment are accordingly required. M₆C carbide (M is Ni, Nb, and Mo) and M₂₃C₆ carbide (M is almost entirely Cr) commonly have a blocky shape and stable up to 1080 °C and 700 to 800 °C

respectively [57]. γ'' is a main strengthening precipitate of this alloy whose strengthening mechanism comes from having coherence with the γ -FCC matrix. This precipitate presents an elliptical disc shape from the tetragonal crystal structure. Its strengthening mechanism is, analogous to γ' , formation of APB or SF between two partial dislocations when a dislocation tries to pass through this particle. Formation of γ'' requires aging treatment in a temperature range of 600 to 650 °C for over 20 hours, whereas it can be formed by short-term aging when it is aged at higher temperature about 650 to 750 °C [58]. This phase is thermally unstable; it ultimately changes to equilibrium phase δ . The δ orthorhombic incoherent phase presents an acicular shape. It can be formed by transformation from the γ'' phase or directly by aging treatment [59].

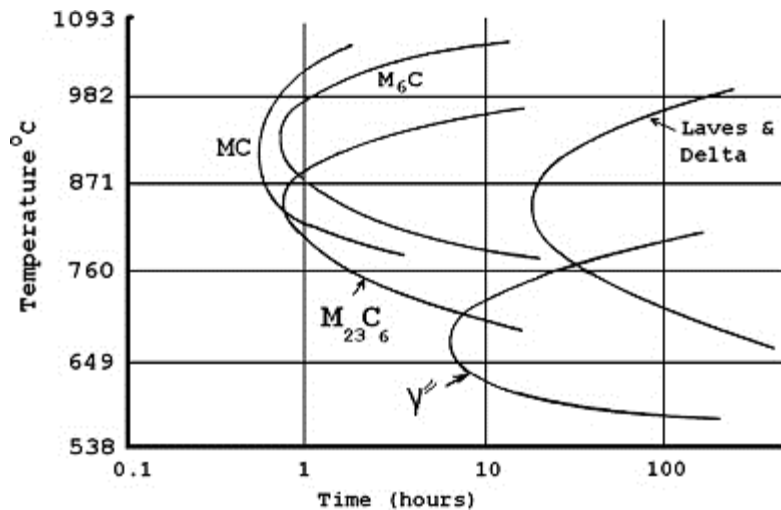


Figure 10. Time-temperature transformation (TTT) diagram of Alloy 625 [56].

3.2.5 L-PBF manufacturing of Alloy 625

Alloy 625 is one of the most widely used Ni-based superalloys along with 718 for

AM fabrication by PBF. This alloy, in particular, is usually used for the manufacture of parts through the PBF method. On the surface, unmelted powder particles are often observed because of the low chance of re-melting which is something in common of most additive manufactured part. In addition, for samples with curved or sloped surfaces, due to the AM nature of layer-by-layer scanning, step marks appear on the surface called staircase effect requiring proper surface treatment according to the application environment of the sample. The L-PBF method results in relatively better surface properties because of the smaller melt pool size from the lower heat source compared to EBM.

Alloy 625 produced by L-PBF varies slightly depending on the processing conditions, but generally Nb and C are segregated on the liquid/solid interface during manufacture, resulting in NbC carbides. However, because this is caused by rapid heating/cooling, segregation in the form of a very thin film appears, and the resulting carbide size is as small as submicron size. This has a better effect on the mechanical properties than a large primary NbC carbides found in wrought Alloy 625, which is likely to be a crack initiation site, which appears during standard solidification. In addition, high density of dislocations generated by rapid heating/cooling contributes to high strength together with fine NbC. A high density of dislocation is observed in columnar arrangements according to the scanning direction; NbC of submicro size is mainly observed at the columnar interface (figure 11).

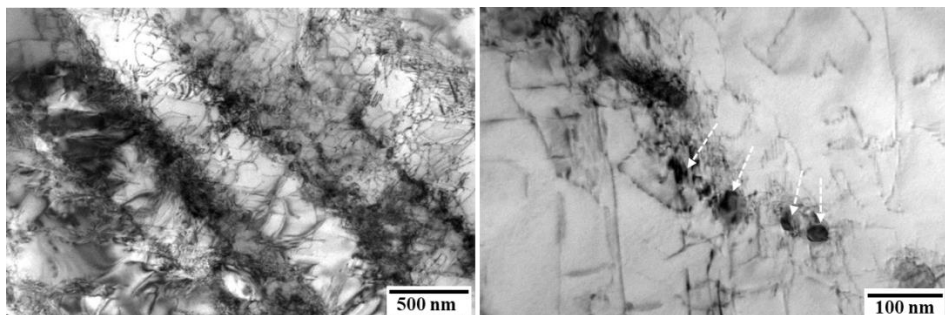


Figure 11. (left) High density of dislocations forming columnar structure in L-PBF Alloy 625

and (right) fine NbC precipitated at the columnar interface.

Alloy 625 made by L-PBF is known to begin to recrystallize after heat treatment at temperatures higher than 1000 °C, and heat treatment alone can lead to recrystallization because of the high density of dislocations generated during the manufacturing process. With a high density of dislocations, the as-built sample has very high strength with low elongation capacity; thus, it requires heat treatment to recover some ductility. Accordingly, several studies have been conducted to compare the mechanical properties of Alloy 625 after heat treatment, and the findings are summarized in the table below.

Table 7. Comparison of room-temperature tensile properties of Alloy 625 manufactured by the PBF method and performed heat treatments.

Manufacturing / condition	Tensile property (YS(MPa)/UTS(MPa)/El.(%))	reference
ASTM (standard) F3056–14	275/485/30	
L-PBF/as-built	800 ± 20/1030 ± 50/8–10	[60]
L-PBF/as-built (modified 625 composite)	641.5 ± 23.5/878.5 ± 1.5/30 ± 2	[61]
EBM/ annealing treatment (1120C/100MPa/4h)	360/-/58	[62]
L-PBF/ Stress-relieved + HIP (1120C/100MPa/4h)	507/ 827/69..3	[63]

All of the above mentioned studies were conducted at room temperature; very few studies have been conducted on the mechanical properties of the alloy at high temperatures, which are the conditions under which this alloy is actually used. Furthermore, most of the studies were performed with L-PBF as-built without any microstructure control through post-heat treatment.

3.3 Introduction of coatings on superalloys

Superalloys are generally used in environments in which oxidation and hot corrosion can easily occur, such as high temperature and seawater applications. In addition to this, degradation caused by oxidation tends to be worse with increased temperature. However, application at very high temperatures is required with the development of technologies. In addition, it is desirable for superalloys to keep their mechanical properties as long as possible in harsh environments [64].

For the long-term performance of the alloy, degradation due to external factors must be minimized. Coating on the alloy surface is essential to maintain its mechanical properties. Surface coating improves resistance to oxidation/corrosion, and reduction of temperature enables the alloy to operate above its incipient melting temperature. A ceramic material used as a coating is able to drop the surface temperature due to its low thermal conductivity [65]. Some coating possesses an elements reservoir for the formation of a protective dense oxide layer at the interface between the coating surface and air. The elements react with detrimental factors attacking alloys to protect them [66]. There are three types of coatings generally used in industry; diffusion coatings, overlay coatings, and thermal barrier coatings (TBCs) as shown in Figure 12.

Diffusion coatings are most commonly used; they use at least one of the major constituents from the base metal by diffusion for the coating property. This type of coating is composed of an external diffusion zone and an internal diffusion zone. An external diffusion zone is developed by reaction with the elements in the alloy substrate, and the internal diffusion zone is a mixed zone of the substrate and coating elements. Diffusion of Cr, Si, and other elements can be used for the prevention of Type II corrosion (650 to 800 °C), and Al diffusion with Pt, Pd, and/or rare earth elements can contribute powerful resistance to Type I corrosion (800 to 950 °C). However, it has an oxidation resistance limit, which led to greater interest in overlay

coatings [68].

Overlay coating, also called MCrAlY coating (M stands for Ni or Co or Ni+Co), has independence from the substrate elements as opposed to diffusion coatings. It supplies all the constituents in the coating itself. This method has the advantage that it provides resistance to both Type I and Type II corrosion and oxidation. The coating thickness is not limited by process considerations, and the thicker the coating is, the better oxidation/corrosion properties it can have. High-temperature heat treatment is required to homogenize the coating and ensure its adherence to the substrate [69].

TBCs are composed of a bond coating part (MCrAlY) and a ceramic top coat part (ZrO_2 -7 wt% Y_2O_3). The bond coat part is primarily deposited on the substrate alloy surface between the substrate and top coat. It balances the thermal expansion mismatch between two different layers because failures often occur due to delamination of the coating part due to the thermal expansion difference. In addition, it provides oxidation resistance as a reservoir of oxide film formation elements and provides roughness, which improves top coat adherence. Gas turbine engines show improved efficiency when this coating method is adopted. It is used in combustion cans, transition pieces, nozzle guide vanes, and blade platforms [66, 70].

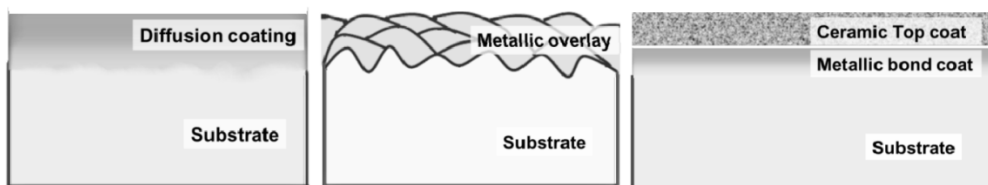


Figure 12. Schematic of general coatings used for superalloy applying at high temperature; diffusion coating, overlay coating, thermal barrier coating (from left to right) [67].

3.3.1 Introduction of MCrAlY coatings

MCrAlY coating is often applied to structural materials used at high temperatures, such as turbine blades and vanes. Oxidation/corrosion damage of Ni-based superalloys can be generally prevented by overlay MCrAlY coating. The element M depending on the substrate matrix, is usually composed of Ni, Co, or NiCo. Cr is added to provide resistance to hot-corrosion, and Al is required to form the surface oxide layer on the surface of the superalloy substrate. Most of the MCrAlY is composed of FCC- γ matrix due to its high solubility of Cr and Al, 25% and 11%, respectively, and preferable mechanical properties like high temperature characteristics and good toughness. The Y elements improve resistance to oxygen diffusion taking place along grain boundaries and a thermally grown oxide (TGO) layer by substituting into the alumina or segregating at the grain boundaries (GBs). Moreover, Y-oxide pegs can act as anchors on the coating surface to enhance the TGO adhesion. It plays different roles depending on the oxide type; it promotes the formation of chromia scale, decreases the scale growth rate, improves scale adherence in chromia-forming alloys, whereas its major role is improving the adherence of the scale in alumina-forming alloys [71–73].

The coated MCrAlY shows four types of representative phases as seen in Table 8, namely, γ , β -NiAl, γ' , and α -Cr. Based on the predicted phase map (Figure 13) of NiCrAl (typically 22 wt% Cr and 10 wt% Al, bal. Ni, the very low amount of Y was not taken into account), γ and β -NiAl phases appear at high temperature, and they would transform to γ' and α -Cr phases around 975 °C having volumetric change. This volumetric change may lead to internal stress within the coating part; therefore, care must be taken when it is subjected to thermal treatment [74, 75]. Meanwhile, the coating property depends on the diffusion rates of active metal elements and oxygen atoms. If the diffusion rate of active metal elements, especially Al and Cr, is faster than that of oxygen atoms attacking the alloy, external oxidation, TGO, takes place at the surface of the coating part. Otherwise, if the reverse is true, internal oxidation may take place at the interface of the substrate and coating. This internal oxidation is highly undesirable because it does not protect the alloy substrate from the external

environment, and it generates volumetric change, which gives rise to tension stresses at the surface, which causes susceptibility to thermomechanical fatigue and the development of an inhomogeneous surface oxide layer [76].

Table 8. Phase information of NiCrAlY alloy.

Phase	Crystal structure	Lattice parameter (Å)
γ (NiCr)	fcc	3.52
γ'	ordered fcc, $L1_2$	3.572
β -NiAl	ordered fcc, B2	2.88
α -Cr	BCC	2.88

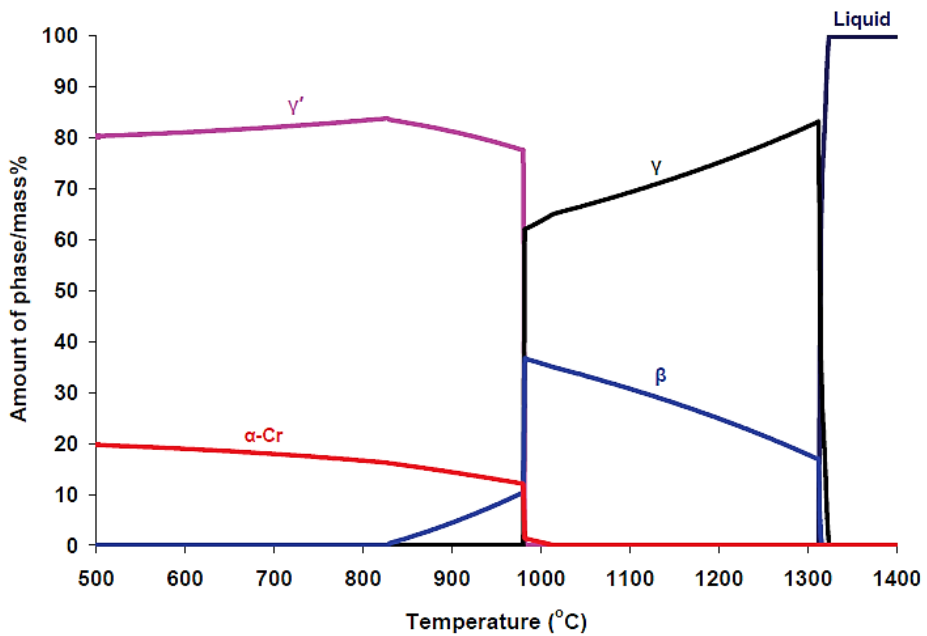


Figure 13. Predicted phase map of NiCrAlY alloy (typically 22 wt% Cr and 10 wt% Al, bal. Ni, the very low amount of Y was not taken into account) [77].

For the evaluation of the oxidation properties and estimation of the remaining life

of the coating part for the high temperature, the volume fraction of the β -NiAl phase is often measured. The β -NiAl phase functions as a reservoir of Al, which is an important element in the formation of an Al_2O_3 surface oxide layer interacting with oxygen. As the Al element is consumed by internal/external oxidation, a β -NiAl phase depletion zone develops near the coating surface and coating-substrate interface part like figure 14. Based on the remaining volume fraction of the β -NiAl phase, the oxidation life and oxidation property can be estimated.

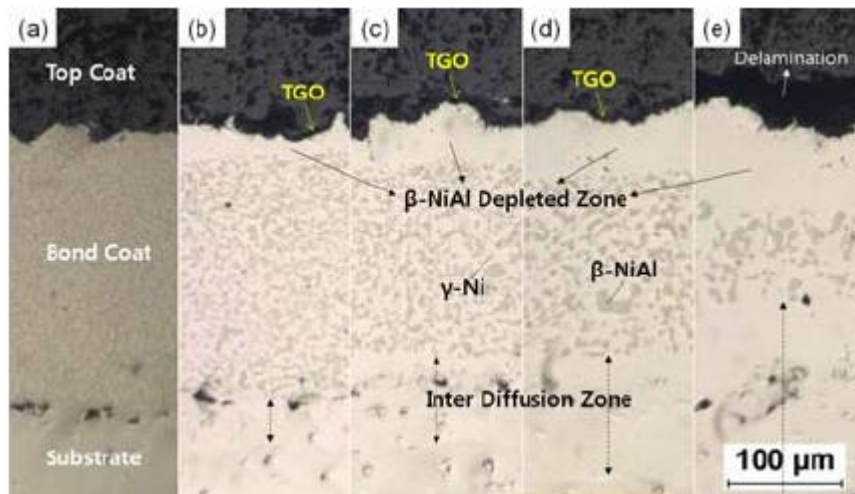


Figure 14. One example of heat-exposed (from (a) to (e)) MCrAlY coated GTD-111DS sample at 1100 °C. Volume fraction of β -NiAl phase in the bond coat part is decreased and depleted zone is increase with longer exposure time [78].

The present study, to improve the high-temperature properties of Alloy 625 produced by L-PBF, a multi-material was fabricated by bonding MCrAlY to the alloy surface in the same way. Recent research on the production of multi-materials by AM includes studies on stainless steel and copper alloys [1–3], a composite material mixing two different powders [79, 80], NiCrAlY cladding [81–83], a developed

methodology based on the selective laser melting (SLM) concept [84] innovative AM of a steel-ceramic multi-material [85] among others. In this work, MCrAlY was introduced for the L-PBF production of MCrAlY coated Alloy 625 for the first time, to the best of our knowledge; by verifying its validity, it will be able to take the first step to contribute more efficiently to the production of coating alloys in the industrial field, and further lay the groundwork for future equipment improvement and research directions in the AM field.

3.4 Grain boundary strengthening of γ matrix

GBs play a key role when a sample is subjected to creep condition. Generally, high-angle GBs are very weak at high temperatures due to the GB sliding effect, especially under creep condition. Therefore, single-crystal alloys which have no grain boundaries being produced by directional solidification method are preferred in very high-temperature applications, such as turbine blade. Each of their brief microstructure is indicated in Figure 15. However, the particular manufacturing process of single-crystal alloys has led to interest in GB strengthening of polycrystalline alloys due to its difficult manufacturing process. Therefore, two representative grain-boundary-strengthening methods were described in the following section.

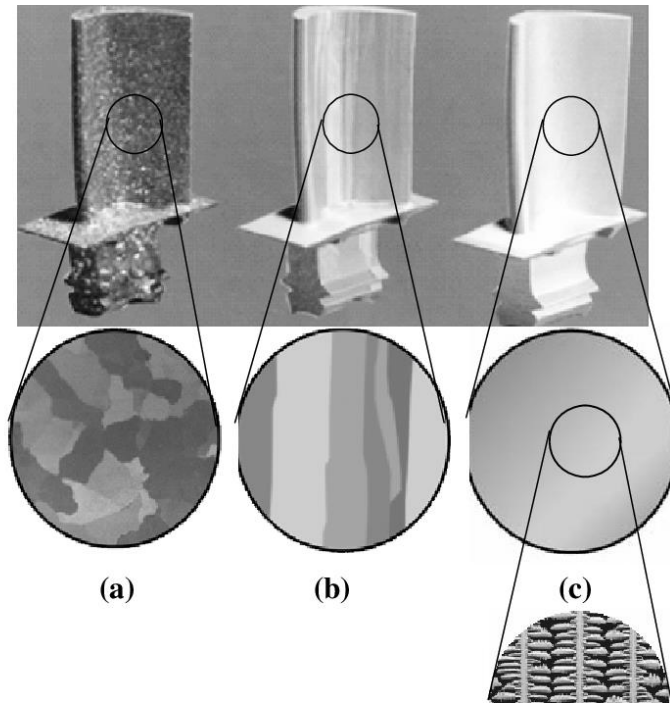


Figure 15. Comparison of polycrystalline, directional, and single-crystal alloys [86].

3.4.1 Improvement of GB cohesion strength in Ni-based superalloy

There are various ways to achieve GB strengthening by improving GB cohesion. The first method is adding GB-strengthening elements, which are generally known elements, such as B, C, Zr, Hf, and Y. These elements in small quantities can improve the mechanical properties of alloys significantly due to their effects on GBs. They tend to move to the GBs on account of their different atomic sizes and electronic properties, which results in GB stabilization, providing high cohesive strength [42, 44]. The effect of each element has been studied. B is good for ductility and having a highly strengthening influence with Hf, whereas C has little or no effect. Regarding Zr, it has been reported that it shows a slight embrittlement effect. Moreover, regarding their contribution to the high-temperature mechanical properties, they inhibit the formation

of GB carbides, such as $M_{23}C_6$ and M_6C , which are brittle when they are coarsened and have the potential to initiate cracks easily when the Ni-based superalloy is exposed to high temperatures [87].

In the second method, the proportion of special GBs is increased, known as GB engineering (GBE), typically for the face-centered cubic (FCC) system. A special GB is a low-index boundary plane or low-coincidence site lattice (CSL) plane like twin boundaries ($\Sigma 3$) that have resistance to intergranular degradation due to their very low disorientation and stable configuration of the interface. Its mechanism is explained by the term ‘ $\Sigma 3$ regeneration’ based on $\Sigma 3^n + \Sigma 3^{n+1} \rightarrow \Sigma 3$. This method requires a threshold level of $\Sigma 3$ s and a driving force for selective GB (mainly incoherent $\Sigma 3$ s and some $\Sigma 9$ s) migration. It can be achieved by generating a proper amount of annealing twins and replacing the random boundary (high CSL) with the incoherent $\Sigma 3$ s [88].

GB serration is another method to improve GB cohesive strength. The concept of the GB serration method is similar to GBE, which produces special boundaries. Through this method, GBs are produced with a wavy configuration via specialized heat treatment. Although the total area of the GB plane is increased, so it is not expected to have a positive effect on grain boundary sliding occurring condition, it has been proved by some studies that serrated GBs are arranged along the low index plane (close to $\{111\}$) of each neighboring grain alternately. Thus, the alloy was highly resistant to crack initiation and propagation. This method is based on the GB phase-transition theory suggested by Hsieh et al. who observed GBs with a flat and smoothly curved interface with temperature change [89].

3.4.2 GB serration

Grain boundary serration (GBS) refers to wavy grain boundaries (GBs) having an amplitude and a period, usually occurring during cooling after homogenization heat

treatment [90, 91]. When a Ni-based superalloy is under creep condition, cracks initiate and propagate along the GBs, which are vulnerable at high temperature, while the serrated GBs make the sample resistant to the crack propagation due to its specific GB configuration; therefore, creep life is extended by improvement of creep rupture strength [91].

A study to figure out the mechanism of GBS is still ongoing. The mechanism for generating GBS [90–93] has been attributed to the interaction between GBs and precipitates, which is preferentially precipitated around GBs during slow cooling. For example, as the γ' phase grows asymmetrically in the direction of a GB, the GB is pushed to be moved by the γ' phase [92], the suppression of GB motion when the γ' phase is pre-precipitated around the GB [94], or the GB is led and moved as the γ' phase moves toward the GB [91]. This GBS mechanism theory assumes that the γ' phase has to be preferentially precipitated before the formation of GBS.

Hong et al. [4,5] reported that high-temperature mechanical properties were improved by introducing GBS into solid-solution-strengthened alloys, namely, Alloy 230 and Alloy 617, which both have very low γ' volume fractions. In addition, they demonstrated that GBs become serrated without any influence of inter/intra granular precipitates during slow cooling of the heat-treatment process. They also confirmed that the direction of the serrated GBs was almost $\{111\}$, which is a close-packed plane in FCC; thus, the GBs were stabilized by lowering the interface energy. According to this new theory, GBS can be introduced considering following conditions. First, the newly attempted GBS formation theory is unlike the conventional GBS formation theory [88, 90]; GBs are independent of precipitates, and GBS is formed preferentially by GB motion prior to GB precipitation. Therefore, for a GB moving freely, the precipitates that were inhibiting the free movement of the GB must be completely dissolved during solid-solution treatment, and precipitation should be delayed as much as possible during the process of GBS formation. Secondly, sufficient thermal activation energy should be provided to allow the GB itself to move smoothly. Finally,

the GBS phenomenon is similar to phase transition, which occurs spontaneously to reduce free energy at each temperature during cooling [89, 95]; that is, sufficient time should be provided to maintain an equilibrium configuration of GBs at each temperature during cooling from high temperature to low temperature.

Several studies related to inducing GBS have been reported [4, 5, 95]; however, no study about the Nb-rich solid-solution strengthened Alloy 625 has been reported ever. The target alloy has a relatively high Nb content, which easily appears in the NbC-type carbide as opposed to the previous studies [4, 5, 95]. Therefore, the above theory of GBS formation was newly introduced for the Nb-added solid-solution-strengthened Alloy 625, and in-depth analysis of the mechanism of GBS formation was conducted.

IV. Methodology

The commonly used equipment and methods are described here, but special methods and machines are indicated in each paper (Section 4.3 Introduction of articles)

4.1 Alloy 625 and MCrAlY powders

The element composition of each powder was analyzed by Inductively coupled plasma atomic emission spectroscopy (ICP-OES), and the results are shown in Table 9. Alloy 625 powder provided by the L-PBF machine manufacturer was used to build substrate material. Most particles were spherical with some satellite particles. The powder-size distribution was measured by using a laser particle-size analyzer. The particles had a size distribution between 20 μm (D10) and 44 μm (D90) with an average volume diameter around 29 μm . Additionally, the powder flow rate was measured by the Hall flow method (standard ASTM B 213); 50 g of powder was passed through a funnel, and the time it took was registered as the flow rate. The funnel had a 30° cone angle and a \varnothing 2.5-mm outlet hole. The results of the powder flow rate were 12.6 sec.

NiCrAlY powder provided by DUCAL Corporation composed with generally known element composition (Table 9) has same powder morphology as that of Alloy 625. The powder-size distribution resulted in between 24 μm (D10) and 51 μm (D90) with an average volume diameter around 35 μm (Figure 16). The powder flowability, which was measured in the same manner as Alloy 625 was 17.4 sec.

Table 9. Chemical composition in wt.% of the Alloy 625 and NiCrAlY powders used.

	Ni	Cr	Mo	Fe	Co	C	Nb	Al	Y
Alloy 625	Bal.	20.80	8.27	3.49	0.6	0.08	3.12	0.35	-

NiCrAlY	Bal.	22.01	-	-	-	-	-	9.34	1.17
---------	------	-------	---	---	---	---	---	------	------

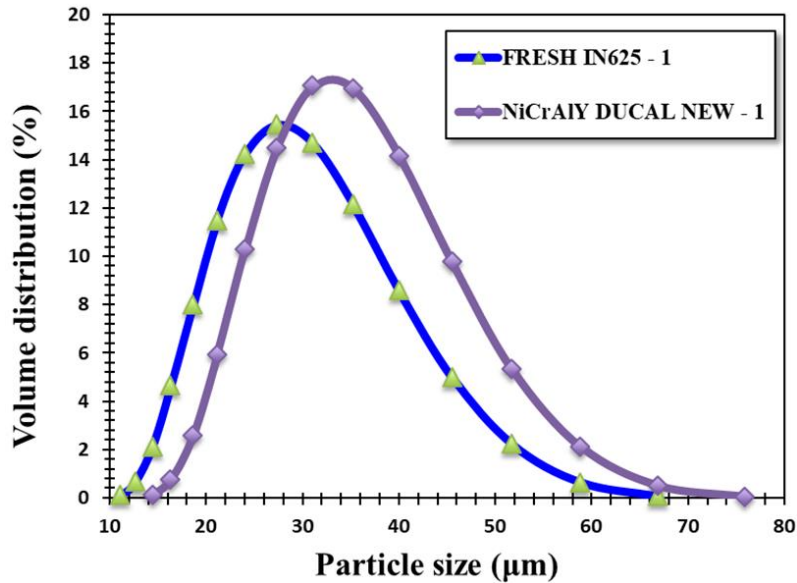


Figure 16. Comparison of powder size distribution.

4.2 Additive manufacturing

A SLM 125 HL (SLM Solutions) L-PBF machine, which has a build chamber size of 125 mm × 125 mm × 125 mm was used to manufacture all samples in this study. The machine system is equipped with a 400-watt fiber laser as the energy source (80-µm laser beam diameter). Argon was used as an inert gas in the build chamber. The stripe scanning strategy with stripe length of 10 mm and 33° orientation rotated incrementally between layers was used for Alloy 625 fabrication by adopting default parameter condition (power: 275 W, scanning speed: 760 mm/s, hatch distance: 120 µm, layer thickness: 50 µm) and non-rotation for NiCrAlY (for the oxidation test samples, rotation was exceptionally adopted with 67° to give same condition with substrate manufacturing). For the parameter condition of NiCrAlY, the optimization of

L-PBF fabrication of a NiCrAlY bond coat onto an Alloy 625 substrate, itself produced by L-PBF has been studied as one part of this thesis [4.3.1]. Therefore, laser power $P=250$ W, laser scanning speed $v=800$ mm/s were selected based on several criteria. The process environment conditions, such as platform preheating ($T = 200$ °C) and O_2 content ($<0.10\%$) remained unchanged in all research series. A constant layer thickness of 50 μm was set by lowering the build platform. A low carbon steel plate that could handle heat conduction of the Alloy 625 substrate was placed on the building platform (x-y table) and levelled.



Figure 17. L-PBF machine used in present study.

4.3 Microstructure analysis

Sample preparation: All samples were mounted and polished with SiC abrasive paper down to 1200 grit followed by sequential polishing with 1- μm diamond paste. They were then etched using Aqua Regia (as-built, heat treated, oxidation tested and thermal shock tested samples) and 100 ml of HCl with 0.5 g of CrO_3 mixed etchant

(tensile tested samples) for optical microscopy (OM) and scanning electron microscopy (SEM) analysis.

Transmission electron microscopy (TEM) samples were prepared by polishing to a thickness of ~200 μm . Then 3-mm diameter discs were punched from these thinned samples, which were electropolished to electron transparency in a TenuPol-5 jet polisher operated at a polishing current of 50 mA at a voltage of ~25 V, using a solution consisting of 200 ml of perchloric acid and 800 ml of methanol at $-26\text{ }^{\circ}\text{C}$ to $-28\text{ }^{\circ}\text{C}$.

4.4 Observation

- Optical microscope (OM, OLYMPUS BX51M)
- Scanning electron microscope (SEM, JSM-6510)
- Field-emission transmission electron microscope (FETEM - JEOL JEM-2100F operating at 200 kV) equipped with energy dispersive X-ray spectroscopy (EDS) detector at 200 kV

4.5 Experiments

- **Tensile test:** Tensile specimens were tested with an RB 301 Unitech-T electromechanical machine using a strain rate of 1.5 mm/min at room temperature and 0.5 mm/min at high temperature
- **Heat treatment:** All heat treatments were performed using a box-furnace-equipped programmable controller that was able to control the temperature, time, and cooling rate
- **TGA test:** Isothermal oxidation tests were conducted in air at 800, 900, and 1000 $^{\circ}\text{C}$ for a maximum duration of 200 hours. Bulk Alloy 625 and NiCrAlY samples were oxidized for 48 hours in a SETSYS thermobalance from SETARAM to continuously

record the mass evolution during the high-temperature exposure. Samples were directly hung in the furnace using a platinum suspension. For NiCrAlY-coated Alloy 625 samples, thermogravimetric analysis was performed using a NABERTHERM N 11/H furnace. The temperature was verified with a K-type thermocouple, and the mass evolution was measured using a precision balance (SARTORIUS MC5). The samples were hung in an alumina crucible with platinum wires to expose all sample faces to the environment. Interruptions at definite exposure times were carried out at 5, 10, 20, 50, 100, and 200 hours to document the evolution of the mass gain and the nature of the oxidation products.

-Thermal shock test: The machine used for the thermal shock test was a specifically designed ‘Burner Rig’ produced by Hysytech SRL Corporation. For each sample, 450 cycles were carried out. Considering the nature of the superalloy substrate, a maximum temperature of 950 °C (2 min plateau) and quenching to 300 °C was conducted. Heating to 950 °C took approximately 1 h, and quenching to 300 °C took under 1 min. Only methane was burnt, and the air/methane ratio was set to 1.2 to provide an oxidizing environment. The specimens were weighted with a precision balance (0.1 mg) and photographed after each 30-cycle session to study the evolution of the materials.

V. Publications and scientific contribution

5.1 Focus of research

- Manufacturing an operational NiCrAlY coated Alloy 625 bi-material system by L-PBF.

⇒ Each property of only substrate and coated alloy has to be evaluated and improved to certify for commercialization/application.

- The microstructure of various heat treated L-PBF Alloy 625 was investigated and their tensile properties were compared at room temperature.

⇒ For considering real operation conditions of the alloy, high temperature properties investigation was considered. Furthermore, GBS was chosen as a one way to improve the high temperature mechanical properties. Therefore, GBS mechanism is needed to be investigated for the first step to apply to Nb added Ni-based superalloy (Alloy 625) for the first time.

- GBS mechanism was understood for the first time with a model alloy.

⇒ The next step is applying GBS to wrought Alloy 625, the standard alloy.

- Application of GBS to wrought Alloy 625 was succeeded.

⇒ Finally it was ready to apply GBS to L-PBF Alloy 625.

- GBS was successfully induced in L-PBF Alloy 625 and its high temperature tensile properties were assessed with recrystallized L-PBF, L-PBF As-built and wrought Alloy 625. Microstructure controlled L-PBF Alloy 625 showed higher strength than wrought one and higher ductility than L-PBF As-built at high temperature. Especially GBS induced sample has resistance to DSA occurrence.

⇒ Further study about resistance to oxidation and thermal shock of L-PBF

NiCrAlY coated alloy is required.

- TGA test for the bulk Alloy 625, bulk NiCrAlY and NiCrAlY coated Alloy 625 all manufactured by L-PBF was conducted and coated sample showed intermediate oxidation resistance between two bulk samples. Therefore, the fabrication of coated components by L-PBF is not trivial.
- Thermal shock test was tested for As-NiCrAlY coated sample with and without top coat. Additionally GBS heat treated As-NiCrAlY coated sample with top coat was also applied. There was no delamination between substrate and NiCrAlY bond coat layer, which means its thermal expansion/contraction property is stable even in the rapid cooling/heating condition.

The optimized parameters of L-PBF fabrication of a NiCrAlY bond coat onto an Alloy 625 substrate are described based on several criteria. Significant remelting of the underlying substrate led to the formation of an intermediate dilution zone, which indicates excellent metallurgical bonding. This result suggests the feasibility of L-PBF as an alternative method for the deposition of coatings in TBC systems or MCrAlY coating itself. Prior to evaluation of the properties of each coated sample, the reliability of the mechanical properties of the Alloy 625 substrate was firstly evaluated. Because of this reason, tensile testing at ambient temperature of the L-PBF fabricated Alloy 625 was firstly conducted.

Three different heat treatments were performed to obtain the specific mechanical properties of the L-PBF Alloy 625. Through direct aging treatment, solid-solution treatment, solid-solution followed by aging treatments, the samples showed three different microstructures and tensile properties, which were compared to those of the as-built sample. The as-built sample showed high tensile strength due to the high dislocation density and fine MC carbides with very fine dendritic structures. Solution

treatment alone at 1150 °C for 2 h led to recrystallization due to high density of dislocations through the repetition of rapid cooling and heating, which increased the ductility. Aging treatment at 700 °C for 24 hours contributed to γ'' and $M_{23}C_6$ formation. Each heat treatment and their combination affected each sample's microstructure, which was the basic cause of their mechanical properties. Furthermore, from this study, it was verified that simple solutionizing heat treatment can induce recrystallization in Alloy 625 fabricated by L-PBF. This room temperature tensile test results led to the interest in mechanical property improvement at high temperature.

The high temperature tensile test was conducted with the L-PBF manufactured Alloy 625 as-built and microstructure-controlled samples. The recrystallized/solution sample showed a high possibility to improve the mechanical property, especially with regard to ductility by microstructure control. We now focused on the ductility improvement of L-PBF Alloy 625. Therefore, GBS was considered as a one way to improve ductility of the sample by enhancing GBs. GBS is intended to strengthen the GBs, which are likely to be weakened at high temperature by improving the GB energy. For the successful application of GBS to L-PBF manufactured Alloy 625, an in-depth analysis and understanding of GBS is essential. The principle of GB-strengthening by GBS can be demonstrated by phase transformation from straight GB to serrated GB due to the decrement of interfacial energy through serrated GB transition. Its mechanism was explained by investigation of a Ni-20Cr model alloy in which enrichment of Cr near and at GBs exerted strain on the GBs for the onset of GB serration. The actual minimum critical strain energy needed for GBS onset was determined to be at least 0.97 kJ/mol by first-principle calculation. Thus, GBS can be brought about by introducing a proper amount of atoms having a large diameter, such as Cr, Zr, and Nb, to provide enough strain energy as its trigger.

We then wondered if we could apply this GBS to L-PBF Alloy 625, thus the first trial to induce GBS of Alloy 625 was made on a wrought alloy as a standard. Based on

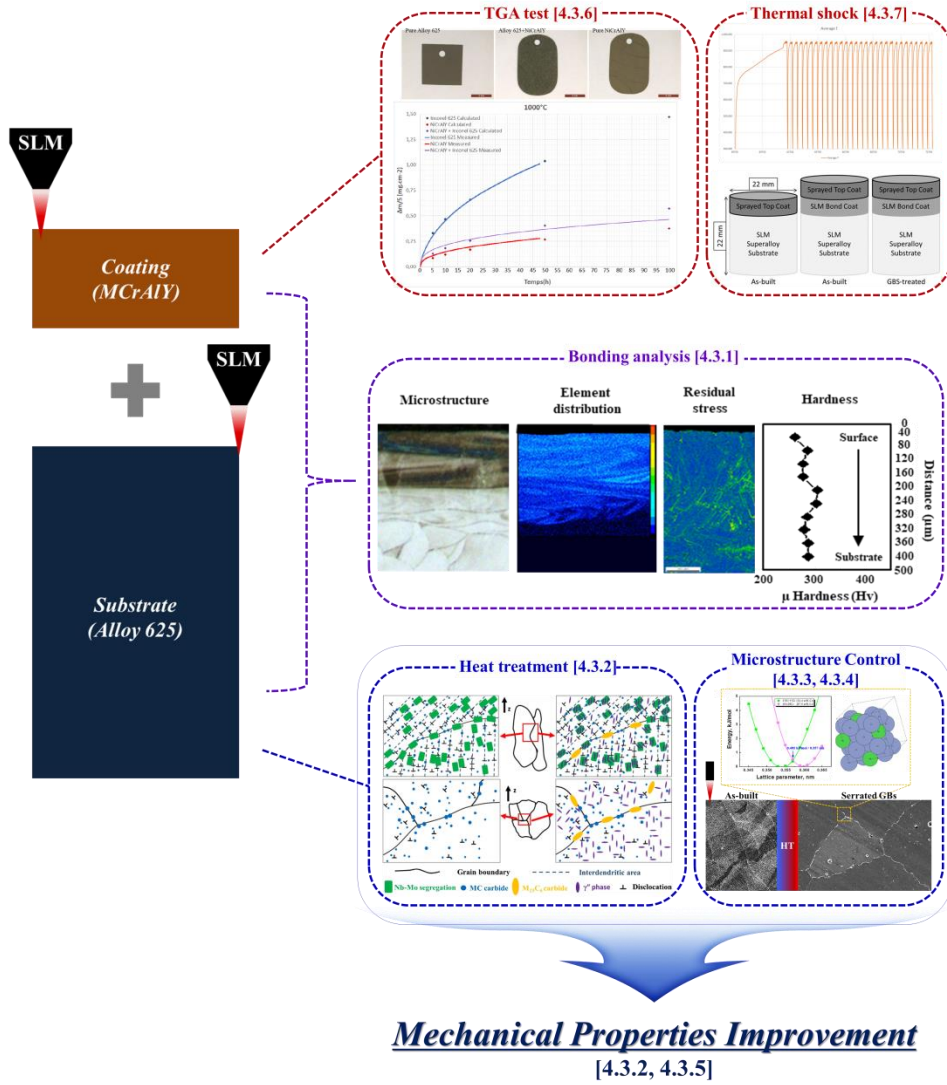
its mechanism, firstly it was realized that precipitates have to be dissolved for employment of enough solute atoms in the Ni–Cr matrix and letting the GBs move freely, and then the solute atoms have to approach to the GBs as much as possible during slow cooling. Accordingly the starting temperature for solution heat treatment was higher than in previous study related to GBS of Alloy 617 (1200 °C→1250 °C) to dissolve as much as possible precipitations, especially primary NbC, which has a relatively high solvus temperature. The modified heat treatment introduced GBS to wrought Alloy 625 successfully. The successfully induced serrated GBs were decorated with $M_{23}C_6$ as well as NbC. After the new attempt to promote GBS in wrought Alloy 625, it was assessed whether GBS induced in Alloy 625 would be more effective than the conventional wrought alloy for high-temperature mechanical properties and the possibility to introduce GBS to Alloy 625 fabricated by L-PBF as well.

The introduction of GBS in L-PBF manufactured Alloy 625 has been for the first time ever, the microstructure of the L-PBF Alloy 625 was firstly analyzed. First of all, it was necessary to remove precipitates as much as possible so that the GBs could move freely. L-PBF Alloy 625 is composed of a fine columnar structure with NbC at the interface of each columnar structure. This columnar structure with NbC, which has a GB pinning effect is not preferred. Thus, a higher solutionizing temperature than that of wrought Alloy 625 was chosen (1250 °C→1300 °C). Furthermore, the final aging temperature was also modified (800 °C→870 °C) considering the MCrAlY coating stabilization/diffusion heat treatment for the future study to adapt this heat treatment to the Alloy 625/MCrAlY bi-material. The application of modified GBS heat treatment (1300 °C/90 min-direct aging/slow cooling-870 °C/2 h) to the L-PBF alloy was the first successful attempt ever. This GBS heat-treated sample and recrystallized/solid-solution treated (1200 °C /1 h) sample were subjected to high-temperature tensile testing with the L-PBF as-built and wrought Alloy 625 as the counterparts. The two heat-treated samples seem to show superior tensile properties at high temperature in

comparison to the as-built sample. Even the GB serrated sample showed a higher elongation value than the recrystallized/solid-solution sample at a much higher temperature. However, they could not match the outstanding elongation value of the wrought alloy sample. The reason for the ductility loss of the L-PBF samples was investigated through analysis of their typical microstructures. In addition, the positive effect on the dynamic strain aging (DSA) of each heat treatment was also assessed.

Now, in order to make sure that the reliability of NiCrAlY coating on Alloy 625 substrate by L-PBF, the oxidation/hot corrosion behavior and stability in rapid cooling/heating condition was investigated by TGA testing and thermal shock testing. The TGA test was performed for the L-PBF manufactured bulk Alloy 625, L-PBF manufactured bulk MCrAlY and L-PBF coated sample. The coated sample showed an intermediate result of oxidation kinetics compared to the bulk Alloy 625 and bulk NiCrAlY samples from the TGA tested at 800 °C, 900 °C, and 1000 °C. It shows that improvement in high temperature oxidation properties of L-PBF processed Alloy 625 is possible using a L-PBF processed NiCrAlY coating. Moreover, the adhesion of the bond coat and the substrate was excellent with no signs of delamination in thermal shock conditions. The L-PBF coating properties were validated by TGA testing and thermal shock testing, and consequently, it was demonstrated that the feasibility of the application of L-PBF for TBC coating on the Ni-based superalloy substrate was certified to be commercialized.

5.2 Graphical abstract

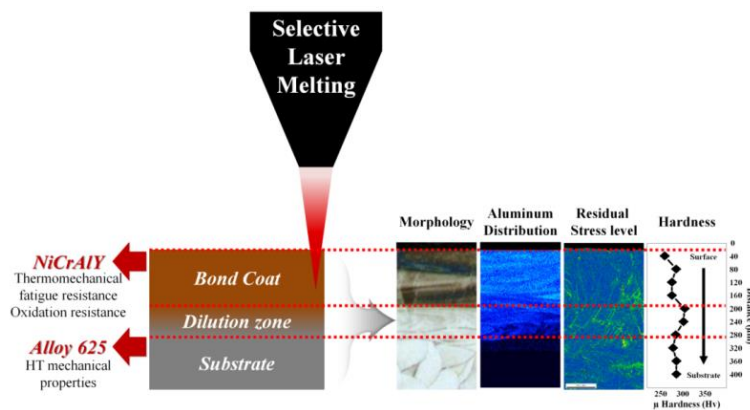


5.3 Introduction of articles

1. A novel approach to the production of NiCrAlY bond coat onto IN625 superalloy by selective laser melting

This study was about the feasibility of producing MCrAlY bond coat material directly on an Alloy 625 substrate produced by L-PBF. In the present study, L-PBF was used to fabricate both the Ni-based superalloy substrate and the MCrAlY bond coat, which is the first time this has been studied, to the best of our knowledge, in relation to AM fabrication. Fifteen different processing parameters were tested, and all cases showed substantial dilution between NiCrAlY and superalloy substrate due to the typical remelting characteristic of the L-PBF process, ensuring an excellent metallurgical bonding. The optimum process parameters, layer thickness $t = 50 \mu\text{m}$, hatch spacing $h = 120 \mu\text{m}$, laser power $P = 250 \text{ W}$, and laser scanning speed $v = 800 \text{ mm/s}$, were selected based on several criteria. An approximately 250- μm -thick NiCrAlY coating was obtained with a very low residual porosity $\leq 0.1\%$, including a $\sim 35\%$ dilution zone, a smooth hardness profile between 275 and 305 Hv, low residual stress levels, and a progressive Al concentration distribution. These results confirmed the feasibility of L-PBF as an alternative method for the deposition of coatings in TBC systems or MCrAlY coating itself.

This section is based on an article which has been published in **J. W. Lee, M. Terner, E. Copin, P. Lours, H. -U. Hong**, *Additive manufacturing*, “A novel approach to the production of NiCrAlY bond coat onto IN625 superalloy by selective laser melting”, 31 (2020) 100998, DOI: <https://doi.org/10.1016/j.addma.2019.100998>.



A novel approach to the production of NiCrAlY bond coat onto IN625 superalloy by selective laser melting

Jiwon Lee^{a,b}, Mathieu Ternier^a, Etienne Copin^b, Philippe Lours^{b,*}, Hyun-Uk Hong^{a,*}

*^aDepartment of Materials Science and Engineering, Changwon National University
20 Changwondaehak-ro, Changwon, Gyeongnam 51140, Republic of Korea*

*^bInstitut Clément Ader (ICA) ; Université de Toulouse ; CNRS, IMT Mines Albi, INSA, ISAE-SUPAERO,
UPS ; Campus Jarlard, F-81013 Albi, France*

Abstract

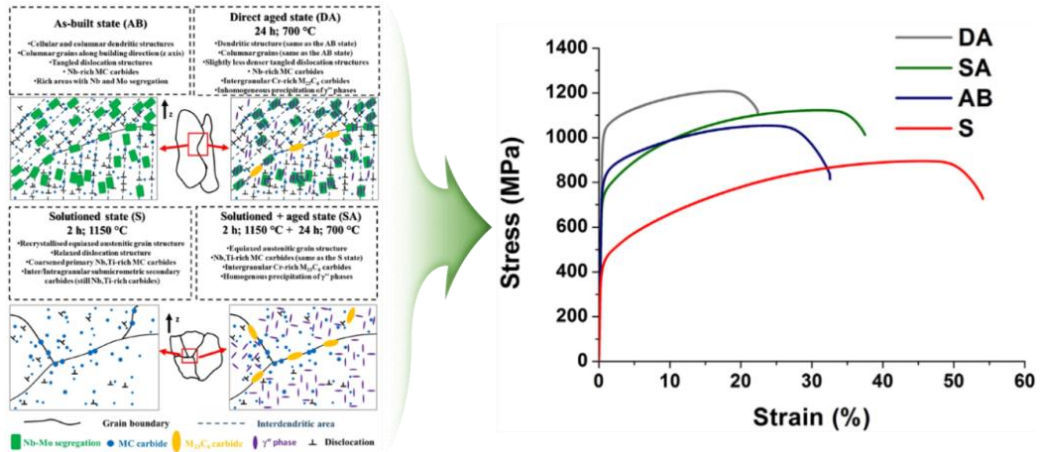
The present study investigated for the first time the feasibility of producing by Selective Laser Melting (SLM) a NiCrAlY bond coat material directly onto an IN625 substrate itself produced by SLM. A typical parameters optimization was conducted by varying laser power (P) and scanning speed (v). Single-line scanning tracks and two-layer coatings were carried out and analyzed for 15 different P/v conditions. Several criteria were defined for the selection of appropriate SLM parameters. The results showed significant remelting of the underlying substrate, which is a typical feature of SLM manufacturing. This led to the formation of an intermediate dilution zone characterized by substantial mixing between IN625 superalloy substrate and NiCrAlY bond coat suggesting excellent metallurgical bonding. Optimum processing conditions were found for $P = 250$ W and $v = 800$ mm/s. It produced a dense 242 μm thick bond coat including a 36% dilution zone. The SLMed <NiCrAlY-IN625> system exhibited a smooth microhardness profile slightly increasing from 275 Hv in the bond coat to 305 Hv in the substrate. A progressive Al concentration distribution between the phases and low residual stress levels were found in the system.

2. Influence of heat treatments on microstructure evolution and mechanical properties of Inconel 625 processed by laser powder bed fusion

This study was about the mechanical behavior at room temperature and microstructure of as-built and heat-treated Alloy 625 samples fabricated by L-PBF. On contrary to the rest of the work, in this case the samples were produced with different machine (EOSINT M270 Dual Mode machine, which is equipped with a 200W Yb fiber laser with a spot diameter of 100 μm) with powder (size distribution between d_{30} of 16 μm and d_{90} of 48 μm) from a different source (laser power of 195 W, scan speed of 1200 mm/s, hatching distance of 0.09mm and layer thickness of 0.02 mm) as one part of collaborated study with Politecnico di Torino in Italy. Although the L-PBF manufactured as-built sample showed good tensile properties, post-heat treatment is recommended to obtain specific mechanical properties to satisfy industrial requirements. Various types of heat treatments were performed to produce each microstructure and selected each representative heat treatment by comparison of Brinell hardness. γ'' and M_{23}C_6 carbides with recrystallized grains appeared in direct aging (DA) treated sample (700 $^{\circ}\text{C}/24$ hrs), produced from the as-built microstructure, which showed columnar structures with high density of dislocation and NbC carbides. Solution (S) treatment (1150 $^{\circ}\text{C}/2$ hrs) made the sample have a recrystallized equiaxed austenitic grain structure with primary and secondary MC carbides. Furthermore, the solution/aging (SA) treated sample (1150 $^{\circ}\text{C}/2$ hrs - 700 $^{\circ}\text{C}$ 24 hrs) showed the same microstructure as that of the S sample, but with γ'' and M_{23}C_6 carbides. The optimal temperature for the heat treatments was selected by a comparison of Brinell hardness values and microstructure observation. Four types of samples were subjected to tensile testing at room temperature with the as-built sample as a counterpart. The as-built sample showed yield strength (YS) and ultimate tensile strength (UTS) values of 783 MPa and 1,041 MPa respectively, with a ductility of 33%. The DA sample exhibited YS and UTS values of 1,012 MPa and 1,222 MPa, with the lowest ductility of 23%. The S sample showed the lowest YS and UTS values of 396 MPa and 883 MPa with the highest increment of ductility of 55%. The SA sample showed a significant increase in strength: YS = 722 MPa, UTS=1,116 MPa and correlate ductility of 35%. According to the tensile results, solution treatment contributes to the ductility increment, and aging treatment improves the strength. Therefore, it was demonstrated that the microstructure evolution of L-PBF Alloy 625 under various heat treatments provides a wide spectrum of possible mechanical properties.

This section is based on an article which has been published in G. Marchese, M. Lorusso, S. Parizia, E. Bassini, **J. W. Lee**, F. Calignano, D. Manfredi, M. Terner, H. -U. Hong, D. Ugues,

M. Lombardi, S. Biamino, *Mat. Sci. Eng. A*, “Influence of heat treatments on microstructure evolution and mechanical properties of Inconel 625 processed by laser powder bed fusion”, 729 (2018) 64-75, DOI: <https://doi.org/10.1016/j.msea.2018.05.044>.



Influence of heat treatments on microstructure evolution and mechanical properties of Inconel 625 processed by laser powder bed fusion

Giulio Marchese¹, Massimo Lorusso², Simone Parizia^{1,2}, Emilio Bassini¹, Ji-Won Lee³, Flaviana Calignano², Diego Manfredi², Mathieu Terner³, Hyun-UK Hong³, Daniele Ugues¹, Mariangela Lombardi^{1,2}, Sara Biamino^{1,2}

¹Department of Applied Science and Technology, Politecnico di Torino, Corso Duca degli Abruzzi 24, 10129 Torino, Italy

²Center for Sustainable Future Technologies - CSFT@PoliTo, Istituto Italiano di Tecnologia, Corso Trento 21, 10129 Torino, Italy

³Department of Materials Science and Engineering, Changwon National University, 20 Changwondaehak-ro, 51140 Changwon, Republic of Korea

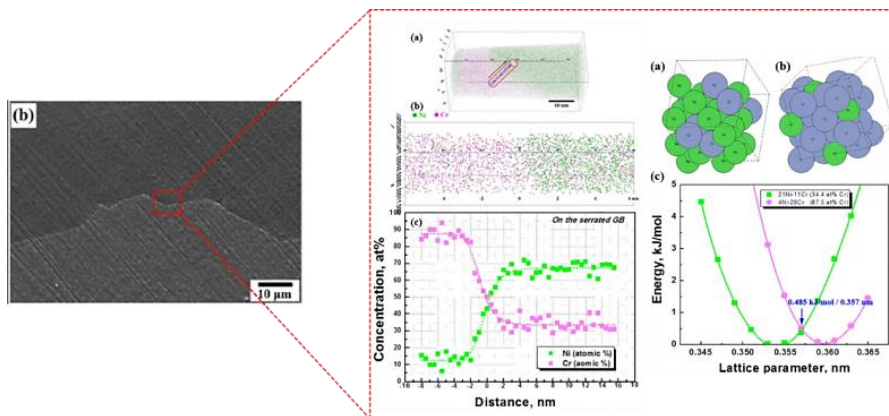
Abstract

This study investigated the mechanical behaviour and microstructure of as-built and heat-treated Inconel 625 (IN625) samples processed by laser powder bed fusion (LPBF). This process offers a high degree of design freedom to build complex IN625 components in order to overcome extensive machining trouble. However, post heat treatments must be performed to obtain desired mechanical properties to match industrial requirements. For this purpose, optimised heat treatment parameters (solutioning and aging temperature and time) were determined through hardness measurements on IN625 samples subjected to different heat-treatment trials. Afterwards, the tensile properties of as-built and optimised heat-treated IN625 samples were determined, showing superior values to standard wrought IN625 alloys. Heat treatment trials involving

3. A new observation of strain-induced grain boundary serration and its underlying mechanism in a Ni–20Cr binary model alloy

In this study, as a purpose of the GB strengthening at high temperature, the mechanism of GBS was investigated through a Ni-20Cr binary model alloy to prepare applying to additive manufactured Alloy 625 in the further study. A fully solid-solution-treated alloy was heat treated based on the previous study adapted for an Ni–Cr matrix alloy [4, 5, 95]. According to the hypothesis of the GBS mechanism, there was no occurrence of GBS anywhere as expected. However, the sign of GBS occurred by giving a 5% strain during the direct aging/slow cooling process in which GBS took place, which was conducted after the solid-solution process. The microstructure of the sample in which GBS occurred was analyzed by TEM and the 3D-APT method. There was a high density of dislocations around the GBs due to 5% straining during the aging/slow cooling process, which promoted Cr enrichment near and at the GBs. To make the sample show the same behavior just by heat treatment, the solutionizing temperature was increased to induce Cr enrichment near and at the GBs with the vacancy-assisted diffusion concept, and it worked well. The in-depth 3D-APT analysis showed that the serrated samples displayed wide Cr enrichment at the serrated GBs. The common feature of both samples was Cr enrichment, and strain on the GBs was considered as the trigger of GBS. The strain by first-principle calculation was ~ 0.97 kJ/mol. Thus, it was demonstrated that the minimum 0.97 kJ/mol of strain can lead to GBS by interstitial atoms at the GBs.

This section is based on an article which has been published in **J. W. Lee**, M. Terner, H. -U. Hong, S. H. Na, J. B. Seol, J. H. Jang, T. H. Lee, *Mater. Charact.*, “A new observation of strain-induced grain boundary serration and its underlying mechanism in a Ni–20Cr binary model alloy”, 135 (2018) 146-153, DOI: <https://doi.org/10.1016/j.matchar.2017.11.047>.



A new observation of strain-induced grain boundary serration and its underlying mechanism in Ni-20Cr binary model alloy

J.W. Lee ^a, M. Turner ^a, S.H. Na ^b, J.B. Seol ^b, J.H. Jang ^c, T.H. Lee ^c, H.U.

Hong ^{a,*}

^a*Department of Materials Science and Engineering, Changwon National University, Changwon 51140, Republic of Korea*

^b*Department of Material Science Engineering, Pohang University of Science and Technology (POSTECH), Pohang 37673, Republic of Korea*

^c*Ferrous Alloy Department, Korea Institute of Materials Science Changwon 51508, Republic of Korea*

Abstract

The formation of serrated grain boundaries and its mechanism correlated with straining exerted on grain boundaries was investigated in a Ni-20Cr binary model alloy. This model alloy is a full solid-solution which is deliberately free of carbon and aluminum to exclude precipitation of second phase. A special heat treatment involving slow cooling adapted from alloy 617 was

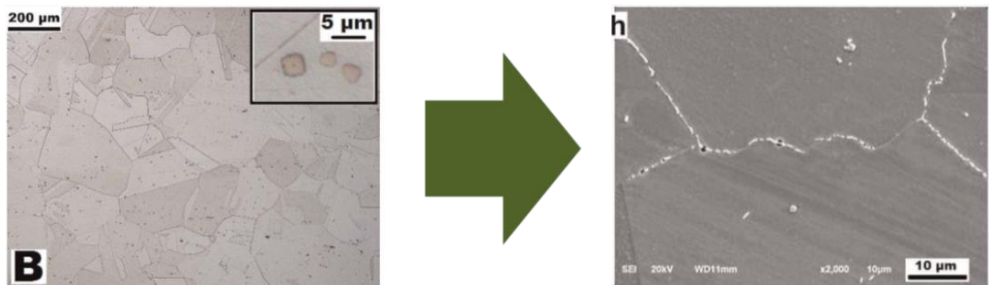
*Corresponding author. Changwon National University, Changwon 51140, Republic of Korea.

E-mail address: huhong@changwon.ac.kr (H.U. Hong).

4. First evidence of grain boundary serration in a specifically heat treated wrought Alloy 625 Ni-based superalloy

Recently, the introduction of GBS has been studied mainly for solid-solution-strengthened Ni-based superalloys with low γ' volume fraction, such as Alloy 230 and Alloy 617. The present work studied inducing GBS in Alloy 625, which is a solid-solution-strengthened Ni-based superalloy having a minority of precipitation-strengthening characterization by MC carbide and γ'' . The specially designed heat treatment (1250 °C /30 min - 5°C/min of slow cooling - 800°C/0-1000hrs) was applied to wrought Alloy 625 based on the previous work [4, 5, 95], and significant serration was observed for the first time. $M_{23}C_6$ carbides together with significant amount of MC carbides were observed at the GBs, whereas there was no evidence of γ'' precipitation. The slow cooling treatment was found to effectively promote the formation of serrated grain boundaries, even in the absence of aging. Meanwhile, as the aging time is increased, precipitation of the δ phase was evident.

This section is based on an article which has been published in M. Ternier, **J. W. Lee**, J. H. Kim, H. -U. Hong, *Int. J. Mater. Res.*, “First evidence of grain boundary serration in a specifically heat treated wrought Alloy 625 Ni-based superalloy” 109 (2018) 1-8, DOI: <https://doi.org/10.3139/146.111674>.



First evidence of grain boundary serration in a specifically heat treated wrought Alloy 625 Ni-based superalloy

Mathieu Ternier, Ji-Won Lee, Jin-Hyeok Kim, Hyun-Uk Hong

Department of Materials Science and Engineering, Changwon National University

20 Changwondaehak-ro, Changwon, Gyeongnam 51140, Republic of Korea

Abstract

Grain boundary serration is an effective way to increase the high temperature resistance of superalloys and steels. The popular Alloy 625 Ni-based superalloy was until now believed not to form serrated grain boundaries based on previous considerations of serrability criteria. Following the recent strain-induced serration mechanism, a special heat treatment involving continuous slow cooling between the solution and aging temperature was designed. As a result, significant serration was observed for the first time for Alloy 625 promoted by slow cooling. Grain boundary M₂₃C₆ carbides were systematically detected from either degeneration of solidification MC carbides or heterogeneous nucleation. Upon aging, serration amplitude increased and precipitation of the δ phase proliferated.

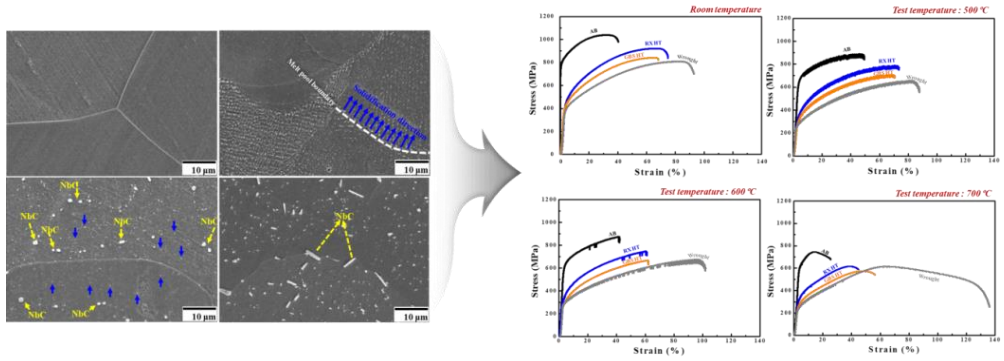
Keywords: Grain boundary serration; Alloy 625; Precipitation; Heat treatment

5. Heat treatment design for superior high-temperature tensile properties of Alloy 625 produced by SLM

L-PBF manufactured Alloy 625 was subjected to high-temperature tensile testing. Considering the recent study which described a tensile test performed at ambient temperature with L-PBF as-built and various heat-treated samples, modified GBS heat treatment (solid solution temperature increase from 1250→1300 °C) was applied to L-PBF Alloy 625 ('GBS HT' sample). This heat treatment was developed to improve the GB strengthening that typically occurs at high temperature with low-stress condition. Through this heat treatment, the columnar structure of As-built sample was destroyed, and all grains were equiaxed. Additionally, serrated GBs were successfully produced, and most of the GBs were decorated with NbC carbides. Furthermore, recrystallization heat treatment (RX HT) was also performed to induce the recrystallization and proper solid-solution state having a high hardness value. These two heat-treated samples were subjected to high-temperature tensile testing with L-PBF as-built (AB) and wrought Alloy 625 samples. The tensile tests were conducted at room temperature, 500 °C, 600 °C, and 700 °C under the same condition in air. A room-temperature tensile test was conducted to verify the reliability of each sample and its results can be compared with previous study of [4.3.2] in aspect of sample manufacturing conditions. The tensile graphs of the two heat-treated samples were located between those of the AB and wrought samples. Thus, their strengths were higher than that of the wrought sample, and they had higher ductility values than the AB sample. These results may be attributed to the differences in whether the initial microstructure is columnar or equiaxed, whether there are straight GBs or serrated GBs, and whether or not there is precipitation. As in a previous study in which tensile testing was conducted at room temperature, the three samples (wrought, RX HT, GBS HT) having equiaxed grain structure showed improved ductility. On the other hand, the other three samples (AB, RX HT, GBS HT) having precipitates showed improved strength values. Although heat treatments could not improve the ductility as much as the wrought sample, the DSA phenomenon, which shows an unexpected tensile property at a typical strain rate and temperature, was rarely observed in the GBS HT sample. Therefore, the GBS HT sample seemed to have a good effect on some part in the L-PBF manufactured Alloy 625.

This section is based on an article which has been published in **J. W. Lee**, M. Terner, S. Y. Jun, E. Copin, P. Lours, H. -U. Hong, *Mat. Sci. Eng. A*, "Heat treatments design for superior high-temperature tensile properties of Alloy 625 produced by Selective Laser Melting" 790 (2020)

139720, DOI: <https://doi.org/10.1016/j.msea.2020.139720>.



Heat treatments design for superior high-temperature tensile properties of Alloy 625 produced by Selective Laser Melting

**Jiwon Lee^{a, b}, Mathieu Terner^a, Sunyoung Jun^a, Hyun-Uk Hong^{a,*}
Etienne Copin^b, Philippe Lours^{b,*}**

^a*Department of Materials Science and Engineering, Changwon National University, 20 Changwondaehak-ro, Changwon, Gyeongnam 51140, Republic of Korea*

^b*Institut Clément Ader (ICA), Université de Toulouse, CNRS, IMT Mines Albi, INSA, ISAE-SUPAERO, UPS, Campus Jarlard, F-81013 Albi, France*

Abstract

The popular superalloy Alloy 625 was produced by Selective Laser Melting (SLM) and post-processing heat treatments were designed to optimize the inhomogeneous and constrained as-built microstructure (AB) for high temperature structural applications. A single-step solution heat treatment (RX) was designed to promote full recrystallization and approach the conventional wrought microstructure. To enhance high temperature properties, a grain boundary serration heat treatment (GBS) was successfully designed involving higher solution temperature and time to promote recrystallization and homogeneity, and a direct slow cooling step followed by a short aging to assist solute diffusion and grain boundary motion. The resulting microstructures were characterized by fully recrystallized fine equiaxed grains and fine intra and intergranular NbC precipitates. The GBS alloy also exhibited as much as 80 % of serrated grain boundaries with enhanced resistance to cracking at high temperatures. Tensile properties of all three materials were evaluated at room temperature,

* Corresponding authors.

E-mail addresses: huhong@changwon.ac.kr (Hyun-Uk Hong), philippe.lours@mines-albi.fr (Philippe Lours).

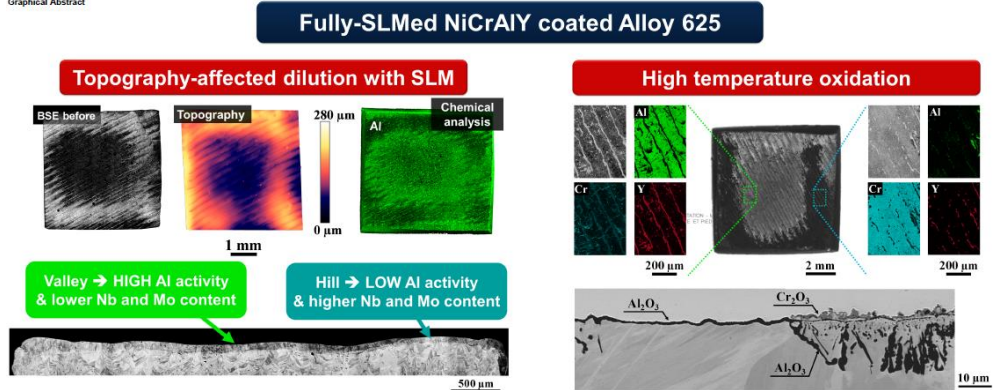
6. High temperature oxidation of NiCrAlY coated Alloy 625 manufactured by selective laser melting

L-PBF manufacturing is considered particularly appropriate for parts with complex geometry with a multilayered microstructure, including thermal barrier and/or environmental coating systems, to satisfy both structural and environmental specifications. From the point of environmental specifications, the high-temperature oxidation of fully L-PBF processed NiCrAlY by the previously tested and succeeded optimal parameter conditions ($P = 250 \text{ W}$, $v = 800 \text{ mm/s}$) [4.3.1] overlaying Alloy 625 substrate parts was investigated at temperatures between $800 \text{ }^\circ\text{C}$ and $1000 \text{ }^\circ\text{C}$. Freestanding bulk NiCrAlY, Alloy 625, and bi-materials were fabricated using the L-PBF method. To be representative of coated components, two thin layers (about $100 \text{ }\mu\text{m}$) of NiCrAlY powder were laser scanned at the surface of Alloy 625 to form the multi-material. The coated samples were then extracted using a gentle mechanical polishing technique to ensure repeatable thickness and surface finishing of the specimen. It is worth noting that the fabrication of L-PBF NiCrAlY was particularly difficult and resulted in macro cracks within the bulk NiCrAlY specimens due to the large volumetric residual stress, whereas the reason why micro cracks are observed at the laser bead level for coating is predicted by delayed cracking. However, it was not damaged enough to prevent the study to be done. As expected, the bulk NiCrAlY and bi-materials demonstrated an improved oxidation behavior compared to Alloy 625. Indeed, the oxidation of bulky freestanding NiCrAlY resulted in a dense and continuous Al_2O_3 layer in this temperature range, which was what was expected for this composition of NiCrAlY. This means no evaporation effect of Al was observed (an issue observed sometimes in L-PBF). However, the formation of oxides at the surface of the bi-layer material differed from that of the bulky freestanding NiCrAlY. As a comparison, the oxidation of the bi-layer material resulted in regions with a dense and continuous Al_2O_3 layer as well as regions composed of a mixture of external Cr_2O_3 and internal Al_2O_3 . Extended EDS maps at the surface of the bi-material highlighted the heterogeneous distribution of the constitutive elements of the NiCrAlY coating, resulting in some regions with Al activity lower than that required for the formation of a continuous and dense Al_2O_3 layer. Low-Al-activity and high-Al-activity regions were related to the topography of the L-PBF surface and corresponded to peak and valley regions, respectively where it comes from the in homogeneous thickness of the powder layer deposited. Furthermore, cracks were mainly found in high-Al-activity regions and they could be attenuated by applying a stress relieving heat treatment or the diffusion. The fabrication of coated but small components with a

brittle coating by L-PBF is not trivial and need further investigation.

This section is based on an article which has been published in D. Texier, E. Copin, A. Flores, **J.W. Lee**, M. Terner, H. -U. Hong, P. Lours, *Surf. Coat.*, “High temperature oxidation of NiCrAlY coated Alloy 625 manufactured by selective laser melting” *Tech.*, 398 (2020) 126041, DOI: <https://doi.org/10.1016/j.surfcoat.2020.126041>.

Graphical Abstract



High temperature oxidation of NiCrAlY coated Alloy 625 manufactured by selective laser melting

Damien Texier^{a,*}, Etienne Copin^a, Agustin Flores^a, Jiwon Lee^{a,b}, Mathieu Terrier^b,
Hyun-Uk Hong^b, Philippe Lours^a

^a*Institut Clement Ader (ICA) - UMR CNRS 5312, Université de Toulouse, CNRS, INSA, UPS, Mines
Albi, ISAE-SUPAERO, Campus Jarlard, 81013 Albi Cedex 09, France*

^b*Department of Materials Science and Engineering, Changwon National University, 20
Changwondachak-ro, Changwon, Gyeongnam 51140, Republic of Korea*

Abstract

The high temperature oxidation of fully SLM-processed NiCrAlY coated Alloy 625 parts was investigated between 800°C and 1000°C. For comparison, bulk NiCrAlY and bulk Alloy 625 were also fabricated using SLM. Two thin layers of NiCrAlY powder were lasered at the surface of Alloy 625 to form the bi-materials. Bulk NiCrAlY and bi-materials showed an improved oxidation behavior compared to Alloy 625. The oxidation of the NiCrAlY coating results in regions with a dense and continuous external Al₂O₃ layer and regions composed of a mixture of external Cr₂O₃ and internal Al₂O₃. Large EDS maps at the surface and cross-sections of the bi-material highlighted a heterogeneous distribution of constitutive elements of the NiCrAlY coating, resulting in some regions with an Al activity lower than the one required for the formation of a continuous and dense Al₂O₃ layer (≤ 10 atomic percent). Low Al activity and high Al activity regions were related to the topography of the SLMed surface and correspond to hill and valley regions, respectively. In addition, cracks, mainly occurring in high Al activity regions, were observed across NiCrAlY specimens. The fabrication of coated but small components with a brittle coating by SLM is not trivial and needs further investigations.

Keywords: MCrAlY bond-coating, Superalloy, Additive manufacturing, Selective laser melting, Oxidation, Interdiffusion

1. INTRODUCTION

Nickel-based superalloys are intensively used in the aerospace industry for high temperature applications because of their excellent mechanical strength combined with their resistance to high temperature oxidation and corrosion [1–3]. Alloy 625, consisting of a Ni base FCC γ -Ni matrix solution strengthened by significant additions of Cr, Nb and Mo,

*Corresponding author

Email address: damien.texier@mines-albi.fr (Damien Texier)

7. Thermal shock resistance of the NiCrAlY coated Alloy 625 multi material manufactured by L-PBF (paper in preparation)

This is the first time to our knowledge that a superalloy + bond coat system is produced by L-PBF at once. Investigation of the oxidation behavior, previously reported, highlighted the reliability of the bi-material. This bi-material is intended for use in high temperature exposure conditions such as aeroengine gas turbine applications. For this reason, resistance to thermal shock (rapid heating and cooling cycles) is also critical. A Burner Rig approaching the severe conditions which could be experienced during operation imposing very rapid heating and cooling was used. This study was conducted in collaboration with our colleagues in Italy from the Department of Applied Science and Technology of Politecnico di Torino. The Burner Rig in Politecnico di Torino (Fig. 18) is a custom made apparatus specifically designed to reproduce the severe temperature conditions experienced in a gas turbine engine. The machine is equipped in particular with a burning chamber consisting of a heat resistant ceramic plate machined to host up to 10 specimens, 20 air quenching tubes for fast cooling of the top and/or bottom surface of each specimens, 20 thermocouples for precise measurements of the top and bottom surface of each specimens. On top of the plate, a burner delivers an actual flame by burning either methane or a mixture of regulated methane+fuel. Only methane was used in the present study. A system of manual valves with manometer allows the regulation of the air flow rate for quenching. The Burner Rig is controlled manually by means of a software which allows to regulate the methane flow and the air/methane ratio, trigger air quenching and monitor/control the temperatures. The maximum designed temperature is 1300°C. In the present study, the methane flow was set to 1 m³/h, the air/methane ratio was set to 1.2, the maximum temperature was set to 950°C and the quenching temperature was set to 300°C. All experimental tests were carried out in the frame of a two month testing campaign in Turin. Also part of the international collaboration created around the present Ph.D. thesis, characterization of the materials was the subject of a 4-month

internship program. A student from IMT Mines-Albi, supervised by the present author Jiwon Lee, was responsible for the characterization.

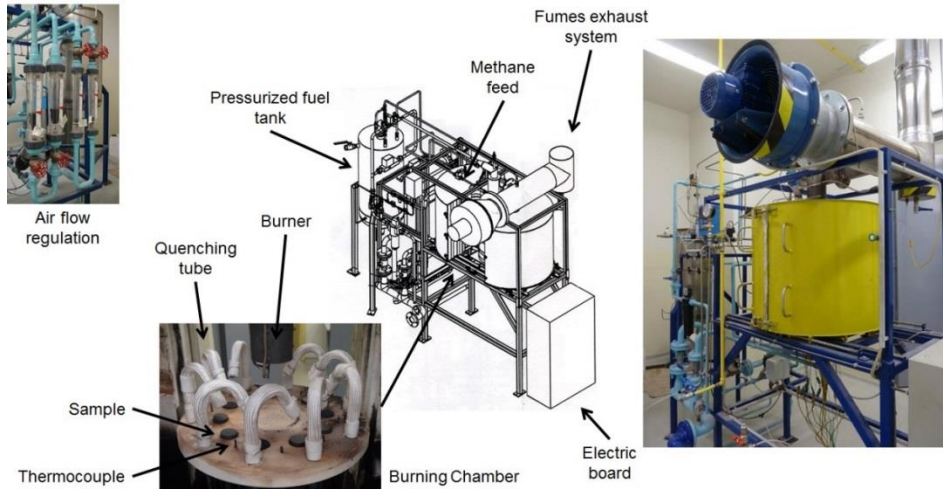


Figure 18. Politecnico's Burner Rig hardware

Cylindrical samples specifically designed for the equipment were produced, with three specimen conditions tested (Fig. 19):

- L-PBF Superalloy 625 substrate + L-PBF NiCrAlY bond coat (as-built): **As-built (AB)**
- L-PBF Superalloy 625 substrate + L-PBF NiCrAlY bond coat (as-built) + sol-gel YSZ Top Coat: **As-built + Top Coat (AB+TC)**
- L-PBF Superalloy 625 substrate + L-PBF NiCrAlY bond coat (GBS-heat treated) + sol-gel YSZ Top Coat: **GBS-treated + Top Coat (GBS+TC)**

Two samples were tested for each condition and placed on diametrically opposite sides of the ceramic plate in the Burner Rig chamber.

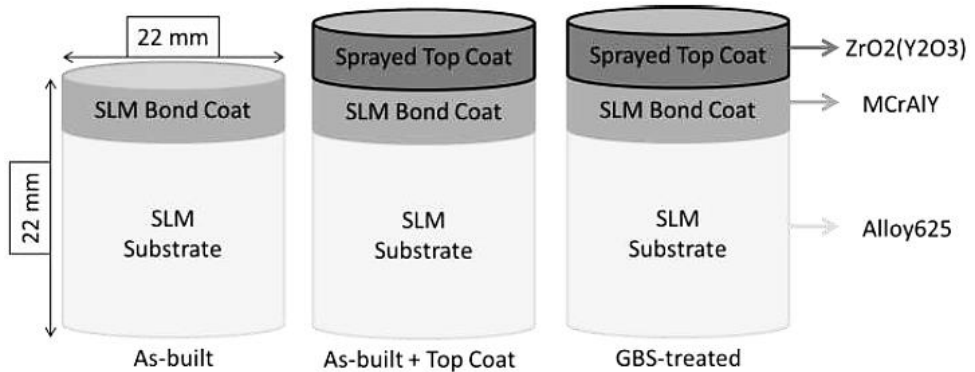


Figure 19. Geometry of each specimen and composition of materials in each layer.

The details of these different conditions are described in the following:

- **L-PBF superalloy substrate:** the substrate, Alloy 625, is produced in all the cases by L-PBF with an SLM Solution SLM125HL machine according to the optimum conditions given by the manufacturer and verified using the recommended process conditions, as in the rest of the study [4.3.1].

- **L-PBF Bond Coat:** The NiCrAlY bond coat L-PBF processing optimization campaign has been described previously [4.3.1] and adapted same way.

- **GBS heat treatment:** This heat treatment was adapted to assess if this heat treatment is effective for coated sample either. The GBS heat treatment applied was also previously described in [4.3.5].

- **Sprayed Top Coat:** At last, after all heat treatments had been carried out, a YSZ top coat was deposited using sol-gel process. This deposition was realized in IMT-Mines Albi. 8mol% $Y_2O_3 - ZrO_2$ (Tosoh) was dispersed into a zirconium propoxide-based sol and was subsequently deposited on substrates by air spraying. Consolidation was then carried out by a heat treatment at moderate temperature (600 °C) for 4h in order to avoid any significant alteration of the previous microstructure-setting treatments of the bond coated substrates.

The test conditions for the materials were ideally the most representative of the severe conditions envisaged in-use. As many as 450 cycles were carried out under very aggressive conditions for the tested materials. Further cycling was avoided to prevent complete degradation of the ceramic top coat for further analysis. With regards to the nature of the superalloy substrate, a maximum temperature of 950°C (2 min plateau) and quenching to 300°C was considered. Note that the 950°C is the average temperature in the chamber. The actual temperature for each individual specimen varied significantly and was conveniently recorded by 20 thermocouples for precise measurements of the top and bottom surface of each specimen. Nevertheless, the gradient of temperature was lower than 100 °C. Fig. 20 shows the first 30 cycles, totally 15 times of repetition were carried out for each sample.

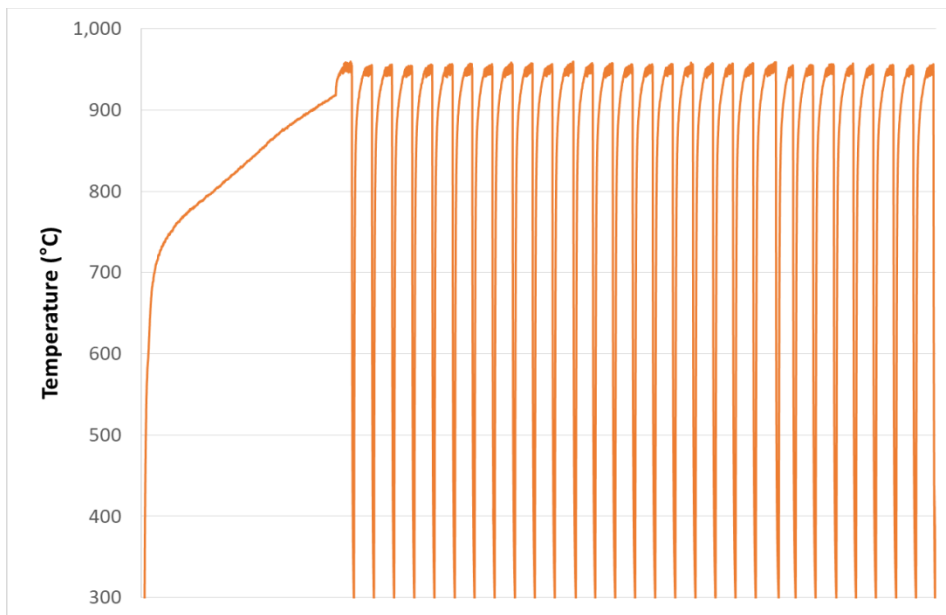


Figure 20. Recorded average temperature in the chamber for the first 30 cycles for thermal shock test.

The Burner Rig is entirely manually operated for safety considerations. The first heating of each 30-cycles session took approximately 1h, quenching to 300°C took

only under 1 min and the reheating to 950°C took approximately 4 min. After each session, the machine had to be cooled down and opened. Each sample was photographed and weighed with a precision balance (0.1 mg), before being repositioned in the chamber for the next session on the next day. Slight maintenance of the machine was also necessary after each session to avoid in particular degradation of the quenching tubes. Only methane was used as burning means and the air/methane ratio was set 1.2 to provide an oxidizing environment.

Fig. 21 shows the samples as-prepared ($t = 0$ cycle) and after the entire thermal shock testing campaign ($t = 450$ cycles). Degradation of the sample (the ceramic Top Coat in particular) due to thermal shock was clear, and it seems that the samples subjected to the GBS heat treatment experienced the most severe degradation. There was no obvious sign of oxidation despite the oxidizing environment and the high temperature.

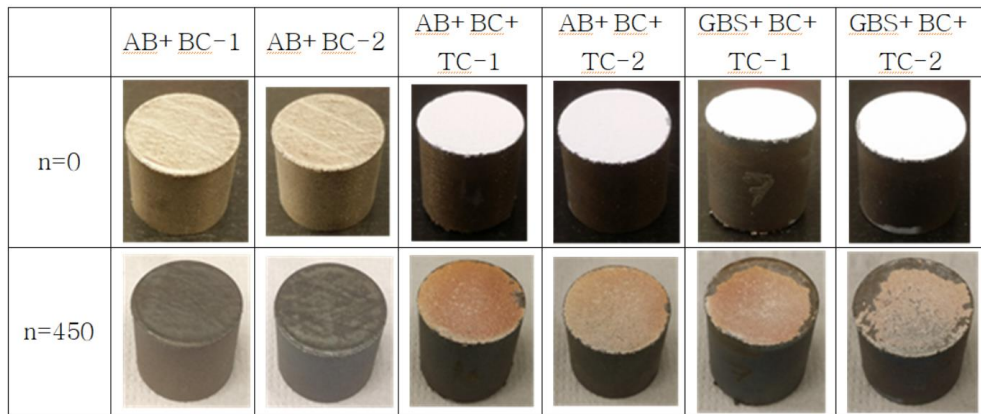


Figure 21. The comparison of the samples' surface change before and after thermal shock tests.

In Fig. 22, the weight difference in % (compared to the original sample's weight) is plotted as a function of the number of thermal cycles. The AB material only showed a

slight increase in weight, which quickly stabilized, as the number of cycles increased. This suggested that samples did not experience significant oxidation (otherwise the mass change would increase). The samples having the ceramic top coat sprayed on their surface however exhibited decreasing mass. The mass loss is attributed to spallation of the ceramic top coat, which is also clearly observed in Fig. 21. It was considered that local buckling or edging effect is occurred.

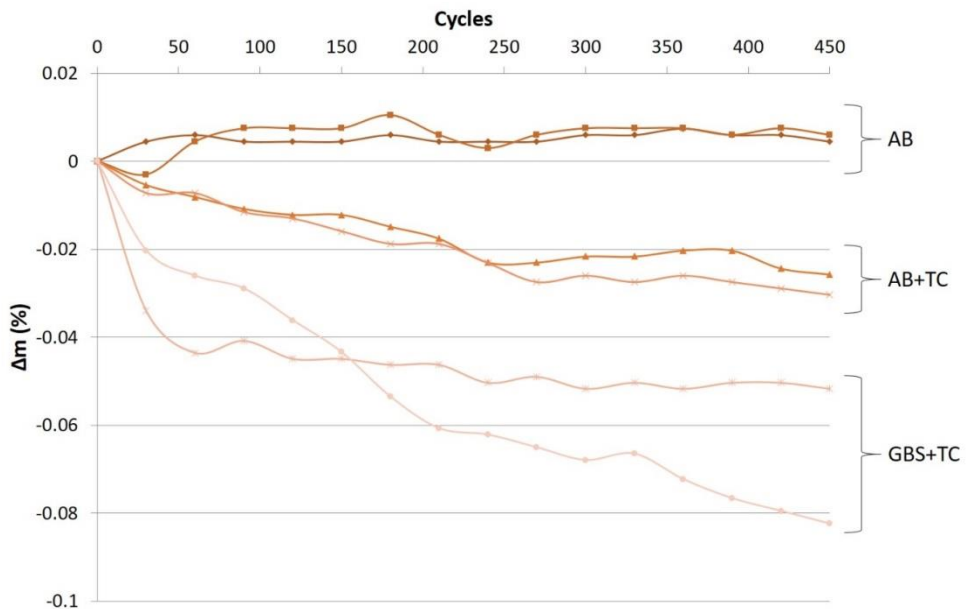


Figure 22. Mass change during thermal shock testing.

Nevertheless, it seems clear in Fig. 22 that applying the GBS treatment before deposition of the top coat (GBS+TC) was found detrimental to the coating's adherence and weight loss due to coating's spallation was significant after only few cycles as opposed to AB+TC. It is assumed that some oxidation may have taken place during the GBS heat treatment realized in a tubular furnace under protective argon flow, however no clear evidence could be detected. SEM-EDS analysis revealed the

presence of Al-rich oxides in the as-prepared GBS+TC specimen, as shown in Fig. 23.

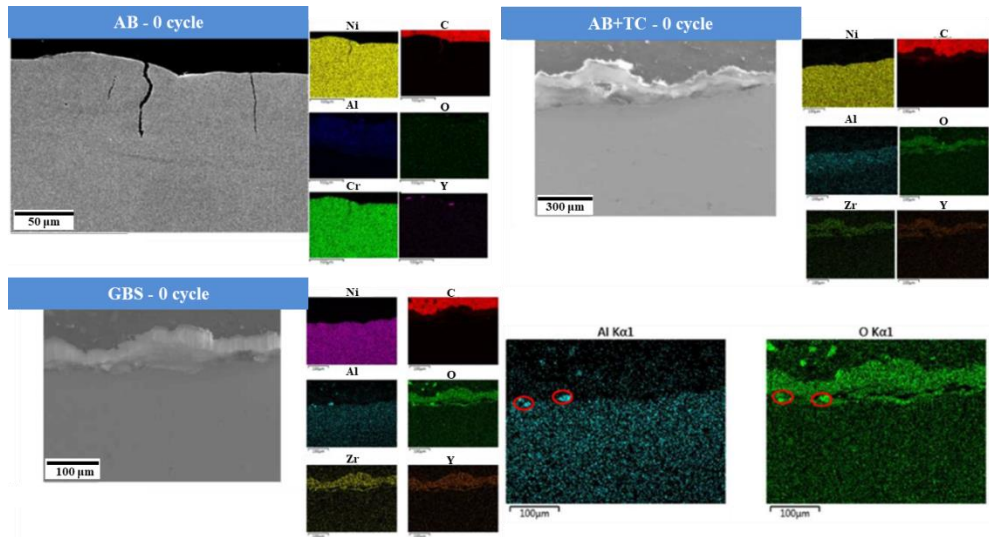


Figure 23. SEM/ESD mapping results for AB (top left), AB+TC (top right) and GBS+TC (bottom) showing Al-rich oxides in the later before the thermal cycling testing.

All specimens were hot mounted in phenolic resin and carefully subjected to conventional metallographic preparation of grinding with abrasive SiC papers and fine polishing with diamond pastes down to 1 μm. Fig. 24 shows OM micrographs of the top surface of as-received AB specimens (top) and after 450 cycles (bottom). Significant cracking was observed within the bond coat in both states. It was expected that it is occurred due to delayed cracking, which is already discussed in [4.3.6].

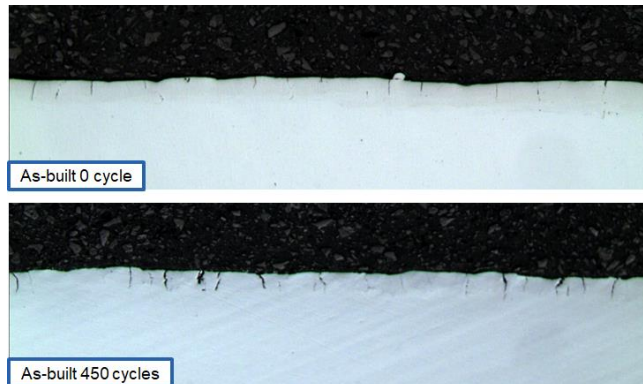


Figure 24. OM micrographs showing cracking in the as-prepared AB specimens (top) and after 450 cycles (bottom).

Hardness was measured every 20 μm from the top surface of the bond coat to 200 μm deep into the substrate for all conditions using a test load of 50g (Fig. 25). The hardness values increased significantly after thermal cycles for the un-heat treated materials (AB and AB+TC), as opposed to GBS+TC material, especially within the bond coat part. The higher hardness was attributed to precipitation during thermal cycling between 300°C and 950°C (γ'' in particular), though evidence are not yet available. On the contrary, heat treated sample GBS+TC showed only a little difference at the bond coat and substrate interface.

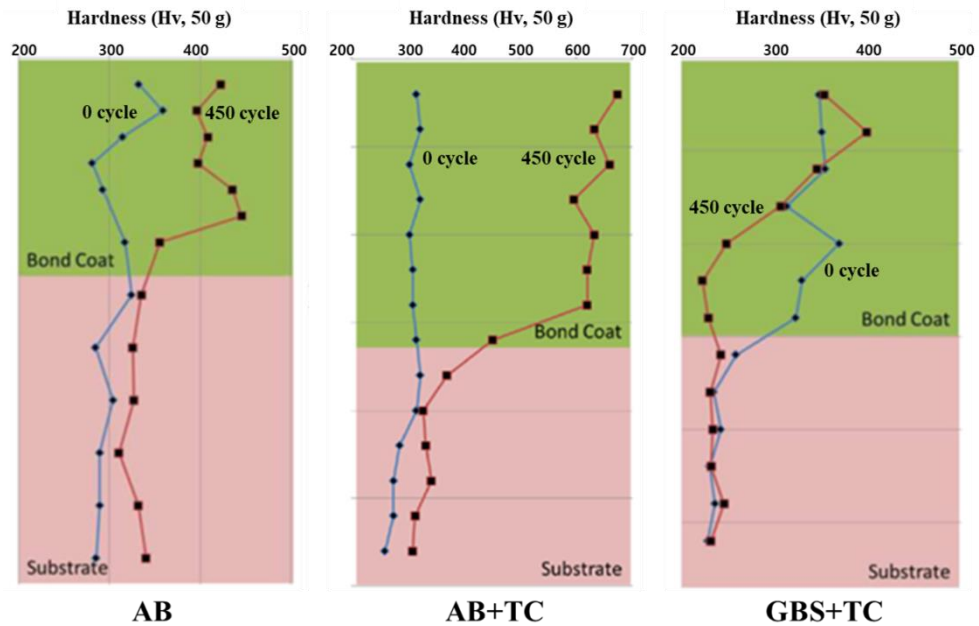


Figure 25. Vickers hardness profiles from the surface into the substrate for all three materials conditions before (0 cycle, blue) and after (450 cycles, red) thermal cycling between 300°C and 950°C.

It could also be noted that the hardness values of the substrate of the GBS+TC material was significantly lower than those of the as-built substrate (AB and AB+TC) in Fig. 25, which could be expected due to recrystallization and grain growth resulting for the heat treatment. This is consistent with the results of the mechanical properties in tension characterization [4.3.5]. This recrystallization and grain growth was also confirmed by EBSD analysis in Fig. 26.

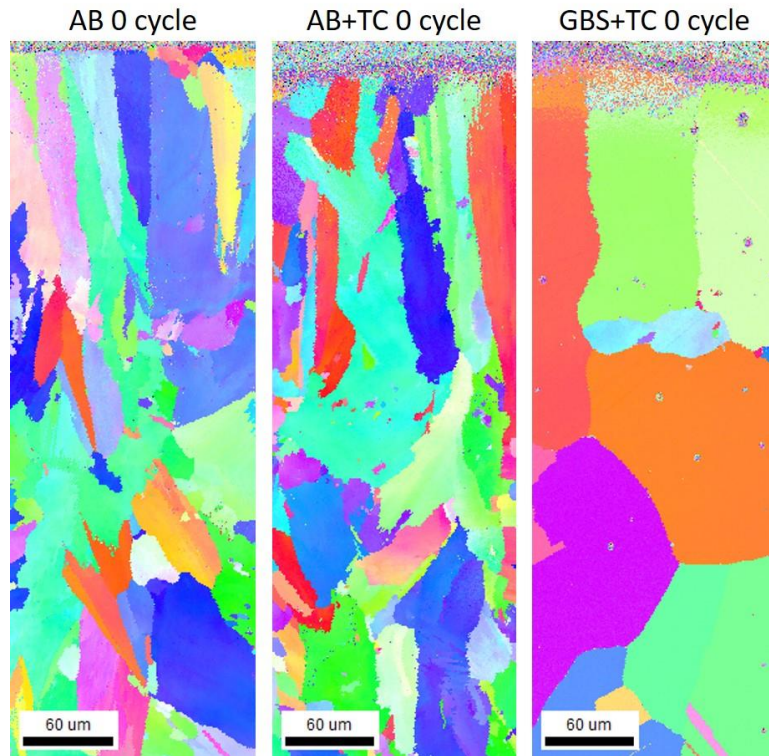


Figure 26. EBSD grain orientation map showing recrystallization and grain growth of GBS+TC (right) compared to AB (left) and AB+TC (center) as a result of heat treatment.

While the characterization campaign of the tested specimens is still in progress, all materials exhibited good adhesion of the bond coat and the substrate was excellent with no signs of delamination due to thermal shock testing.

VI. Conclusions

This research investigated the feasibility of producing a NiCrAlY bond coat on an Alloy 625 substrate by L-PBF. The properties of both an Alloy 625 substrate and an NiCrAlY-coated Alloy 625 substrate were evaluated. In addition, the optimum parameter conditions for MCrAlY coating of an Alloy 625 substrate by L-PBF were verified for the first time based on the welding metallurgy theory. In addition, GBS was successfully introduced in an L-PBF manufactured Alloy 625 substrate to strengthen its grain boundary. Therefore, this study demonstrated that Alloy 625 fabricated by L-PBF has high potential for real industrial applications by improving its manufacturing efficiency together with its high-temperature properties by L-PBF coating, which provides resistance to oxidation/hot corrosion, and GBS heat treatment, which provides resistance to GB cracking. Key contents of each paper are summarized as follows.

1. The optimum parameter conditions for MCrAlY bond coating by L-PBF on an Alloy 625 substrate were selected as follows: layer thickness $t = 50 \mu\text{m}$, hatch spacing $h = 120 \mu\text{m}$, laser power $P = 250 \text{ W}$, and laser scanning speed $v = 800 \text{ mm/s}$. These settings were based on several criteria, such as an approximately 250- μm -thick NiCrAlY coating with a very low residual porosity of $\leq 0.1\%$, including a $\sim 35\%$ dilution zone, a smooth hardness profile between 275 and 305 Hv, low residual stress levels, and a progressive Al concentration distribution.
2. For the mechanical properties' evolution of L-PBF processed Alloy 625, various heat treatments were adopted, and each sample was evaluated through microstructure analysis. A fine columnar/dendritic structure with a high density of dislocations composed the as-built sample, and it contributed to its high strength. Direct aging showed the highest strength effect through the precipitation of γ'' phases and the discontinuous formation of elongated Cr-

rich M₂₃C₆ carbides in the remaining columnar/dendritic structure. A solid-solution treatment caused recrystallization. This sample showed increased strength due to the added post-aging treatment. To achieve the required mechanical properties, appropriate post-heat treatment is required for L-PBF manufactured Alloy 625 to improve its mechanical properties.

3. Before application of the GBS to the L-PBF fabricated Alloy 625, the formation mechanism of GBS was investigated. Only in the case of Cr atom enrichment near and at the GBs, serrated GBs were observed from the experiment with a model alloy. This means that Cr atom enrichment caused the minimum strain of 0.97 kJ/mol on the GBs, which led to the onset of GBS.
4. Based on the GBS mechanism, GBS was introduced to Alloy 625 for the first time. A specialized heat treatment (1300°C/90min-5°C /slow cooling-870°C /2hrs) was designed to induce GBS for Alloy 625, and it worked well. Unlike the results of a previous study, the serrated GBs were decorated not only with M₂₃C₆ but also MC carbides.
5. For the high-temperature tensile test application, GBS heat treatment was newly introduced to the L-PBF fabricated Alloy 625 ('GBS HT' sample). The as-built sample has significantly higher strength; however, its ductility was too low. Therefore, it was modified by GBS HT, which showed the increment of ductility from 600 °C, while its strength remained higher than that of wrought Alloy 625. Recrystallized L-PBF Alloy 625 also showed higher strength than that of wrought Alloy 625, while its ductility was lower than that of the GBS HT sample at temperatures higher than 600 °C. The recrystallization and fine precipitates contributed to relatively high strength and high ductility. The GBS HT sample showed results similar to those of the RX HT sample in terms of both strength and ductility, but it showed a small difference in the DSA phenomenon. The temperature range at which the undesirable DSA

phenomenon occurred was smaller in the L-PBF manufactured samples, especially in the GBS HT sample due to the lack of solute atoms like Nb and C.

6. After the mechanical properties of the superalloy substrate itself and the heat treated one were verified, the oxidation properties of the MCrAlY-coated Alloy 625 fabricated by L-PBF were evaluated. In the weight gain test, the MCrAlY-coated Alloy 625 sample showed intermediate properties in comparison to pure MCrAlY and pure Alloy 625. The new coating process was performed by the L-PBF method; the resulting sample showed good oxidation properties, and this work is step towards the feasibility of real industrial applications.
7. GBS heat treatment was applied to the MCrAlY-coated Alloy 625 fabricated by L-PBF, and its thermal shock properties were compared to the non-heat-treated sample. After 450 cycles of thermal shock testing in the temperature range from 300 to 950 °C, the weight gain was increased in the non-heat-treated sample, while the heat-treated sample showed weight loss. The result of weight gain in the non-heat-treated sample can be attributed to the surface oxide layer forming as the sample endures each cycle. The weight loss is due to delamination of the top coating due to the surface oxide layer after heat treatment while the delayed cracking phenomenon in bond coat part was decreased after heat treatment. In all cases, samples exhibited no signs of oxidation and adhesion of the bond coat and the substrate was excellent with no signs of delamination due to thermal shock testing.
8. From present study, the feasibility of L-PBF manufacturing of TBC coating on the Ni-based substrate was certified to be commercialized. In addition to that, the effect of GBS heat treatment for Alloy 625 to high temperature properties showed positive effect and it will be continued to applied and studied for the

other high temperature properties.

VII. References

- [1] Z.H. Liu, D.Q. Zhang, S.L. Sing, C.K. Chua, L.E. Loh, Interfacial characterization of SLM parts in multi-material processing: metallurgical diffusion between 316L stainless steel and C18400 copper alloy, *Mater. Charact.*, 94 (2014) 116–125, <https://doi.org/10.1016/j.matchar.2014.05.001>.
- [2] J. Chen, Y. Yang, C. Song, M. Zhang, S. Wu, D. Wang, Interfacial microstructure and mechanical properties of 316L/CuSn10 multi-material bimetallic structure fabricated by selective laser melting, *Mat. Sci. Eng. A*, 752 (2019) 75–85, <https://doi.org/10.1016/j.msea.2019.02.097>.
- [3] S.L. Sing, L.P. Lam, D.Q. Zhang, Z.H. Liu, C.K. Chua, Interfacial characterization of SLM parts in multi-material processing: intermetallic phase formation between AlSi10Mg and C18400 copper alloy, *Mater. Charact.*, 107 (2015) 220–227, <https://doi.org/10.1016/j.matchar.2015.07.007>.
- [4] J. G. Yoon, J. W. Jeong, Y. S. Yoo, H. U. Hong, Influence of initial microstructure on creep deformation behaviors and fracture characteristics of Haynes 230 superalloy at 900 °C, *Mater. Charact.*, 101 (2015) 49–57, <http://dx.doi.org/10.1016/j.matchar.2015.01.002>.
- [5] J. W. Lee, D. J. Kim, H. U. Hong, A new approach to strengthen grain boundaries for creep improvement of a Ni-Cr-Co-Mo superalloy at 950 °C, *Mat. Sci. Eng. A*, 625 (2015) 164–168, <http://dx.doi.org/10.1016/j.msea.2014.12.010>.
- [6] M. Daroonparvar, M.S. Hussain, M.A.M. Yajid, The role of formation of continuous thermally grown oxide layer on the nanostructured NiCrAlY bond coat during thermal exposure in air, *Appl. Surf. Sci.*, 261 (2012) 287–297, <https://doi.org/10.1016/j.apsusc.2012.08.002>.
- [7] W. Leng, R. Pillai, P. Huczowski, D. Naumenko, W.J. Quadackers,

Microstructural evolution of an aluminide coating on alloy 625 during wet air exposure at 900 °C and 1000 °C, *Surf. Coat. Tech.*, 354 (2018) 268–280, <https://doi.org/10.1016/j.surfcoat.2018.09.043>.

[8] F.A. Khalid, N. Hussain, A.H. Qureshi, Microstructural study on oxidation of aluminized coating on Inconel 625, *J. Mater. Eng. Perform.*, 11 (2002) 211–214, <https://doi.org/10.1361/105994902770344286>.

[9] P.W. Schike, *Advanced gas turbine materials and coatings*, GE Energy, (2004).

[10] D.R. Clarke, M. Oechsner, N.P. Padture, Thermal-barrier coatings for more efficient gas-turbine engines, *MRS Bull.* 37 (2012) 891–898, <https://doi.org/10.1557/mrs.2012.232>.

[11] M. J. Donachie, S. J. Donachie, *Superalloys: A Technical Guide* 2nd ed. ASTM International, the Materials Information Society, ISBN: 0-87170-749-7.

[12] R. C. Reed, *The Superalloys: Fundamentals and Applications*, Cambridge University Press, ISBN: 978-0-511-24546-6.

[13] N.P. Padture, M. Gell, E.H. Jordan, Thermal barrier coatings for gas-turbine engine applications, *Science's compass*, 296 (2002) 280–284, <https://doi.org/10.1126/science.1068609>.

[14] J.D. Osorio, A. Toro, J.P. Hernandez–Ortiz, Thermal barrier coatings for gas turbine applications: failure mechanisms and key microstructural features, *DYNA*, 79 (2012) 149–158
http://www.scielo.org.co/scielo.php?script=sci_arttext&pid=S001273532012000600018&lng=en&nrm=iso.

[15] N. Zotov, M. Bartsch, L. Chernova, D.A. Schmidt, M. Havenith, G. Eggeler, Effects of annealing on the microstructure and the mechanical properties of EB-PVD thermal barrier coatings, *Surf. Coat. Tech.*, 205 (2010) 452–464,

<https://doi.org/10.1016/j.surfcoat.2010.07.008>.

[16] J. Alcisto, A. Enriquez, H. Garcia, S. Hinkson, T. Steelman, E. Silverman, P. Valdovino, H. Gigerenzer, J. Foyos, J. Ogren, J. Dorey, K. Karg, T. McDonald, and O.S. Es-Said, Tensile Properties and Microstructures of Laser-Formed Ti-6Al-4V, *JMEP*, 20 (2011) 203–212, <https://doi.org/10.1007/s11665-010-9670-9>.

[17] Reports and data, March 18, 2019, Increasing adoption of Additive Manufacturing in automotive and aerospace industry is projected to stimulate market demand.

[18] M. Zenou, L. Grainger, 3-Additive manufacturing of metallic materials, *Addit. Manuf.*, (Materials, Processes, Quantifications and Applications) (2018) 53-103, <http://dx.doi.org/10.1016/B978-0-12-812155-9.00003-7>.

[19] B. E. Carroll, T. A. Palmer and A. M. Beese, Anisotropic tensile behavior of Ti–6Al–4V components fabricated with directed energy deposition additive manufacturing, *Acta Mat.*, 87 (2015) 309-320, <https://doi.org/10.1016/j.actamat.2014.12.054>.

[20] 3D experience, 3D printing-additive, Introduction to 3D printing-additive processes.

[21] J. P. Moore and C. B. Williams, Fatigue properties of parts printed by PolyJet material jetting, *Rapid Prototyp. J.*, 21 (2015) 675-685, <https://doi.org/10.1108/RPJ-03-2014-0031>.

[22] M. M. –Hou, Overview of additive manufacturing process, *Addit. Manuf.*, (Materials, Processes, Quantifications and Applications) (2018) 1-38, <http://dx.doi.org/10.1016/B978-0-12-812155-9.00001-3>.

[23] Additive manufacturing (A game changer for the manufacturing industry?), Roland Berger, (2013).

- [24] T. Duda, L. V. Raghavan, 3D metal printing technology: the need to re-invent design practice, *AI&SOCIETY* 33 (2018) 241-252, <https://doi.org/10.1007/s00146-018-0809-9>.
- [25] W. Liu, J. N. Dupont, Fabrication of functionally gaded TiC/Ti composites by Laser Engineered Net Shaping, *Scr. Mater.*, 48 (2003) 1337-1342, [https://doi.org/10.1016/S1359-6462\(03\)00020-4](https://doi.org/10.1016/S1359-6462(03)00020-4).
- [26] W. Cong, F. Ning, A fundamental investigation on ltrasonic vibration-assisted laser engineered net shaping of stainless steel, *Int. J. Mach. Tool. Manu.*, 121 (2017) 61-69, <http://dx.doi.org/10.1016/j.ijmachtools.2017.04.008>.
- [27] D. –S. Shim, G. –Y. Baek, J. –Seon. Seo, G. –Y. Shin, K. –P. Kim, K. –Y. Lee, Effect of layer thickness setting on deposition characteristics in direct energy deposition (DED) process, *Opt. Laser Technol.*, 86 (2016) 69-78, <http://dx.doi.org/10.1016/j.optlastec.2016.07.001>.
- [28] M. Javidani, J. A. –Zavala, J. Danovitch, Y. Tian, M. Brochu, Additive Manufacturing of AlSi10Mg Alloy Using Direct Energy Deposition: Microstructure and Hardness Characterization, *J. Therm. Spray Tech.*, 26 (2017) 587-597, <http://dx.doi.org/10.1007/s11666-016-0495-4>.
- [29] Y. Z. Zhang, Y. T. Liu, X. H. Zhao, Y. J. Tang, The interface microstructure and tensile properties of direct energy deposited TC11/Ti2AlNb dual alloy, *Mater. Design*, 110 (2016) 571-580, <http://dx.doi.org/10.1016/j.matdes.2016.08.012>.
- [30] X. Ahang, Y. Chen, T. Pan, W. Cui, L. Li, F. Liou, Joining of copper and stainless steel 304L using direct metal deposition, *Solid Freeform Fabrication 2019:Proceedings of the 30th Annual International*
- [31] T. Bhardwaj, M. Shukla, C. P. Paul, K. S. Bindra, Direct Energy Deposition-Laser Additive Manufacturing of Titanim-Molybdenum alloy Parametric studies,

microstructure and mechanical properties, *J. Alloys Compd.*, 787 (2019) 1238-1248, <https://doi.org/10.1016/j.jallcom.2019.02.121>.

[32] Digital Alloys' Guide to Metal Additive Manufacturing-Part11, Surface Roughness (2019).

[33] S. Gasman, 15-Additive aerospace considered as a business, *Additive Manufacturing for the Aerospace Industry* (2019) 327-340, <https://doi.org/10.1016/B978-0-12-814062-8.00017-0>.

[34] G. SERIN, M. KAHYA, H. Ö. ÜNVER, Y. GÜLEÇ, N. DURLU, O. EROĞUL, A review of additive manufacturing technologies, *The 17th International Conference on Machine Design and Production*, (2016).

[35] L. Hongjun, F. Zitian, H. Naiyu, D. Xuanpu, A note on rapid manufacturing process of metallic parts based on SLS plastic prototype, *J. Mater. Process Tech.*, 142 (2003) 710-713, [https://doi.org/10.1016/S0924-0136\(03\)00811-2](https://doi.org/10.1016/S0924-0136(03)00811-2).

[36] B. Wysocki, P. Maj, R. Sitek, J. Buhagiar, K. J. Kurzydłowski and W. Swieszkowski, Laser and Electron Beam Additive Manufacturing Methods of Fabricating Titanim Bone Implants, *Res. J. Appl. Sci.*, 7 (2017) 657, <https://doi.org/10.3390/app7070657>.

[37] P. K. Gokuldoss, S. Kolla and J. Eckert, Additive Manufacturing Processes: Selective Laser Melting, Electron Beam Melting and Binder Jetting-Selection Guidelines, *Materials* 10 (2017) 672, <https://doi.org/10.3390/ma10060672>.

[38] M. Fousová, D. Vojtěch, K. Doubrava, M. Daniel, C.-F. Lin, Influence of Inherent Surface and Internal Defects on Mechanical Properties of Additively Manufactured Ti6Al4V Alloy: Comparison between Selective Laser Melting and Electron Beam Melting, *Materials* 11 (2018) 537, <https://doi.org/10.3390/ma11040537>.

[39] L. Caprio, G. Chiari, A. G. Demir, B. Previtali, Development of novel high

- temperature laser powder bed fusion system for the processing of crack-susceptible alloys, *Solid Freeform Fabrication 2018: Proceedings of the 29th Annual International*.
- [40] Y. Yoo, Nickel Base Superalloys, *KIC News* 17 (2014) 1-9.
- [41] J. M. Byun, S. H. Hwang, S. Lee, Y. D. Kim, Research Trend of Mo based Superalloys, *J. Kor. Powd. Met. Inst.*, 20 (2013) 487-493, <https://doi.org/10.4150/KPMI.2013.20.6.487>.
- [42] C. T. Sims, N. S. Stoloff, W. C. Hagel, *Superalloys II*, *Mater. Manuf. Process*, 7 (1992) 463-468, <https://doi.org/10.1080/10426919208947432>.
- [43] C. T. Sims, A history of superalloy metallurgy for superalloy metallurgists, GE company, (1984) 399-419.
- [44] C. R. Brooks, *Heat Treatment, Structure and Properties of Nonferrous Alloys*, ASM, (1982).
- [45] *Superalloys 718, 625, 706 and derivatives 2005* edited by E. A. Loria, TMS (1997)
- [46] W. F. Hosford, *Mechanical Behavior of Materials*, 1st ed.; Cambridge University Press: New York, NY, USA, 2 (2005).
- [47] A. Kelly, *Strengthening methods in crystals*, Edited by A. Kelly and R. B. Nicholson, Elsevier Pub. Co., (1971).
- [48] M. Sundararaman, P. Mukhopadhyay, S. Banerjee, Some aspects of the precipitation of metastable intermetallic phases in INCONEL 718, *Met. Trans. A*, 23 (1992) 2015-2028, <https://doi.org/10.1007/BF02647549>.
- [49] C. Shankar, K. B. S. Rao, S. L. Mannan, Microstructure and mechanical properties of Inconel 625 superalloy, *J. Nucl. Mater.*, 288 (2001) 222-232, [https://doi.org/10.1016/S0022-3115\(00\)00723-6](https://doi.org/10.1016/S0022-3115(00)00723-6).

- [50] R. F. Decker and C. T. Sims, The Superalloys, C. T. Sims and W. C. Hagel (eds), John & Sons, chap.2 (1972).
- [51] J. R. Mihalisin, C. C. Bieber, R. T. Grant, Sigma-its occurrence, effect, and control in nickel-base superalloys, Trans. Am. Inst. Min. Metall. Eng., 242 (1968) 2399,
- [52] W.G. Kim, S.N. Yin, G.G. Lee, Y.W. Kim, S.J. Kim, Creep oxidation behavior and creep strength prediction for Alloy 617, Int. J. Pres. Ves. Pip., 87 (2010) 289, <https://doi.org/10.1016/j.ijpvp.2010.03.008>.
- [53] Nickel Alloy 625, Metals 28.
- [54] A. J. Sedriks, Nickel Alloys: Corrosion, Encyclopedia of Materials: Science and Technology (Second Edition), (2001) 6140-6141, <https://doi.org/10.1016/B0-08-043152-6/01086-X>.
- [55] Inconel Alloy 625, Special metals data sheet (2013).
- [56] J. Mitra, S. Banerjee, R. Tewari, G. D. Dey, Fracture behavior of Alloy 625 with different precipitate microstructures, Mat. Sci. Eng. A, 574 (2013) 86-93, <https://doi.org/10.1016/j.msea.2013.03.021>.
- [57] S. Floreen, G. E. Fuchs, W. J. Yang, The Metallurgy of Alloy 625, Knolls Atomic Power Laboratory, https://doi.org/10.7449/1994/Superalloys_1994_13_37.
- [58] M. Sundararamman, L. Kumar, G. E. Prasad, P. Mukhopadhyay, S. Baneree, Precipitation of an intermetallic phase with Pt₂Mo-type structure in alloy 625, Metal. Mat. Trans. A, 30 (1999) 41-52, <https://doi.org/10.1007/s11661-999-0194-6>.
- [59] M. D. Mathew, P. Parameswaran, K. B. S. Rao, Microstructural changes in alloy 625 during high temperature creep, Mat. Char., 59 (2008) 508-513, <https://doi.org/10.1016/j.matchar.2007.03.007>.

[60] I. Yadroitsev, L. Thivillon, P. Bertrand, I. Smurov, Strategy of manufacturing components with designed internal structure by selective laser melting of metallic powder, *Appl. Surf. Sci.* 254 (2007) 980–983, <http://dx.doi.org/10.1016/j.apsusc.2007.08.046>.

[61] P. Wang, B. Zhang, C.C. Tan, S. Raghavan, Y.-F. Lim, C.-N. Sun, et al., Microstructural characteristics and mechanical properties of carbon nanotube reinforced Inconel 625 parts fabricated by selective laser melting, *Mater. Des.* 112 (2016) 290–299, <http://dx.doi.org/10.1016/j.matdes.2016.09.080>.

[62] K. N. Amato, J. Hernandez, L. E. Murr, E. Martinez, S. M. Gaytan, P. W. Shindo, Comparison of Microstructures and Properties for a Ni-Base Superalloy (Alloy 625) Fabricated by Electron and Laser Beam Melting, *J. Mater. Sci. Res.*, 1 (2012) 3-41, <http://dx.doi.org/10.5539/jmsr.v1n2p3>.

[63] H. Wong, K. Dawson, G. A. Ravi, L. Howlett, R. O. Jones, C. J. Sutcliffe, Multi-Laser Powder Bed Fusion Benchmarking-Initial Trials with Inconel 625, *Int. J. Adv.*, 105 (2019) 2891-2906, <https://doi.org/10.1007/s00170-019-04417-3>.

[64] R. C. Reed, *The Superalloys Fundamentals and Applications*, Cambridge (2006).

[65] N. R. Muktinutalapati, *Materials for gas turbines-An overview* (2011), <https://doi.org/10.5772/20730>.

[66] H. M. Tawancy, N. Sridhar, N. M. Abbas, D. Rickerby, Failure mechanism of a thermal barrier coating system on a nickel-base superalloy, *J. Mater. Sci.*, 33 (1998) 681-686, <https://doi.org/10.1023/A:1004333627312>.

[67] M. C. Galetz, *Coatings for Superalloys*, (2015), <https://doi.org/10.5772/61141>.

- [68] T. F. An, H. R. Gua, X. F. Sun, Z. Q. Hu, Effect of the θ - α -Al₂O₃ Transformation in Scales on the Oxidation Behavior of a Nickel-Base Superalloy with an Aluminide Diffusion Coating, *Oxid. Met.*, 54 (2000) 301-316, <https://doi.org/10.1023/A:1004654429687>
- [69] M. P. Taylor, An oxidation study of an MCrAlY overlay coating, *Mater. High Temp.*, 22 (2005) 433-436, <https://doi.org/10.1179/mht.2005.051>.
- [70] A Bennett, F. C. Roriz, A. B. Thaakker, A philosophy for thermal barrier coating design and its corroboration by 10000h service experience on RB211 nozzle guide vanes, *Surf. Coat.*, 32 (1987) 359-375, [https://doi.org/10.1016/0257-8972\(87\)90120-4](https://doi.org/10.1016/0257-8972(87)90120-4).
- [71] T. J. Nijdam, W. G. Sloof, Effect of reactive element oxide inclusions on the growth kinetics of protective oxide scales, *Acta Mater.*, 55 (2007) 5980-5987, <https://doi.org/10.1016/j.actamat.2007.07.007>.
- [72] H. Guo, D. Li, L. Zheng, S. Gong, H. Xu, Effect of co-doping of two reactive elements on alumina scale growth of β -NiAl at 1200 °C, *Corros. Science*, 88 (2014) 197-208, <https://doi.org/10.1016/j.corsci.2014.07.036>.
- [73] T. J. Nijdam, W. G. Sloof, Effect of Y Distribution on the Oxidation Kinetics of NiCoCrAlY Bond Coat Alloys, *Oxid. Met.*, 69 (2008) 1-12, <https://doi.org/10.1007/s11085-007-9080-z>.
- [74] C.S.Richard, G.Béranger, J.Lu, J.F.Flavenot, The influences of heat treatments and interdiffusion on the adhesion of plasma-sprayed NiCrAlY coatings, *Surf. Coat.*, 82 (1996) 99-109, [https://doi.org/10.1016/0257-8972\(95\)02640-1](https://doi.org/10.1016/0257-8972(95)02640-1).
- [75] K. Fritscher, C. Leyens, U. Schulz, Investigation of an as-sprayed NiCoCrAlY overlay coating: A thermoanalytical approach, *Mat. Sci. Eng. A*, 369 (2004) 144-150, <https://doi.org/10.1016/j.msea.2003.10.319>.
- [76] A. M. Villafane, J. G. C. Nava, C. G. Tiburcio, F. M. A. Calderon, J. G. G.

Rodriguez, Oxidacion en alta temperatura, Instituto Politecnico Nacional.

[77] M. T. Pace, R. C. Thomson, J. Wells, Oxidation of MCrAlY coating on Ni-based superalloys, *Superalloys 2008 (TMS 2008)*, 2 (2007) 181-190, <https://doi.org/10.1179/174892408X373545>.

[78] D. J. Kim, I. H. Shin, J. M. Koo, C. S. Seok, M. Y. Kim, Evaluation on the delamination life of isothermally aged plasma sprayed thermal barrier coating, *KSME, A* (2009) 162-168, <https://doi.org/10.3795/KSME-A.2009.33.2.162>.

[79] A.G. Demir, B. Previtali, Multi-material selective laser melting of Fe/Al-12Si components, *Manuf. Lett.* 11 (2017) 8-11, <https://doi.org/10.1016/j.mfglet.2017.01.002>.

[80] C. Wei, L. Li, X. Zhang, Y.-H. Chueh, 3D printing of multiple metallic materials via modified selective laser melting, *CIRP Ann. Manuf. Technol.* 67 (2018) 245-248, <https://doi.org/10.1016/j.cirp.2018.04.096>.

[81] K. Partes, C. Giolli, F. Borgioli, U. Bardi, T. Seefeld, F. Vollertsen, High temperature behavior of NiCrAlY coatings made by laser cladding, *Surf. Coat. Tech.* 202 (2008) 2208-2213, <https://doi.org/10.1016/j.surfcoat.2007.09.010>.

[82] M.J. Tobar, J.M. Amado, A. Yanez, J.C. Pereira, C. Amigo, Laser cladding of MCrAlY coatings on stainless steel, *Phys. Procedia* 56 (2014) 276-283, <https://doi.org/10.1016/j.phpro.2014.08.172>.

[83] R. Vilar, E.C. Santos, P.N. Ferreira, N. Franco, R.C. da Silva, Structure of NiCrAlY coatings deposited on single-crystal alloy turbine blade material by laser cladding, *Acta Mater.* 57 (2009) 5292-5302, <https://doi.org/10.1016/j.actamat.2009.06.049>.

[84] Y. Chivel, New approach to multi-material processing in selective laser melting, *Phys. Procedia* 83 (2016) 891-898, <https://doi.org/10.1016/j.phpro.2016.08.093>.

- [85] J. Koopmann, J. Voigt, T. Niendorf, Additive manufacturing of a steel-ceramic multi-material by selective laser melting, *Metall. Mater. Trans. B* 50 (2019) 1042–1051, <https://doi.org/10.1007/s11663-019-01523-1>.
- [86] H.J. Dai, J-C. Gebelin, M. Newell, R.C. Reed, N.D. Souza, P.D. Brown, H.B. Dong, GRAIN SELECTION DURING SOLIDIFICATION IN SPIRAL GRAIN SELECTOR, *Superalloys 2008 (TMS 2008)*, (2008) 367-374, https://doi.org/10.7449/2008/Superalloys_2008_367_374.
- [87] V. I. Razumovskiy, A. Y. Lozovoi, I. M. Razumovskii, First-principles-aided design of a new Ni-base superalloy: Influence of transition metal alloying elements on grain boundary and bulk cohesion, *Acta Mater.*, 82 (2015) 369-377, <http://dx.doi.org/10.1016/j.actamat.2014.08.047>.
- [88] V. Randle, Grain boundary engineering: an overview after 25 years, *J. Mater. Sci. Technol.*, 26 (2010) 253-261, <https://doi.org/10.1179/026708309X12601952777747>.
- [89] T. E. Hsieh, R. W. Balluffi, Observations of roughening/de-faceting phase transitions in grain boundaries, *Acta Mater.*, 37 (1989) 2133-2139, [https://doi.org/10.1016/0001-6160\(89\)90138-7](https://doi.org/10.1016/0001-6160(89)90138-7).
- [90] A. K. Koul, G. H. Gessinger, On the mechanism of serrated grain boundary formation in Ni-based superalloys, *Acta Mater.*, 31 (1983) 1061-1069, [https://doi.org/10.1016/0001-6160\(83\)90202-X](https://doi.org/10.1016/0001-6160(83)90202-X).
- [91] J. M. Larson, S. Floreen, Metallurgical factors affecting the crack growth resistance of a superalloy, *Met. Trans. A*, 8 (177) 51-55, <https://doi.org/10.1007/BF02677263>.
- [92] M. F. Henry, Y. S. Yoo, D. Y. Yoon, J. Choi, The dendritic growth of γ' precipitates and grain, *Met. Trans. A*, 24 (1993) 1733-1743, <https://doi.org/10.1007/BF02657848>.

- [93] R. J. Mitchell, H. Y. Li, Z. W. Huang, On the formation of serrated grain boundaries and fan type structures in an advanced polycrystalline nickel-base superalloy, *J. Mater.*, 209 (2009) 1011-1017, <https://doi.org/10.1016/j.jmatprotec.2008.03.008>.
- [94] H. L. Danflou M. Marty, A. Walder, Formation of Serrated Grain Boundaries and Their Effect on the Mechanical Properties in a Nickel Base Superalloy, *Superalloys 1992*, TMS Warrendale PA, (1992) 63-72.
- [95] H. U. Hong, H. W. Jeong, I. S. Kim, B. G. Choi, Y. S. Yoo, C. Y. Jo, Significant decrease in interfacial energy of grain boundary through serrated grain boundary transition, *Phil. Mag.*, 9 (2012) 2809-2825, <http://dx.doi.org/10.1080/14786435.2012.676212>.



A novel approach to the production of NiCrAlY bond coat onto IN625 superalloy by selective laser melting

Jiwon Lee, Mathieu Ternier, Etienne Copin, Philippe Lours, Hyun-Uk Hong

► **To cite this version:**

Jiwon Lee, Mathieu Ternier, Etienne Copin, Philippe Lours, Hyun-Uk Hong. A novel approach to the production of NiCrAlY bond coat onto IN625 superalloy by selective laser melting. Additive Manufacturing, Elsevier, 2020, 31, pp.1-8/100998. 10.1016/j.addma.2019.100998 . hal-02404143

HAL Id: hal-02404143

<https://hal-mines-albi.archives-ouvertes.fr/hal-02404143>

Submitted on 4 Feb 2020

HAL is a multi-disciplinary open access archive for the deposit and dissemination of scientific research documents, whether they are published or not. The documents may come from teaching and research institutions in France or abroad, or from public or private research centers.

L'archive ouverte pluridisciplinaire **HAL**, est destinée au dépôt et à la diffusion de documents scientifiques de niveau recherche, publiés ou non, émanant des établissements d'enseignement et de recherche français ou étrangers, des laboratoires publics ou privés.

A novel approach to the production of NiCrAlY bond coat onto IN625 superalloy by selective laser melting

Jiwon Lee^{a,b}, Mathieu Terner^a, Etienne Copin^b, Philippe Lours^{b,*}, Hyun-Uk Hong^{a,*}

^a Department of Materials Science and Engineering, Changwon National University, 20 Changwondaehak-ro, Changwon, Gyeongnam 51140, Republic of Korea

^b Institut Clément Ader (ICA), Université de Toulouse, CNRS, IMT Mines Albi, INSA, ISAE-SUPAERO, UPS, Campus Jarlard, F-81013 Albi, France

Keywords:

MCrAlY bond coat
Superalloy
Additive manufacturing
Powder bed fusion
Selective laser melting

The present study investigated for the first time the feasibility of producing by Selective Laser Melting (SLM) a NiCrAlY bond coat material directly onto an IN625 substrate itself produced by SLM. A typical parameters optimization was conducted by varying laser power (P) and scanning speed (v). Single-line scanning tracks and two-layer coatings were carried out and analyzed for 15 different P/v conditions. Several criteria were defined for the selection of appropriate SLM parameters. The results showed significant remelting of the underlying substrate, which is a typical feature of SLM manufacturing. This led to the formation of an intermediate dilution zone characterized by substantial mixing between IN625 superalloy substrate and NiCrAlY bond coat suggesting excellent metallurgical bonding. Optimum processing conditions were found for $P = 250$ W and $v = 800$ mm/s. It produced a dense $242\ \mu\text{m}$ thick bond coat including a 36% dilution zone. The SLMed \langle NiCrAlY-IN625 \rangle system exhibited a smooth microhardness profile slightly increasing from 275 Hv in the bond coat to 305 Hv in the substrate. A progressive Al concentration distribution between the phases and low residual stress levels were found in the system. This suggested that SLM might be a valuable alternative manufacturing process for bond coat systems promoting excellent adhesion for high temperature applications.

1. Introduction

Additive Manufacturing (AM) has become an outstanding alternative to conventional manufacturing, part of what is now commonly referred to as the 4th industrial revolution. AM presents many advantages such as versatility, complex and near-net-shape manufacturing, elimination of tooling, waste reduction, shorter lead time, etc. [1–3]. AM technologies have been classified into seven categories according to raw materials type, power source and processing technique [4]. For the production of metallic materials, Directed Energy Deposition (DED) and Powder Bed Fusion (PBF) are the most attractive and the most popular methods [1–6]. DED consists of direct deposition of material, usually spraying a powder simultaneously melted by a focused energy source through coaxial nozzles. Although the resolution is limited, these methods are particularly adapted to direct fabrication of rather simple shapes, cladding and remanufacturing/repair. By contrast, PBF consists in selective melting of powder layers by a focused power source, usually a laser or an electron beam. This allows the production of both internal and external complex geometries with much greater resolution therefore particularly suitable for direct manufacturing. There has been extensive research on these PBF

technologies in particular for the fabrication of CoCr-Mo alloys, aluminum alloys and superalloys by Selective Laser Melting (SLM) for applications in aerospace, medical, automotive and power generation.

Ni-based superalloy Inconel 625 (IN625) is a popular material for gas turbine applications characterized by good high temperature strength, creep resistance, corrosion resistance and excellent weldability [7–10]. Due to this excellent weldability, fabrication of IN625 by SLM is particularly appropriate and has been properly optimized [11–14]. In order to enhance properties and increase operating temperatures of superalloys, Thermal Barrier Coating (TBC) have been developed to protect the substrates at high temperature so that they could retain their superior properties for longer time during operation [15–18]. Typically, TBCs provide insulation to enable superalloys to operate at about $150\ ^\circ\text{C}$ above their usual upper limit [19–23]. These TBCs commonly consist in an external ceramic top coat (TC) for thermal insulation and an intermediate MCrAlY metallic bond coat (BC, where typically $M = \text{Ni, Co, Fe}$ or a combination of those) to accommodate the difference in coefficient of thermal expansion between TC and superalloy substrate, and to grow a thin, compact and adherent protective oxide scale promoting optimized hot corrosion resistance [19–24].

As opposed to conventional casting and forging for substrate metals,

* Corresponding authors.

E-mail addresses: huhong@changwon.ac.kr (H.-U. Hong), philippe.lours@mines-albi.fr (P. Lours).

these protective layers are generally coated onto the substrate by different conventional methods such as air or vacuum plasma spray (APS/VPS), electron beam-physical vapor deposition (EB-PVD) and arc ion plating (AIP) [20,21]. These separated processes require much manpower, cost and time. In addition, when coatings are conventionally applied, especially by plasma spraying, substantial residual stresses may be induced in the deposits, notably at the substrate-coating interface. This can generate delamination which is also a critical concern [25,26]. For these considerations, SLM of NiCrAlY bond coat onto IN625 substrate, itself produced by SLM, is considered in the present study. We believe that due to the nature of the SLM process, and in particular the typical remelting of underlying layers, excellent bonding between substrate and BC could be achieved. Although the ultimate production of complex coated geometries, such as blades, is challenged by the nature of PBF technologies requiring deposition of an entire layer of powder, therefore presently limiting the deposition onto flat surfaces, this issue could very well be addressed for example by selective deposition of different powders within a single layer by multiple powder containing tanks. There have been several studies regarding multi-material processing by SLM, as for instance with stainless steel and copper alloys [27–29], composite material mixing two different powders [30,31], NiCrAlY cladding [32–34], developed methodology accepting SLM concept [35] and innovative additive manufacturing of a steel-ceramic multi-material [36]. However, this is the first time to the best of our knowledge that SLM is used to produce both the superalloy substrate and the NiCrAlY bond coat.

In the present paper, we study the optimization of SLM fabrication of a NiCrAlY bond coat onto an IN625 superalloy substrate, itself produced by SLM. The optimization of the process parameters is described on the basis of several criteria and the as-produced materials are thoroughly analyzed. We conclude with a set of processing conditions which shows very promising results. This suggests the feasibility of selective laser melting as an alternative method for the deposition of coatings in TBC systems.

2. Experimental procedure

2.1. Raw materials: pre-alloyed powders

The IN625 powder used in this study was a commercial gas-atomized pre-alloyed powder supplied by the SLM manufacturer SLM Solutions. The element composition of the powder, determined by inductively coupled plasma optical emission spectrometry (ICP-OES), is given in Table 1. The SEM micrograph in Fig. 1(a) shows the powder morphology: most powder particles were spherical with a small amount of irregular particles and aggregates. The powder size distribution was measured with a laser diffraction particle size analyzer (Malvern Mastersizer 3000). The particles had a size distribution between 20 μm (D_{10}) and 44 μm (D_{90}) with an average diameter of 29 μm (Fig. 1(c)). The powder flow rate was conveniently measured with a Hall flowmeter according to ASTM B213 standard and was 12.6 s. Such a powder with these characteristics is appropriate for SLM.

The main metallic element M for an NiCrAlY bond coat generally depends on the substrate composition and is commonly Ni, Co or NiCo. To match the Ni-rich IN625 substrate, NiCrAlY was therefore selected in the present study (Table 1). Unconventional gas atomized NiCrAlY pre-alloyed powder with characteristics appropriate for SLM processing was

Table 1
Chemical composition in wt. % measured by ICP-OES of IN625 and NiCrAlY pre-alloyed powders used for SLM manufacturing.

	Ni	Cr	Mo	Fe	Co	C	Nb	Al	Y
Inconel 625	Bal.	20.08	8.27	3.49	0.6	0.08	3.12	0.35	–
NiCrAlY	Bal.	22.01	–	–	–	–	–	9.34	1.165

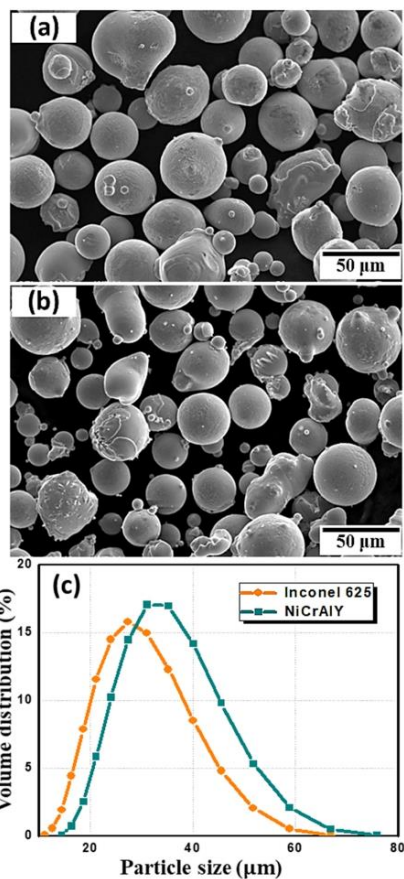


Fig. 1. SEM micrographs showing the (a) Inconel 625 and (b) NiCrAlY powders. (c) Particle size distribution showing the similarity of both powders.

specially ordered to Ducal International. The powder morphology was similar to that of IN625 with mostly spherical shape particles (Fig. 1(b)). The powder size distribution was measured between 24 μm (D_{10}) and 51 μm (D_{90}) with an average diameter of approximately 35 μm (Fig. 1(c)). The flowability was measured at 17.4 s. Although the particle size and flow time of the NiCrAlY powder were slightly higher than those of IN625, it is believed to have no significant influence on its processability by SLM since they remain in the processability window recommended by the manufacturer of the machine.

2.2. SLM processing

The equipment used for additive manufacturing was an SLM 125 H L commercialized by SLM Solutions equipped with a 400 W Yb laser with a Gaussian beam focus diameter of 70–100 μm (constant in the present study for all processing conditions). The volume of fabrication allowed by the machine is 125 × 125 × 125 mm^3 . The process was carried out under a protective argon atmosphere and the building platform was

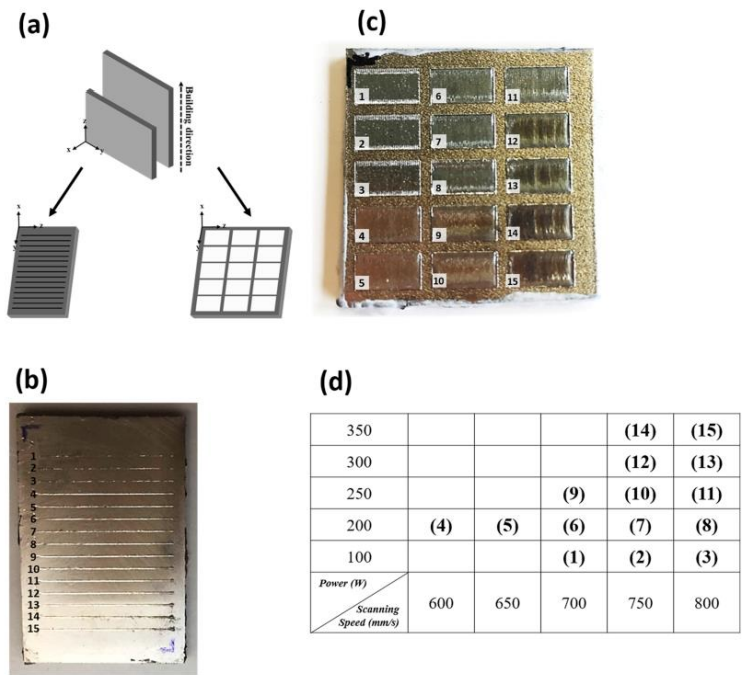


Fig. 2. (a) Schematics of the fabrication and experimental results of (b) single-line scanning tracks and (c) two-layer NiCrAlY coatings onto IN625 plate all produced by SLM according to P/v parameters conditions shown in (d).

held at 150 °C to reduce stress. Fabrication of IN625 by SLM has been studied and optimized extensively [11–14]. Due to its excellent weldability, this superalloy has been an interesting candidate for the early development of this technology. The processing conditions used for the fabrication of IN625 samples were: power $P = 275$ W, scanning speed $v = 760$ mm/s, hatch spacing $h = 120$ μ m, layer thickness $t = 50$ μ m. The scanning strategy includes contours and uses a stripes fill pattern type with stripes of length 10 mm and a rotation angle of the scanning directions of 33° between consecutive layers. These conditions, which could be further optimized, resulted in a residual porosity measured here below 0.5% considered more than acceptable for the purpose of the present study.

Two millimeters thick IN625 plates were built vertically to serve as substrate for subsequent NiCrAlY coatings (Fig. 2(a)). A 30 mm \times 20 mm \times 2 mm plate was polished down to grit 1200 SiC abrasive papers ($R_a \leq 20$ nm) to remove the typical roughness resulting from SLM manufacturing measured at $R_a = 37 \pm 3$ μ m. This plate was used as the IN625 substrate for single-line NiCrAlY depositions (Fig. 2(b)) in order to evaluate track stability and bead geometry without artifacts due to roughness of the substrate base-plate otherwise substantial as well as to provide a clear contrast for optical analyses. Another as-built 30 mm \times 30 mm \times 2 mm plate, was used as-is as substrate for multi-layers NiCrAlY coating (Fig. 2(c)). After processing, plate's removal and thorough cleaning of the SLM machine, the IN625 superalloy substrate plates were fixed horizontally on the steel building platform using an OMEGABOND® OB-600 ceramic cement and a thermally conductive paste. The platform was then levelled so that the zero position would match the substrate plate surface for processing of the NiCrAlY coatings directly onto the IN625 substrates.

To the best of the author's knowledge, there is not any reference in the literature about SLM processing of NiCrAlY. For this reason, the Granta CES EduPack™ 2017 database was used to identify typical SLM materials with physical and thermal properties close to that of NiCrAlY (melting point, thermal conductivity etc.), so as to use the set of parameters available in the literature for those materials as starting points for the parametric study. A process parameters optimization matrix was accordingly designed with 15 different values set of power P (W) and scanning speed v (mm/s) in reference to IN625 and CoCr-Mo alloys (Fig. 2(d)). The SLM process was conventionally carried out using a layer thickness of $t = 50$ μ m, a hatch spacing of $h = 120$ μ m, and scanning strategy similar to that of the IN625 substrate, though rotation between layers were not included. Single-line scanning NiCrAlY tracks, as in Fig. 2(b), were performed to analyze the track stability and bead or melt pool geometry. Furthermore, 8 mm \times 4 mm NiCrAlY coatings consisting of two 50 μ m layers were built, as in Fig. 2(c). Given the apparent density of the powder (approximately 60%) this theoretically corresponds to a coating thickness of about 70 μ m, which is close to the typical thickness of MCrAlY bond coats in TBC systems [20].

2.3. Materials characterization

The single-line scanning tracks were cut perpendicular to the scanning direction to observe the bead or melt pool geometry in cross-section by optical microscopy. Top-views of the single-line scanning tracks were also taken by optical microscopy to measure more accurately the bead width and evaluate track stability. The two-layer coatings were cut perpendicular to the longitudinal direction, i.e. along the scanning direction. All specimens were then mounted and carefully

subjected to conventional metallographic preparation of grinding with abrasive SiC papers and fine polishing with diamond pastes down to 1 μm for observation by microscopy. The residual porosity of the SLMed NiCrAlY coatings was measured by microscopy according to the ASTM standard E2109-01. Due to the small area of the BC, the porosity was measured systematically within the bond coat alone in five consecutive planes by grinding a few tens of micrometers, and averaged for each coating for statistical purpose. The microstructure was revealed by chemical etching with *aqua regia* solution and observed by optical microscopy (OM, Nikon EPIPHOT 200) and scanning electron microscopy (SEM, JEOL JSM-5800) equipped with energy dispersive X-ray spectroscopy (EDS). Kernel average misorientation (KAM) data acquired from electron backscattering diffraction (EBSD) with a field-emission scanning electron microscope (FE-SEM, MIRA-II) were used to measure local misorientation [37–41] and thereby assess qualitatively residual stress. To avoid artifacts from metallographic preparation, the final 1 μm polishing step was carried out using a colloidal silica suspension. Electron probe micro-analysis (EPMA, JEOL JXA-8100) was performed on unetched specimens to accurately determine the elemental distribution from the NiCrAlY bond coat surface to 300 μm in depth. Vickers microhardness (Mitutoyo HM-122) was measured every 40 μm from the top surface of the bond coat to 400 μm deep into the substrate for all conditions using a test load of 500 g.

3. Results and discussion

3.1. Single-line scanning analysis

Single-line scanning were processed, Fig. 2(b), in order to study the stability and geometry of the weld tracks for each condition. Although it was difficult to obtain conclusive results due to the instability of the weld track expected in SLM manufacturing and questioned representativity with respect to bulk processing due to the influence of processing adjacent tracks, these single-line scanning tracks were nevertheless found informative for preselection of the most appropriate processing conditions. Fig. 3 shows optical micrographs of the cross-section and the top-view of each single-line scanning track according to the different sets of power and scanning speed P/v . The bead or melt pool aspect was significantly different among all conditions.

As first consideration in Fig. 3, it was clear that remelting of the underlying IN625 substrate was substantial. This was evidenced by the measured values of geometrical dilution, as defined in Fig. 3, between 70 and as high as 90%. In cladding, the geometrical dilution should be as low as possible so as to have the composition of the bead close to the filler material. In conventional welding, gas metal arc welding (GMAW) for example, the geometrical dilution is often close to 50–60% [42]. Although SLM or PBF for that matter can arguably be assimilated to micro-welding, high geometrical dilution is typical due to remelting of underlying layers, leading to epitaxial columnar structures with grains elongated along the direction of the heat flux, that is perpendicular to the melt pools boundary [43]. Since bonding between superalloy substrate and NiCrAlY bond coat is critical in TBC systems, this specificity is most certainly desirable.

The bead or melt pool shape was unclear due to this high amount of dilution and therefore very similar chemical composition and microstructure with the substrate. While for some conditions melt pools clearly exhibited the typical “fish scale” elliptical geometry often observed in SLM as-built materials (for example when $P = 100$ W), for others the melt pool resembled the typical “keyhole” shape characteristic of conventional welding (for example when $P = 250$ W). This keyhole shape is formed by the displacement of the melt induced by evaporation recoil pressure, while surface tension and hydrostatic pressure oppose cavity formation [44]. An advantage of the keyhole shape is to limit the heat affected zone (HAZ) [44,45]. This HAZ, which is generally characterized by locally heat affected grains and precipitates, is a weak part in welded material due to inhomogeneous

microstructure and coarsened precipitates and grains. While subsequent laser melting of adjacent tracks significantly affects microstructure due to overlapping and remelting, limited HAZ is certainly more favorable. In Fig. 3, several melt pools seem to exhibit voids within the melt pool or at interface. These were artifacts from chemical etching, as confirmed by unetched conditions, and therefore not relevant. The bead or melt pool widths, indicated in Fig. 3, were also significantly affected by the processing conditions. A hatch spacing of 120 μm was selected for manufacturing the two-layer plates, and an overlapping between adjacent tracks of about 20–30% is usually desired for SLM [46]. For these reasons, a bead width between 150 and 180 μm was considered appropriate. As a result, with regards to melt pool geometry and width, laser powers of $P = 100$ W and $P = 350$ W incidentally corresponding to the lowest and highest energy density as defined in Fig. 3, respectively, were discarded.

3.2. NiCrAlY bond coat onto IN625 substrate

3.2.1. Morphology and hardness

Two-layer NiCrAlY 8 mm \times 4 mm bond coats were successfully produced by SLM directly onto IN625 substrates using different parameters sets, as shown in Fig. 2(c). Macroscopically, the general aspect of the coatings is appropriate in most cases, except for laser powers of 100 and 350 W which were therefore not selected and will not be shown. This was consistent with the results of single-line scanning discussed in the previous section. Cross-section of the bond coats were evaluated and the corresponding optical micrographs are reported in Fig. 4 for all conditions. The thickness and porosity associated with different processing conditions were measured and reported in Fig. 4. The interface between substrate and bond coat could be comfortably identified thanks to the different building directions for substrate and bond coat. As first consideration, the micrographs in Fig. 4 highlight large voids or cavities at the edge of the coatings. This was caused by the considerable thermal contraction or shrinking during cooling, even causing the coatings to slightly bend upward at higher energy density. This is known as distortion caused by large thermal gradients in the workpiece [47]. Apart from that, bonding seemed excellent in all cases. Another surprising observation was that specimens produced with $P/v = 200/600$ and $P/v = 200/650$, which actually did not correspond to the lowest theoretical energy densities, exhibited the thinnest coatings with a thickness ≤ 75 μm . For the other conditions, all NiCrAlY bond coats appeared appropriate with a thickness between approximately 180 and 350 μm and low residual porosity $\leq 0.5\%$. The actual thickness of the coatings was significantly higher than the 100 μm thickness of the two NiCrAlY powder layers. Consistently with single-line scanning tracks observations in the previous section, this indicates that substantial remelting occurred. In fact, the micrographs in Fig. 4 suggest that rather than being deposited onto the IN625 substrate, the bond coat material is diluted into the superalloy substrate. This is most certainly valuable to ensure excellent bonding between bond coat and substrate.

Fig. 5 shows in more details the interface between bond coat and substrate. As mentioned above, this interface was clear due to the different building directions. The micrographs in Fig. 5 indicate that the bond coat was actually divided into two regions, clearly evidenced as a result of chemical etching. The brighter inner region was a dilution zone resulting from SLM of the first layer accompanied by significant remelting of the underlying IN625 substrate. The resulting material is a highly NiCrAlY/IN625 mixed zone. The darker outer region corresponded to the selective melting of the second NiCrAlY layer. There was as well significant remelting of the underlying layer, as evidenced by the effective thickness significantly larger than 50 μm . The presence of these dilution zones strongly suggests that SLM is highly appropriate. As opposed to conventional bond coat deposition methods such as PS and EB-PVD which typically exhibited a clear interface between bond coat and substrate often requiring a long diffusion heat treatment, the

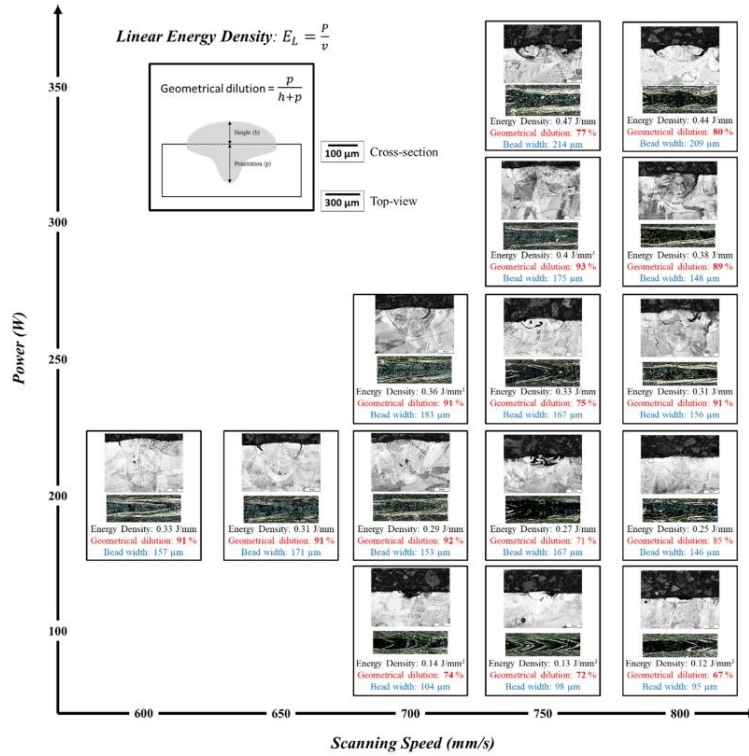


Fig. 3. Etched optical micrographs of the single-line scanning tracks showing the cross-section of the bead or melt pool and below the top view of the welding track for each processing condition. The corresponding values of energy density are reported as well as the measured values of geometrical dilution and bead width.

adhesion as a result of SLM processing appears to be excellent.

This was further evidenced by microhardness measurements from the top surface of the bond coat into the substrate, as reported in Fig. 5 for all conditions. Because of the similar chemical composition between NiCrAlY and IN625, the values of microhardness were similar as can be seen in Fig. 5. It was however found that the hardness was slightly higher in the substrate. This may result from the presence of Nb and Mo

in solid solution in the as-built IN625 substrate. In the NiCrAlY bond coat, a gradual increase of hardness from the surface to the interface is observed, associated with the progressive chemical composition gradient. Hardness was often non-negligibly higher in the vicinity of the interface between substrate and bond coat corresponding to the heat affected zone. The hardness profile of the specimen produced with $P/v = 300/750$, corresponding to the highest energy density of 66.7 J/

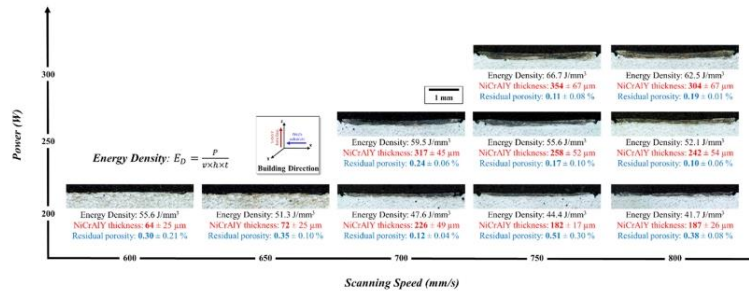


Fig. 4. Etched optical micrographs showing the cross section of the two-layer NiCrAlY coatings deposited onto IN625 substrate for each condition. The corresponding values of energy density are reported as well as the measured coating thickness and residual porosity.

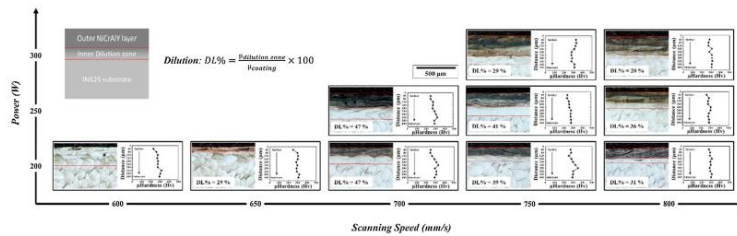


Fig. 5. Etched optical micrographs showing the details of the cross section of the two-layer NiCrAlY coatings deposited onto IN625 substrate for each condition. The dilution zones were highlighted and their values in % were reported. The micro hardness profile was included for each condition.

mm³, indicated that hardness was significantly higher at the surface of the NiCrAlY bond coat. This suggests inhomogeneous phase distribution within the bond coat which may be detrimental to its performance. One of the critical function of MCrAlY bond coats in TBC systems is the accommodation of the significantly different coefficient of thermal expansion shown between the superalloy metallic substrate and insulating ceramic top-coat. To ensure appropriate bonding between substrate and bond coat, similar hardness between the two is preferred, particularly at the interface.

With considerations of thickness, residual porosity, dilution zone and hardness profile, the results exhibited in Figs. 4 and 5 allowed to proceed to a finer selection of the most appropriate processing conditions. Additionally, higher scanning speed is usually preferred in SLM manufacturing to promote faster solidification which prevents pre-judicial segregation. In such light, NiCrAlY coatings produced with $P/v = 200/600$ and $P/v = 200/650$ were considered too thin. These conditions could therefore be eliminated. NiCrAlY coatings produced with $P/v = 200/700$ and $P/v = 250/700$ could also be discarded as there were no evident benefit in using lower scanning speed of 700 mm/s and the dilution zone was large above 45%. We therefore considered the most appropriate SLM processing to be $P/v = 200\text{--}300/750\text{--}800$ and selected these six conditions for further analyses. Under these conditions, NiCrAlY coatings had an appropriate thickness of approximately 180–350 μm including the dilution zone, a low residual porosity of 0.1–0.5% and a dilution of 20–40%.

3.2.2. Element distribution

One apparent advantage of considering SLM for coating NiCrAlY onto an IN625 substrate is the inherent remelting occurring during processing which generated what we called a dilution zone, as indicated and discussed in the previous section, suggesting excellent bonding between bond coat and substrate. Further evidence of this excellent combination was given by EPMA element distribution analyses, in particular the distribution of Al (Fig. 6). As indicated in Table 1, NiCrAlY shows a higher content of Al (9.34 wt.%) than IN625 (0.35 wt.%) to allow the growth of a stable protective Al₂O₃ layer at high temperature. The concentration profile of Al is therefore a key indicator of the interface position and the extent of the dilution zone between the substrate and the bond coat. In Fig. 6, the various regions of the NiCrAlY/IN625 system are clearly highlighted. The outer NiCrAlY was distinctly enriched with Al while the substrate exhibited low Al content. The dilution zones defined above were also clear with apparent mixing between bond coat and substrate. There was a clearly high Al concentration at the top of the NiCrAlY coating in all the cases, approximately 5 μm thick, likely due to the formation of a thin Al₂O₃ oxide layer. The micrographs in Fig. 6 most interestingly highlighted notable differences between processing conditions. With a laser power $P = 200$ W, the concentration of Al was significantly different between the regions showing clearly delimited layers. With a laser power $P = 250$ W, although the concentration profile of Al was certainly uneven, there was a more gradual variation and the interfaces were less pronounced.

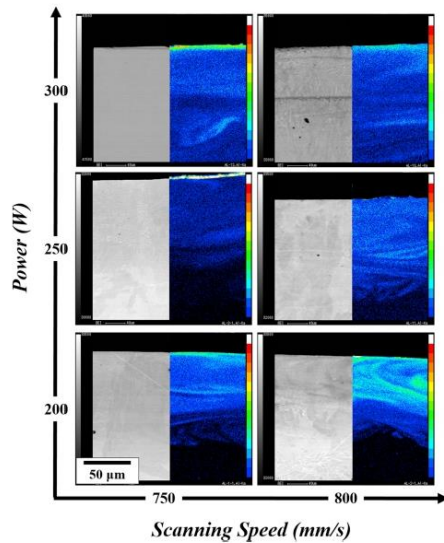


Fig. 6. EPMA results of aluminum content and corresponding backscattered electron imaging (BED) micrographs showing the gradient of Al concentration (all scales are consistent). (For interpretation of the references to colour in this figure legend, the reader is referred to the Web version of this article.)

This was clearer with $P = 300$ W though the actual interface with the substrate was out of range (NiCrAlY thickness approximately ≥ 300 μm in Fig. 4).

EPMA results, although not decidedly conclusive, contribute to the appropriate selection of the optimum processing parameters. Excellent bonding is assumed by SLM due to appropriate mixing between the bond coat and the substrate to avoid clear interface between the two chemically different materials as observed in conventional APS/VPS or EB-PVD depositions. Most defects in these systems are evidenced by significant cracking at the interface during thermal cycles which often cause delamination and failure of the TBC. This is generally avoided to some extent by a long and costly diffusion heat treatment. The standard diffusion treatment for APS bond coat is 6 h at 1080 °C followed by 20 h at 870 °C [48]. Because the NiCrAlY coating processed by SLM advantageously exhibited the so-called dilution zone, such a diffusion treatment becomes unnecessary, at least for the purpose of inter-diffusion and adhesion. In such conditions, it appears that the NiCrAlY coating produced with $P/v = 250/800$ exhibiting a thickness of

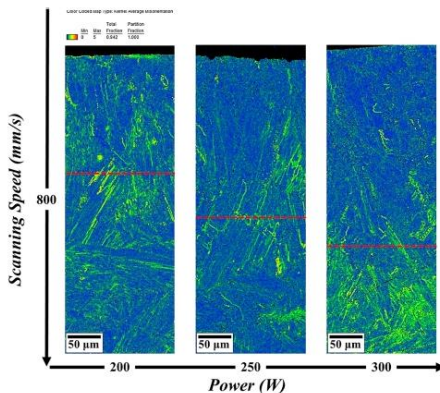


Fig. 7. Kernel Average Misorientation (KAM) maps highlighting residual stress levels. The interface between substrate and dilution zone was indicated by all dashed lines. (For interpretation of the references to colour in this figure legend, the reader is referred to the Web version of this article.)

approximately 250 μm including a roughly 35% dilution zone and low residual porosity about 0.1% seems most appropriate.

3.2.3. Residual stress

Kernel average misorientation (KAM) maps were generated from EBSD analyses. KAM is generally used for characterizing local misorientation. It calculates the average misorientation of a given point with all of its neighbors. This is a good qualitative indicator of deformed grain or strain induced grain, and therefore stress in crystalline materials at the microscale level. There are several reported methods for quantifying residual stresses in materials, which is particularly critical for SLM, such as the destructive hole-drilling method and the X-ray diffraction method [49]. Due to very fast solidification and cooling rates as well as multiple thermal cycles experienced during SLM processing, residual stress is often very high in the as-built materials as evidenced in particular by a high density of dislocations [11,50]. It is reasonable to assume that strain as measured by KAM maps in EBSD is due to residual stress built up during SLM processing, and therefore allows to qualitatively assess residual stress levels visually on a microscale at the expense of appropriately quantified values. Fig. 7 shows KAM maps for NiCrAlY coating produced with $P/v = 200/800$, $P/v = 250/800$ and $P/v = 300/800$. The evaluated interface corresponding to the interface between IN625 substrate and dilution zone as measured in Fig. 4 were included as dashed red lines in Fig. 7. Although the residual stress, amount of average misorientation, were qualitatively similar, as expected due to the very high solidification rate estimated around $10^5 \sim 10^6$ °C/s regardless of slightly different processing conditions [11], there were noticeable differences highlighted in Fig. 7.

For the NiCrAlY coating produced with $P/v = 300/800$, higher levels of misorientation were concentrated in the substrate in the vicinity of the interface with the bond coat. Further analyses need to be carried out to explain this behavior. However, it is reasonable to assume that higher energy density due to higher laser power generates more heat and therefore a larger heat affected zone within the unmelted substrate. Coatings produced with $P/v = 200/800$ and $P/v = 250/800$ exhibited relatively low levels of misorientation. Although more analysis is needed to assure the consistency of residual stress profile, the $P/v = 250/800$ condition showed the lowest stress levels and therefore the lowest risks of failure. For this reason, it was considered the most appropriate SLM condition for the production of NiCrAlY coating onto the IN625 substrate itself produced by SLM.

4. Conclusions

The present study investigated for the first time the feasibility of producing by SLM a NiCrAlY bond coat material onto an IN625 superalloy substrate, itself produced by SLM. Key contents are summarized as follows:

- 15 processing conditions were tested by varying the laser power between 100 and 350 W and the scanning speed between 600 and 800 mm/s. The results showed that in all cases, substantial dilution of the NiCrAlY layer into the IN625 substrate occurred due to the typical remelting characteristic of SLM manufacturing.
- Several criteria were defined to determine the most appropriate processing conditions. An approximately 250 μm thick NiCrAlY coating is obtained with a very low residual porosity $\leq 0.1\%$ including a ~35% dilution zone, smooth hardness profile between 275 and 305 Hv, low residual stress levels and progressive Al concentration distribution for the following SLM processing conditions: layer thickness $t = 50$ μm, hatch spacing $h = 120$ μm, laser power $P = 250$ W and laser scanning speed $v = 800$ mm/s.
- Future work will focus on a thorough characterization of this < NiCrAlY-IN625 > system produced by SLM in terms of composition, phase formation, mechanical properties and durability which will be appropriately compared to conventional systems produced by APS/VPs.

CRedit authorship contribution statement

Jiwon Lee: Conceptualization, Methodology, Validation, Formal analysis, Investigation, Writing - original draft. **Mathieu Terner:** Investigation, Writing - review & editing. **Etienne Copin:** Methodology, Writing - review & editing. **Philippe Lours:** Writing - review & editing, Supervision. **Hyun-Uk Hong:** Writing - review & editing, Supervision.

Declaration of Competing Interest

None.

Acknowledgment

The authors acknowledge the financial support of the Global Expert Technology Development Program grant funded by the Korean government (MOTIE, 10076876) and the National Research Foundation of Korea (NRF) grant funded by the Korean government (MSIP, NRF-2017R1A1A1A05000754 and NRF-2018R1A5A6075959).

References

- [1] W.E. Frazier, Metal additive manufacturing: a review, *J. Mater. Eng. Perform.* 23 (2014) 1917–1928, <https://doi.org/10.1007/s11665-014-0958-z>.
- [2] K.V. Wong, A. Hernandez, A review of additive manufacturing, *ISRN Mechanical Engineering A 1* (2012), <https://doi.org/10.5402/2012/208760>.
- [3] B. Baufeld, O.V. Biest, R. Gault, Additive manufacturing of Ti-6Al-4V components by shaped metal deposition: microstructure and mechanical properties, *Mater. Des.* 31 (2010) S106–S111, <https://doi.org/10.1016/j.matdes.2009.11.032>.
- [4] ISO/ASTM 52900, ASTM International, The Global Leader in Additive Manufacturing Standards-The Committee on Additive Manufacturing Technologies (F42).
- [5] ASTM International Committee F42 on Additive Manufacturing Technologies; Roland Berger.
- [6] A. Lundbäck, L.-E. Lindgren, Finite element simulation to support sustainable production by additive manufacturing, *Procedia Manuf.* 7 (2017) 127–130, <https://doi.org/10.1016/j.promfg.2016.12.033>.
- [7] L.M. Suave, J. Cormier, P. Villechaise, A. Soula, Z. Hervier, D. Bertheau, J. Laigo, Microstructural Evolutions During Thermal Aging of Alloy 625: Impact of Temperature and Forming Process, *Metall. Mater. Trans. A* (45A) (2014) 2963–2982, <https://doi.org/10.1007/s11661-014-2256-7>.
- [8] S.J. Patel, G.D. Smith, The role of niobium in wrought superalloys, *International Symposium Niobium 2001, Orlando, Florida, USA, TMS, 2001*, pp. 1081–1102.
- [9] D. Liu, X. Zhang, X. Qin, Y. Ding, High-temperature mechanical properties of Inconel-625: role of carbides and delta phase, *Mater. Sci. Tech.* 33 (2017)

- 1610-1617, <https://doi.org/10.1080/02670836.2017.1300365>.
- [10] M.D. Mathew, P. Parameswaran, K. Bhanu Sankara Rao, Microstructural changes in alloy 625 during high temperature creep, *Mater. Charact.* 59 (2008) 508-513, <https://doi.org/10.1016/j.matchar.2007.03.007>.
 - [11] G. Marchese, M. Lorusso, S. Parizia, E. Bassini, J.W. Lee, F. Calignano, D. Manfredi, M. Temer, H.U. Hong, D. Ugues, M. Lombardi, S. Biamino, Influence of heat treatments on microstructure evolution and mechanical properties of Inconel 625 processed by laser powder bed fusion, *Mater. Sci. Eng. A* 729 (2018) 64-75, <https://doi.org/10.1016/j.msea.2018.05.044>.
 - [12] G. Marchese, X.G. Coera, F. Calignano, M. Lorusso, S. Biamino, P. Minetola, D. Manfredi, Characterization and comparison of Inconel 625 processed by selective laser melting and laser metal deposition, *Adv. Eng. Mater.* 19 (2016) 1-9, <https://doi.org/10.1002/adem.201600635>.
 - [13] S. Li, Q. Wei, Y. Shi, Y. Shi, Z. Zhu, D. Zhang, Microster-by-layer printing of laminated graphene-based interdigitatedure by Selective Laser Melting, *J. Mater. Sci. Technol.* 31 (2015) 946-952, <https://doi.org/10.1016/j.jmst.2014.09.020>.
 - [14] I. Koutiri, E. Pessard, P. Peyre, O. Amlou, T.D. Terris, Influence of SLM process parameters on the surface finish, porosity rate, and fatigue behavior of as-built Inconel 625 parts, *J. Mater. Process. Technol.* 255 (2018) 536-546, <https://doi.org/10.1016/j.jmatprotec.2017.12.043>.
 - [15] M. Daroonparvar, M.S. Hussain, M.A.M. Yajid, The role of formation of continuous thermally grown oxide layer on the nanostructured NiCrAlY bond coat during thermal exposure in air, *Appl. Surf. Sci.* 261 (2012) 287-297, <https://doi.org/10.1016/j.apsusc.2012.08.002>.
 - [16] W. Leng, R. Pillai, P. Huczakowski, D. Naumenko, W.J. Quadackers, Microstructural evolution of an aluminate coating on alloy 625 during wet air exposure at 900 °C and 1000 °C, *Surf. Coat. Tech.* 354 (2018) 268-280, <https://doi.org/10.1016/j.surfcoat.2018.09.043>.
 - [17] F.A. Khalid, N. Hussain, A.H. Qureshi, Microstructural study on oxidation of alumitized coating on Inconel 625, *J. Mater. Eng. Perform.* 11 (2002) 211-214, <https://doi.org/10.1361/105994902770344286>.
 - [18] P.W. Schike, Advanced gas turbine materials and coatings, GE Energy, (2004).
 - [19] D.R. Clarke, M. Oechsner, N.P. Padture, Thermal-barrier coatings for more efficient gas-turbine engines, *MRS Bull.* 37 (2012) 891-898, <https://doi.org/10.1557/mrs.2012.232>.
 - [20] M. J. Donachie, S. J. Donachie, *Superalloys: A Technical Guide 2nd ed.* ASTM International, the Materials Information Society, ISBN: 0-87170-749-7.
 - [21] R. C. Reed, *The Superalloys: Fundamentals and Applications*, Cambridge University Press, ISBN: 978-0-511-24546-6.
 - [22] N.P. Padture, M. Gell, E.H. Jordan, Thermal barrier coatings for gas-turbine engine applications, *Science's compass* 296 (2002) 280-284, <https://doi.org/10.1126/science.1068609>.
 - [23] J.D. Osoorio, A. Toro, J.P. Hernandez-Ortiz, Thermal barrier coatings for gas turbine applications: failure mechanisms and key microstructural features, *DYNA* 79 (2012) 149-158 http://www.sciebo.org.co/scielo.php?script=sci_arttext&pid=S0012-73532012000600018&lng=en&nm=iso.
 - [24] N. Zotov, M. Bartsch, L. Chernova, D.A. Schmidt, M. Havenith, G. Eggeler, Effects of annealing on the microstructure and the mechanical properties of EB-PVD thermal barrier coatings, *Surf. Coat. Tech.* 205 (2010) 452-464, <https://doi.org/10.1016/j.surfcoat.2010.07.008>.
 - [25] C.S. Richard, G. Beranger, J. Lu, J.F. Flavenot, The influences of heat treatments and interdiffusion on the adhesion of plasma-sprayed NiCrAlY coatings, *Surf. Coat. Tech.* 82 (1996) 99-109, [https://doi.org/10.1016/0257-8972\(95\)02640-1](https://doi.org/10.1016/0257-8972(95)02640-1).
 - [26] P.R. Chalker, S.J. Bull, D.S. Rickerby, A review of the methods for the evaluation of coating-substrate adhesion, *Mat. Sci. Eng. A* 140 (1991) 583-592, [https://doi.org/10.1016/0921-5093\(91\)90482-3](https://doi.org/10.1016/0921-5093(91)90482-3).
 - [27] Z.H. Liu, D.Q. Zhang, S.L. Sing, C.K. Chua, L.E. Loh, Interfacial characterization of SLM parts in multi-material processing: metallurgical diffusion between 316L stainless steel and C18400 copper alloy, *Mater. Charact.* 94 (2014) 116-125, <https://doi.org/10.1016/j.matchar.2014.05.001>.
 - [28] J. Chen, Y. Yang, C. Song, M. Zhang, S. Wu, D. Wang, Interfacial microstructure and mechanical properties of 316L/CuSn10 multi-material bimetallic structure fabricated by selective laser melting, *Mat. Sci. Eng. A* 752 (2019) 75-85, <https://doi.org/10.1016/j.msea.2019.02.097>.
 - [29] S.L. Sing, L.P. Lam, D.Q. Zhang, Z.H. Liu, C.K. Chua, Interfacial characterization of SLM parts in multi-material processing: intermetallic phase formation between AlSi10Mg and C18400 copper alloy, *Mater. Charact.* 107 (2015) 220-227, <https://doi.org/10.1016/j.matchar.2015.07.007>.
 - [30] A.G. Demir, B. Previtali, Multi-material selective laser melting of Fe/Al-12Si components, *Manuf. Lett.* 11 (2017) 8-11, <https://doi.org/10.1016/j.mfglet.2017.01.002>.
 - [31] C. Wei, L. Li, X. Zhang, Y.-H. Chueh, 3D printing of multiple metallic materials via modified selective laser melting, *CIRP Ann. Manuf. Technol.* 67 (2018) 245-248, <https://doi.org/10.1016/j.cirp.2018.04.096>.
 - [32] K. Partes, C. Giolli, F. Borgioli, U. Bardi, T. Seebeck, F. Vollertsen, High temperature behavior of NiCrAlY coatings made by laser cladding, *Surf. Coat. Tech.* 202 (2008) 2208-2213, <https://doi.org/10.1016/j.surfcoat.2007.09.010>.
 - [33] M.J. Tobar, J.M. Amado, A. Yanez, J.C. Pereira, C. Amigo, Laser cladding of MCrAlY coatings on stainless steel, *Phys. Procedia* 56 (2014) 276-283, <https://doi.org/10.1016/j.phpro.2014.08.172>.
 - [34] R. Vilar, E.C. Santos, P.N. Ferreira, N. Franco, R.C. da Silva, Structure of NiCrAlY coatings deposited on single-crystal alloy turbine blade material by laser cladding, *Acta Mater.* 57 (2009) 5292-5302, <https://doi.org/10.1016/j.actamat.2009.06.049>.
 - [35] Y. Chivél, New approach to multi-material processing in selective laser melting, *Phys. Procedia* 83 (2016) 891-898, <https://doi.org/10.1016/j.phpro.2016.08.093>.
 - [36] J. Koopmann, J. Voigt, T. Niendorf, Additive manufacturing of a steel-ceramic multi-material by selective laser melting, *Metall. Mater. Trans. B* 50 (2019) 1042-1051, <https://doi.org/10.1007/s11663-019-01523-1>.
 - [37] Y. Sakakibara, K. Kubushiro, Stress evaluation at the maximum strained state by EBSD and several residual stress measurements for plastic deformed austenitic stainless steel, *World J. Mech.* 7 (2017) 195-210, <https://doi.org/10.4236/wjcm.2017.78018>.
 - [38] L. Saraf, Kernel average misorientation confidence index correlation from FIB sliced Ni-Fe-Cr alloy surface, *Microsc. Microanal.* 17 (2011) 424-425, <https://doi.org/10.1017/S1431927611002996>.
 - [39] M. Calagnotto, D. Ponge, E. Demir, D. Raabe, Orientation gradients and geometrically necessary dislocations in ultrfine grained dual-phase steels studied by 2D and 3D EBSD, *Mat. Sci. Eng. A* 527 (2010) 2738-2746, <https://doi.org/10.1016/j.msea.2010.01.004>.
 - [40] J. Hou, Q. J. Peng, Z.P. Lu, T. Shoji, J.Q. Wang, E.-H. Han, W. KE, Effects of cold working degrees on grain boundary characters and strain concentration at grain boundaries in Alloy 600, *Corros. Sci.* 53 (2011) 1137-1142, <https://doi.org/10.1016/j.corsci.2010.11.022>.
 - [41] D.J.-Badiola, A.I.-Mendia, I. Gutierrez, Study by EBSD of the development of the substructure in a hot deformed 304 stainless steel, *Mat. Sci. Eng. A* 394 (2005) 445-454, <https://doi.org/10.1016/j.msea.2004.11.049>.
 - [42] M. Turner, T.-A. Bayarsalkhan, H.-U. Hong, J.-H. Lee, Influence of gas metal arc welding parameters on the bead properties in automatic cladding, *J. Korean Weld. Join. Soc.* 35 (2017) 16-25, <https://doi.org/10.5781/JWJ.2017.35.1.16>.
 - [43] T. Dehroy, H.L. Wei, J.S. Zubaack, T. Mukherjee, J.W. Elmer, J.O. Milewski, A.M. Beese, A. Wilson-Heid, A. De, W. Zhang, Additive manufacturing of metallic components-Process, structure and properties, *Prog. Mater. Sci.* 92 (2018) 112-224, <https://doi.org/10.1016/j.pmatsci.2017.10.001>.
 - [44] J.Y. Lee, S.H. Ko, D.F. Farson, C.D. Yoo, Mechanism of keyhole formation and stability in stationary laser welding, *J. Phys. D Appl. Phys.* 35 (2002) 1570-1576, <https://doi.org/10.1088/0022-3727/35/13/320>.
 - [45] E. Akman, A. Demir, T. Canel, T. Simnazerlik, Laser welding of Ti6Al4V titanium alloys, *J. Mater. Process. Technol.* 209 (2009) 3705-3713, <https://doi.org/10.1016/j.jmatprotec.2008.08.026>.
 - [46] X. Su, Y. Yang, J. Liu, Theoretical study on overlapping mechanism in SLM based on interlayer-staggered scan strategy, *Appl. Mech. Mater.* 44 (2010) 1482-1486, <https://doi.org/10.4028/www.scientific.net/AMM.44-47.1482>.
 - [47] E.R. Denlinger, P. Michaleris, Effect of stress relaxation on distortion in additive manufacturing process modeling, *Addit. Manuf.* 12 (2016) 51-59, <https://doi.org/10.1016/j.addma.2016.06.011>.
 - [48] D. Texier, D. Monceau, Z. Hervier, E. Andrieu, Effect of interdiffusion on mechanical and thermal expansion properties at high temperature of a MCrAlY coated Ni-based superalloy, *Surf. Coat. Tech.* 307 (2016) 81-90, <https://doi.org/10.1016/j.surfcoat.2016.08.059>.
 - [49] J.S. Bartlett, X. Li, An overview of residual stresses in metal powder bed fusion, *Addit. Manuf.* 27 (2019) 131-149, <https://doi.org/10.1016/j.addma.2019.02.020>.
 - [50] L.E. Murr, S.M. Gaytan, D.A. Ramirez, E. Martinez, J. Hernandez, K.N. Amato, P.W. Shindo, F.R. Medina, R.B. Wicker, Metal fabrication by additive manufacturing using laser and electron beam melting technologies, *J. Mater. Sci. Technol.* 28 (2012) 1-14, [https://doi.org/10.1016/S1005-0302\(12\)60016-4](https://doi.org/10.1016/S1005-0302(12)60016-4).

Influence of heat treatments on microstructure evolution and mechanical properties of Inconel 625 processed by laser powder bed fusion

Giulio Marchese^{a,*}, Massimo Lorusso^b, Simone Parizia^{a,b}, Emilio Bassini^a, Ji-Won Lee^c,

Flaviana Calignano^d, Diego Manfredi^b, Mathieu Ternier^c, Hyun-Uk Hong^c, Daniele Ugues^a,
Mariangela Lombardi^{a,b}, Sara Biamino^{a,b}

^a Department of Applied Science and Technology, Politecnico di Torino, Corso Duca degli Abruzzi 24, 10129 Torino, Italy

^b Center for Sustainable Future Technologies - CSFT@PolITo, Istituto Italiano di Tecnologia, Corso Trento 21, 10129 Torino, Italy

^c Department of Materials Science and Engineering, Changwon National University, 20 Changwondaehak-ro, 51140 Changwon, Republic of Korea

^d Department of Management and Production Engineering, Politecnico di Torino, Corso Duca degli Abruzzi 24, 10129 Torino, Italy

Keywords:

Laser powder bed fusion
Nickel superalloys
Tensile behaviour
Microstructure
Hardness

This study investigated the mechanical behaviour and microstructure of as-built and heat-treated Inconel 625 (IN625) samples processed by laser powder bed fusion (LPBF). This process offers freedom in design to build complex IN625 components in order to overcome extensive machining. However, post heat treatments must be performed to obtain specific mechanical properties to match industrial requirements. For this purpose, different heat treatments were performed on IN625 samples, and through hardness measurements, three different heat treatments were selected, as optimised conditions. A direct ageing, a solutioning and a solutioning followed by ageing treatments were chosen to study the effects of these specific heat treatments on the microstructure and tensile properties, comparing them to those of as-built condition. The tensile properties of as-built and selected heat-treated IN625 samples showed superior values to minimum requirements for wrought IN625 alloys, whereas the investigation on the microstructures and fracture surfaces of as-built and heat-treated IN625 contributed to an understanding of the tensile properties evolution. The high tensile strength of as-built samples essentially derived from very fine dendritic structures mainly below 1 μm with high dislocation density and nanometric MC carbides. The high tensile properties of ageing treatments performed at 700 °C for 24 h, whether directly aged or post-solutioning, were found to be primarily dependent on γ' phases (10–30 nm) and M_{23}C_6 carbides formation. By contrast, the tensile properties of solution-treated IN625 samples at 1150 °C for 2 h showed higher ductility coupled to lower strength than other conditions, due to the grain growth.

1. Introduction

Inconel 625 (IN625) is a solid-solution strengthened nickel-based superalloy derived from refractory elements including niobium and molybdenum, in a nickel-chromium matrix. The high temperature strength, corrosion resistance as well as an excellent weldability offered by IN625 has led to its application in different areas such as aeronautics, aerospace, marine, nuclear, chemical and petrochemical industries [1–3]. However, machining IN625 components into elaborate shapes is remarkably difficult and expensive by subtractive manufacturing, due to the material is characterised by high hardness and high-temperature strength as well as low thermal diffusivity [4–6].

Nowadays, it is possible to overcome the obstacles and problems

related to traditional subtractive manufacturing by means of additive manufacturing (AM) technologies [7]. AM in fact has attracted massive interest due to the possibility to use a layer by layer process to build near-net shape components with very complex geometries combined to a high efficiency of material usage [8]. One of the main AM technologies used to build nickel-based superalloy components is laser powder bed fusion (LPBF) process, also known as selective laser melting (SLM). In this process, consecutive layers of loose powders are melted by a focused laser beam in specific areas according to the computer-aided design (CAD) data [8–10]. In literature, several works are concentrated on understanding the phenomenology of the process as well as the influence of process parameters to generate dense components [10–14]. In particular, for IN625 alloy produced by LPBF, Sateesh et al. [15]

* Corresponding author.

E-mail addresses: giulio.marchese@polito.it (G. Marchese), massimo.lorusso@iit.it (M. Lorusso), simone.parizia@polito.it (S. Parizia), emilio.bassini@polito.it (E. Bassini), jwlee10@changwon.ac.kr (J.-W. Lee), flaviana.calignano@polito.it (F. Calignano), diego.manfredi@iit.it (D. Manfredi), mathieu@changwon.ac.kr (M. Ternier), huhong@changwon.ac.kr (H.-U. Hong), daniele.ugues@polito.it (D. Ugues), mariangela.lombardi@polito.it (M. Lombardi), sara.biamino@polito.it (S. Biamino).

studied the interaction of different parameters on dimensional accuracy, micro hardness and densification levels. Carter et al. [12] focused their attention on the energy density necessary to obtain IN625 components with a relative density close to 100%, whereas Wang et al. [16] fabricated IN625 samples with a relative density of 99.95%. A previous work presented by Marchese et al. [17] investigated the effect of a combination of various parameters on densification level and Brinell hardness, which led to a relative density as high as 99.96% and IN625 microstructures with very fine dendrite structures. Yadroitsev et al. [18] mainly evaluated the impact of different hatching distance values and scanning strategies, reaching a residual porosity lower than 1%. Moreover, they assessed that as-built IN625 samples had higher tensile strength and lower ductility compared to wrought IN625 alloy.

The high tensile properties of LPBF superalloys can be attributed to the extremely fast solidification rates (10^5 – 10^6 °C/s) involved in the LPBF, generating a fine dendritic architectures and the suppression of macro segregation or formation of large Laves phases or carbides that can be detrimental to the mechanical properties [19–21]. On the other hand, these microstructural features as well as the high thermal residual stresses induced by the process are not desired for high temperature applications [19,21,22]. It is therefore necessary to perform post-processing heat treatments [10,21–24]. In fact, heat treatment is a key factor to reduce residual stresses, to eliminate the segregation of elements, to promote grain growth and phase precipitation, thus obtaining specific microstructure and mechanical properties suitable for different conditions. For instance, Li et al. [22] studied the microstructure, texture, grain morphology and hardness of as-built and heat-treated IN625 for short heat treatments. Brown et al. [25] investigated the tensile properties of stress relieved IN625 specimens built by different LPBF machines, showing that the tensile properties can change based on the basis of the different building strategies of the used machines, because of different thermal flows. Witkin et al. [26] studied the tensile and fatigue properties of as-built and hot isostatically pressed (HIPed) IN625 LPBF specimens compared with standard wrought IN625. They showed that HIPed IN625 samples have lower strength and higher ductility than as-built ones and that their fatigue behaviour can be clearly improved by machining or shot peening of the surface. Kreitzberg et al. [27] studied the microstructure of the as-built, three heat-treated and HIPed IN625 samples, mainly showing the grain size and morphology evolution correlated to the tensile properties. In a successive work Kreitzberg et al. [28] chiefly focused on the microstructure of heat-treated LPBF IN625 samples and their impact on the elevated temperature tensile properties.

However, so far very little attention has been paid to the microstructural evolution of LPBF as-built IN625 parts under different heat treatments, investigating the microstructure development coupled with the influence on hardness and tensile properties. In fact, a similar investigation is crucial to better understanding whether the very particular microstructures of LPBF parts require different heat treatments with respect to the traditional IN625 alloys. Therefore, in the present study, the mechanical behaviour at room temperature of as-built and heat-treated IN625 samples were correlated to their microstructural features and tensile fracture surfaces. The tensile properties of these IN625 samples were compared to those of wrought IN625 alloys in order to show the effect of selected heat treatments on rapidly solidified IN625 derived from LPBF process.

2. Materials and methods

2.1. IN625 specimens built by LPBF

In this study, gas atomised IN625 powder by EOS GmbH (Germany) company was employed. The powder chemical composition declared by the supplier is reported in Table 1, and it is in accordance with UNS N06625.

The powder consisted of fairly spherical particles with some

satellites and clusters as shown in Fig. 1a. The particle size distribution had a d_{10} of 16 μm and d_{90} of 48 μm and the powder presented a good flowability, as reported in a previous study [17]. Test samples were built using an EOSINT M270 Dual Mode machine, which is equipped with a 200 W Yb fiber laser with a spot diameter of 100 μm . The process was carried out in a protective argon atmosphere and the building platform was held at 80 °C. The optimised operative parameters were: laser power of 195 W, scan speed of 1200 mm/s, hatching distance of 0.09 mm and layer thickness of 0.02 mm. The EOS scanning strategy using stripes of 5 mm and an overlapping of 0.12 mm with the laser scanning direction rotated of 67° between subsequent layers was employed [17]. IN625 cubic ($15 \times 15 \times 15 \text{ mm}^3$) and cylindrical (length of 110 mm and diameter of 15 mm) samples were fabricated. The applied parameters enabled the production of cubic and cylindrical specimens with a residual porosity less than 0.1%. The cubic samples were used to study the microstructure of as-built and heat-treated IN625 and also to determine Brinell hardness. The cylindrical samples, on the other hand, were machined to obtain tensile specimens, with a gauge length of 40 mm, a diameter of 8 mm a length of reduced section of 51 mm as well as radius of fillets of 8 mm, consistent with ASTM E8/EBM-09. It should be noticed that the cylindrical samples were built parallel to the building platform (xy plane), as illustrated in Fig. 1b.

2.2. Heat treatment conditions

The as-built IN625 samples were subjected to various heat treatments: direct ageing, solution treatments as well as solution followed by ageing treatments for different temperatures and times, as schematised in Fig. 2. The direct ageing and ageing treatments were carried out at 600, 700, 800 and 900 °C for different times up to 24 h, whereas the solutioning were carried out at 1000 °C and 1150 °C up to 2 h.

It should be noticed that all these heat treatments were performed using a muffle furnace with a ± 5 °C precision, equipped with a K-type thermocouple located close to the samples. Furthermore, all the heat-treated IN625 samples were water quenched (WQ) in order to avoid any microstructure evolution during cooling, as recommended in the literature for large sections [29].

2.3. Microstructure and mechanical characterisation

The as-built and three chosen heat-treated LPBF-IN625 samples were cut along the z plane (parallel to the building direction), subsequently ground and polished down to 1 μm using SiC abrasive papers and diamond suspensions, and then etched using Kalling's No.2 etchant (5 g CuCl_2 in 100 ml HCl and 100 ml $\text{CH}_3\text{CH}_2\text{OH}$) or mixed acids (15 ml HCl, 10 ml CH_3COOH and 10 ml HNO_3). Afterwards, the microstructures were investigated by means of optical microscope (OM - Leica DMI 5000 M), by Field Emission Scanning Electron Microscope (FESEM - Zeiss SupraTM40), and by Field Emission Transmission Electron Microscope (FETEM - JEOL JEM-2100F operating at 200 kV) equipped with Energy Dispersive X-ray Spectroscopy (EDS) detector. The fracture surface of tensile samples were observed by Scanning Electron Microscope (SEM - Leo 1450VP).

A Brinell hardness test was applied to provide a good understanding of the relative level of strength of the IN625 alloy underwent different heat treatments. The Brinell hardness tests were carried out on all the samples polished up to 4000 fine grit SiC paper along the z plane, by means of an EMCO TEST M4U test machine with a load of 62.5 kg_f for 15 s (HBW2.5/62.5), in accordance with the ASTM E10–14 standard. The hardness values were assessed using three samples, five indentations on each sample.

Tensile specimens were tested by a Zwick-Roell BT1 - FR100 testing machine at room temperature using a strain rate of 8.10^{-3} s^{-1} following the ASTM E8/EBM-09 standard. The tensile tests were performed at least on three specimens for each condition.

Engineering strain and stress obtained by tensile test at a fixed strain

Table 1
Chemical composition in weight percentage of IN625 powder.

Ni	Cr	Mo	Fe	Nb	Co	Si	Ti	Al	C
≥ 58.0	20-23	8-10	≤ 5	3.15-4.15	≤ 1.0	≤ 0.5	≤ 0.4	≤ 0.4	≤ 0.1

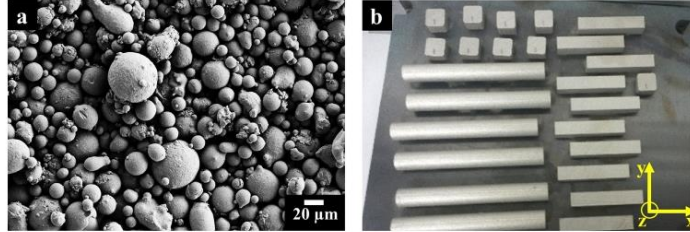


Fig. 1. a) LPBF IN625 powder; b) LPBF-built IN625 specimens on the building platform.

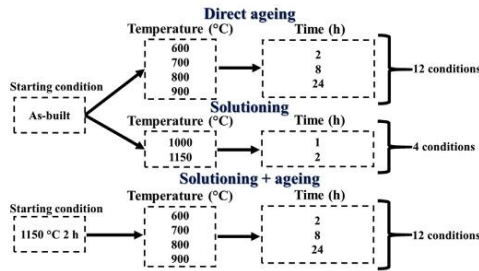


Fig. 2. Schematic representation of heat treatments performed on as-built IN625 processed by LPBF (all the heat-treated IN625 were water quenched).

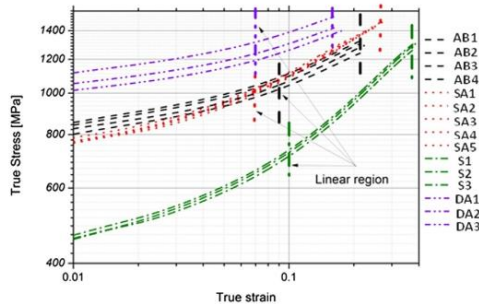


Fig. 3. Log-Log plot of true stress and true strain data recorded for the different metallurgical states investigated on IN625: as built (AB); solutioned (S); solutioned and aged (SA); direct aged (DA). Progressive numbers refer to the sample indexing.

rate were converted to true strain and true stress. In order to evaluate the strain hardening behaviour only the part of the stress-strain curve where uniform plastic deformation occurs was considered, i.e. the portion of the curve between the yield and the maximum strength. True strain and true stress data within this range were thus plotted in a double logarithmic diagram (Fig. 3) [30]. All curves in Fig. 3 present a first stage with a marked non-linear increase followed by a linear stage,

which ends with the maximum strength as recorded in tensile tests (i.e. the last point before the onset of geometrical instability). According to the heat treatment history of the different samples, the onset of the linear stage can be identified at different levels of true strains, as highlighted in figure.

In order to avoid errors caused by eventual nonhomogeneous deformations occurring within the strain gauge range only data lying within the linear portion of the curves were used to derive the fitting parameters. Two different flow stress models, the Hollomon (Eq. (1a)) and the Voce models (Eq. (1b)), were applied to the true stress-strain data set of the different samples [30]:

$$\Delta\sigma = \sigma - \sigma_Y = K \cdot \epsilon^n \quad (1a)$$

$$\Delta\sigma = \sigma - \sigma_Y = A \cdot [1 - e^{(-B \cdot \epsilon^C)}] \quad (1b)$$

In Eq. (1a) K and n are classical strain hardening fitting parameters, which do not have a particular relation with any specific microstructural parameters. These parameters can be derived by a linear regression on a logarithmic treatment. According to literature [31,32] the fitting parameters in Eq. (1b) can be expressed as $A = q/k_2$, $B = Mk_2$ and $C = p$. In such definitions M is the Taylor's factor ($M = 3$), q is a parameter inversely proportional to the dislocation free path (λ), k_2 is the recovery rate and the exponent p is a material constant. Parameters q , k_2 and p were derived by non-linear regression using the Levenberg-Marquardt least square method.

To assess the quality of both fitting models the Average Absolute Relative Error (AARE) and the maximum relative error (MRXE) were computed further to the coefficient of determination, COD (R^2). Between the two models, the Voce model always resulted in providing a better fitting of the as-built and heat-treated IN625 state and consequently only the derived parameters of such model will be used. Moreover, these parameters are more interesting since the fitting parameters of the Voce model, in particular, q has a direct relation to some microstructural features, such as grain size, second phase particles size as well as their volume fraction [31]. The true strain and true stress data within this range were plotted in a double logarithmic diagram as reported in literature [30].

3. Results and discussion

3.1. Brinell hardness determination

Fig. 4 shows the Brinell hardness values of as-built and direct aged samples, as well as the OM and FESEM micrographs of the different direct aged samples for 24 h. All the direct ageing treatments tend to

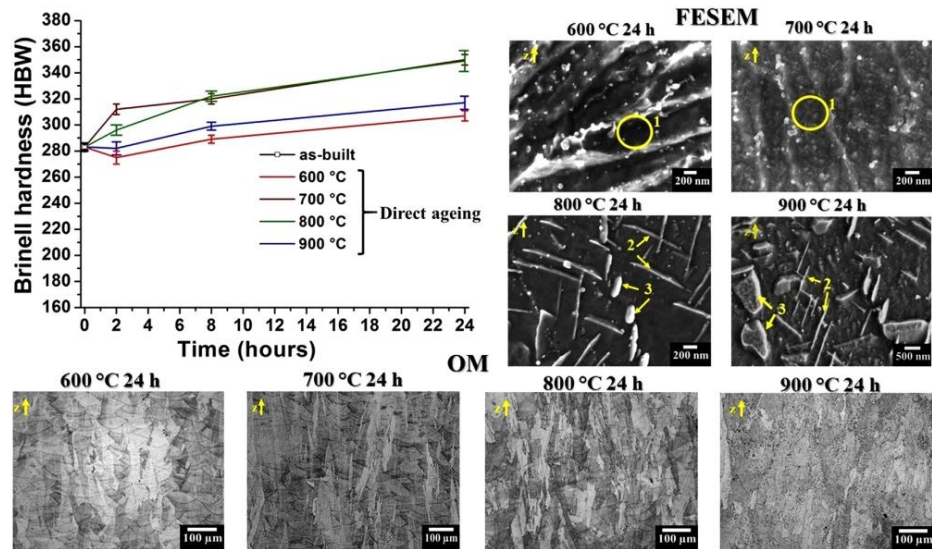


Fig. 4. Brinell hardness of as-built and after direct ageing carried out from 600 to 900 °C up to 24 h together with OM and FESEM images of heat-treated samples for 24 h along the building direction (z -axis), where number 1 indicated γ' phases and number 2 and 3 pointed out δ and Laves phases, respectively.

increase the hardness, reaching maximum values for thermal exposures at 700 °C and 800 °C for 24 h. The various direct ageing from 600 °C to 900 °C did not remarkable modify the columnar grains as visible in the OM images, as well as the melt pool contours remained visible up to thermal exposures at 700 °C for 24 h. The hardness improvement can be correlated with the type and size of the formed precipitates under the different thermal exposures. At higher magnification view by FESEM analysis, the direct aged samples at 600 °C and 700 °C revealed the precipitation of nanometric phases which can be attributed to γ' phases indicated by number 1 in FESEM images, showing a higher concentration for the samples heat treated at 700 °C, thus explaining the drastic hardness improvement. Differently, both thermal exposures at 800 °C and 900 °C promoted δ and Laves phases formation pointed out by arrows 2 and 3, respectively. The direct aged samples at 800 °C exhibited smaller precipitates than direct aged ones at 900 °C leading to a greater hardness improvement. From hardness measurements coupled with microstructural observations, it was chosen to further investigate the direct aged samples at 700 °C for 24 h characterised by the highest hardness, among these heat treatment conditions, derived from the precipitation of γ' phases without exhibiting detrimental phases such as δ and Laves phases. The determined phases of the heat-treated IN625 samples are in agreement with the time-temperature-transformation (T-T) diagram of Inconel 625 alloy [3,33].

The hardness and microstructure evolution of the different solutioned samples up to 2 h are reported in Fig. 5. The thermal exposures tend to reduce the hardness essentially due to the recrystallisation generating equiaxed grains as displayed in OM micrographs. FESEM images close to the grain boundaries exhibited the presence of inter/intragranular sub-micrometric carbides. From the investigation, it was chosen to further characterised the samples solutioned at 1150 °C for 2 h, which is the recommended solutioning for IN625 according to the literature [29]. The selected condition (1150 °C for 2 h) presented lower hardness than samples heat-treated at 1000 °C for 1 and 2 h, probably due to slightly larger grains. Moreover, a thermal exposure at 1150 °C should guarantee higher chemical elements homogenisation with

respect to 1000 °C, promoting a more distributed precipitation of phases during the subsequent ageing treatments.

The hardness values and microstructure of the various solutioned and consecutive aged samples for 24 h are provided in Fig. 6. The ageing treatments tend to increase the hardness, except for aged samples at 900 °C. The OM images revealed similar grain size as the solutioned state, suggesting that the thermal exposures did not trigger a notable grain growth. Likewise, for the direct ageing, the hardness can be connected to phases formation. FESEM investigations revealed that thermal exposures at 600 °C and 700 °C form nanometric γ' phases indicated by the number 1, together with intergranular Cr-rich $M_{23}C_6$ carbides for samples heat treated at 700 °C indicated by arrow 2 in FESEM image. The higher hardness of samples heat treated at 700 °C with respect to 600 °C may derive from higher formation of nanometric γ' phases. However, quantification analyses will be performed in future works. On the other hand, the aged samples at 800 °C and 900 °C exhibited the presence of δ and Laves phases pointed out by arrows 3 and 4, respectively. Moreover, from the FESEM images, it is evident that samples aged at 900 °C exhibited very large δ and Laves phases, which may explain the limited hardness increment. Also in this case, it was chosen to investigate in detail the microstructure and tensile properties of aged samples at 700 °C for 24 h, which revealed the highest hardness, among the investigated aged IN625 conditions, due to the formation of γ' phases without the formation of detrimental phases.

Finally, it is interesting to note that the as-built and solutioned samples subjected to 700 °C exhibited a different hardness evolution. In fact, the direct aged samples (heat-treated at 700 °C for 24 h) revealed a hardness improvement around 24% with respect to the as-built state. On the other hand, the solutioned and aged samples (heat-treated at 1150 °C 2 h and 700 °C for 24 h) exhibited a hardness increment around 48% with respect to the solutioned state. This remarkable difference in hardness values seems to be caused by a different degree of element homogenisation between the as-built and solutioned states. In fact, the microstructure of as-built samples is characterised by dendritic structures with the presence of highly segregated elements as Nb within

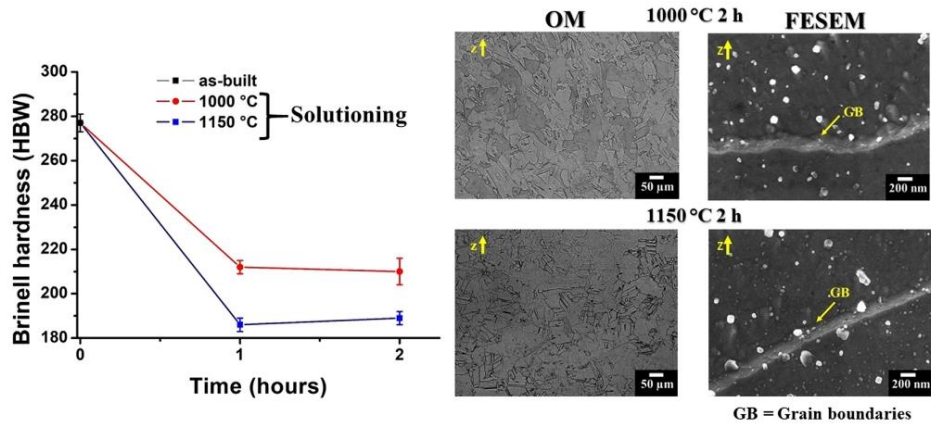


Fig. 5. Brinell hardness of as-built and after solutioning at 1000 °C and 1150 °C up to 2 h together with the OM and FESEM images of heat-treated samples for 2 h along the building direction (z-axis).

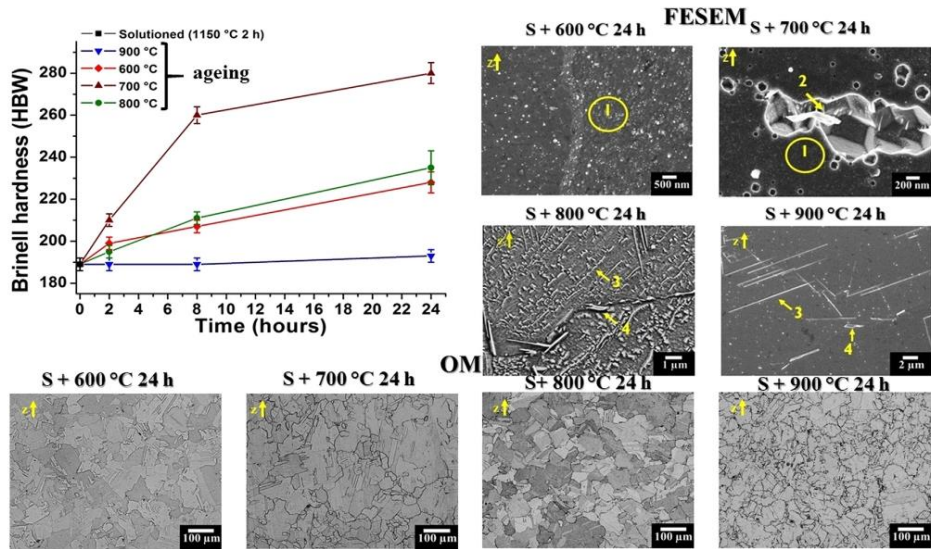


Fig. 6. Brinell hardness of solutioned and subsequently aged samples carried out from 600 to 900 °C up to 24 h together with OM and FESEM images of heat-treated samples for 24 h along the building direction (z-axis), where number 1 indicated γ'' phases, number 2 pointed out intergranular Cr-rich $M_{23}C_6$ carbides and number 3 and 4 indicated δ and Laves phases, respectively.

interdendritic areas, thus limiting the generation of γ'' phases. On the other hand, the solution treatment dissolves the dendrite structures involving the homogenous distribution of the elements throughout the materials, including Nb essential for the γ'' phases formation.

3.2. Tensile behaviour

The tensile engineering stress-strain curves of as-built, direct aged (700 °C for 24 h), solutioned (1150 °C for 2 h), and solutioned and aged (1150 °C for 2 h and 700 °C for 24 h) LPBF IN625 samples are illustrated

in Fig. 7. The as-built samples showed a yield strength (YS) and ultimate tensile strength (UTS) values of 783 ± 23 and 1041 ± 36 MPa, respectively, with a ductility of $33 \pm 1\%$. All the heat treatments had a significant influence on the tensile properties. Among all the selected conditions, the direct aged samples exhibited the maximum increment of YS (1012 ± 54 MPa) and UTS (1222 ± 56 MPa), associated with the lowest ductility ($23 \pm 1\%$). On the other hand, the solutioned samples exhibited the lowest YS and UTS (396 ± 9 and 883 ± 15 MPa, respectively), while the highest increment in ductility ($55 \pm 1\%$) could be noticed. In the case of the solutioned and aged

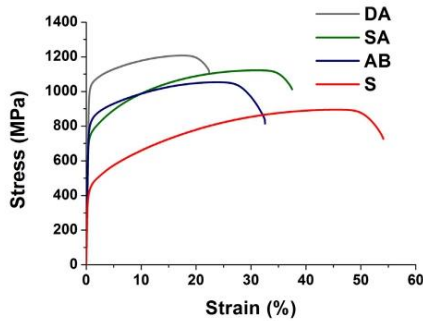


Fig. 7. Tensile stress-strain curves for the as-built (AB), direct aged at 700 °C for 24 h (DA), solutioned at 1150 °C for 2 h (S) and solutioned + aged 1150 °C for 2 h and 700 °C 24 h (SA) samples.

samples a remarkable increase in both YS and UTS (722 ± 7 and 1116 ± 6 MPa, respectively) was recorded, correlated to a ductility reduction ($35 \pm 5\%$) with respect to solutioned condition.

The tensile properties and hardness values of as-built and heat-treated IN625 samples will be discussed by means of microstructural and fractures surfaces observation.

3.3. Microstructural evolution

3.3.1. As-built condition

The microstructure of as-built samples consisted of columnar grains growing epitaxially thus intersecting multiple melt pools along the building direction, as can be seen in Fig. 8a. These columnar grains had a large size distribution, with the maximum around 350–400 μm and the minimum around 5–10 μm . At higher magnification by means of FESEM analysis, the very fine structures of as-built samples could be observed (Fig. 8b, c and d).

The cellular structures were characterised by size up to around 1 μm , also revealing areas with very fine dimension of 300 nm. The columnar dendrites typically exhibited primary dendritic arm spacing (PDAS) up to 1 μm , while only partially formed secondary dendritic arms were found in some areas (Fig. 8c).

The dendritic structures are commonly reported for LPBF Ni-based superalloys, and they derive from the extremely high cooling rates of the LPBF process around 10^6 °C/s [17,19,22,34]. In particular, the cellular structures are believed to be altered primary dendritic structures caused by the extremely high cooling rates [35]. However, this fine dendritic structures exhibited interdendritic nanometric Nb-rich MC carbides while interdendritic regions were found to be enriched in Nb and Mo, as indicated respectively by arrows 1 and 2 in Fig. 8c and d.

Analysis of the as-built sample microstructure by TEM (Fig. 8e) revealed that the very fine dendritic microstructure is characterised by a high density of tangled dislocations in the interdendritic regions resulting from the very high temperature gradient and rapid solidification

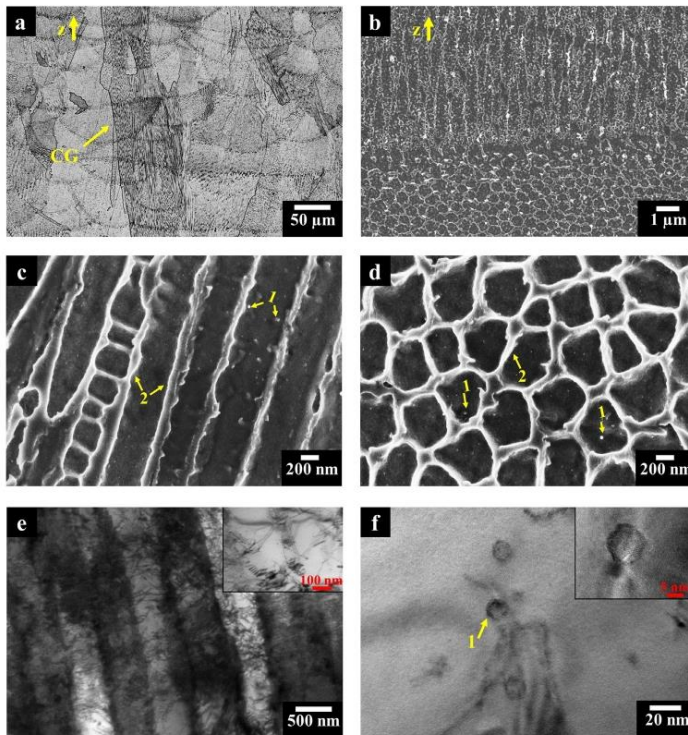


Fig. 8. a) optical micrograph showing columnar grains (CG) and melt pools for as-built sample; b) FESEM image exhibiting columnar and cellular primary dendrites for as-built samples; c-d) FESEM images: showing columnar and cellular dendritic structures with arrows 1 and 2 that indicate Nb-rich MC carbides and Nb, Mo-rich areas in interdendritic regions, respectively; e-f) TEM bright field images: e) showing columnar dendrites with high density of dislocation mainly located in the interdendritic areas, with an inset of not completely formed Nb-rich MC carbides; f) Nb-rich MC carbides in the dendrite core; with inset showing the carbide coherency with the matrix.

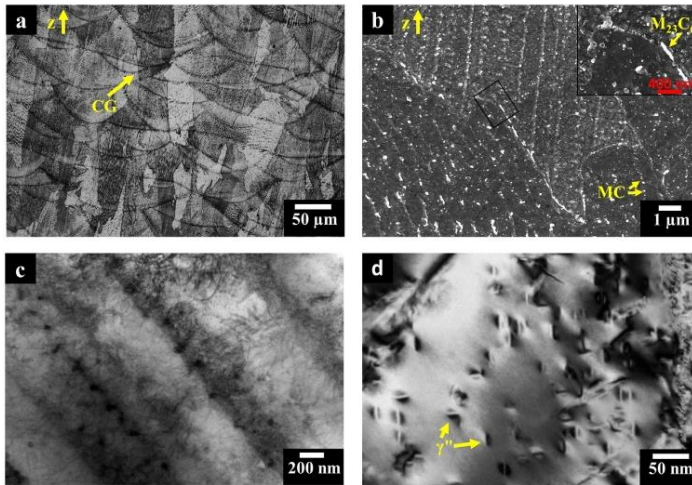


Fig. 9. Direct aged IN625 sample: a) optical micrograph showing columnar grains (CG) and melt pools; b) FESEM image exhibiting dendritic structures with grain boundaries, and inset of an intergranular $M_{23}C_6$ carbide; c, d) TEM bright field images: c) showing columnar dendrites with high dislocation mainly in the interdendritic areas; d) γ' phases.

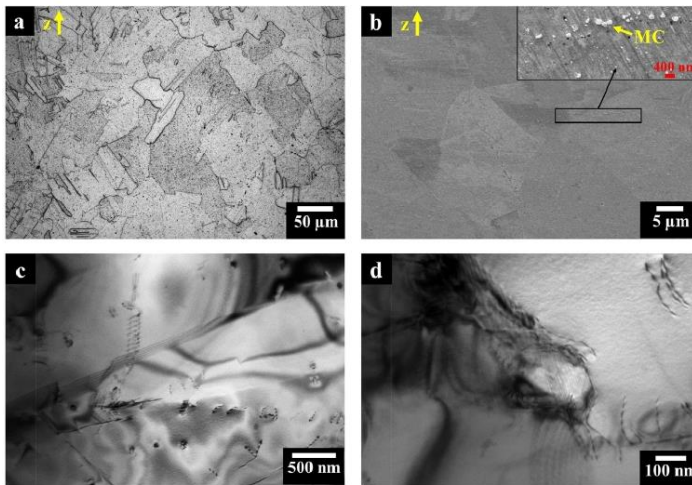


Fig. 10. Solutioned IN625 sample: a) optical micrograph showing equiaxed grains with twin boundaries; b) FESEM image exhibiting equiaxed grains with an inset of precipitate line of fine intergranular MC carbides; c, d) TEM bright field images: c) showing the matrix with very low dislocation density; d) intergranular Nb, Ti-rich MC carbides.

experienced during the LPBF process. TEM analyses also revealed indefinite/confusing precipitate-like features lined up along the interdendritic region. Although a comprehensive investigation will be done in future work to draw any conclusion, the authors speculate these features may result from an early stage of fine MC carbides precipitation caused by the fast solidification and cooling rate together with the segregation of Nb in the interdendritic region. EDS analysis in fact indicated a rather high concentration of such element. Nb-rich MC carbides with a size around 10–50 nm were also detected at high magnification in the dendrites' core. These nano-sized MC carbides were formed during solidification by the eutectic reaction ($L \rightarrow \gamma + MC$), even though the eutectic reactions generally occur in the interdendritic region. However, it should be noticed that the very high cooling rate promotes solute trapping, therefore increasing the quantity of solute

atoms such as Nb and Mo that remain entrapped in the dendritic core [22]. It is thus possible to suppose that higher Nb content may promote eutectic reactions involving the formation of NbC carbides in dendrite cores. The inset in Fig. 8f demonstrates the coherence of these carbides with the matrix, whereas EDS values revealed greater Nb concentration than in the austenitic matrix. Although a precise determination of the composition was not allowed, the solidification study on IN625 and the carbides coherence with the matrix as well as the Nb increment revealed by EDS seem to indicate they may be Nb-rich MC carbides [3]. There was no evidence of the presence of Laves phase. This further suggested that the bright irregular phases observed by FESEM in interdendritic regions (Fig. 8c and d), which could be misidentified as Laves phases, may rather correspond to heavy metals segregation such as Nb and Mo. A possible explanation for this can be the chemical

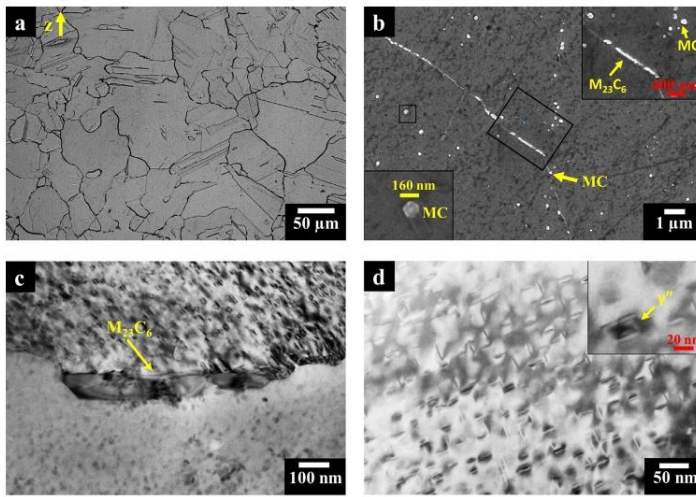


Fig. 11. Solutioned and aged IN625 sample: a) optical micrograph showing equiaxed grains with twin boundaries and carbides at grain boundaries; b) FESEM image exhibiting fine elongated Cr-rich $M_{23}C_6$ and Nb-rich MC carbides at the grain boundaries and intragranular Nb-rich MC carbides; c, d) TEM bright field images: c) intergranular Cr-rich $M_{23}C_6$ carbide; d) γ' phases.

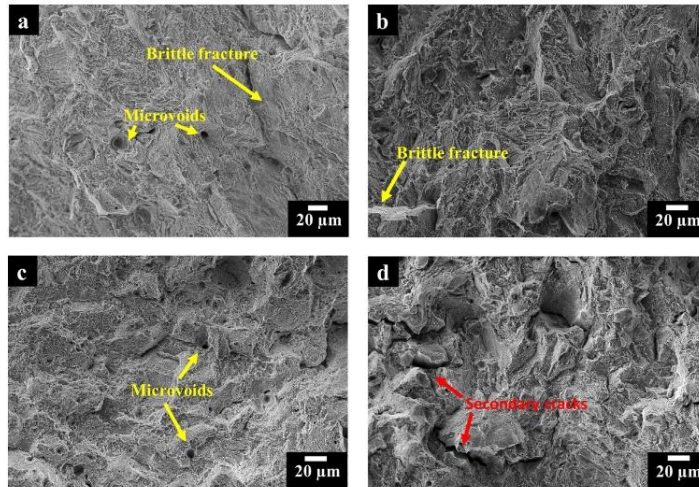


Fig. 12. SEM images of fracture surfaces of IN625 specimens a) as-built state; b) direct aged state; c) solutioned state; d) solutioned and aged state.

composition of the starting powder. It was demonstrated that a high C/Nb ratio promotes the formation of Nb-rich MC carbides without precipitation of Laves phase, and that low Fe and Si concentrations can reduce their formation [3,36]. These microstructural observations can be compared with the alloys produced by another rapid solidification process, as melt spinning involving cooling rates around 10^5 – 10^7 °C/s [37].

The microstructure of melt-spun ribbons made of IN625 revealed several similarities, such as very fine cellular structures and columnar primary dendrite structures without fully formed secondary arm spaces. Besides, they reported the presence of very fine Nb-rich particles within interdendritic areas due to C segregation, suggesting the formation of NbC carbides [38].

3.3.2. Direct aged condition

The microstructure at low magnification of direct aged samples in Fig. 9a was very similar to that of the as-built materials. In fact, the presence of melt pools and columnar grains with similar size was still clearly visible. The direct ageing at 700 °C for 24 h did not alter the dendritic structures, which had a similar PDAS and cellular dendritic structures up to 1 μ m. FESEM analysis (Fig. 9b) revealed the precipitation of different phases such as the discontinuous formation of elongated precipitates along the grain boundaries and Nb-rich MC carbides within the grains. Although slightly less pronounced, TEM micrographs highlighted columnar dendritic size as well as high density of tangled dislocations in the interdendritic region similar to the as-built materials and Nb-rich precipitate-like lines were still observed

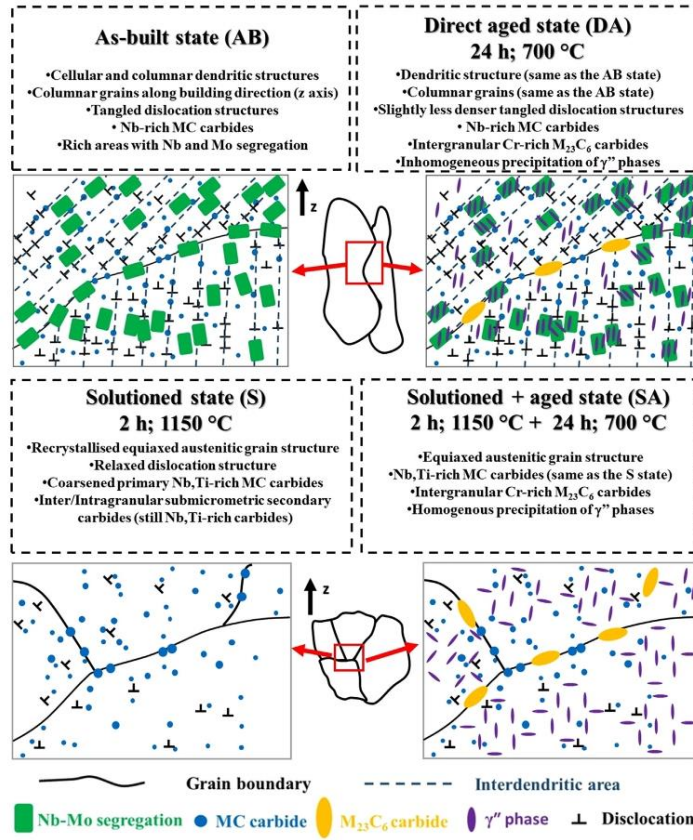


Fig. 13. Schematic of the major microstructure modifications occurring on IN625 samples fabricated by LPBF upon different heat treatment stages.

(Fig. 9c). Nevertheless, as a result of the direct ageing treatment, significant differences were also observed. First, fine elongated precipitates could be occasionally spotted along grain boundaries (inset in Fig. 9b). Although no definite evidence could be presented, according to their morphology and location and considering the T-T-T diagrams of IN625, these grain boundary precipitates were most likely Cr-rich $M_{23}C_6$ carbides [3,33]. Furthermore, as clearly observed by TEM micrograph in Fig. 9d, the direct aged samples exhibited precipitation of fine γ'' phases with a size of 10–30 nm displaying their typical disc morphology. The precipitation of the γ'' phase was inhomogeneous and some clusters of γ'' precipitates were observed along with γ'' -depleted zones (Fig. 9d). This phenomenon should be studied in details, and may be responsible for the significant deviation of the tensile properties, as discussed in Section 3.5. It is believed that the inhomogeneous solute concentration (Nb in particular) resulting from the very fast solidification leads to Nb-rich and Nb-depleted region in the dendrites core therefore responsible for the observed inhomogeneous precipitation of γ'' phases. Finally, it is worth to note that several microstructural features of direct aged samples are analogous to melt-spun ribbons heat-treated at 700 °C for 24 h reported in literature. In fact, the heat-treated melt-spun ribbons revealed the formation of γ'' phases scattered

throughout the material and $M_{23}C_6$ carbides along the grain boundaries [38].

3.3.3. Solutioned condition

The solution treatment generated a recrystallised microstructure eliminating the fine dendritic and columnar grains microstructure of the as-built samples developing equiaxed grains, which are recognised to lead to more isotropic mechanical properties. This microstructure highlights that occurs recrystallisation during the solution treatment. The microstructure of solutioned samples consisted in equiaxed grains with numerous twin boundaries, as can be observed in Fig. 10a. The OM investigation revealed a large presence of grains with dimensions around 90 μ m and a fraction of fine grains, the smallest ones with size around 10 μ m. The FESEM micrograph in Fig. 10b highlights that the dendritic structures disappeared as an effect of the solution treatment, and some fine sub-micrometric carbides could also be observed. Accordingly, the solution treatment performed at 1150 °C seems to promote the growth of primary carbides and the formation of high temperature secondary carbides. This is consistent with the fact that MC carbides are generally dissolved at higher temperature, i.e. around 1200 °C [3]. The fine secondary inter/intragranular carbides were

Table 2

Comparison of tensile properties of as-built (AB), direct aged (DA), solutioned (S) and solutioned and subsequently aged (SA) IN625 specimens built along the xy plane, together with other LPBF-built IN625 along the xy plane reported in literature and wrought IN625 alloys.

Inconel 625 sample	Young's modulus (GPa)	YS (MPa)	UTS (MPa)	Elongation (%)
This study				
AB	182 ± 13	783 ± 23	1041 ± 36	33 ± 1
DA	204 ± 3	1012 ± 54	1222 ± 56	23 ± 1
S	181 ± 16	396 ± 9	883 ± 15	55 ± 1
SA	200 ± 7	722 ± 7	1116 ± 6	35 ± 5
Other works and specifications				
LPBF ASTM F3056-14	-	275 (min)	485 (min)	30 (min)
LPBF ^a [43]	170 ± 20	725 ± 50	990 ± 50	35 ± 5
LPBF [18]	-	800 ± 20	1030 ± 50	8-10
LPBF [16]	196 ± 12	641.5 ± 23.5	878.5 ± 1.5	30 ± 2
As-rolled [44]	-	414 (min)	827 (min)	30 (min)
Wrought	-	276 (min)	690 (min)	(min)
ASTM B443 ^b	-	-	-	-

^a As-built state according to EOS data sheet.

^b Wrought grade 2 solution annealed at least at 1093 °C.

homogeneously dispersed within the matrix and had a size between 30 and 400 nm. The coarser carbides were generally located along the grain boundaries as can be observed in the inset in Fig. 10b. The TEM image in Fig. 10c reveals low dislocation density of the solutioned state as a result of the recrystallisation. TEM analysis also showed that intergranular and intragranular carbides had high concentrations of Ti and Nb, therefore suggesting Nb,Ti-rich MC carbides (Fig. 10d). These results are consistent with previous studies which revealed the presence of Nb,Ti-rich MC carbides after solution treatments performed on traditional IN625 alloy [3,39,40].

3.3.4. Solutioned and aged condition

Solutioned and aged samples exhibited equiaxed grains with a size similar to solutioned samples, pointing out that the ageing treatment did not affect the grain size, as can be observed in Fig. 11a. At higher magnification, FESEM and TEM micrographs (Fig. 11b and c) revealed the presence of grain boundary Cr-rich $M_{23}C_6$ carbides as confirmed by EDS results with size from 100 nm up to microns, whereas intragranular Nb,Ti rich-carbides formed during solidification or solution treatment were still visible. The TEM images (Fig. 11c and d) also revealed the presence of intragranular ellipsoidal γ'' phases with a size between 10 and 30 nm resulting from ageing treatment. In contrast to direct aged materials, the precipitation of these γ'' was homogeneous throughout the grains (Fig. 11d). This can be explained by the homogenisation of solute atoms in solid solution achieved by the solution treatment. The phases presented are in agreement with the T-T diagrams of IN625 alloy mentioned in the literature [3,33].

Table 3

Fitting parameters of the flow curve using Voce model and related fitting quality assessment parameters for as-built (AB), direct aged (DA), solutioned (S) and solutioned and subsequently aged (SA) IN625 specimens built along the xy plane (deviation standard abbreviated as d.s.).

Metallurgical state	Fitting parameters of VOCE model								
	q		k ₂		P		R ² (COD)	AARE [%]	MXRE [%]
	Value	d.s.	Value	d.s.	Value	d.s.			
AB	1014	53	1.07	0.07	0.94	0.03	0.9999	0.07	0.51
S	970	27	0.49	0.03	0.92	0.02	0.9998	0.32	1.95
SA	1267	73	1.01	0.11	0.94	0.02	0.9999	0.08	0.46
DA	898	89	0.9	0.14	0.87	0.02	0.9999	0.06	0.55

3.4. Fracture surface analyses

The fracture surfaces of tensile specimens were investigated by SEM. The fracture surface of the as-built sample (Fig. 12 a) mainly revealed a ductile fracture mode with microvoids coalescence together with some brittle fractures that may be attributed to the presence of Nb-rich MC carbides, as indicated on LPBF Inconel 718 in literature [41]. Differently, the direct aged state (Fig. 12b) exhibited higher number of brittle fractures. In this case, the brittle fractures may be caused by the presence of Nb-rich MC carbides, $M_{23}C_6$ carbides as well as γ'' phases [39,42]. The solutioned sample exhibited a ductile fracture mode with microvoids coalescence, as can be seen in Fig. 12c. In this case, the larger size of microvoids with respect to as-built samples can be correlated to its higher ductility. By contrast, the solutioned and aged samples revealed mixed ductile and brittle fractures, with the presence of secondary cracks (Fig. 12d). In this case, the brittle fractures and crack areas may be attributed to intergranular $M_{23}C_6$ carbides and γ'' phases.

3.5. Microstructural and mechanical properties correlation

The microstructural investigation of as-built and heat-treated IN625 specimens obtained by LPBF process presented in the previous section allowed to propose a microstructure development model, which is summarised and graphically described in Fig. 13.

According to the above reported observations, it can be concluded that the solution treatment is essential to eliminate some of the detrimental features deriving from LPBF manufacturing. It is particularly important to release the segregation elements and to reduce the tangled dislocation structures. Ageing either performed after solutioning or directly after LPBF fabrication promotes the formation of intergranular $M_{23}C_6$ carbides and fine metastable intragrain γ'' phases. The coupling of solutioning and ageing is also capable to induce the precipitation of a fine secondary carbides structure, which is particularly promising in terms of strengthening effects. The consequences of these microstructural evolutions can be assessed through the analysis of tensile results and the related fracture surfaces features.

The tensile properties of as-built and heat-treated IN625 samples are summarised in Table 2. The mechanical properties of the company data sheet and other LPBF IN625 alloys similarly built perpendicular to the building direction (xy plane) are also given as reference, as well as those of wrought IN625 alloys reported in the ASTM B443 standard and commercially available. The as-built IN625 samples exhibited superior mechanical properties than those of LPBF IN625 alloy reported in the ASTM F3056-14 standard, whereas they showed values compatible with the company data sheet. Regarding other investigations, the mechanical properties of as-built samples resulted to be similar to other as-built LPBF IN625 produced by Yadroitsev et al. [18], although materials under investigation in this research exhibited higher ductility. This large difference in ductility can be explained by the difference in porosity levels. Actually, Yadroitsev roughly determined a porosity lower than 1%, whereas a porosity of 0.064 ± 0.014% was assessed in a

previous work [17] for the same set of process parameters applied to manufacture the samples used in the current research. On the other hand, the ductility of IN625 processed by Wang et al. [16] was similar to the present as-built samples, but significantly lower YS and UTS were reported in their research. In this case, the difference of tensile properties can be correlated to the use of different process parameters or machine with different scanning strategy, as pointed out in literature [25]. The high mechanical properties of these materials can be attributed to the very fine dendritic structures and high dislocation density resulting from the fast solidification and cooling rates of the LPBF process. All the heat-treated IN625 specimens exceeded the mechanical properties presented in the ASTM F3056-14. Only direct aged samples exhibited a ductility 7% lower than the reference ASTM standard. Comparing the mechanical properties with traditional wrought IN625 alloy, it is worthwhile to note that as-built samples revealed higher strength and similar ductility with respect to the minimum values of as-rolled IN625 alloy, whereas the solutioned samples exhibited higher YS and UTS and ductility than minimum requirements for wrought grade 2 IN625 according to ASTM B443.

The flow curve was modelled through the Voce model thus deriving q , K_2 , p , R^2 (COD), AARE [%] and MXRE [%] for all the selected LPBF IN625 states given in Table 3.

The combined analysis of microstructural evolutions and the calculated q parameter of LPBF IN625 samples lead to the following conclusions, starting from the condition with the highest q , and consequently the lowest dislocation free path. The solutioned and aged samples presented a homogeneous precipitation of γ'' phases and intergranular Cr-rich $M_{23}C_6$ carbides, clearly resulting in the highest q and therefore the lowest dislocation free path. The as-built state revealed the second highest q values mainly due to very high tangled dislocation density as well as fine dendritic structures. Then the solutioned state exhibited a slightly lower value than as-built state, and this limited difference is most likely to cause by the remarkable formation of sub-micrometric carbides dispersed within the material, restricting the dislocation free path. Finally, the direct aged state surprisingly showed the lowest q values that may be associated with an initial dislocation recovery coupled with the nonhomogeneous formation of nanometric phases (generating a large standard deviation for q), thus increasing the average free path for the dislocation without finding obstacles.

It was therefore demonstrated that the microstructure evolution of the LPBF IN625 under various heat treatments provides a wide spectrum of possible mechanical behaviour.

4. Conclusion

The research provides a framework for the microstructure and mechanical properties evolution of as-built and different heat-treated IN625 processed by laser powder bed fusion process (LPBF). The main findings can be summarised as follows:

1. The as-built microstructure of IN625 consisted of columnar grains and very fine dendritic structures with high density of dislocations. This led to high mechanical properties, generally higher than minimum values for as-rolled IN625 alloy, with mixed ductile and brittle fractures. FESEM and TEM analyses revealed the presence of very fine Nb-rich MC carbides (10–50 nm) in dendritic cores as a result of eutectic reaction during the solidification.
2. Directly aged materials at 700 °C for 24 h exhibited similar columnar grains and very fine dendritic structures as as-built materials, indicating that direct ageing did not alter these microstructural features. Meticulous analysis of the microstructure revealed the presence of very fine (10–30 nm) discoidal γ'' phases as well as the discontinuous formation of elongated Cr-rich $M_{23}C_6$ carbides at grain boundaries. Although this considerably improved the strength of IN625 alloy, the ductility significantly decreased and the fracture surface showed larger amount of brittle fracture with respect to the

as-built condition.

3. A solutioning treatment at 1150 °C for 2 h interestingly led to recrystallisation (with large grains around 90 μ m and also fine grains, the smallest around 10 μ m) accompanied by recovery of the dislocations and dissolution of the dendritic structures. This resulted in far lower strength levels and much higher ductility, showing a ductile fracture mode. FESEM and TEM analyses highlighted the presence of fine inter/intragranular Nb,Ti-rich MC carbides from 30 to 400 nm.
4. A Solutioning treatment at 1150 °C for 2 h followed by ageing at 700 °C for 24 h resulted in a recrystallised microstructure similar to that of solutioned materials, together with the presence of fine intragranular γ'' phases homogeneously distributed and intergranular Cr-rich $M_{23}C_6$ carbides. This led to high levels of strength while the ductility decreased in comparison with solutioned materials as precipitation induced mixed brittle and ductile fractures.

References

- [1] F.J. Xu, Y.H. Lv, B.S. Xu, Y.X. Liu, F.Y. Shu, P. He, Effect of deposition strategy on the microstructure and mechanical properties of Inconel 625 superalloy fabricated by pulsed plasma arc deposition, *Mater. Des.* 45 (2013) 446–455, <http://dx.doi.org/10.1016/j.matdes.2012.07.013>.
- [2] V. Shankar, K.B.S. Rao, S.L. Mannan, Microstructure and mechanical properties of inconel 625 superalloy, *J. Nucl. Mater.* 288 (2001) 222–232, [http://dx.doi.org/10.1016/S0022-3115\(00\)00723-6](http://dx.doi.org/10.1016/S0022-3115(00)00723-6).
- [3] S. Floren, G.E. Fuchs, W.J. Yang, *Metallurgy of alloy 625*, in: E.A. Loria (Ed.), *Superalloys 718, 625 and Various Derivatives*, The Minerals, Metals and Materials Society, Pittsburgh, PA, USA, 1994, pp. 13–37.
- [4] G.P. Dinda, A.K. Dasgupta, J. Mazumder, Laser aided direct metal deposition of Inconel 625 superalloy: microstructural evolution and thermal stability, *Mater. Sci. Eng. A* 509 (2009) 98–104, <http://dx.doi.org/10.1016/j.msea.2009.01.009>.
- [5] I.A. Choudhury, M.A. El-Baradie, Machinability of nickel-base super alloys: a general review, *J. Mater. Process. Technol.* 77 (1998) 278–284, [http://dx.doi.org/10.1016/S0924-0136\(97\)00429-9](http://dx.doi.org/10.1016/S0924-0136(97)00429-9).
- [6] E.O. Ezugwu, Key improvements in the machining of difficult-to-cut aerospace superalloys, *Int. J. Mach. Tools Manuf.* 45 (2005) 1353–1367, <http://dx.doi.org/10.1016/j.jmactools.2005.02.003>.
- [7] F. Trevisan, F. Calignano, A. Aversa, G. Marchese, M. Lombardi, S. Biamino, et al., Additive manufacturing of titanium alloys in the biomedical field: processes, properties and applications, *J. Appl. Biomater. Funct. Mater.* (2017), <http://dx.doi.org/10.5301/jahfm.5000371>.
- [8] D. Herzog, V. Seyda, E. Wycisk, C. Emmelmann, Additive manufacturing of metals, *Acta Mater.* 117 (2016) 371–392, <http://dx.doi.org/10.1016/j.actamat.2016.07.019>.
- [9] D.D. Gu, W. Meiners, K. Wissenbach, R. Poprawe, Laser additive manufacturing of metallic components: materials, processes and mechanisms, *Int. Mater. Rev.* 57 (2012) 133–164, <http://dx.doi.org/10.1179/1743280411Y.0000000014>.
- [10] R. Acharya, J.A. Sharon, A. Starosecky, Prediction of microstructure in laser powder bed fusion process, *Acta Mater.* 124 (2017) 360–371, <http://dx.doi.org/10.1016/j.actamat.2016.11.018>.
- [11] P. Bidare, I. Bitharas, R.M. Ward, M.M. Attallah, A.J. Moore, Fluid and particle dynamics in laser powder bed fusion, *Acta Mater.* 142 (2018) 107–120, <http://dx.doi.org/10.1016/j.actamat.2017.09.051>.
- [12] L.N. Carter, X. Wang, N. Read, R. Khan, M. Aristizabal, K. Essa, et al., Process optimisation of selective laser melting using energy density model for nickel based superalloys, *Mater. Sci. Technol.* 32 (2016) 657–661, <http://dx.doi.org/10.1179/1743284715Y.0000000108>.
- [13] Q. Jia, D. Gu, Selective laser melting additive manufacturing of Inconel 718 superalloy parts: densification, microstructure and properties, *J. Alloy. Compd.* 585 (2014) 713–721, <http://dx.doi.org/10.1016/j.jallcom.2013.09.171>.
- [14] J.P. Choi, G.H. Shin, S. Yang, D.Y. Yang, J.S. Lee, M. Brochu, et al., Densification and microstructural investigation of Inconel 718 parts fabricated by selective laser melting, *Powder Technol.* 310 (2017) 60–66, <http://dx.doi.org/10.1016/j.powtec.2017.01.030>.
- [15] N.H. Sateesh, G.C.M. Kumar, K. Prasad, C.K. Srinivasa, A.R. Vinod, Microstructure and mechanical characterization of laser sintered inconel-625 superalloy, *Procedia Mater. Sci.* 5 (2014) 772–779, <http://dx.doi.org/10.1016/j.mpspr.2014.07.327>.
- [16] P. Wang, B. Zhang, C.C. Tan, S. Raghavan, Y.-F. Lim, C.-N. Sun, et al., Microstructural characteristics and mechanical properties of carbon nanotube reinforced Inconel 625 parts fabricated by selective laser melting, *Mater. Des.* 112 (2016) 290–299, <http://dx.doi.org/10.1016/j.matdes.2016.09.080>.
- [17] G. Marchese, X. Garmendia Colera, F. Calignano, M. Lorusso, S. Biamino, P. Minetola, et al., Characterization and comparison of inconel 625 processed by selective laser melting and laser metal deposition, *Adv. Eng. Mater.* 19 (2017) 1600635, <http://dx.doi.org/10.1002/adem.201600635>.
- [18] I. Yadroitsev, L. Thivillon, P. Bertrand, I. Smurov, Strategy of manufacturing components with designed internal structure by selective laser melting of metallic powder, *Appl. Surf. Sci.* 254 (2007) 980–983, <http://dx.doi.org/10.1016/j.apsusc.2007.08.046>.

- [19] D. Zhan, W. Niu, X. Cao, Z. Liu, Effect of standard heat treatment on the microstructure and mechanical properties of selective laser melting manufactured Inconel 718 superalloy, *Mater. Sci. Eng. A* 644 (2015) 32–40, <http://dx.doi.org/10.1016/j.msea.2015.06.021>.
- [20] X. Wang, L.N. Carter, B. Pang, M.M. Attallah, M.H. Loretto, Microstructure and yield strength of SLM-fabricated CM247LC Ni-Superalloy, *Acta Mater.* 128 (2017) 87–95, <http://dx.doi.org/10.1016/j.actamat.2017.02.007>.
- [21] M.M. Attallah, R. Jennings, X. Wang, L.N. Carter, Additive manufacturing of Ni-based superalloys: the outstanding issues, *MRS Bull.* 41 (2016) 758–764, <http://dx.doi.org/10.1557/mrs.2016.211>.
- [22] S. Li, Q. Wei, Y. Shi, Z. Zhu, D. Zhang, Microstructure characteristics of inconel 625 superalloy manufactured by selective laser melting, *J. Mater. Sci. Technol.* 31 (2015) 946–952, <http://dx.doi.org/10.1016/j.jmst.2014.09.020>.
- [23] T. Vilaro, C. Colin, J.D. Bartout, L. Nazé, M. Sennour, Microstructural and mechanical approaches of the selective laser melting process applied to a nickel-base superalloy, *Mater. Sci. Eng. A* 534 (2012) 446–451, <http://dx.doi.org/10.1016/j.msea.2011.11.092>.
- [24] B. Song, X. Zhao, S. Li, C. Han, Q. Wei, S. Wen, et al., Differences in microstructure and properties between selective laser melting and traditional manufacturing for fabrication of metal parts: a review, *Front. Mech. Eng.* 10 (2015) 111–125, <http://dx.doi.org/10.1007/s11465-015-0341-2>.
- [25] C.U. Brown, G. Jacob, M. Stoudt, S. Moylan, J. Slotwinski, A. Donmez, Interlaboratory study for nickel alloy 625 made by laser powder bed fusion to quantify mechanical property variability, *J. Mater. Eng. Perform.* 25 (2016) 3390–3397, <http://dx.doi.org/10.1007/s11665-016-2169-2>.
- [26] D.B. Witkin, P. Adams, T. Albright, Microstructural evolution and mechanical behavior of nickel-based superalloy 625 made by selective laser melting, *Laser 3D Manuf. II* 9353 (2015) 93530B, <http://dx.doi.org/10.1117/1.2.2083699>.
- [27] A. Kreitzberg, V. Brailovski, S. Turenne, Effect of heat treatment and hot isostatic pressing on the microstructure and mechanical properties of Inconel 625 alloy processed by laser powder bed fusion, *Mater. Sci. Eng. A* 689 (2017) 1–10, <http://dx.doi.org/10.1016/j.msea.2017.02.038>.
- [28] A. Kreitzberg, V. Brailovski, S. Turenne, Elevated temperature mechanical behavior of IN625 alloy processed by laser powder-bed fusion, *Mater. Sci. Eng. A* 700 (2017) 540–553, <http://dx.doi.org/10.1016/j.msea.2017.06.045>.
- [29] H. Chandler, *Heat Treater's Guide Practices and Procedures for Nonferrous Alloys*, ASM International, Materials Park, OH, 1996, pp. 88–97.
- [30] C. Gupta, B. Kumawat, Analysis of flow behaviour of iron and steel using power law models, *Mater. Sci. Technol.* 33 (2017) 971–983, <http://dx.doi.org/10.1080/02670836.2016.1246697>.
- [31] B.S. Xie, Q.W. Cai, W. Yu, J.M. Cao, Y.F. Yang, Effect of tempering temperature on resistance to deformation behavior for low carbon bainitic YP960 steels, *Mater. Sci. Eng. A* 618 (2014) 586–595, <http://dx.doi.org/10.1016/j.msea.2014.09.054>.
- [32] B. Xie, Q. Cai, W. Yu, S. Xu, B. Wang, A Flow Stress, Model for high strength steels with low carbon bainite structure, *J. Iron Steel Res. Int.* 23 (2016) 372–379, [http://dx.doi.org/10.1016/S1006-706X\(16\)30059-0](http://dx.doi.org/10.1016/S1006-706X(16)30059-0).
- [33] L.E. Shoemaker, Alloys 625 and 725: trends in properties and applications, in: E.A. Loria (Ed.), *Superalloys 718, 625 and Various Derivatives*, The Minerals, Metals and Materials Society, Pittsburgh, PA, USA, 2005, pp. 409–418.
- [34] N.J. Harrison, I. Todd, K. Mumtaz, Reduction of micro-cracking in nickel superalloys processed by selective laser melting: a fundamental alloy design approach, *Acta Mater.* 94 (2015) 59–68, <http://dx.doi.org/10.1016/j.actamat.2015.04.035>.
- [35] E. Chlebus, K. Gruber, B. Kuźnicka, J. Kurzac, T. Kurzynowski, Effect of heat treatment on the microstructure and mechanical properties of Inconel 718 processed by selective laser melting, *Mater. Sci. Eng. A* 639 (2015) 647–655, <http://dx.doi.org/10.1016/j.msea.2015.05.035>.
- [36] J.N. DuPont, C.V. Robino, A.R. Marder, Solidification modeling of Nb bearing superalloys, in: E.A. Loria (Ed.), *Superalloys 718, 625 and Various Derivatives*, The Minerals, Metals and Materials Society, Pittsburgh, PA, USA, 1997, pp. 87–98.
- [37] E.J. Lavernia, T.S. Srivatsan, The rapid solidification processing of materials: science, principles, technology, advances, and applications, *J. Mater. Sci.* 45 (2010) 287–325, <http://dx.doi.org/10.1007/s10853-009-3995-5>.
- [38] G.K. Dey, S. Albert, D. Srivastava, M. Sundararaman, P. Mukhopadhyay, Microstructural studies on rapidly solidified inconel 625, *Mater. Sci. Eng. A* 119 (1989) 175–184, [http://dx.doi.org/10.1016/0921-5093\(89\)90537-6](http://dx.doi.org/10.1016/0921-5093(89)90537-6).
- [39] C. Vernot-Loier, F. Cortial, Influence of heat treatments on microstructure, mechanical properties and corrosion behaviour of alloy 625, in: *Forged Rod*, E.A. Loria (Eds.), *Superalloys 718, 625 and Various Derivatives*, The Minerals, Metals and Materials Society, Pittsburgh, PA, USA, 1991, pp. 409–422.
- [40] L. Ferrer, B. Pieraggi, J.F. Ugnet, Microstructure evolution during thermo-mechanical processing of alloy 625, in: E.A. Loria (Ed.), *Superalloys 718, 625 and Various Derivatives*, The Minerals, Metals and Materials Society, Pittsburgh, PA, USA, 1991, pp. 217–228.
- [41] V.A. Popovich, E.V. Borisov, A.A. Popovich, V.S. Sufiiarov, D.V. Masaylo, L. Alzine, Functionally graded Inconel 718 processed by additive manufacturing: crystallographic texture, anisotropy of microstructure and mechanical properties, *Mater. Des.* 114 (2017) 441–449, <http://dx.doi.org/10.1016/j.matdes.2016.10.075>.
- [42] J. Mitra, S. Banerjee, R. Tewari, G.K. Dey, Fracture behavior of Alloy 625 with different precipitate microstructures, *Mater. Sci. Eng. A* 574 (2013) 86–93, <http://dx.doi.org/10.1016/j.msea.2013.03.021>.
- [43] EOS, Material data sheet – www.eos.info/ material-m (Accessed 18 July 2017).
- [44] SpecialMetals www.specialmetals.com/assets/smc/documents/alloy-625.pdf (Accessed 18 July 2017).

A new observation of strain-induced grain boundary serration and its underlying mechanism in a Ni–20Cr binary model alloy

J.W. Lee^a, M. Turner^a, H.U. Hong^{a,*}, S.H. Na^b, J.B. Seol^{b,**}, J.H. Jang^c, T.-H. Lee^c

^a Department of Materials Science and Engineering, Changwon National University, Changwon 51140, Republic of Korea

^b Department of Material Science Engineering, Pohang University of Science and Technology (POSTECH), Pohang 37673, Republic of Korea

^c Ferrous Alloy Department, Korea Institute of Materials Science, Changwon 51508, Republic of Korea

Keywords:

Ni–20Cr binary model alloy
Thermomechanical processing
Grain boundary serration
Segregation
Atom probe tomography
First-principles calculation

The formation of serrated grain boundaries and its mechanism correlated with straining exerted on grain boundaries were investigated in a Ni–20Cr binary model alloy. This model alloy is a full solid-solution which is deliberately free of carbon and aluminum to exclude precipitation of second phase. A special heat treatment involving slow cooling was used to promote grain boundary serration, which is known to enhance creep properties by decreasing interfacial free energy. No sign of serration could be observed for the Ni–20Cr model alloy, as expected. However, we found that a compressive 5% strain hold applied during slow cooling successfully induced grain boundary serration. The compressive 5% strain hold generated dislocations near the grain boundary, which promoted Cr enrichment near and at the grain boundary. To dismiss the effect of dislocations, straining was removed and the solutionizing temperature was increased in order to promote Cr enrichment near and at grain boundaries by means of vacancy-assisted diffusion of Cr atoms from the bulk to grain boundaries during slow cooling. Significant grain boundary serration was again observed. Atom probe tomography analyses showed that the serrated grain boundary with a wide width of ~10 nm was enriched with Cr atoms, as much as 87 at.%, while the γ matrix only contained 34 at.%. First-principles calculations showed that the strain energy necessary for the onset of grain boundary serration is lower than 0.97 kJ/mol.

1. Introduction

Grain boundary (GB) serration can be defined as the phenomenon leading to the formation of serrated GBs, showing a wavy morphology in nature. The serrated GBs are distinguishable from straight or smoothly-curved GBs by their amplitude larger than 0.5 μm [1–3]. It has been observed that GB serration can occur in nickel-based superalloys when specifically controlled heat treatments are employed [1–12]. Recently, GB serration has been reappraised because it can be considered as an alternative approach of GB engineering (GBE) applicable to alloys without γ' particles [10–13]. Serration was proven to significantly enhance creep properties due to the lower interfacial free energy of serrated GBs. According to previous research by Hong et al. [2,3,9,12,13], it was found that GBs serratate to have specific segments approaching {111} low-index planes at a boundary so that the interfacial free energy of the GB decreases. This is believed to be responsible for the driving force of GB serration.

There have been many attempts to elucidate the mechanism for GB serration. For example, mechanisms include Larson's model [4], Kou's

model [5], Henry & Yoo's model [6] and Tu & Turnbull's model [14]. All of these models describe the formation of serrated GBs as a result of an interaction between GB motion and various precipitates. Additionally, Koul and Thamburaj [8] claimed that in order to obtain serrated GBs in superalloys, the γ' solvus temperature should be higher than the solvus temperature of the GB carbides ($M_{23}C_6$ or M_6C), and the size of γ' particles adjacent to GBs should exceed 0.8 μm . However, Hong et al. [2,3,9,12,13] demonstrated several times that GB serration can take place in absence of carbides or γ' particles. It was therefore suggested that the onset of GB serration could be promoted by the lattice strain energy built up in the vicinity of GBs as a result of diffusion and segregation of alloying elements during slow cooling from the solutionizing temperature [2,15,16]. Nevertheless, substantial evidence to support their model is still lacking, and it remains to be rationalized in terms of quantification of the lattice strain energy at GBs to allow serration. Moreover, little is known concerning the nature of serrated GB, and further understanding of the underlying mechanism responsible of the solute behavior is needed. Hence, an accurate determination of the chemical composition in the vicinity of serrated GBs

* Correspondence to: H.U. Hong, Changwon National University, Changwon 51140, Republic of Korea.

** Correspondence to: J.B. Seol, National Institute for Nanomaterials Technology, POSTECH, Pohang 37673, Republic of Korea.

E-mail addresses: huhong@changwon.ac.kr (H.U. Hong), jb_seol@postech.ac.kr (J.B. Seol).

in Ni-based alloys is essential to comprehend the GB serration phenomenon enhancing creep properties.

In the present study, a binary Ni-20Cr model alloy was used to attempt to elucidate the mechanism for the formation of serrated GBs. This model alloy is a full solid-solution which is deliberately free of carbon and aluminum to exclude any precipitation of second phase such as Cr-rich carbides or γ' particles. According to the previous models mentioned above [1,4-8,10,11,14], no serration can therefore be expected in this model alloy. However, GB serration was successfully induced in this precipitate-free model alloy by means of a thermo-mechanical treatment specifically designed for straining GBs so as to diffuse Cr atoms to GBs. Atom probe tomography (APT) was employed to quantify the degree of Cr atoms at GB. Indeed, APT is the ideal tool to resolve direct chemical characterization on the GB segregation in polycrystalline materials. It also offers near-atomic spatial resolution and equal detection sensitivity to alloying elements decorated at GBs. The strain energy exerted on a GB, which is associated to the segregation of Cr atoms at the GB, was calculated by first-principles calculations.

2. Experimental Procedure

A binary Ni-20Cr model alloy (in wt%), which is the typical core composition of Ni-based superalloys, was used for investigation in the present study. Button type ingots with 40 mm diameter and 15 mm height, were prepared from high purity raw materials by means of vacuum arc remelting. The ingots were machined to obtain small cylindrical specimens with 8 mm diameter and 12 mm height. These small specimens were subjected to hot compression at 1050 °C, with a strain rate of 1 s^{-1} and a strain of 58% in order to trigger recrystallization. The specimens were subsequently subjected to a solutionizing treatment at 1150 °C for 100 min to obtain a fully recrystallized γ grain structure with 100 μm size.

The serration heat treatment was designed with reference to a previous study on the solid-solution-strengthened Alloy 617 (Ni-22Cr-12.3Co-9.5Mo-0.39Ti-0.99Al-0.08C) [12]. A similar yet shorter serration heat treatment was therefore applied to the present Ni-20Cr model alloy: solution-annealing at 1200 °C for 5 min immediately followed by slow-cooling down to 800 °C with a cooling rate of 5 °C/min and subsequent water-quenching. In order to impose external strain near GBs, some samples were subjected to a thermomechanical treatment conducted in a Gleeble 3500 (Dynamic Systems Inc., Poestenkill, NY) using cylindrical specimens of 4 mm diameter and 12 mm length. The thermomechanical treatment included a compressive 5% strain hold during the slow cooling from 1200 °C to 800 °C, while the rest of the heat treatment was similar to the serration heat treatment mentioned above.

Scanning electron microscopy (SEM) was performed with a JEOL JSM-5800 microscope (Jeol, Tokyo, Japan) with a tungsten filament operating at 20 keV. Bright-field, high-angle annular dark-field (HAADF) images, and energy dispersive spectroscopy (EDS) were obtained using a JEOL JEM-2010F analytical transmission electron microscopy (TEM) system equipped with an aberration corrector; the

system was operated at an acceleration voltage of 200 kV. Samples for APT analyses were prepared by a focused ion beam milling system (FIB, FEI Helios Nanolab 650i). The machined tips were analyzed using a local-electrode AP (Cameca LEAP 4000 \times HR). During analysis, APT tips were maintained in a vacuum of 2.7×10^{-11} Torr at temperature of -243 °C and laser pulsing (wavelength of 355 nm, pulse width of 10 ps, repetition rate of 200 kHz, and energy of 100 pJ) was used for field evaporation.

In order to estimate the extent of strain energy built up at serrated GBs highly enriched with Cr atoms, spin-polarized first-principles electronic structure calculations were performed. The Vienna ab-initio simulation package VASP [17,18], was employed in the projector augmented-wave (PAW) formalism for the calculations of the total energy. All self-consistent calculations were performed using generalized gradient approximation (GGA) for the exchange-correlation functional [19,20]. A plane-wave basis set with a cut-off energy level of 720 eV was used in all calculations. Brillouin zone sampling was performed using a $24 \times 24 \times 24$ k-point grid for the 4-atom unit cell of fcc Ni and fcc Cr. Such a k-point grid is appropriate for total energies and magnetic moments to converge to less than 10^{-4} eV and 0.01 μ_B , respectively. Binary Ni-Cr solution states were modeled using a $2 \times 2 \times 2$ supercell (32 atoms) with the number of k-points reduced accordingly. The equilibrium fcc structure was determined by calculating the total energy for nine different lattice parameters in 0.5% increments from -4% to 4% based on the experimentally measured lattice parameter. The equilibrium volume, equilibrium total energy, and bulk modulus were determined by means of third-order Birch-Murnaghan fitting using the total energy changes based on different atomic volumes [21].

3. Results and Discussion

3.1. The Occurrence of GB Serration Promoted by Thermomechanical Treatment

As a foundation to the present study, we found earlier that a solid-solution-strengthened Alloy 617 showed serrated GBs with a proportion of over 80% when the alloy was subjected to a proprietary heat treatment. The alloy was solution-annealed at 1200 °C for 2 h, followed by an appropriate slow-cooling down to 800 °C with a cooling rate of 5 °C/min and subsequently aged for 2 h at this temperature [12]. From this concept, a similar heat treatment was conducted for the Ni-20Cr model alloy: shorter holding time was applied because of the simpler nature of its chemical composition. This specific heat treatment is shown in Fig. 1(a). As a result, clearly unserrated straight GBs were observed throughout the material which compared to the as-solutionized state (Fig. 1(b) and (c)). In accordance with the previous models mentioned in introduction, which attribute GB serration to GB motion and precipitation, no serration can be expected for this model alloy [1,4-8,10,11,14]. Fig. 2 shows the TEM micrograph of a straight GB after the unsuccessful serration-aiming heat treatment. It should be noted that only few dislocations were present around the GB, and no

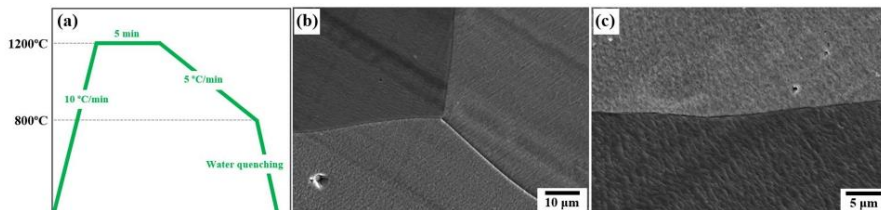


Fig. 1. Special serration-aiming heat treatment adapted from [12] designed to produce GB serration in Ni-20Cr model alloy. The schematic diagram of the heat treatment is shown in (a). However, no serration was found, as shown in SEM micrographs (b) and (c).

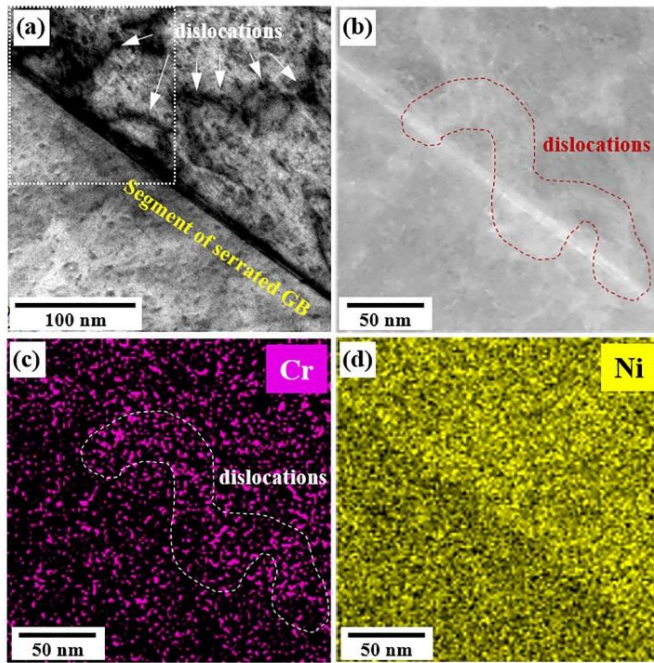


Fig. 4. TEM micrographs showing a segment of a serrated GB as produced by the thermomechanical treatment: (a) Bright-field TEM image and (b) corresponding enlarged view of HAADF TEM image. Note that no secondary precipitate is observed, and a high density of dislocations is observed near the serrated GB. The high magnification view of the dashed box in Fig. 4(a) is shown in Fig. 4(b) and the corresponding TEM/EDS elemental mapping image for (c) Cr and (d) Ni. (For interpretation of the references to color in this figure legend, the reader is referred to the web version of this article.)

3.2. Atom Probe Tomography Demonstrating Cr Enrichment at the Serrated GB

APT analyses were performed to determine to what extent Cr atoms were enriched at serrated GBs as produced by the optimized serration-aiming heat treatment. For reference, APT results for a straight GB after the initial serration-aiming heat treatment (Fig. 1(a)) are first presented. Fig. 6(a) shows the unserrated straight GB, and the marked area indicated by a yellow arrow corresponds to the Pt-passivated area for FIB machining the APT sample. The side view of the marked area, observed during the FIB machining process, can be seen in Fig. 6(b) where the straight GB is clearly observed. The tip sample was prepared so as for the straight GB to be captured for APT analysis (Fig. 6(c)). Fig. 6(d), (e) and (f) exhibit the 3-D reconstruction of Ni, Cr and Ni + Cr, respectively. It is evident that both Ni and Cr atoms are uniformly distributed across the straight GB, and no significant enrichment of Cr atoms is found. The 1D concentration profile for the unserrated sample

was generated by positioning a 6 nm diameter virtual cylinder traversing the two adjacent grains (Fig. 7(a)). Fig. 7 confirms that the enrichment of Cr atoms near or at the straight GB is negligible. The average concentration of Ni and Cr atoms partitioned to the γ matrix was measured to be 74.2 at.% and 23.5 at.%, respectively. Only a slight increased concentration of Cr atoms was detected along the straight GB with an approximately 7.5 nm width: the concentration of Cr atoms increased from 23.5 at.% (matrix) to 25.1 at.% (GB) (Fig. 7(c)).

Fig. 8(a) shows the serrated GB produced by the optimized serration-aiming heat treatment. The yellow marked area corresponds to the Pt-passivated area for FIB machining the APT sample. The side view of the serrated GB is shown in Fig. 8(b). It was interesting to observe that the sinusoidal-shape of the GB as seen through the top view appeared as faceted GB when seen through the side view. Although this is not the scope of the present paper, this will be studied with interest in the future, i.e. the three-dimensional aspect of a serrated GB plane. The tip sample was prepared so as for the serrated GB to be captured for APT

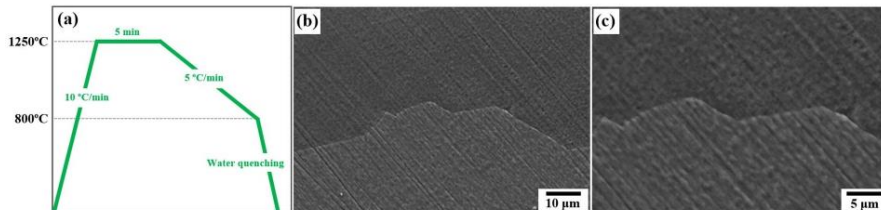


Fig. 5. Optimized heat treatment aiming to induce GB serration, with an increased solutionizing temperature from 1200 to 1250 °C to promote vacancy-assisted diffusion of Cr atoms. The schematic diagram of the heat treatment is shown in (a). GB serration occurred, as shown in SEM micrographs (b) and (c).

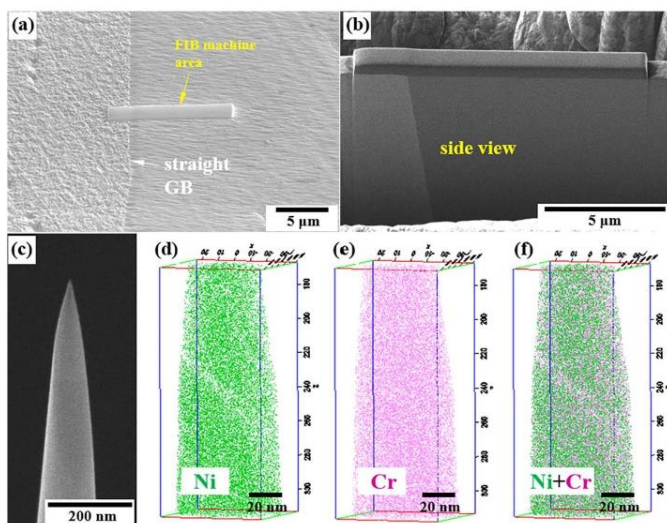


Fig. 6. SEM micrographs showing the unserrated GB after the serration-aiming heat treatment: (a) top view and (b) side view of the trench machined by FIB. The marked area in Fig. 6(a) corresponds to the Pt-passivated area for machining the APT sample by FIB system. The sub-micrometric tip sample for APT analysis is shown in (c). The 3-D reconstructed APT maps for the unserrated GB are shown in (d) for Ni, (e) for Cr and (f) for Ni + Cr. (For interpretation of the references to color in this figure legend, the reader is referred to the web version of this article.)

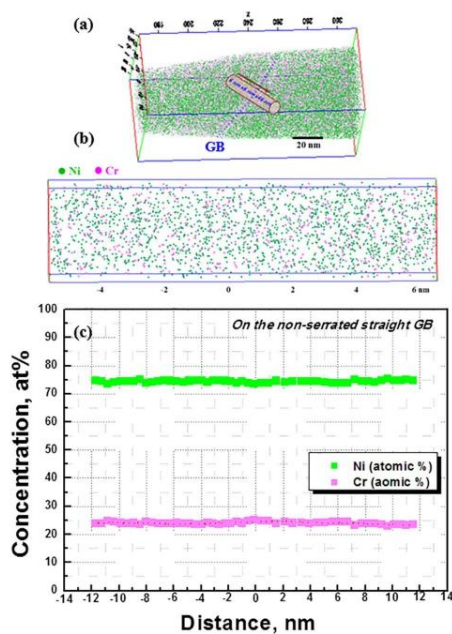


Fig. 7. (a) Reconstructed APT volume map for the unserrated sample shows the location of the 6 nm diameter virtual cylinder used to generate the concentration profile. (b) 3-D atomic distribution in the region of the 6 nm diameter virtual cylinder is presented for the unserrated sample. (c) Concentration profile of Ni and Cr atoms across the unserrated GB is plotted. (For interpretation of the references to color in this figure legend, the reader is referred to the web version of this article.)

analysis (Fig. 8(c)). Fig. 8(d), (e) and (f) display the 3-D reconstructed APT map of Ni, Cr and Ni + Cr, respectively. APT analyses clearly showed that the serrated GB is enriched with Cr atoms. Compared with the straight GB (Figs. 6 and 7), the serrated GB also appears significantly wider (~ 10 nm, note the scale difference). This observation remains to be rationalized in terms of geometrical configuration of serrated GBs in a further study. In Fig. 8(f), a 60 at.% Cr iso-concentration surface delineate the serrated GB from the γ matrix on each side. It is evident that the serrated GB is highly enriched with Cr atoms, leading to the appearance of a Cr-rich solid solution phase within the serrated GB. Fig. 9(a) shows the reconstructed APT volume map for the serrated sample, together with the location of the 3 nm diameter cylinder used to generate the concentration profile. In Fig. 9(b), the 3-D atomic distribution in the region is presented for the serrated sample. From Fig. 9(c), it is clear that the serrated GB is enriched with Cr atoms as much as 87 at.%, while the γ matrix contains only 34 at.%. This result indicates that Ni-rich solid solution matrix phase (65.6 at.% Ni-34.4 at.% Cr) is in contact with Cr-rich solid solution phase (87.5 at.% Cr-12.5 at.% Ni) at the serrated GB, although a transient region of about 5 nm width is present. It is therefore reasonable to infer that strain could be developed across the GB because these two different phases meet together to form the GB. As previously mentioned, recent studies [2,15,16,24] proposed that the onset of GB serration could be promoted by the lattice strain energy built up in the vicinity of GBs as a result of diffusion and segregation of alloying elements during slow cooling. Hong et al. [2] in particular found from EELS analysis that both C and Cr atoms segregated at particular regions on the initial straight GB prior to serration in Nimonic 263 superalloy. It was then suggested that the onset of GB serration may be triggered by this co-segregation of C and Cr atoms at GBs for the purpose of relieving the excessive unbalanced elastic strain. Furthermore, in order to verify that the onset of GB serration can be promoted by the distortional lattice stresses exerted on GBs, Turner et al. [16] and Hong et al. [24] added large-sized Zr atoms to Ni-based model alloys. They proved that the small addition of Zr was found to induce GB serration. Finally, Latief et al. [15] demonstrated that in Ni-xCr-0.1C model alloys, higher Cr content promoted a substantial increase in lattice distortion energy, which resulted in serrated GBs of higher amplitude. In the present

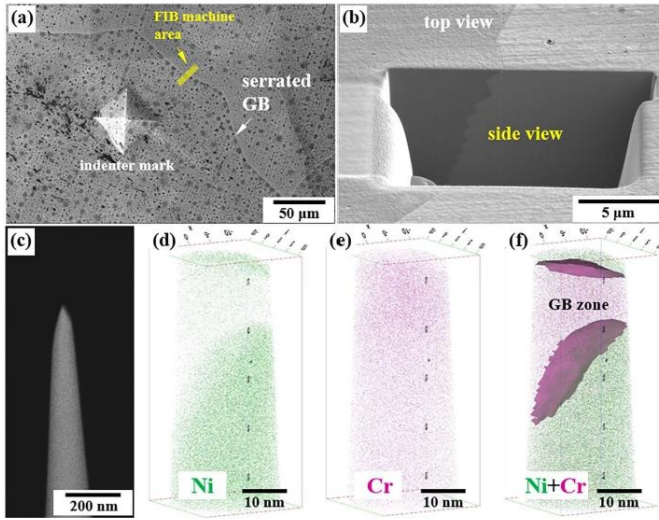


Fig. 8. SEM micrographs showing the serrated GB produced by the optimized serration-aiming heat treatment: (a) top view and (b) side view of the trench machined by FIB. The yellow marked area in Fig. 8(a) corresponds to the Pt-passivated area for machining the APT sample by FIB system. The sub-micrometric tip sample for APT analysis is shown in (c). The 3-D reconstructed APT maps for the serrated GB are shown in (d) for Ni, (e) for Cr and (f) for Ni + Cr. In Fig. 8(f), 60 at.% Cr isoconcentration surfaces delineate the GB from the γ matrix. (For interpretation of the references to color in this figure legend, the reader is referred to the web version of this article.)

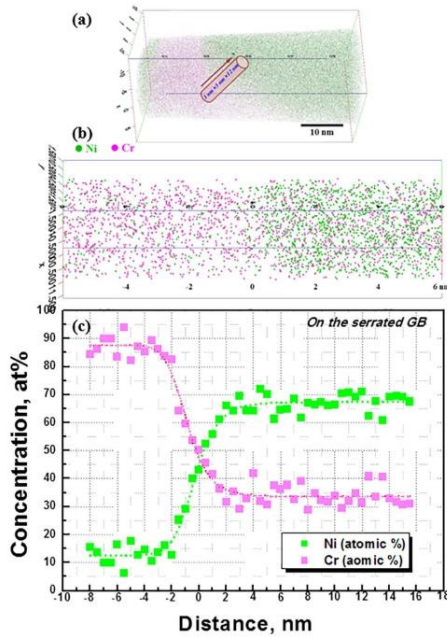


Fig. 9. (a) Reconstructed APT volume map for the serrated sample shows the location of the 3 nm diameter virtual cylinder used to generate the concentration profile. (b) 3-D atomic distribution in the region of the 3 nm diameter virtual cylinder is presented for the serrated sample. (c) Concentration profile of Ni and Cr atoms across the serrated GB is plotted. (For interpretation of the references to color in this figure legend, the reader is referred to the web version of this article.)

study, high degree of Cr segregation was observed only at the serrated GBs. This is in a good agreement with the previous research [2,15,16,24] dealing with the underlying mechanism of GB serration. The segregation-induced GB serration which has been demonstrated by the above series of studies, lies in 'GB segregation engineering (GBSE)' that was first introduced by Raabe et al. [26]. GBSE is referred to as the manipulation of GBs via solute decoration and even confined transformation for improving material performance. Raabe et al. [26,27] also claimed that segregation could be strong enough, in conjunction with the available interfacial energy and local stresses, to result in a phase transformation of, or at, the GB region. They proposed the possibility of the formation of complexions, i.e., interface stabilized phases [28–32]. From this perspective, we can carefully regard serrated GBs as 'complexion' formed by the phase transformation (or transition) of straight GBs, since the interfacial energy of GB is significantly decreased through serrated GB transition [2,3,9,12,13,24].

Although this has to be decidedly confirmed in future research, it can be expected that Cr enrichment near and at GB just before the serration, is lower than that after the serration. Accordingly, the critical strain energy necessary for the onset of GB serration would be lower than that calculated from the serrated GB. The following section deals with this strain predicted by first-principles calculations.

3.3. First-Principles Calculations

The enthalpy of formation for Ni–Cr binary solutions can be calculated as follows,

$$\Delta H(Ni_xCr_y) = \frac{E(Ni_xCr_y) - xE(Ni) - yE(Cr)}{(x + y)} \quad (1)$$

where $E(X)$ represents the equilibrium total energy of X. Although the most stable crystal structure of Cr is known as bcc, the enthalpies of formation at -273°C were calculated based on fcc Cr as a reference state in order to understand the element distribution in the fcc crystal structure.

Table 1 gives the calculated equilibrium atomic volumes, lattice parameters, bulk moduli and magnetic moments for fcc Ni and fcc Cr, respectively. The equilibrium lattice parameters of Ni and Cr were

Table 1
Calculated equilibrium atomic volumes, lattice parameters, bulk moduli and magnetic moments of the reference materials of fcc Ni and fcc Cr.

	Atomic volume/ \AA^3	Lattice parameter/ \AA	Bulk modulus/GPa	Magnetic moment/ μ_B
Ni	10.91	3.521	198.2	0.656
Cr	11.86	3.619	238.6	0

determined to be 0.3521 nm and 0.3619 nm, respectively. Hence, the lattice parameter of a Cr atom is larger than that of a Ni atom by 2.7%. The magnetic moment of Ni was calculated to be 0.656 μ_B , while that of Cr disappears at the equilibrium atomic volume, which is in good agreement with previous calculations [33]. Based on the lattice parameter calculation results for Ni–Cr binary solution systems, it was determined that the addition of Cr atoms to Ni increases the lattice parameter. Furthermore, the enthalpy of formation (ΔH) decreases with increasing Cr contents, and is the lowest (-60.8 kJ/mol) at approximately 75 at.% Cr addition, above which the ΔH increases. This points out a stabilizing effect of Cr segregation for the Ni–Cr binary solid solution.

As previously discussed from Fig. 9(c), it can be considered that the

Ni-rich solid solution γ matrix phase (65.6 at.% Ni–34.4 at.% Cr) is in contact with the Cr-rich solid solution phase (87.5 at.% Cr–12.5 at.% Ni) at the serrated GB. The addition of Cr atoms was modeled using a 32-atom supercell for fcc Ni. For the γ matrix phase with 34.4 at.% Cr concentration, the supercell was composed of 21 Ni atoms and 11 Cr atoms (Fig. 10(a)). Its equilibrium lattice parameter was determined to be 0.3543 nm. For the Cr-rich phase within the serrated GB zone (87.5 at.% Cr), the supercell was composed of 4 Ni atoms and 28 Cr atoms (Fig. 10(b)). Its equilibrium lattice parameter was determined to be 0.3732 nm. The relationship between the lattice parameter of each phase and the strain energy according to their interaction to make the interface was obtained (Fig. 10(c)). It can be predicted from Fig. 10(c) that the lattice parameters of both phases would be 0.357 nm to reach to the equilibrium state when the two phases meet and make the GB, and the strain energy developed for each phase would be 0.485 kJ/mol. As a result, the strain energy developed at the serrated GB would be 0.97 kJ/mol if the cubic symmetry is preserved for both phases. This calculated value of strain energy might be an upper bound, since the relaxation mechanism has not been considered in this calculation. Moreover, Cr enrichment near and at GB just before the serration, which produces the critical strain energy necessary for the onset of GB serration, might be lower than that after the serration. Therefore, it can

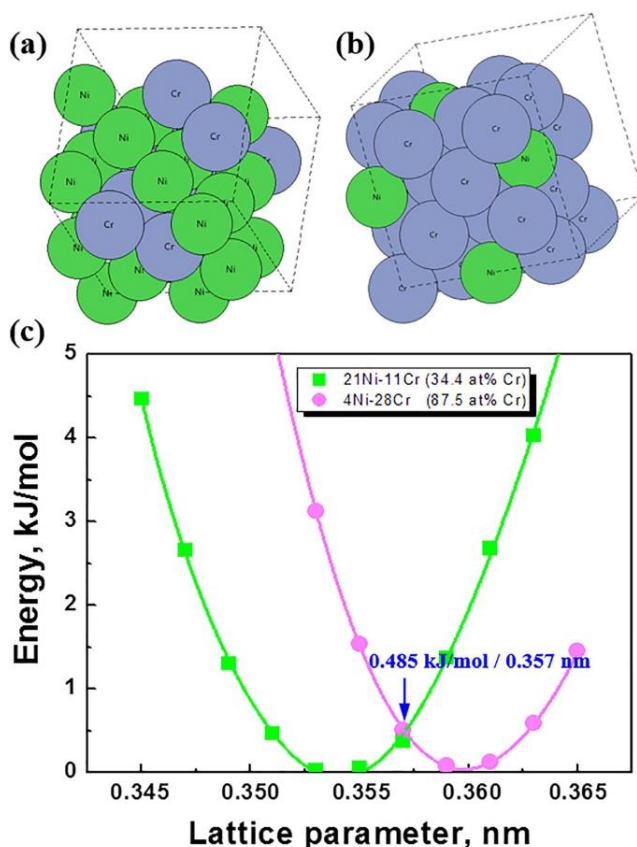


Fig. 10. First-principles calculations were used to estimate the extent of strain energy developed at the serrated GB enriched with Cr atoms. A 32-atom supercell was used to make (a) the Ni-rich solid solution matrix and (b) the Cr-rich solid solution present within the serrated GB. The relationship between the lattice parameter of each phase and the strain energy according to their interaction to make the interface is shown in (c).

be concluded that the strain energy necessary for the onset of GB serration in N-Cr binary model alloy is lower than 0.97 kJ/mol.

4. Conclusions

In the present study, the formation of serrated GBs and its mechanism correlated with straining exerted on GBs as a result of Cr segregation, have been investigated in a Ni-20Cr binary model alloy. Based on the results obtained from TEM/APT analyses and first-principles calculations, the following conclusions can be drawn:

(1) The special heat treatment involving slow cooling proven to induce considerable GB serration in Alloy 617 superalloy failed to produce serrated GBs in the Ni-20Cr model alloy. However, it was found for the first time that a compressive 5% strain hold during slow cooling successfully induced GB serration in this model alloy. The compressive 5% strain hold generated dislocations nearby GBs, which promoted Cr enrichment near and at GBs.

(2) A slow cooling process from a higher solutionizing temperature, which was designed to promote Cr enrichment near and at GBs by means of vacancy-assisted diffusion of Cr atoms from the bulk to GBs, induced GB serration in the precipitate-free Ni-20Cr model alloy. This outstanding result highlights the fundamental mechanism responsible for GB serration. The onset of GB serration may be essentially related to the straining exerted on GBs due to the segregation near and at GBs.

(3) APT analyses confirmed that the serrated GB with a wide width of ~10 nm was enriched with Cr atoms as much as 87 at.% while the γ matrix only contained 34 at.%. On the other hand, the enrichment of Cr atoms near or at the unserrated GB was negligible.

(4) First-principles calculations showed that while the actual minimum value of the critical strain energy necessary for the onset of GB serration is hard to determine considering phenomenon such as relaxation, a strain energy of at least 0.97 kJ/mol will guarantee the occurrence of GB serration in Ni-20Cr based superalloys.

Acknowledgments

This work was supported by the National Research Foundation of Korea (NRF) grant funded by the Korean government (MSIP) (NRF-2017R1A1A1A05000754). This research is also financially supported by the Korea Institute of Materials Science.

References

- [1] H. Loyer Danflou, M. Marty, A. Walder, Formation of serrated grain boundaries and their effect on the mechanical properties in a P/M nickel base superalloys, in: S.D. Antolovich, R.W. Stusrud, R.A. MacKay, D.L. Anton, T. Khan, R.D. Kissinger, D.L. Klarstrom (Eds.), *Superalloys, The Minerals, Metals & Materials Society*, Warrendale, PA, 1992, pp. 63-72.
- [2] H.U. Hong, H.W. Jeong, I.S. Kim, B.G. Choi, Y.S. Yoo, C.Y. Jo, Significant decrease in interfacial energy of grain boundary through serrated grain boundary transition, *Philos. Mag.* 92 (2012) 2809-2825.
- [3] H.U. Hong, I.S. Kim, B.G. Choi, Y.S. Yoo, C.Y. Jo, On the role of grain boundary serration in simulated weld heat-affected zone liquation of a wrought nickel-based superalloy, *Metall. Mater. Trans. A* 43 (2012) 173-181.
- [4] J.M. Larson, S. Floreen, Metallurgical factors affecting the crack growth resistance of a superalloy, *Metall. Trans. A* 8 (1977) 51-55.
- [5] A.K. Koul, G.H. Gessinger, On the mechanism of serrated grain boundary formation in Ni-based superalloys, *Acta Metall.* 31 (1983) 1061-1069.
- [6] M.F. Henry, Y.S. Yoo, D.Y. Yoon, J. Choi, The dendritic growth of γ' precipitates and

- grain boundary serration in a model nickel-base superalloy, *Metall. Trans. A* 24 (1993) 1733-1743.
- [7] R.J. Mitchell, H.Y. Li, Z.W. Huang, On the formation of serrated grain boundaries and fan type structures in an advanced polycrystalline nickel-base superalloy, *J. Mater. Process. Technol.* 209 (2009) 1011-1017.
- [8] A.K. Koul, R. Thamburaj, Serrated grain boundary formation potential of Ni-based superalloys and its implications, *Metall. Trans. A* 16 (1985) 17-26.
- [9] H.U. Hong, I.S. Kim, B.G. Choi, M.Y. Kim, C.Y. Jo, The effect of grain boundary serration on creep resistance in a wrought nickel-based superalloy, *Mater. Sci. Eng. A* 517 (2009) 125-131.
- [10] L. Jiang, R. Hu, H. Kou, J. Li, G. Bai, H. Fu, The effect of $M_{23}C_6$ carbides on the formation of grain boundary serrations in a wrought Ni-based superalloy, *Mater. Sci. Eng. A* 536 (2012) 37-44.
- [11] Y.S. Lim, D.J. Kim, S.S. Hwang, H.P. Kim, S.W. Kim, $M_{23}C_6$ precipitation behavior and grain boundary serration in Ni-based Alloy 690, *Mater. Charact.* 96 (2014) 28-39.
- [12] J.W. Lee, D.J. Kim, H.U. Hong, A new approach to strengthen grain boundaries for creep improvement of a Ni-Cr-Co-Mo superalloy at 950 °C, *Mater. Sci. Eng. A* 625 (2015) 164-168.
- [13] J.G. Yoon, H.W. Jeong, Y.S. Yoo, H.U. Hong, Influence of initial microstructure on creep deformation behaviors and fracture characteristics of Haynes 230 superalloy at 900 °C, *Mater. Charact.* 101 (2015) 49-57.
- [14] K.H. Tu, D. Turnbull, Morphology of cellular precipitation of tin from lead-tin bicontinuous, *Acta Metall.* 15 (1967) 369-376.
- [15] F.H. Latief, H.U. Hong, T. Blanc, I.S. Kim, B.G. Choi, C.Y. Jo, J.H. Lee, Influence of chromium content on microstructure and grain boundary serration formation in a ternary Ni-xCr-0.1C model alloy, *Mater. Chem. Phys.* 148 (2014) 1194-1201.
- [16] M. Terner, H.U. Hong, J.H. Lee, B.G. Choi, On the role of alloying elements in the formation of serrated grain boundaries in Ni-based alloys, *Int. J. Mater. Res.* 107 (2016) 229-238.
- [17] G. Kresse, J. Hafner, Ab initio molecular dynamics for liquid metals, *J. Phys. Condens. Matter* 6 (1994) 8245-8257.
- [18] G. Kresse, J. Furthmüller, Efficient iterative schemes for ab initio total-energy calculations using a plane-wave basis set, *Phys. Rev. B* 54 (1996) 11169-11186.
- [19] J.P. Perdew, K. Burke, M. Ernzerhof, Generalized gradient approximation made simple, *Phys. Rev. Lett.* 77 (1996) 3865-3868.
- [20] L. Bartlett, D. Van Aken, J. Medvedeva, D. Isheim, N. Medvedeva, K. Song, An atom probe study of kappa carbide precipitation and the effect of silicon addition, *Metall. Mater. Trans. A* 45 (2014) 2421-2434.
- [21] F. Birch, Elasticity and constitution of the earth's interior, *J. Geophys. Res.* 57 (1952) 227-286.
- [22] A.T. Lim, D.J. Srolovitz, M. Haataja, Low-angle grain boundary migration in the presence of extrinsic dislocations, *Acta Mater.* 57 (2009) 5013-5022.
- [23] M. Winning, G. Gottstein, L.S. Shvindlerman, Migration of grain boundaries under the influence of an external shear stress, *Mater. Sci. Eng. A* 317 (2001) 17-20.
- [24] H.U. Hong, I.S. Kim, B.G. Choi, Y.S. Yoo, C.Y. Jo, On the mechanism of serrated grain boundary formation in Ni-based superalloys with low γ' volume fraction, in: E.S. Hurn, et al. (Ed.), *12th International Symposium on Superalloys*, TMS, Warrendale, PA, USA, 2012, pp. 53-60.
- [25] P. Doing, P.E.J. Flewitt, Segregation of chromium to prior austenite boundaries during quenching of a 2.25%Cr%Mo steel, *Acta Metall.* 29 (1981) 1831-1841.
- [26] D. Raabe, M. Herbig, S. Sandlöbes, Y. Li, D. Tytco, M. Kuzmina, D. Ponge, P.-P. Choi, Grain boundary segregation engineering in metallic alloys: a pathway to the design of interfaces, *Curr. Opin. Solid State Mater. Sci.* 18 (2014) 253-261.
- [27] D. Raabe, S. Sandlöbes, J. Millán, D. Ponge, H. Assadi, M. Herbig, P.-P. Choi, Segregation engineering enables nanoscale martensite to austenite phase transformation at grain boundaries: a pathway to ductile martensite, *Acta Mater.* 61 (2013) 6132-6152.
- [28] M. Bartram, D. Chatain, W.D. Kaplan, Nanometer-thick equilibrium films: the interface between thermodynamics and atomistics, *Science* 332 (2011) 206-209.
- [29] S.J. Dillon, M.P. Harmer, G.S. Rohrer, The relative energies of normal and abnormal grain boundaries displaying different complexions, *J. Am. Ceram. Soc.* 93 (2010) 1796-1802.
- [30] S.J. Dillon, M. Tang, W.C. Carter, M.P. Harmer, Complexion: a new concept for kinetic engineering in materials science, *Acta Mater.* 55 (2007) 6208-6218.
- [31] M.P. Harmer, The phase behavior of interfaces, *Science* 332 (2011) 182-183.
- [32] P.R. Cantwell, M. Tang, S.J. Dillon, J. Luo, G.S. Rohrer, M.P. Harmer, Grain boundary complexions, *Acta Mater.* 62 (2014) 1-48.
- [33] A. Jain, S.P. Ong, G. Hautier, W. Chen, W.D. Richards, S. Dacek, S. Cholia, D. Gunter, D. Skinner, G. Ceder, K.A. Persson, Commentary: the materials project: a materials genome approach to accelerating materials innovation, *APL Mater.* 1 (2013) 011002-1-011002-11.



Heat treatments design for superior high-temperature tensile properties of alloy 625 produced by Selective Laser Melting

Jiwon Lee, Mathieu Ternier, Sunyoung Jun, Hyun-Uk Hong, Etienne Copin, Philippe Lours

► **To cite this version:**

Jiwon Lee, Mathieu Ternier, Sunyoung Jun, Hyun-Uk Hong, Etienne Copin, et al.. Heat treatments design for superior high-temperature tensile properties of alloy 625 produced by Selective Laser Melting. *Materials Science and Engineering: A*, Elsevier, 2020, 790, pp.1-15/139720. 10.1016/j.msea.2020.139720 . hal-02863894

HAL Id: hal-02863894

<https://hal-mines-albi.archives-ouvertes.fr/hal-02863894>

Submitted on 24 Jun 2020

HAL is a multi-disciplinary open access archive for the deposit and dissemination of scientific research documents, whether they are published or not. The documents may come from teaching and research institutions in France or abroad, or from public or private research centers.

L'archive ouverte pluridisciplinaire **HAL**, est destinée au dépôt et à la diffusion de documents scientifiques de niveau recherche, publiés ou non, émanant des établissements d'enseignement et de recherche français ou étrangers, des laboratoires publics ou privés.



Distributed under a Creative Commons Attribution| 4.0 International License

Heat treatments design for superior high-temperature tensile properties of Alloy 625 produced by selective laser melting

Jiwon Lee^{a,b}, Mathieu Terner^a, Sunyoung Jun^a, Hyun-Uk Hong^{a,*}, Etienne Copin^b, Philippe Lours^{b,**}

^a Department of Materials Science and Engineering, Changwon National University, 20 Changwondaehak-ro, Changwon, Gyeongnam, 51140, Republic of Korea

^b Institut Clément Ader (ICA), Université de Toulouse, CNRS, IMT Mines Albi, INSA, ISAE-SUPAERO, UPS, Campus Jarlard, F-81013, Albi, France

ABSTRACT

Keywords:
Superalloy
Selective laser melting
Heat treatment
Tensile properties
Grain boundary serration

The popular superalloy Alloy 625 was produced by Selective Laser Melting (SLM) and post-processing heat treatments were designed to optimize the inhomogeneous and constrained as-built microstructure (AB) for high temperature structural applications. A single-step solution heat treatment (RX) was designed to promote full recrystallization and approach the conventional wrought microstructure. To enhance high temperature properties, a grain boundary serration heat treatment (GBS) was successfully designed involving higher solution temperature and time to promote recrystallization and homogeneity, and a direct slow cooling step followed by a short aging to assist solute diffusion and grain boundary motion. The resulting microstructures were characterized by fully recrystallized fine equiaxed grains and fine intra and intergranular NbC precipitates. The GBS alloy also exhibited as much as 80% of serrated grain boundaries with enhanced resistance to cracking at high temperatures. Tensile properties of all three materials were evaluated at room temperature, 500 °C, 600 °C and 700 °C and compared with their conventional solutionized wrought Alloy 625 counterpart (Wrought). While the AB material exhibited high strength and low ductility, due for the most part to the high density of tangled dislocations resulting from SLM, both RX and GBS alloys showed tensile properties comparable to the conventional wrought material, higher strength in particular. At all temperatures, all four alloys exhibited yield strength values well over 200 MPa. Due to significantly different microstructures, deformation and fracture behaviors were different. While Wrought clearly presented irregular plastic flow at elevated temperatures typically attributed to dynamic strain aging (DSA), the materials produced by SLM and moreover those subjected to post-processing heat treatments exhibited more stable plastic deformation. The results and characterization reported in the present article highlight the predominant role of microstructure and outstanding potential of SLMed Alloy 625.

1. Introduction

Alloy 625 is an attractive Ni-based superalloy for marine, chemical, aerospace and power generation applications where superior mechanical properties are required. Relatively high contents of Cr, Mo and Nb provide good corrosion resistance and solid solution strengthening. Although this alloy is intended as a solid solution strengthened alloy, several precipitates may form either in service or during a designed age-hardening treatment. Nb in particular promotes the precipitation of fine γ'' (Ni₃Nb) particles and Nb-rich MC carbides [1–4]. The strengthening effect of γ'' precipitates comes from their coherency with the γ -matrix

and the distortion caused by the c-axis of their tetragonal structure, however precipitation kinetics is low [5–7]. This alloy is recognized for exhibiting good strength and ductility, as well as good resistance to creep and rupture at high temperatures. These attractive attributes for materials design however compete with good manufacturability: application of Alloy 625 is limited due to excessive tool wear or in other words low material removal rate, which makes conventional machining difficult after forging [8,9].

The blasting emergence of Additive Manufacturing (AM) technologies in the past decade seems to address this issue. AM enables near net shape production of complex geometries with very limited tooling and is

* Corresponding author.

** Corresponding author.

E-mail addresses: huhong@changwon.ac.kr (H.-U. Hong), philippe.lours@mines-albi.fr (P. Lours).

leading the 4th industrial revolution as an outstanding alternative to conventional manufacturing methods. Due to its excellent weldability, Alloy 625 is an excellent candidate for the now-well-known Laser Powder Bed Fusion (LPBF) process or otherwise known as Selective Laser Melting (SLM). A large number of studies have addressed different aspects of the fabrication of Alloy 625 by SLM from microstructure optimization to mechanical responses [10–14]. Strength and ductility in particular are critical mechanical properties for structural applications and have therefore been studied accordingly. Yadroitsev et al. studied the effect of processing conditions, in particular specimens orientation, on tensile properties [11]. Hack et al. compared several SLMed Alloy 625 conditions to conventional standards [12]. Marchese et al. studied the effects of various heat treatments and resulting microstructures [13]. Tian et al. recently published a review on Alloy 625 produced by SLM including tensile properties results [14]. Most research agree that additively manufactured Alloy 625 by SLM exhibits strength and elongation properties similar or better than its conventional wrought counterpart, and that these properties strongly depend on the microstructure of the alloy. These studies on tensile properties are however mainly focused on room temperature behavior although this alloy is clearly designed for high temperature applications. High temperature tensile properties are therefore needed to appropriately assess its potential and possibly optimize the performance of the alloy when produced by SLM.

It exists several methods to further enhance the high temperature properties of heat resistant metallic alloys. These include careful optimization of the processing conditions to control defects or rigorously designed heat treatments to command microstructure. Grain Boundary Serration (GBS), characterized by the formation of wavy or zigzag grain boundaries which can be triggered by specifically designed heat treatments, has been found particularly efficient to improve high temperature resistance – creep and crack propagation in particular – of low- γ Ni-based superalloys [15–20]. The authors recently designed a specific continuous heat treatment including slow cooling between solution and aging temperature which successfully led to GBS in a wrought Alloy 625 [21]. This heat treatment was modified to be applied to the alloy produced by SLM considering its peculiar microstructure. The present study consequently describes the elaboration of this GBS heat treatment and compares the resulting high temperature tensile properties in the range 500 °C–700 °C to those of a standard wrought Alloy 625 (Wrought), an as-built (AB) SLMed Alloy 625 and an SLMed Alloy 625 subjected to a solution heat treatment to promote full recrystallization (RX). The results highlight the predominant role of microstructure and outstanding potential of SLMed Alloy 625.

2. Materials and methods

2.1. Raw materials

The wrought Alloy 625 used in this study was a standard hot rolled material with nominal chemical composition Ni–22Cr–9Mo–3Fe–4Nb (in wt.%) and solution treated at 1150 °C/1hr. Gas-atomized Alloy 625 powder suitable for SLM production was provided by the machine manufacturer. The element composition of the powder, Ni–22Cr–9Mo–3Fe–3.5Nb (in wt.%), was close to that of the wrought material and satisfied the standards. Most particles were spherical with a typical size distribution measured with a laser particle size analyzer between $D_{10} = 20 \mu\text{m}$ and $D_{90} = 44 \mu\text{m}$ and an average diameter of 29 μm . Samples were produced with a commercial SLM 125HL machine by SLM Solutions. A stripe scanning strategy with a 33° rotation between layers was used and default optimal parameter conditions for Alloy 625 were utilized (laser power $P = 275 \text{ W}$, scanning speed $v = 760 \text{ mm/s}$, hatching distance $h = 120 \mu\text{m}$ and layer thickness $t = 50 \mu\text{m}$) corresponding to an energy density of $60.3 \text{ J mm}^{-3} \times 10 \times 10 \times 10 \text{ mm}^3$ cubes were produced to analyze the as-built microstructure and to optimize heat treatment conditions. 74 mm long cylindrical specimens with a 15 mm diameter were also produced vertically to be machined into

standard tensile test specimens. With these default processing conditions, the residual porosity measured by microscopy [22] was slightly lower than 0.5%, consisting mainly in small spherical pores from entrapped gas. Among other assets, the SLM process is acclaimed to allow production of nearly fully dense materials. Thorough optimization of the process parameters has led to very low amount of residual porosity well below 0.1% [9,23,24]. Although this was beyond the scope of the presently reported study, this suggests that the SLM fabrication of Alloy 625 may be optimized to reduce further the already very low porosity and consequently enhance mechanical properties.

2.2. Heat treatments

Four Alloy 625 conditions were considered in the present study: *i*) conventionally wrought (Wrought), *ii*) as-built SLMed (AB), *iii*) SLMed followed by a recrystallization heat treatment (RX) and *iv*) SLMed followed by a specifically designed heat treatment for grain boundary serration (GBS). Design of the heat treatments is discussed in detail in section 3.2. The recrystallization heat treatment consisted in heating as-built material to 1200 °C for 1 h followed by air cooling to room temperature to avoid stress build up and possible cracking at higher cooling rate such as for water quenching. The grain boundary serration heat treatment consisted in heating as-built material to the higher temperature of 1300 °C for 90 min followed by slow cooling at the controlled cooling rate of 5 °C/min down to the aging temperature of 870 °C at which the material was maintained for 2 h before air cooling to room temperature. All heat treatments were conducted in air using a Marshall box furnace equipped with a programmable controller to precisely control temperature, time and cooling rate.

2.3. Tensile tests

Specimens for tensile tests were prepared by machining to standard round shape with a gauge length of $25 \pm 0.1 \text{ mm}$ and a diameter of $6.0 \pm 0.1 \text{ mm}$ [25]. The tensile direction was parallel to the building direction (z direction) for the SLMed materials and parallel to the rolling direction for the wrought material. All four material conditions were tested at room temperature, 500 °C, 600 °C and 700 °C using a cross-head speed of 1.5 mm/min (strain rate of $1 \times 10^{-3} \text{ s}^{-1}$) for room temperature and of 0.5 mm/min (strain rate of $3.3 \times 10^{-4} \text{ s}^{-1}$) for high temperatures, respectively. An electromechanical tensile test machine was used for all measures (MTDI, UT100F, 10 tonf). The temperature was raised to the test temperature by a sealed furnace at 30 °C/min and a 30 min soak time was considered for homogeneity and stability. Although only one result was considered for each condition, all tensile tests were repeated twice and no significant difference was noticed. It should be noted that the values of yield strength (YS in Fig. 5) were carefully measured according to the $R_{p0.2}$ method [25], which is often challenging at high temperatures. The reported values are therefore approximations with a confidence of about $\pm 3 \text{ MPa}$.

2.4. Microstructure analysis

Specimens for microstructure analyses were sectioned, hot mounted in phenolic resin and conventionally ground with SiC abrasive papers followed by sequential polishing with diamond paste down to 1 μm . The microstructure was revealed by means of a 100 ml HCl + 0.5 g CrO₃ etching solution and investigated by optical microscopy (OM, OLYMPUS BX51 M) and Scanning Electron Microscopy (SEM, JSM-6510) equipped with energy dispersion X-ray spectroscopy (EDS). Electron backscattering diffraction (EBSD) with a field-emission scanning electron microscope (FE-SEM, MIRA-II) was carried to evaluate grain size in particular. To avoid artifacts from metallographic preparation, the final 1 μm polishing step was carried out using a colloidal silica suspension. Electron probe micro-analysis (EPMA, CAMECA SX-100) was also carried out prior to etching in order to investigate the element distribution

and highlight segregation in the AB material. Specimens for transmission electron microscopy (TEM, field-emission type JEOL JEM-2100F operating at 200 kV) equipped with Energy Dispersive X-ray Spectroscopy (EDS) were extracted from the vicinity of the fracture surface after tensile test at 700 °C and from the AB material. Thin foils were prepared by fine grinding and polishing to a thickness of approximately 200 µm, punching of 3 mm diameter discs and electropolishing to perforation with a 200 ml perchloric acid + 800 ml methanol solution at -26 °C ~ -28 °C using a jet polisher (Struers TenuPol-5) operating at 50 mA and 25 V.

3. Results and discussion

3.1. Initial microstructure of raw materials

The microstructure of the conventional solutionized wrought material is shown in Fig. 1 (a) and (b). It consisted in a fine fully-recrystallized equiaxed microstructure, with a grain size measured by electron back-scattered diffraction (EBSD) of approximately 130 µm and primary Nb-rich MC carbides precipitated during solidification and often distributed along the rolling direction. This was typical of the standard wrought Alloy 625 characterized by a single phase FCC γ-matrix where alloying elements are homogeneously distributed in solid solution and no other phase other than primary MC carbides are detected. A corresponding hardness value of 206 Hv was measured.

The microstructure of the as-built material produced by SLM (hereafter referred to as AB), in Fig. 1 (c) and (d), was characterized by a very fine cellular/dendritic structure with grains intercepting several melt pools elongated along the building direction. This peculiar microstructure is typical of alloys produced by AM powder bed fusion processes such as SLM. As the high energy laser beam travels over a layer of powder deposited according to the layer-by-layer production sequence, the high heat input not only causes local melting of the powder but also partial remelting of the underlying consolidated material. As a result, solidification as the laser beam moves away proceeds in the opposite direction of the heat transfer. Furthermore, due to the partial remelting of the underlying material, grains formation is characterized by epitaxial

solidification therefore leading to the observed textured microstructure, often referred to as columnar, where grains intercept several melt pools despite the interrupted solidification process. The very fine cellular/dendritic structure is the result of the very high solidification rate due to the rapid scanning of the laser beam (here 760 mm/s). The inset in Fig. 1 (d) highlights this very fine cellular/dendritic structure. The cooling rate ϵ_c can be calculated as a function of the primary dendrite arm spacing λ_1 , which was systematically measured between approximately 0.7 and 2 µm in several locations. The following equation (1) is generally accepted [10,26-33]:

$$\lambda_1 = a \times \epsilon_c^{-n} \tag{1}$$

where λ_1 is the primary dendrite arm spacing in µm and ϵ_c is cooling rate in °C/s. The constants a and n are materials constants and their values are not clearly available from the current literature for Alloy 625 [26-33]. Nevertheless, computations gave an approximation of the cooling rate of 10^5 - 10^6 °C/s, which is consistent to reported values for SLM [10,13,26-28,34]. The either cellular or dendritic nature of the microstructure is still debated. It has been clearly established that the SLM process occurs under rapid solidification conditions, as just demonstrated. Moreover, it seems clear from the microstructure and it was otherwise confirmed that the cooling rate in SLM is not constant [35]. It becomes a common opinion that the inconsistent rapid solidification taking place during SLM processing oscillates between the formation of high velocity cells and fine dendrites, as both microstructural features are often observed.

The rapidly solidified AB microstructure is also characterized by inhomogeneous distribution of the constituting elements of Alloy 625. Fig. 2 shows the EPMA results clearly highlighting significant segregation of Nb and C, and to a lesser extent Mo, within the intercellular/interdendritic regions. As it is clear from the contrast in SEM micrographs (Fig. 1(d)), the heavily segregated microstructure of multi-constituent alloys produced by SLM and in particular Alloy 625 has been often reported. In particular, it was found that such segregation modifies the precipitation behavior of Alloy 625. Marchese et al. [13] for example observed inhomogeneous precipitation of the γ' -Ni₃Nb phase after direct aging in absence of a solutionizing step, which was attributed to

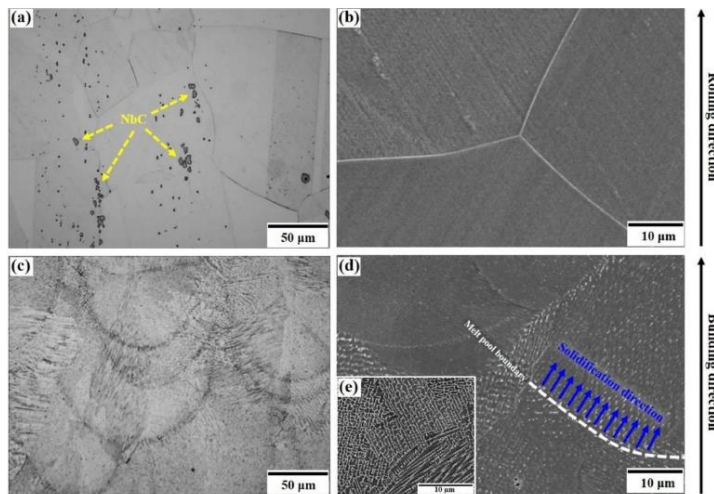


Fig. 1. Micrographs showing the (a) OM and (b) SEM microstructure of the conventional wrought Alloy 625 (Wrought); and the (c) OM and (d) SEM microstructure of the as-built (AB) Alloy 625 produced by SLM.

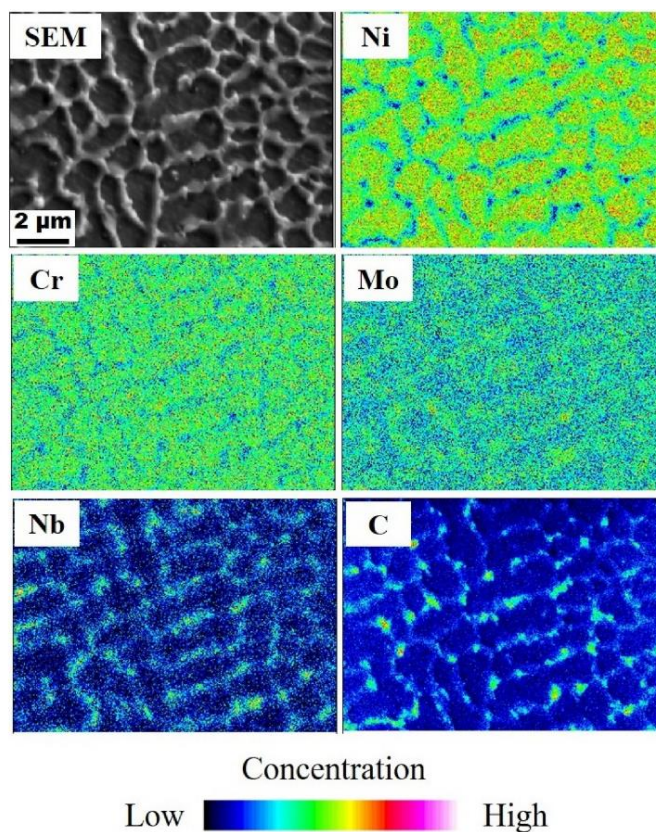


Fig. 2. EPMA maps of the AB material indicating segregation of Nb and C within intercellular/interdendritic regions.

the inhomogeneous distribution of Nb. Lindwall et al. [34,35] used simulation tools to model segregation and explain in particular the more rapid precipitation kinetics of the δ -phase with respect to wrought Alloy 625.

The finer features of the typical AB microstructure were evidenced by the high magnification TEM micrographs in Fig. 3. The microstructure was characterized by the very fine cellular/dendritic structure exhibiting high dislocations density particularly within the interdendritic areas and the presence of very fine precipitates with a size ≤ 50 nm. A corresponding hardness value of 314 Hv was measured, much higher than that of its wrought counterpart. The high density of dislocations is indicative of accommodation for residual thermal stress due to the rapid cooling and heating cycles inherent to the SLM process and illustrates the high levels of residual stress. So much so that average misorientation maps obtained by EBSD have often been used to evaluate, to some extent, residual stress in materials built by SLM [36]. Fine precipitation similar to that observed in Fig. 3 (a) and 3(b) has been previously reported [7,13,14,23,27,34]. These precipitates are primarily aligned along intercellular/interdendritic areas (Fig. 3(b)) due to significant segregation of Nb and C as previously mentioned (Fig. 2), though precipitation within cellular/dendritic cores has also been observed as pointed by arrows in Fig. 3(a). Evidenced by the selective

area diffraction pattern (SADP) in Fig. 3(c), these coherent NbC carbides formed during solidification by the eutectic reaction $L \rightarrow \gamma + MC$. Although this reaction essentially takes place within intercellular/interdendritic regions, the very high cooling rate characteristic of SLM processing promotes solute trapping within cellular/dendritic cores thereby advocating the presence of the fine NbCs. Their coherency with the γ -matrix was confirmed by SADP showing the orientation relationship defined by $\{200\}_{NbC} // \{200\}_{\gamma\text{-matrix}}$, $[001]_{NbC} // [001]_{\gamma\text{-matrix}}$.

3.2. Design of heat treatments and resulting microstructures

3.2.1. Recrystallization heat treatment (RX)

In the attempt to enhance the mechanical behavior of Alloy 625 produced by SLM, two heat treatments were specifically designed to convert the highly segregated, textured and constrained AB microstructure (section 3.1) into a more homogeneous recrystallized microstructure for high temperature applications. The first heat treatment was defined as the recrystallization heat treatment (hereafter referred to as RX) and was an attempt to produce microstructural features resembling those of the conventional wrought and solutionized microstructure (Fig. 1(a) and (b)). For SLM processed materials, it is often found that recrystallization can be promoted by a sole heat treatment step at high

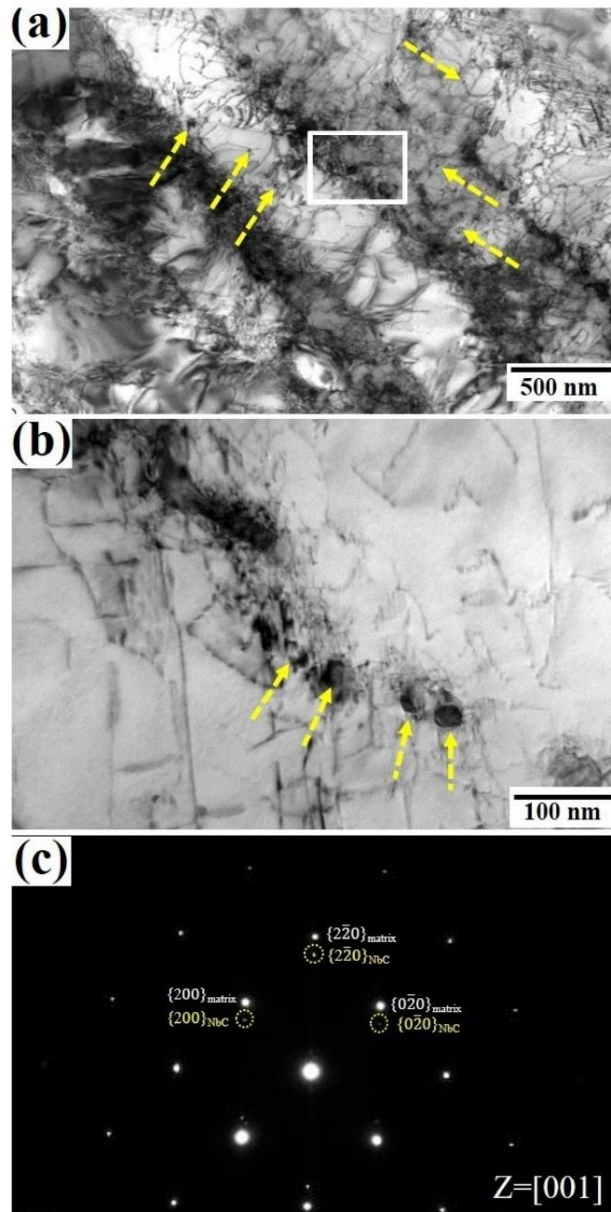


Fig. 3. TEM micrographs of the AB material: (a) high magnification showing high dislocations density and intracellular/intradendritic precipitation of NbC carbides (arrows) and (b) details of the squared region in (a) highlighting intercellular/interdendritic precipitation of NbC carbides within intercellular/interdendritic regions (arrows). SADP in (c) demonstrates the coherency of NbC with the γ -matrix ($\{200\}_{NbC} // \{200\}_{\gamma\text{-matrix}}$, $[001]_{NbC} // [001]_{\gamma\text{-matrix}}$).

enough temperature, in absence of any mechanical operation such as cold or hot working and without the assistance of hot isostatic pressing [36]. This may be attributed to the high density of dislocations discussed previously (Fig. 3(a)), a sign of the high energy stored within the AB material. Accordingly, the recrystallization temperature range typically corresponds to the usual solution temperature range. Recrystallization of Alloy 625 produced by SLM has been reported in several studies after solution treatments between 1100 °C and 1250 °C for 0.5–2 h [13,14,36,37]. In the present investigation, the RX heat treatment consisted in a solution treatment at 1200 °C for 1 h, followed by air cooling to room temperature (Fig. 4(a)).

The resulting microstructure is displayed in Fig. 4(b) and (c). The RX material exhibited fully recrystallized equiaxed grains with an approximate grain size of 80 μm , significantly lower than that of the wrought material (130 μm). The micrographs in Fig. 4(b) and (c) clearly highlighted the large amount of fine globular precipitates all over the material. A large amount of submicrometer particles appeared to be homogeneously distributed within the γ -matrix (solid blue arrows), together with relatively larger particles with a size $\leq 3 \mu\text{m}$ (dashed yellow arrows). The larger particles, within the SEM-EDS detection range, were clearly identified as NbC carbides. Although the finer precipitates could not be definitely identified and require finer analyses, all evidences point to the conclusion that these were also fine NbC particles. According to the standard TTT diagram for Alloy 625 [3], the temperature of 1200 °C is well over the precipitation range of MC particles. Primary NbC formed during solidification are however consistently observed and the start precipitation temperature reported for Alloy 625, promoted by the rather high Nb content, is 1250 °C [38]. This is consistent with the very fine NbC carbides precipitation clearly observed within the AB material (Fig. 3). It is therefore reasonable to assume that the temperature of 1200 °C is not sufficient to dissolve the primary NbC carbides which not only remained after solutionizing for 1 h but also seemed to coarsen (Fig. 4(c), dashed yellow arrows). However, regarding the finer MC precipitated (solid blue arrows), it is not clear whether they resulted from the nucleation of secondary MC carbides or only from coalescence of the very fine primary carbides of the AB condition. Similar NbC precipitates have been reported in Alloy 625 produced by SLM and submitted to solution treatments [13,14,27]. There was no evidence of precipitation of any other phase in the RX material. A corresponding hardness value of 231 Hv was measured, 26% lower

compared to the AB state but slightly larger than that of the Wrought sample.

3.2.2. Grain boundary serration heat treatment (GBS)

The second heat treatment was specifically designed for promoting grain boundary serration, hereafter referred to as GBS. As mentioned in introduction, grain boundary serration is an effective way to strengthen grain boundaries and consequently enhance properties such as creep and crack propagation resistance of solution strengthened Ni-based superalloys at high temperature [15–20]. While the beneficial outcome is not debated, opinions diverge on the driving force and the mechanism for the formation of serrated grain boundaries. Several models describe this phenomenon as an interaction between grain boundary precipitates and grain boundary motion [39–41]. This is however in contradiction with some of our more recent observations where serrated grain boundaries developed spontaneously prior to the formation of precipitates [17,18,42–47]. Moreover, the authors recently reported the occurrence of grain boundary serration in a Ni–20Cr model alloy inherently devoid of any second phase [48]. Observations led to the conclusion that grain boundaries may spontaneously assume a serrated morphology, promoted by lattice strain energy built up in their vicinity as a result of solute diffusion and segregation during slow cooling from solution to aging temperatures, in order to decrease their energy by accommodating the misorientation between adjacent grains [44,49,50]. This model was defined as the strain-induced grain boundary serration model. Based on this model, the authors have reported the possibility to induce grain boundary serration in a wrought Alloy 625 similar to the conventional wrought material used for comparison in the present investigation [21].

The GBS heat treatment presently carried out following the production of Alloy 625 by SLM consisted in a solution treatment at 1300 °C for 90 min followed by slow furnace cooling with a controlled cooling rate of 5 °C/min down to an aging temperature of 870 °C hold for 2 h before air cooling to room temperature (Fig. 4(d)). This differed from the serration heat treatment designed for wrought Alloy 625 [21] (solutionizing at 1250 °C for 30 min, slow cooling at 5 °C/min and aging at 800 °C for 2 h), as a result of the peculiar microstructure of the AB material described in section 3.1. The temperature of the solution step was raised to 1300 °C in order to dissolve as much as possible the numerous primary NbC particles present in the AB material (Fig. 3) and

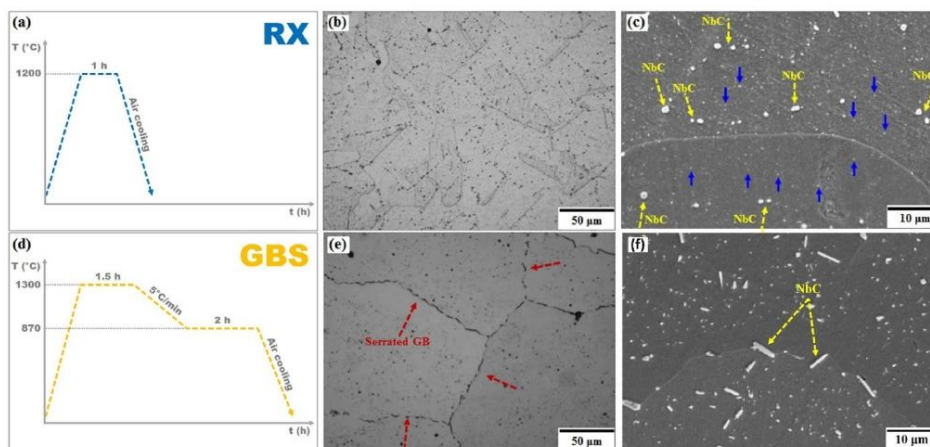


Fig. 4. Schematic diagram of the (a) recrystallization (RX) heat treatment and (d) grain boundary serration (GBS) heat treatment. Micrographs showing the (b) OM and (c) SEM microstructure of the RX Alloy 625; and the (e) OM and (f) SEM microstructure of the GBS Alloy 625.

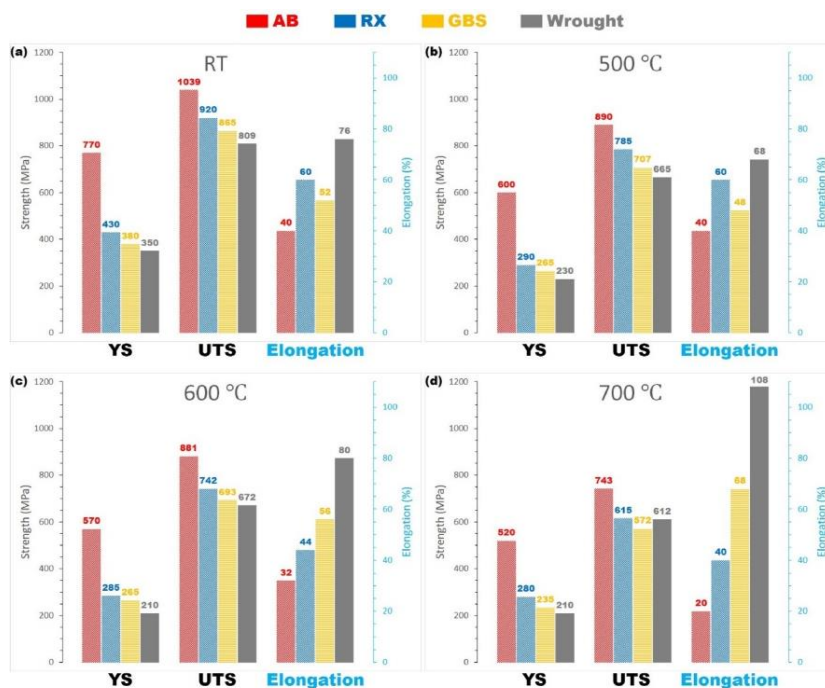


Fig. 5. Yield strength (YS), ultimate tensile strength (UTS) and elongation at break for AB, RX, GBS and wrought materials tested in tension at room temperature (a) RT, (b) 500 °C, (c) 600 °C and (d) 700 °C.

to maximize recrystallized grain boundary motion during slow cooling. Due to the highly segregated nature of the materials produced by SLM, this high solution temperature was also necessary to ensure homogeneous distribution of the alloying elements (Nb, Cr and C in particular) in solid solution within the γ -matrix. For similar considerations, the solutioning time was extended to allow for better dissolution yet short enough to avoid severe grain growth. It should be noted that this high temperature of 1300 °C is slightly above the commonly reported solidus temperature of 1290 °C for Alloy 625 [51,52], which may therefore induce detrimental local melting though it was not evidenced here. Investigation is in progress to optimize the GBS treatment and in particular to reduce the solution treatment temperature below 1285 °C. The slow cooling rate, here 5 °C/min, is considered for the formation of serrated grain boundaries. According to the strain-induced grain boundary serration model, the slow cooling step allows for solutes to diffuse and segregate to grain boundaries as their solubility decreases with decreasing temperature. The discontinuous segregation in the vicinity of the grain boundary and the corresponding lattice strain energy generated is considered responsible for said grain boundary segments to migrate. The temperature of the following aging step corresponds to the stabilization temperature of a NiCrAlY bond coat system which was successfully deposited by SLM on a similar AB Alloy 625 substrate produced by SLM in a concomitant study [53]. Although this temperature of 870 °C lies within all carbides precipitation temperature range according to the equilibrium TTT diagram of Alloy 625 [3], only NbC carbides consuming most of the available C could be expected due to the prior slow cooling step of the GBS heat treatment. According to the

suggested revision of the TTT diagram for Alloy 625 produced by SLM proposed by Lindwall et al. [34], precipitation of the δ -phase may be expected after hold at 870 °C for 2 h. However, their calculations did not take into consideration a preceding solution step.

The resulting GBS microstructure is displayed in Fig. 4(e) and (f). The GBS material exhibited a fully recrystallized microstructure with equiaxed grains of approximate size of 130 μm , similar to the conventional wrought Alloy 625. The general criterion for considering grain boundaries serrated is a minimum amplitude of 0.5 μm . The OM micrograph in Fig. 4(e) clearly shows serrated grain boundaries which indicates that the specifically designed GBS heat treatment was successful (dashed red arrows). As much as 80% of grain boundaries of the GBS material were serrated. The presence of a relatively large amount of precipitates was also observed (Fig. 4(e) and (f)). SEM-EDS analyses revealed that all precipitates were NbC carbides and no other phase was detected. As highlighted by the SEM micrograph in Fig. 4(f), these NbC carbides exhibited a bimodal size distribution similar to that of the RX material. However, their size was clearly larger and rod-shaped precipitates were observed in the GBS material, as opposed to the globular precipitates of the RX material. A significantly higher amount of intergranular carbides was also detected. Also highlighted in Fig. 4(f) was the presence of precipitate-free zones (PFZ) as wide as 5 μm in the vicinity of grain boundaries. PFZ are often observed due to heterogeneous precipitation at grain boundaries. This indicates the anticipated diffusion of solute atoms in solid solution towards grain boundaries to form precipitates, as described in the above-mentioned strain-induced grain boundary serration model briefly described. The hardness of the GBS material was

measured at 231 Hv, which is in line with the value obtained for the RX material. This indicates in particular that nano-size γ'' had not precipitated, as expected for this temperature.

3.3. Tensile properties

3.3.1. Strength and ductility

As discussed in the previous section, the microstructures of the four different Alloy 625 materials were significantly different as a result of different processing routes and heat treatments. In consequence, their mechanical behavior were also significantly impacted. Standard tensile tests were carried on all materials at room temperature (RT), 500 °C, 600 °C and 700 °C which constitute the typical temperature range for Alloy 625 applications. The results are detailed in Fig. 5 as bar charts in order to appreciate and compare tensile properties. It should be noted that the values of elongation in Fig. 5, or ductility, were measured after fracture considering the final gauge length of the test specimens. General

trends clearly emerge in Fig. 5 as follow: strength values, both yield strength and ultimate tensile strength, ranked in decreasing order from the highest for the AB followed by RX, GBS and the lowest for the conventional wrought material at all temperatures considered (only exception for UTS at 700 °C). With regards to ductility, the AB material always exhibited the lowest ductility while the conventional wrought material recorded the highest values and RX and GBS materials had similar intermediate ductility. At higher temperatures however, GBS exhibited significantly higher ductility. These behaviors correlated properly with the different microstructures. As highlighted in Fig. 3, the AB material was characterized by a very high density of dislocations, due to high residual stress as a result of SLM processing, which therefore greatly enhances strength, yield strength in particular, at the expense of ductility due to a limited dislocation activity. On the contrary, the fully recrystallized microstructure of the conventional solutionized wrought alloy 625 characterized by relatively coarser grain size and relatively low amount of precipitation (Fig. 1(a) and (b)) promotes ductility, by far

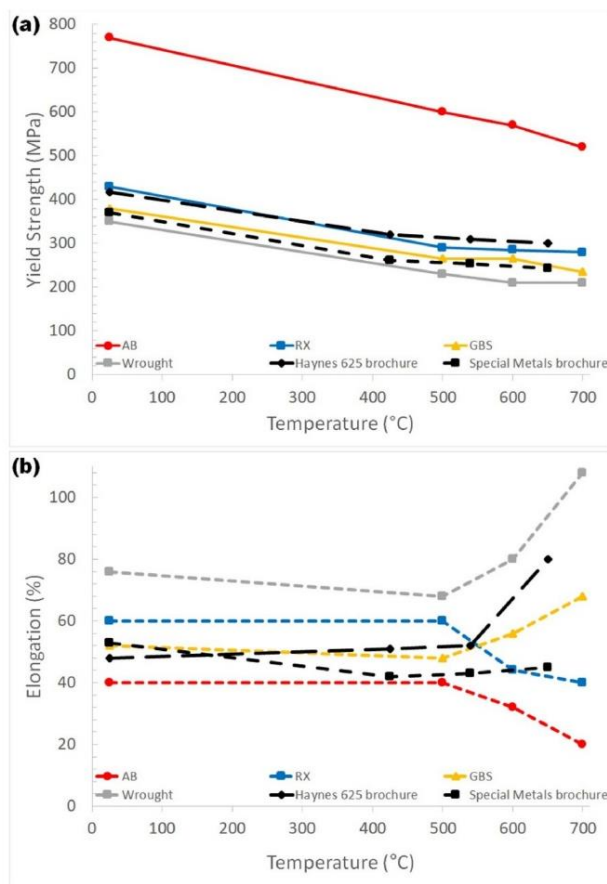


Fig. 6. (a) Yield strength and (b) ductility as a function of temperature for AB (red circles ●), RX (blue squares ■), GBS (orange triangles ▲) and Wrought (grey squares ■). Reference values for a hot-rolled mill-annealed plate (Haynes 265 brochure ◆ [51]) and an hot-rolled solutionized rod (Special Metals brochure ■ [52]). (For interpretation of the references to colour in this figure legend, the reader is referred to the Web version of this article.)

the largest of all samples, yet strength levels remain relatively high due to high levels of solid solution strengthening. Both RX and GBS in Fig. 4 exhibited fully recrystallized equiaxed grains and relatively high amount of precipitation of NbC carbides which are effective barriers to dislocation motion. RX had a smaller grain size as well as finer and more homogeneously distributed carbides which is consistent with higher strength values. In addition, it can be assumed that the coarsening of NbC in the GBS sample, by consuming Nb solute atoms, could also have led to a slight decrease in the solid strengthening of the γ matrix.

Fig. 6 highlights the yield strength and ductility of all four materials as functions of the temperature and shows clearly the above-mentioned trend. The AB material possessed much higher yield strength, decreasing as temperature increased (Fig. 6(a)). RX, GBS and wrought alloys, in decreasing order, exhibited appropriate values of strength, with reasonably constant values at elevated temperatures well over 200 MPa. The values of elongation at break in Fig. 6(b) highlighted a notable feature. While the ductility of the conventional wrought material typically increased with temperature to values over 100% deformation at higher temperatures, the ductility of the AB and RX materials produced by SLM decreased as temperature increased. The loss of ductility between 500 °C and 700 °C was as high as 24% and 28% for AB and RX, respectively. On the contrary, although the GBS alloy also showed a moderate loss in ductility at 500 °C, ductility increased similarly to wrought at 600 °C and 700 °C. This effect could be attributed in part to grain boundary strengthening and therefore resistance to grain boundary crack propagation induced by serrated grain boundaries [18–20,42, 43]. The reasons for the observed decreasing ductility for AB and RX as temperature increased are however not clear and necessitate further attention [54]. Kreitzberg et al. [37] observed similar embrittlement at elevated temperature and attributed the phenomenon to grain boundary carbides.

3.3.2. Fracture behavior

Fig. 7 show cross section micrographs illustrating the cracking behavior of all four alloys upon fracture under tension at high temperatures (500 °C–700 °C). For the conventional solutionized Wrought alloy, cracks initiated at the interface between the γ -matrix and NbC

particles at 500 °C and 600 °C, while grain boundary cracking was observed in the highly deformed alloy at 700 °C. For all temperatures, the AB alloy exhibited cracking primarily at melt pool boundaries characterized by higher solute concentration due to the solidification sequence and relatively coarser submicrometer cellular/dendritic structure. Stress concentration at melt pool boundaries and triple junctions is detrimental to mechanical properties. The cracking behaviors of RX and GBS alloys were similar to each other, exhibiting primarily cracks initiation and propagation at grain boundaries particularly in correspondence to grain boundary precipitates. The severity and frequency of cracking were observed to increase with temperature, for all four materials. It was clear however that the RX and GBS alloys were characterized by relatively weaker grain boundaries compared to grain interiors. Their microstructure exhibited equiaxed grains with little signs of plastic deformation (as opposed to their wrought counterpart for example) and grain boundaries were clearly responsible for fracture. It should also be noted that while cracks initiation and propagation was relatively easy for RX, grain boundaries in the GBS alloy were clearly more resistant to cracking as it can be inferred from the more isolated cracks occurring at a lower frequency. As mentioned in introduction, this resistance to grain boundary cracking at high temperature is one of the positive outcome of grain boundary serration [18–20,42,43]. The very high elongation at 700 °C for wrought was characterized by largely elongated grains in Fig. 7(l). On the other hand, lower deformation levels were recorded in the materials produced by SLM. The significant presence of fine NbC particles in all three AB, RX and GBS materials disrupts the accommodation mechanism relieving stress as extrinsic dislocations move along grain boundaries [55].

3.3.3. Plastic behavior

The tensile properties, strength in particular, of the additively manufactured materials were superior in all the cases when compared to their conventional wrought counterpart as it was highlighted in the previous section 3.3.1. Tensile tests at high temperature also revealed striking differences regarding the plastic deformation behaviors at high temperatures of the alloys under consideration. Fig. 8 shows the details of the True Stress σ_t vs. True Strain ϵ_t curves within the 0–20%

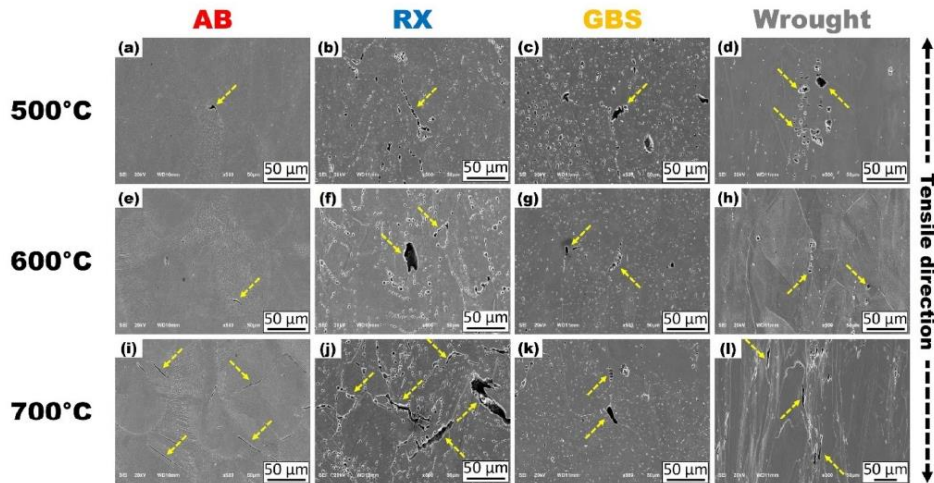


Fig. 7. SEM micrographs showing cracking (dashed yellow arrows) in the vicinity of fracture after tension at 500 °C, 600 °C and 700 °C for as-built (AB), recrystallized (RX), serrated (GBS) and wrought alloys. (For interpretation of the references to colour in this figure legend, the reader is referred to the Web version of this article.)

deformation range for all four materials at 500, 600 and 700 °C. The values σ_r and ϵ_r were calculated from the measured engineering values σ_e and ϵ_e according to the well-known equations $\sigma_r = \sigma_e(1 + \epsilon_e)$ and $\epsilon_r = \ln(1 + \epsilon_e)$, which are widely considered valid before the onset of necking [56]. In Fig. 9, the plastic behaviors of the four materials are clearly different with consideration to dynamic strain aging (DSA) manifested by serrated plastic flow. DSA is a well-known phenomenon occurring at specific strain rate and temperature ranges, attributed to interactions between mobile dislocations and diffusing solute atoms, observed in several steels, aluminum alloys and nickel-based alloys including Alloy 625. DSA is particularly detrimental for structural applications during operation at high temperatures as it leads to localized deformation and reduces fatigue properties.

DSA-induced serrations have been identified into several different types, in particular types A, B and C [57]. Type A serrations are periodic serrations characterized by a sudden rise followed by a drop to or below the general level of the stress-strain curve. These are considered as locking serrations where diffusion of solute atoms to mobile dislocations momentarily inhibit slip (locking) followed by unlocking of these mobile dislocations as they free from the solute atmosphere, leading to continuous deformation bands propagation within the specimen. Type B serrations are characterized by high frequency oscillations around the general level of the stress-strain curve. Incessant locking and unlocking of mobile dislocations within deformation bands due to high mobility of solute atoms lead to discontinuous band propagation. Type C serrations are yield drops below the general level of the stress-strain curve, in absence of momentary hardening. As a result, these are considered to be due to dislocation unlocking. For all three types of serration due to DSA, although interactions between diffusing atoms in solution and mobile dislocations play an important role, the mobility of dislocations itself may not be discounted. As described earlier in the present paper, the microstructures of the materials under consideration are significantly different as a result of the different processing routes and heat treatments with regards to dislocation density, segregation, grains structure and precipitation. Although further analysis is needed, such as tensile tests at different strain rate to evaluate strain rate sensitivity and fine microstructural analyses, the different plastic behaviors exhibited in Fig. 8 should be briefly discussed despite the lack of evidence to elucidate mechanisms.

In an attempt to appropriately compare the plastic behaviors and highlight differences, the flow curves for each alloy were quantified in Table 1. The critical strain ϵ_c for the onset of serration was considered as well as the amplitude $\Delta\sigma$ and wavelength $\Delta\epsilon$ of serrations. The flow curves were analyzed separately between strains of 0–10% and 10–20% to acknowledge arbitrarily early plastic deformation and steady-state regime, respectively. At 500 °C all materials exhibited a serrated plastic flow, a manifestation of DSA in particular with Type C serrations of significant amplitude. While the AB material exhibited the most severe serrations with the largest amplitude (as high as 30 MPa) and increasing frequency as deformation proceeded, the onset of DSA ϵ_c was clearly higher. Although evidence is needed to support this assumption, this may possibly be attributed to a significantly lower density of mobile dislocations due to the very high density of tangled dislocations typical of the AB microstructure as described in section 3.1. The conventional wrought material, despite showing serrations in the flow curve, appeared more stable at 500 °C during plastic deformation with serration of lower amplitude.

At 600 °C and 700 °C however, while the conventional wrought Alloy 625 exhibited significant flow stress irregularities characterized in particular by frequent Type C serrations with load drops often larger than 15 MPa, plasticity of the SLMed materials subjected or not to heat treatment was clearly more consistent. Recently, Beese et al. [58] reported for the first time the absence of DSA at 600 °C and 700 °C in Alloy 625 produced by means of an additive manufacturing (AM) process. There are notable differences with the alloys in the present study, specifically their alloys were produced by laser-based directed energy

deposition instead of powder bed fusion, and their specimens were tested in compression instead of tension. Nevertheless, the microstructure was similar due to comparable rapid solidification and heat cycles during processing, the strain rates were of the same order as presently applied and their conventionally processed wrought reference alloy exhibited similar behavior with Type C serrations with similar amplitude. Beese et al. [58] attributed the absence of serration in the AMed material to two phenomena: the typical crystallographic texture and the peculiar AM microstructure. The latter is particularly characterized by fine closely-spaced secondary phases such as NbC acting as effective sinks for carbon atoms in solution, thus preventing the formation of a carbon atmosphere around mobile dislocations. Our results presented in Fig. 8 however raise a number of questions with regards to the model put forward in their study. In Fig. 8 and Table 1, although much reduced at elevated temperatures of 600 °C and 700 °C, the AB material did show signs of serrated plastic flow, specifically Type A/B of low amplitude and events of Type C. More importantly, the effects of heat treatments for the RX and GBS materials seem contradictory. Beese et al. [58] claimed that subjecting the AMed alloy to heat treatment at high temperature to dissolve to some extent secondary phases led to the appearance of DSA-induced serrated flow in the plastic region, although it is not all that clear and the conclusiveness may be argued. Kreitzberg et al. [37] also evidenced unstable plastic flow at high temperatures for heat treated Alloy 625 specimens produced by SLM, however it was unfortunately not acknowledged in their paper. For the present RX materials in Fig. 8, which experienced full recrystallization and significant dissolution of the finer secondary phases, Type C serrations with relatively large amplitude and frequency were observed at 600 °C only over a short range of deformation followed by smooth deformation and later very low amplitude Type A/B serrations. The RX material only displayed very low amplitude Type A/B serrations at 700 °C, punctuated by two Type C events. More strikingly, the SLMed material subjected to the GBS heat treatment did not exhibit any sign of serrations of the plastic flow curve at either 600 or 700 °C. Plastic deformation of the GBS material was smooth and consistent, with no macroscopic sign of DSA, which greatly differ from its conventional wrought counterpart.

The scope of the present paper is not to address in details the phenomenon/a responsible for serrated plastic flow at high temperatures and low strain rates in Alloy 625. As previously mentioned, further analyses are required to propose more than the following conjectures. Serrated plastic flow is one of the most important manifestations of DSA, characterized by interactions between mobile dislocations and diffusing solute atoms. Due to the significantly different microstructures as a result of different processing conditions and heat treatments, these interactions may vary widely. The conventional wrought alloy is characterized by an equiaxed microstructure with carbides (Fig. 1 (a) and (b)). The relatively coarse carbides and relatively homogeneous distribution of alloying elements in solution, carbon in particular, allow for the formation of carbon atmospheres around mobile dislocations. By contrast, as suggested by Beese et al. [58], the highly segregated microstructure of the AB alloy with closely spaced finer carbides (Figs. 2 and 3) may prevent the formation of the carbon atmosphere due to the competition between the diffusion of carbon atoms in solution towards mobile dislocations and the sink effect of carbides temporarily arresting the dislocations motion. The model however does not address the much higher dislocation density (Fig. 3(a)) which clearly impedes dislocation motion as evidenced by the much higher strength and lower ductility. The RX alloy was fully recrystallized due to the high residual stress characteristic of SLM and evidenced by the aforementioned high dislocation density. However, despite the solution step at high temperature, the microstructure is characterized by significant precipitation of closely spaced and very fine carbides (Fig. 4 (b) and (c)). Similarly to the AB material, this may result in lower propensity to DSA. The GBS alloy exhibited clearly smooth flow curves above 600 °C with no sign of load drops. This may be explained by full recrystallization, significant dissolution of secondary phases and homogenization during the high

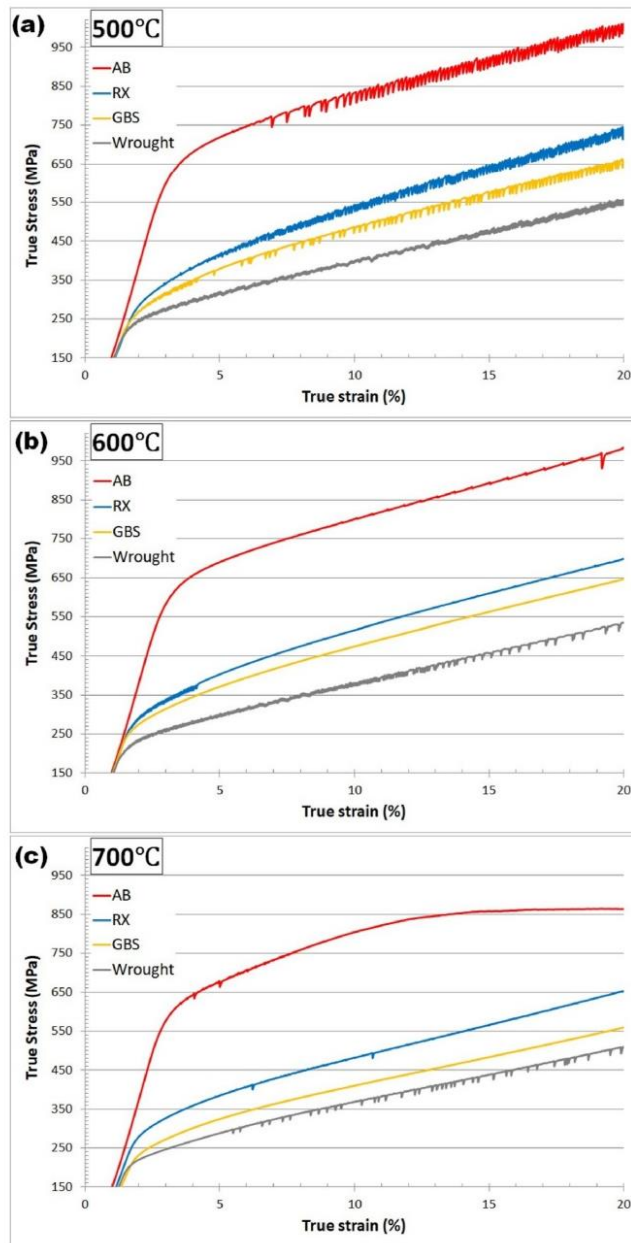


Fig. 8. True Stress - True Strain curves up to 20% elongation for AB, RX, GBS and Wrought materials in tension at (a) 500 °C, (b) 600 °C and (c) 700 °C.

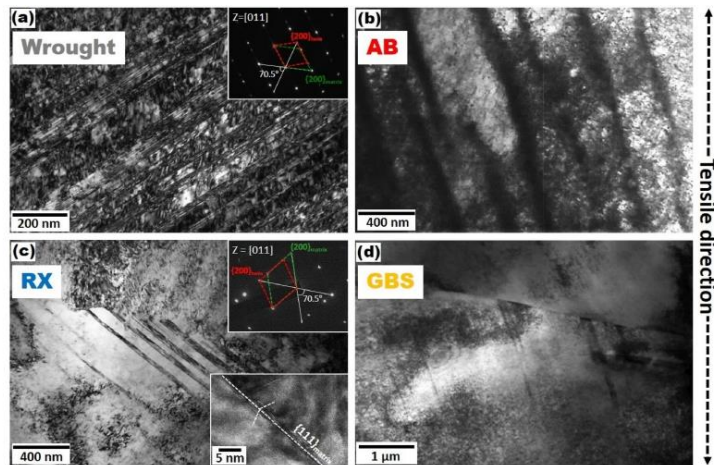


Fig. 9. TEM micrographs in the vicinity of the fracture surface after tensile test at 700 °C for (a) the conventional wrought alloy showing micro-twins, (b) the AB material showing high density of tangled dislocations especially within interdendritic/intercellular regions, (c) RX and (d) GBS alloys low density of micro-twins.

temperature solution step together with relatively dense precipitation of carbides during slow cooling and subsequent aging. As previously discussed, the diffusion of alloying elements in solution to grain boundaries during slow cooling and aging (C, Cr and Nb in particular) is believed essential to produce serrated grain boundaries. As a result, it can be expected that only a very low amount of C remained in solution in the GBS alloy and the formation of a carbon atmosphere around mobile dislocations during tension was therefore hindered, in turns preventing DSA.

While DSA certainly plays an important role to rationalize the different aspect of the stress-strain curve in the plastic region of the materials presently under consideration, other factors of deformation may not be discarded. Several additional causes have been identified to lead to serrations in the flow curve, including in particular continual mechanical twinning [57]. Fig. 9 shows TEM micrographs representative of the microstructure in the vicinity of the fracture surface for the alloys after rupture at 700 °C. The TEM micrograph of the conventional wrought Alloy 625 in Fig. 9(a) exhibits high density of micro-twins as evidenced by the selective area diffraction pattern (SADP). The {200} plane of micro-twins had a 70.5° tilted angle with the {200} plane of the γ -matrix. Micro-twin formation during plastic deformation is promoted by lower stacking fault energy (SFE) in Ni-based superalloys, which is the lowest around 700 °C depending on the element composition of the alloy. Lower SFE stimulates pairing of partial dislocations with perfect dislocations, which forms large dislocation pile-up and in turn leads to micro-twinning. By contrast, TEM micrographs of the AB show no evidence of micro-twins formation. The AB material exhibited high density of tangled dislocation, primarily within interdendritic/intercellular regions (Fig. 9(b)). RX and GBS materials in Fig. 9(c) and (d), respectively, exhibited planar deformation features. SADP confirmed these were micro-twins (insert in Fig. 9(c)).

The evidence provided in the present report are not sufficient to discuss in details the deformation behavior of the materials under consideration. Interrupted tests and thorough microstructural analyses are required to contemplate conclusive mechanisms. Behjati and Asgari [59] interestingly proposed a sequence of mechanisms as deformation proceed to account for similar planar arrangement of dislocations. Despite significantly different conditions – drawn 625 rods solutionized and annealed, tests in compression at room temperature – their

observations suggested competitive contribution to strain hardening between cross-slip and Lomer-Cottrell (LC) locks, followed by deformation twinning at large strains. To the credit of their method, the strain hardening rates were calculated as a function of the true strain. It should be noted that due to noisy signals at high temperatures, the calculated values of true stress and true strain were smoothed over a range of about 0.3% in deformation to reduce noise while maintaining information. It should also be noted that low confidence may only be available in the presented values at large strains, beyond necking. The results are presented in Fig. 10 as transparent calculated values to highlight variations and approximate trends in dotted lines.

The large and frequent variations clearly observed in calculated transparent values in Fig. 10 correspond to instability or the so-called serrated plastic flow discussed earlier. In this regard it is clear that while all four materials exhibited relatively large variations at 500 °C (Fig. 10(a)), the three alloys produced by SLM exhibited more stable behavior at higher temperatures in particular after post-processing heat treatments (Fig. 10(b) and (c)), which supports the previous discussion. With regards to the general trends highlighted by dotted lines in Fig. 10, it could be noted that the approximate average of strain hardening rates for the conventional solutionized wrought alloy is often lower than that of the SLMed alloys particularly at lower strain levels, which testifies for its excellent plasticity. In addition, the strain hardening rate of the wrought alloy significantly increased as deformation increased at all temperatures unlike those of the AB, RX and GBS alloys produced by SLM which exhibited a shortening plateau as temperature increased.

The striking differences at 700 °C highlights the contribution of heat treatments (Fig. 10(c)). Behjati and Asgari [59] discussed the roles of stacking fault energy (SFE), cross-slip of dislocations, large lattice frictional stress due to large solute atoms in solution (Nb and Mo in particular), short range ordering (SRO) promoted by heat treatments, formation of LC locks acting as effective barrier to dislocation motion, increasing dislocation density as deformation proceeds and relatively large homogeneous deformation length (HDL). According to their results, the following conjectures could be put forward to explain the approximate average trends of plastic deformation observed in Fig. 10. Significant lattice frictional stress and SRO expected in Wrought, RX and GBS alloys may stimulate planar configuration of dislocations as this SRO is destroyed by the passing of leading partials and therefore

Table 1 Details of the quantification of flow curves for AB, RX, GBS and Wrought materials at 500 °C, 600 °C and 700 °C (strain rate of $3.3 \times 10^{-4} s^{-1}$). Were considered the critical strain for onset of serration ϵ_s , serration type A, B or C, serration amplitude $\Delta\sigma$ and wavelength $\Delta\lambda$.

	500 °C			600 °C			700 °C							
	$0 \leq \epsilon \leq 10(\%)$			$0 \leq \epsilon \leq 10(\%)$			$0 \leq \epsilon \leq 10(\%)$							
	ϵ_s (%)	Type	Wavelength ($\Delta\lambda$, %)	ϵ_s (%)	Type	Wavelength ($\Delta\lambda$, %)	ϵ_s (%)	Type	Wavelength ($\Delta\lambda$, %)					
AB	5.5	A	$0.2 \sim 0.3$	8	A	0.5	3.5	A	$0.55 \sim 0.7$					
	≤ 1	B	≈ 0.05	≤ 1	B	≈ 0.05	≤ 1	B	≈ 0.05					
	$28 \sim 30$	C	$0.15 \sim 0.55$	≈ 30	C	$0.1 \sim 0.15$	≈ 41	C	1 event					
RX	2.9	A	≈ 3	-	-	-	4.1	A	$0.1 \sim 0.25$					
	≤ 1	B	≈ 0.05	-	-	-	≈ 0.5	B	≈ 0.1					
	$9 \sim 17$	C	$0.05 \sim 0.15$	$21 \sim 27$	C	$0.05 \sim 0.15$	≈ 13	C	1 event					
GBS	2.1	-	-	-	-	-	-	-	-					
	-	-	-	-	-	-	-	-	-					
	6 ~ 18	C	$0.05 \sim 1$	19 ~ 21	C	$0.1 \sim 0.35$	-	-	-					
Wrought	1.4	-	-	-	-	-	3.8	A	≈ 0.2					
	≈ 5	B	≈ 0.05	4 ~ 9	B	$0.05 \sim 0.1$	≈ 2	B	≈ 0.1					
	8 ~ 12	C	$0.3 \sim 0.4$	13 ~ 18	C	0.5	11 ~ 13	C	$0.2 \sim 0.7$					
									10 ~ 16	C	$0.05 \sim 0.8$			
												13 ~ 17	C	$0.1 \sim 0.8$

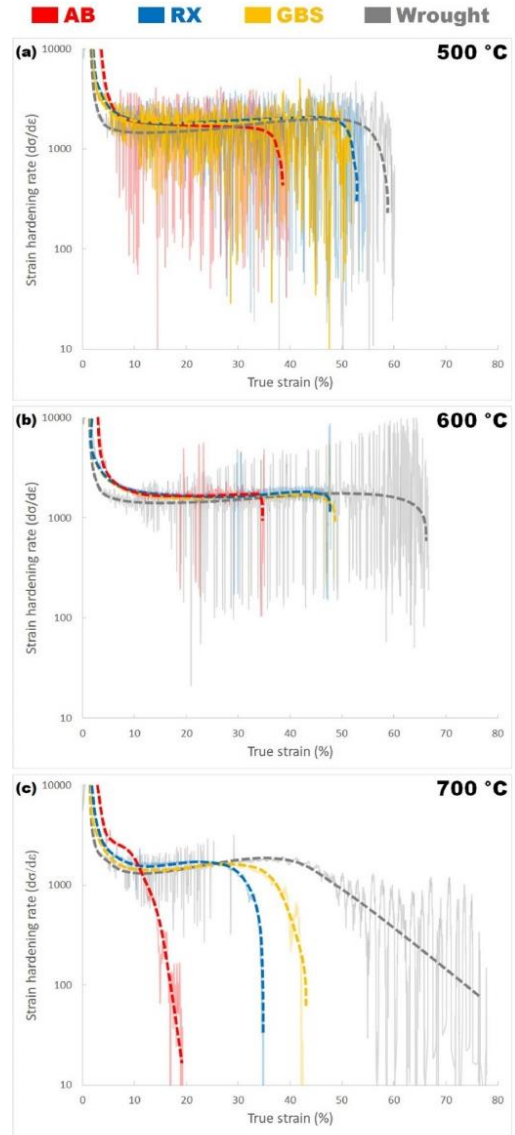


Fig. 10. Strain hardening rate vs. true strain for all four AB (red), RX (blue), GBS (orange) and Wrought (grey) alloys at (a) 500 °C, (b) 600 °C and (c) 700 °C. Actual calculated values are shown as transparent solid lines in the background and approximate average trends were added in dashed lines. (For interpretation of the references to colour in this figure legend, the reader is referred to the Web version of this article.)

becomes an easy path for following dislocations. Strain hardening may be promoted by dislocations piling up behind LC locks or as a result of DSA. This behavior may be favored in the solutionized Wrought alloy characterized by a large amount of solute in solution as opposed to the

significant presence of NbC precipitates in RX and GBS. It coincides in particular with lower strain hardening rate at low strain levels for Wrought however steadily increasing as deformation proceeded. The Wrought alloy may undergo significant deformation twinning at large strains despite its relatively large SFE due to high dislocation density and relatively large homogeneous deformation length (HDL). This contributed to smoothen the decrease in strain hardening rate starting at about 40% true strain. It appears that, at all temperatures in Fig. 10, the four alloys otherwise fracture shortly after the second fall of the strain hardening rate corresponding to the density of piled up dislocations reaching its maximum and the partials able to cross-slip [59]. On the contrary, the dislocation density in the AB material is much too high (Figs. 3(a) and 9(b)) to allow for dislocations to glide appropriately. At 700 °C, the alloy exhibited a plunging strain hardening rate with no sign of mechanical strengthening during tension (Fig. 10(c)). Strain hardening rates for both RX and GBS reported in Fig. 10(c) were fairly stable and slightly increased at medium strain levels. The results presented here and the conjectures put forward highlight the prevailing role of microstructure. The role of heat treatments to modify the AB microstructure for high temperature applications was clear. However further research is much needed to elucidate the mechanisms at hand, and consequently optimize microstructure accordingly.

4. Conclusions

The popular Alloy 625 for high temperature structural applications was produced by Selective Laser Melting (SLM). The microstructure of the as-built (AB) material was typical of powder bed fusion processes. It was characterized by elongated grains intercepting several layers, a very fine cellular/dendritic structure, inhomogeneous distribution of constituents, segregation, very fine NbC precipitates and very high density of tangled dislocations particularly within intercellular/interdendritic regions. A recrystallization heat treatment (RX) and a specific grain boundary serration (GBS) heat treatment were designed to remodel the AB microstructure for enhanced high temperature properties. The RX alloy subjected to a single solution step exhibited fully recrystallized fine equiaxed grains and fine precipitation of NbC precipitates with a bimodal submicrometric and micrometric size distribution. The GBS alloy which experienced in particular slow cooling from the high solution temperature exhibited as much as 80% of serrated grain boundaries and, although slightly larger, similar bimodal precipitation of NbC carbides. There was no evidence of any other phase significantly present in all materials considered other than NbCs and the γ -matrix. The behaviors of the three alloys produced by SLM, as well as their conventionally wrought and solutionized counterpart, were studied in tension at room temperature and at 500 °C, 600 °C and 700 °C. Strength values, yield strength in particular, ranked in decreasing order from the highest for the AB followed by RX, GBS and the lowest for the conventional wrought material at all temperatures considered. On the contrary, the AB material always exhibited the lowest ductility while the conventional wrought material recorded the highest values and RX and GBS materials had similar intermediate ductility, at all temperatures. These behaviors correlated properly with the different microstructures. The highly constrained microstructure of the AB characterized by high dislocation density promoted very high strength and severely decreased plasticity while relatively large grains and homogeneous solid solution of the conventional wrought alloy favored plastic deformation. Fine precipitation in both RX and GBS alloys promoted strength yet recrystallization also allowed for significant plastic deformation. Another valuable behavior evidenced by tensile tests at elevated temperature was the stability of plastic deformation of the materials produced by SLM as opposed to the wrought materials having heavily serrated plastic flow at elevated temperature. The results of the presently reported research work highlights the predominant role of microstructure on the mechanical properties of Alloy 625 and the outstanding potential of additive manufacturing, SLM in particular, when great care is taken to

optimize microstructure.

Declaration of competing interest.

The authors declare that they have no known competing financial interests or personal relationships that could have appeared to influence the work reported in this paper.

This manuscript addresses the thorough characterization of as-SLMed microstructure for Alloy 625 and the design of heat treatments in order to tailor the microstructure for better high temperature properties and stability. This is in particular the first time that a specifically design heat treatment for promoting grain boundary serration in AMed Alloy 625 is reported. The high temperature tensile properties at 500, 600 and 700 °C were evaluated and analyzed in terms of strength and ductility levels, plastic behavior and stability. This is the first time to our knowledge that properties in tension for SLMed Alloy 625 subjected to post-processing heat treatments are presented, moreover for the innovative grain boundary serration treatment. We found in particular that heat treatments significantly promoted ductility at all temperatures compared to as-built materials, as well as maintaining levels of strength higher than those of standard wrought Alloy 625. We also showed that heat treatments, grain boundary serration in particular, promoted stable plastic deformation behavior at high temperature as opposed to the wrought standard which typically experienced dynamic strain aging manifested by irregular flow stress.

Our results highlight the predominant role of microstructure and outstanding potential of SLMed Alloy 625.

CRediT authorship contribution statement

Jiwon Lee: Conceptualization, Methodology, Resources, Writing - original draft, Validation, Formal analysis, Investigation. **Mathieu Ternier:** Formal analysis, Investigation, Writing - review & editing. **Sunyoung Jun:** Methodology. **Hyun-Uk Hong:** Writing - review & editing, Supervision. **Etienne Copin:** Methodology, Writing - review & editing. **Philippe Lours:** Writing - review & editing, Supervision.

Acknowledgment

The authors acknowledge the financial support of the National Research Foundation of Korea (NRF) grant funded by the Korean government (MSIP, NRF-2020R1A2C4002291 and NRF-2018R1A5A6075959).

References

- [1] H.L. Eiselstein, D.J. Tillack, The invention and definition of alloy 625, *superalloys* 718, 625 and various derivatives, TMS (1991) 1–14, https://doi.org/10.7449/1991%2FSuperalloys_1991_1_14.
- [2] G.D. Smith, D.J. Tillack, S.J. Patel, Alloy 625 – impressive past/significant presence/awesome future, 625, 706, *Superalloys 718* (2001) 35–46, https://doi.org/10.7449/2001%2FSuperalloys_2001_35_46. Various Derivatives, TMS.
- [3] L.E. Shoemaker, Alloys 625 and 725: Trends in Properties and Applications, *Superalloys 718, 625, 706 and Various Derivatives*, TMS, 2005, pp. 409–418, https://doi.org/10.7449/2005%2FSuperalloys_2005_409_418.
- [4] S. Floreen, G.E. Fuchs, W.J. Yang, The metallurgy of Alloy 625, *Superalloys* (1994) 625–706, https://doi.org/10.7449/1994%2FSuperalloys_1994_13_37, 718, Various Derivatives, TMS, 13–37.
- [5] P.M. Mignanello, N.G. Jones, E. Pickering, O. Messe, C.M.F. Rae, M.C. Hardy, H. A. Stone, gamma-gamma prime-gamma double prime dual-superalattice superalloys, *Scripta Mater.* (2007) 136–140, <https://doi.org/10.1016/j.scriptamat.2017.04.029>.
- [6] I.J. Moore, M.G. Burke, E.J. Palmiere, Modelling the nucleation, growth and coarsening kinetics of γ' (D022) precipitates in the Ni-base Alloy 625, *Acta Mater.* 119 (2016) 157–166, <https://doi.org/10.1016/j.actamat.2016.08.027>.
- [7] K.N. Amato, J. Hernandez, L.E. Murr, E. Martinez, S.M. Gaytan, P.W. Shindo, Comparison of microstructures and properties for a Ni-base superalloy (alloy 625) fabricated by electron and laser beam melting, *J. Mater. Sci. Res.* 1–2 (2012) 3–41, <https://doi.org/10.5539/jmsr.v1n2p3>.
- [8] T. Borowski, A. Brojanowska, M. Kost, H. Garbacz, T. Wierzczoń, Modifying the properties of the Inconel 625 nickel alloy by glow discharge assisted nitriding, *Vacuum* 83–12 (2009) 1489–1493, <https://doi.org/10.1016/j.vacuum.2009.06.056>.

- [9] M.A. Anam, D. Pal, B. Stucker, Modeling and experimental validation of nickel-based super alloy (Inconel 625) made using selective laser melting, *Sol. Freeform Fabric.* (2013) 463–473. <http://utw10945.utweb.utexas.edu/Manuscripts/2013/2013-36-Anam.pdf>.
- [10] S. Li, Q. Wei, Y. Shi, Z. Zhu, D. Zhang, Microstructure characteristics of inconel 625 superalloy manufactured by selective laser melting, *J. Mater. Sci. Technol.* 31 (2015) 946–952. <https://doi.org/10.1016/j.jmst.2014.09.020>.
- [11] I. Yadroitsev, I. Smurov, Selective laser melting technology: from the single laser melted track stability to 3D parts of complex shape, *Physcs Proc* 5 (2010) 551–560. <https://doi.org/10.1016/j.phpro.2010.08.083>.
- [12] H. Hacka, R. Link, E. Knudsen, B. Baker, S. Olig, Mechanical properties of additive manufactured nickel alloy 625, *Add. Manuf.* 14 (2017) 105–115. <https://doi.org/10.1016/j.addma.2017.02.004>.
- [13] G. Marchese, M. Lorusso, S. Parizia, E. Bassini, J.W. Lee, F. Calignano, D. Manfredi, M. Termer, H.U. Hong, D. Ugues, M. Lombardi, S. Biamino, Influence of heat treatments on microstructure evolution and mechanical properties of Inconel 625 processed by laser powder bed fusion, *Mater. Sci. Eng.* 729 (2018) 64–75. <https://doi.org/10.1016/j.msea.2018.05.044>.
- [14] Z. Tian, C. Zhang, D. Wang, W. Liu, X. Fang, D. Wellmann, Y. Zhao, Y. Tian, A review on laser powder bed fusion of inconel 625 nickel-based alloy, *Appl. Sci.* 10 (2020) 81. <https://doi.org/10.3390/app10010081>.
- [15] A. Wisniewski, J. Beddies, Influence of grain-boundary morphology on creep of a wrought Ni-base superalloy, *Mater. Sci. Eng.* 510–511 (2009) 266–272. <https://doi.org/10.1016/j.msea.2008.04.130>.
- [16] H.U. Hong, S.W. Nam, Improvement of creep-fatigue life by the modification of carbide characteristics through grain boundary serration in an AISI 304 stainless steel, *J. Mater. Sci.* 3–8 (2003) 1535–1542. <https://doi.org/10.1023/A:1022989002179>.
- [17] H.U. Hong, I.S. Kim, B.G. Choi, M.Y. Kim, C.Y. Jo, The effect of grain boundary serration on creep resistance in a wrought nickel-based superalloy, *Mater. Sci. Eng.* 517 (2009) 125–131. <https://doi.org/10.1016/j.msea.2009.03.071>.
- [18] J.W. Lee, D.J. Kim, H.U. Hong, A new approach to strengthen grain boundaries for creep improvement of a Ni-Cr-Co-Mo superalloy at 950 °C, *Mater. Sci. Eng.* 625 (2015) 164–168. <https://doi.org/10.1016/j.msea.2014.12.010>.
- [19] H. Loyer Danflou, M. Marty, A. Walder, Formation of serrated grain boundaries and their effect on the mechanical properties in a P/M nickel base superalloy, *Superalloys* (1992) 63–72. https://doi.org/10.7449/1992%2FSuperalloys_1992_63_72. TMS (1992).
- [20] J.M. Larson, S. Floren, Metallurgical factors affecting the crack growth resistance of a superalloy, *Metall. Trans. A* 8 (1977) 51–55. <https://doi.org/10.1007/BF02677263>.
- [21] M. Termer, J.W. Lee, J.H. Kim, H.U. Hong, First evidence of grain boundary serration in a specifically heat treated wrought Alloy 625 Ni-based superalloy, *Int. J. Mater. Res.* 109–9 (2018) 803–810. <https://doi.org/10.3139/146.111674>.
- [22] ASTM E2109-01(2014), Standard Test Methods for Determining Area Percentage Porosity in Thermal Sprayed Coatings, ASTM International, West Conshohocken, PA, 2014. <https://www.astm.org/cgi-bin/resolver.cgi?E2109>.
- [23] G. Marchese, X.G. Colera, F. Calignano, M. Lorusso, S. Biamino, P. Minetola, D. Manfredi, Characterization and comparison of inconel 625 processed by selective laser melting and laser metal deposition, *Adv. Eng. Mater.* 19 (2016). <https://doi.org/10.1002/adem.201606005>.
- [24] L.N. Carter, X. Wang, N. Read, R. Khan, M. Aristizabal, K. Essa, M.M. Attallah, Process optimization of selective laser melting using energy density model for nickel based superalloys, *Mater. Sci. Technol.* 32–7 (2016) 657–661. <https://doi.org/10.1179/1743284715Y.0000000108>.
- [25] ASTM E8/E8M-16e1, Standard Test Methods for Tension Testing of Metallic Materials, ASTM International, West Conshohocken, PA, 2016. <http://www.astm.org/cgi-bin/resolver.cgi?E8E8M-16e1>.
- [26] T. DebRoy, H.L. Wea, J.S. Zubacka, T. Mukherjee, J.W. Elmer, J.O. Milewski, A. M. Beese, A. Wilson-Heid, A. De, W. Zhang, Additive manufacturing of metallic components – process, structure and properties, *Prog. Mater. Sci.* 92 (2018) 112–224. <https://doi.org/10.1016/j.pmatsci.2017.10.001>.
- [27] P. Wang, B. Zhang, C.C. Tan, S. Raghavan, Y.F. Lin, C.N. Sun, J. Wei, D. Chi, Microstructural characteristics and mechanical properties of carbon nanotube reinforced Inconel 625 parts fabricated by selective laser melting, *Mater. Des.* 112 (2016) 290–299. <https://doi.org/10.1016/j.matdes.2016.09.080>.
- [28] N.J. Harrison, I. Todd, K. Mumtaz, Reduction of micro-cracking in nickel superalloys processed by Selective Laser Melting: a fundamental alloy design approach, *Acta Mater.* 94 (2015) 59–68. <https://doi.org/10.1016/j.actamat.2015.04.035>.
- [29] H. Heubner, M. Köhler, B. Prinz, Determination of the Solidification Behaviour of Some Selected Superalloys, *Superalloys*, 1988, pp. 437–447. https://doi.org/10.7449/1988%2FSuperalloys_1988_437_447. TMS (1988).
- [30] Y. Zhang, B. Huang, J. Li, Microstructural evolution with a wide range of solidification cooling rates in a Ni-based superalloy, *Metall. Mater. Trans.* 44 (2013) 1641–1644. <https://doi.org/10.1007/s11661-013-1645-7>.
- [31] D.M. Stefanescu, R. Ruxunda, Fundamentals of Solidification, in: *Metallurgy and Microstructures, Fundamentals of Solidification*, vol. 9, ASM International, 2004. ASM Handbook, https://www.researchgate.net/publication/260038120_Fundamentals_of_Solidification/citations.
- [32] J.N. Dupont, C.V. Robino, A.R. Marder, M.R. Notis, Solidification of Nb-bearing superalloys: Part II. Pseudoternary solidification surfaces, *Metall. Mater. Trans.* 29 (1998) 2797–2806. <https://doi.org/10.1007/s11661-998-0320-x>.
- [33] M.C. Flemings, Solidification processing, *Metall. Trans. B* 5 (1974) 2121–2134. <https://doi.org/10.1007/BF02643923>.
- [34] G. Lindwall, C.E. Campbell, E.A. Lass, F. Zhang, M.R. Stoudt, A.J. Allen, L. E. Levine, Simulation of TTT curves for additively manufactured inconel 625, *Metall. Mater. Trans.* 50 (2019) 457–467. <https://doi.org/10.1007/s11661-018-4959-7>.
- [35] T. Keller, G. Lindwall, S. Ghosh, L. Ma, B.M. Lane, F. Zhang, U.R. Kattner, E.A. Lass, J.C. Heigel, Y. Idell, M.E. Williams, A.J. Allen, J.E. Guyer, L.E. Levine, Application of finite element, phase-field, and CALPHAD-based methods to additive manufacturing of Ni-based superalloys, *Acta Mater.* 139 (2017) 244–253. <https://doi.org/10.1016/j.actamat.2017.05.003>.
- [36] J.L. Bartlett, X. Li, An overview of residual stresses in laser powder bed fusion, *Add. Manuf.* 27 (2019) 131–149. <https://doi.org/10.1016/j.addma.2019.02.020>.
- [37] A. Kreitzberg, K. Inaekyan, S. Turenne, V. Brallovski, Temperature- and time-dependent mechanical behavior of post-treated IN625 alloy processed by laser powder bed fusion, *J. Manuf. Mater. Process.* 3–3 (2019) 75. <https://doi.org/10.3390/jmmp3030075>.
- [38] K. Zhao, L. Lou, Y. Ma, Z. Hu, Effect of minor niobium addition on microstructure of a nickel-base directionally solidified superalloy, *Mater. Sci. Eng.* 476 (2008) 372–377. <https://doi.org/10.1016/j.msea.2007.06.041>.
- [39] A.K. Koul, R. Thamburaj, Serrated grain boundary formation potential of Ni-based superalloys and its implications, *Metall. Trans. A* 16 (1985) 17–26. <https://doi.org/10.1007/BF02656707>.
- [40] M.F. Henry, Y.S. Yoo, D.Y. Yoon, J. Choi, The dendritic growth of γ precipitates and grain boundary serration in a model nickel-base superalloy, *Metall. Trans. A* 24 (1993) 1733–1743. <https://doi.org/10.1007/BF02657848>.
- [41] H. Loyer Danflou, M. Macia, T.H. Sanders, T. Khan, Mechanisms of formation of serrated grain boundaries in nickel base superalloys, *Superalloys* (1996) 119–127. https://doi.org/10.7449/1996%2FSuperalloys_1996_119_127. TMS (1992).
- [42] J.G. Yoon, H.W. Jeong, Y.S. Yoo, H.U. Hong, Influence of initial microstructure on creep deformation behaviors and fracture characteristics of Haynes 230 superalloy at 900 °C, *Mater. Char.* 101 (2015) 49–57. <https://doi.org/10.1016/j.matchar.2015.01.002>.
- [43] H.U. Hong, I.S. Kim, B.G. Choi, Y.S. Yoo, C.Y. Jo, On the role of grain boundary serration in simulated weld heat-affected zone liquation of a wrought nickel-based superalloy, *Metall. Mater. Trans.* 43 (2012) 173–181. <https://doi.org/10.1007/s11661-011-0837-2>.
- [44] H.U. Hong, H.W. Jeong, I.S. Kim, B.G. Choi, Y.S. Yoo, C.Y. Jo, Significant decrease in interfacial energy of grain boundary through serrated grain boundary transition, *Philos. Mag.* A 92–22 (2012) 2809–2825. <https://doi.org/10.1080/14786435.2012.676212>.
- [45] H.U. Hong, I.S. Kim, B.G. Choi, Y.S. Yoo, C.Y. Jo, On the mechanism of serrated grain boundary formation in Ni-based superalloys with low γ volume fraction, in: E.S. Huron, R.C. Reed, M.C. Hardy, M.J. Mills, R.E. Montero, P.D. Portella, J. Telesman (Eds.), *Superalloys 2012*, 2012. <https://doi.org/10.1002/9781118516430.ch6>.
- [46] K.J. Kim, H.U. Hong, S.W. Nam, A study on the mechanism of serrated grain boundary formation in an austenitic stainless steel, *Mater. Chem. Phys.* 126 (2011) 489–493. <https://doi.org/10.1016/j.matchemphys.2010.12.025>.
- [47] K.J. Kim, H.U. Hong, S.W. Nam, Investigation on the formation of serrated grain boundaries with grain boundary characteristics in an AISI 316 stainless steel, *J. Nucl. Mater.* 393 (2009) 249–253. <https://doi.org/10.1016/j.jnucmat.2009.06.011>.
- [48] J.W. Lee, M. Termer, H.U. Hong, S.H. Na, J.B. Seol, J.H. Jang, T.H. Lee, A new observation of strain-induced grain boundary serration and its underlying mechanism in a Ni–20Cr binary model alloy, *Mater. Char.* 135 (2018) 146–153. <https://doi.org/10.1016/j.matchar.2017.11.047>.
- [49] M. Termer, H.U. Hong, J.H. Lee, B.G. Choi, On the role of alloying elements in the formation of serrated grain boundaries in Ni-based alloys, *Int. J. Mater. Res.* 109–9 (2018) 803–810. <https://doi.org/10.3139/146.111674>.
- [50] R.W. Balluffi, J.W. Cahn, Mechanism for diffusion induced grain boundary migration, *Acta Metall.* 29–3 (1981) 493–500. [https://doi.org/10.1016/0001-6160\(81\)90073-0](https://doi.org/10.1016/0001-6160(81)90073-0).
- [51] Haynes® 625 Alloy Brochure. <http://haynesintl.com/docs/default-source/pdfs/new-alloy-brochures/high-temperature-alloys/brochures/625-brochure.pdf?sfvrsn=14>.
- [52] Special Metals Inconel® Alloy 625 Brochure. <https://www.specialmetals.com/assets/smc/documents/alloys/inconel/inconel-alloy-625.pdf>.
- [53] J. Lee, M. Termer, E. Copin, P. Lours, H.U. Hong, A novel approach to the production of NiCrAlY bond coat onto IN625 superalloy by selective laser melting, *Add. Manuf.* 31 (2020). <https://doi.org/10.1016/j.addma.2019.100998>.
- [54] L. Zheng, G. Schmitz, Y. Meng, R. Chellali, R. Schlesiger, Mechanism of intermediate temperature embrittlement of Ni and Ni-based superalloys, *Crit. Rev. Solid State* 37–3 (2012) 181–214. <https://doi.org/10.1080/1040436.2011.613492>.
- [55] M.T. Perez-Prado, M.E. Kassner, Superplasticity, *Fundamentals of Creep in Metals and Alloys*, 2015, pp. 139–157. <https://doi.org/10.1016/B978-0-08-099427-7.00005-2> (Chapter 6).
- [56] W.D. Callister, G.G. Rethwisch, *Materials Science and Engineering: an Introduction*, tenth ed., Wiley, 2018. ISBN 978-1-119-40549-8.
- [57] P. Rodriguez, Serrated plastic flow, *Bull. Mater. Sci.* 6–4 (1984) 653–663. <https://doi.org/10.1007/BF02743993>.
- [58] A.M. Beese, Z. Wang, A.D. Stoica, D. Ma, Absence of dynamic strain aging in an additively manufactured nickel-base superalloy, *Nat. Commun.* 9 (2018) 2083. <https://doi.org/10.1038/s41467-018-04473-5>.
- [59] P. Behjati, S. Asgari, Microstructural characterisation of deformation behaviour of nickel base superalloy IN625, *Mater. Sci. Technol.* 27–12 (2011) 1858–1862. <https://doi.org/10.1179/1743284711Y.0000000056>.



High temperature oxidation of NiCrAlY coated Alloy 625 manufactured by selective laser melting

Damien Texier, Etienne Copin, Augustin Flores, Jiwon Lee, Mathieu Ternier, Hyun-Uk Hong, Philippe Lours

► To cite this version:

Damien Texier, Etienne Copin, Augustin Flores, Jiwon Lee, Mathieu Ternier, et al.. High temperature oxidation of NiCrAlY coated Alloy 625 manufactured by selective laser melting. *Surface and Coatings Technology*, Elsevier, 2020, 398, pp.1-14/126041. 10.1016/j.surfcoat.2020.126041 . hal-02872096

HAL Id: hal-02872096

<https://hal-mines-albi.archives-ouvertes.fr/hal-02872096>

Submitted on 25 Jun 2020

HAL is a multi-disciplinary open access archive for the deposit and dissemination of scientific research documents, whether they are published or not. The documents may come from teaching and research institutions in France or abroad, or from public or private research centers.

L'archive ouverte pluridisciplinaire **HAL**, est destinée au dépôt et à la diffusion de documents scientifiques de niveau recherche, publiés ou non, émanant des établissements d'enseignement et de recherche français ou étrangers, des laboratoires publics ou privés.



Distributed under a Creative Commons Attribution | 4.0 International License

High temperature oxidation of NiCrAlY coated Alloy 625 manufactured by selective laser melting

Damien Texier^{a,*}, Etienne Copin^a, Agustin Flores^a, Jiwon Lee^{a,b}, Mathieu Terner^b, Hyun-Uk Hong^b, Philippe Lours^a

^a Institut Clement Ader (ICA) - UMR CNRS 5312, Université de Toulouse, CNRS, INSA, UPS, Mines Albi, ISAE-SUPAERO, Campus Jarlard, 81013 Albi Cedex 09, France

^b Department of Materials Science and Engineering, Changwon National University, 20 Changwondaehak-ro, Changwon, Gyeongnam 51140, Republic of Korea

ABSTRACT

Keywords:
MCrAlY bond-coating
Superalloy
Additive manufacturing
Selective laser melting
Oxidation
Dilution

The high temperature oxidation of fully SLM-processed NiCrAlY coated Alloy 625 parts was investigated between 800 °C and 1000 °C. For comparison, bulk NiCrAlY and bulk Alloy 625 were also fabricated using SLM. Two thin layers of NiCrAlY powder were lasered at the surface of Alloy 625 to form the bi-materials. Bulk NiCrAlY and bi-materials showed an improved oxidation behavior compared to Alloy 625. The oxidation of the NiCrAlY coating results in regions with a dense and continuous external Al₂O₃ layer and regions composed of a mixture of external Cr₂O₃ and internal Al₂O₃. Large EDS maps at the surface and cross-sections of the bi-material highlighted a heterogeneous distribution of constitutive elements of the NiCrAlY coating, resulting in some regions with an Al activity lower than the one required for the formation of a continuous and dense Al₂O₃ layer (≤ 10 atomic percent). Low Al activity and high Al activity regions were related to the topography of the SLMed surface and correspond to hill and valley regions, respectively. In addition, cracks, mainly occurring in high Al activity regions, were observed across NiCrAlY specimens. The fabrication of coated but small components with a brittle coating by SLM is not trivial and needs further investigations.

1. Introduction

Nickel-based superalloys are intensively used in the aerospace industry for high temperature applications because of their excellent mechanical strength combined with their resistance to high temperature oxidation and corrosion [1–3]. Alloy 625, consisting of a Ni base FCC γ -Ni matrix solution strengthened by significant additions of Cr, Nb and Mo, was purposely developed to achieve an interesting trade-off between mechanical strength, fracture toughness, weldability, manufacturing and corrosion/oxidation performance under aggressive environments [4–8]. Its good resistance to high temperature surface reactivity derives from the considerable amount of chromium present in the alloy, *i.e.* about 20% in weight and 24 atomic %, promoting the formation of a continuous and protective external Cr₂O₃ oxide layer and internal Al₂O₃ oxides in a large temperature window [5,9–12]. Alloy 625 exhibits a parabolic oxidation behavior between 600 °C and 1050 °C [9]. The parabolic constant of oxidation follows an Arrhenius relation with a frequency factor k_0 of $8.3 \cdot 10^{-2} \pm 2.7 \text{ g}^2 \cdot \text{cm}^{-4} \cdot \text{s}^{-1}$ and an activation energy Q of $232 \pm 11 \text{ kJ} \cdot \text{mol}^{-1}$ regardless of the partial pressure of oxygen between 0.12 and 10.3 kPa in the 1050 °C–1250 °C

temperature range [9]. Above 1050 °C, Nb and Ti are found in the upper regions of the oxide scale and a slight decrease in oxidation rate is noticed as a function of the exposure time. This could be caused by either changes in the oxide-film composition or by the possible volatilization of Cr₂O₃ due to the formation of the CrO₃ (g) compound [13]. Cr₂O₃ volatilization is accelerated with the increase in temperature, in partial pressure of oxygen or in the presence of water [13,14]. Both the chromium depletion associated with the formation of Cr₂O₃ and its volatilization impair the subsurface microstructure and the high temperature structural performance of Alloy 625. Such an oxidation-assisted degradation of component integrity is particularly harmful for small-size and/or thin structural components. Therefore, improvement in surface reactivity of Alloy 625 at high temperature is of high interest. High temperature protective coatings, such as aluminide diffusion coatings or MCrAlY overlay coatings, are commonly used onto nickel-based superalloys to promote the formation of dense and very low-growth-rate α -Al₂O₃ and/or Cr₂O₃ oxide scale [15–18]. The improvement in high temperature oxidation properties above 1000 °C of NiCrAlY coatings containing more than 10 atomic % of aluminum was demonstrated from decades due to the formation and growth of a

* Corresponding author.

E-mail address: damien.texier@mines-albi.fr (D. Texier).

Table 1

Nominal composition of the Alloy 625 and NiCrAlY powders used for SLM manufacturing measured by ICP-OES (in % at.), and composition range for bulk Alloy 625, bulk NiCrAlY and NiCrAlY coated Alloy 625 measured by EDS (in % at.).

Element	Ni	Cr	Mo	Fe	Co	C	Nb	Al	Y
Alloy 625 (powder)	Bal.	22.9	5.10	3.70	0.60	0.39	1.99	0.76	–
NiCrAlY (powder)	Bal.	21.9	–	–	–	–	–	17.9	0.7
Bulk Alloy 625 (SLM)	Bal.	23–25	5–6	3–5	0.5–0.7	–	1.7–2.3	0.5–1.5	–
Bulk NiCrAlY (SLM)	Bal.	18–25	–	–	–	–	–	17–21	0.2–0.5
NiCrAlY Coating (SLM)	Bal.	21–24	3–5	0.3–0.6	–	–	2–3	3–12	0.1–0.3

continuous, compact, and adherent α -Al₂O₃ [19–21]. However, the oxidation performance of NiCrAlY alloys below 1000 °C could be significantly impaired, and can be even worse than Alloy 625 in terms of mass evolution [22–24]. This change in oxidation behavior is attributed to the growth of other Al₂O₃ allotropic variants, i.e. θ -Al₂O₃ and γ -Al₂O₃, showing higher oxidation kinetics, and/or the growth of external Cr₂O₃. Therefore, improving the oxidation resistance of Alloy 625 using NiCrAlY coatings for temperature lower than 1000 °C is of high interest, but not straightforward.

The need for improved performance while satisfying both structural and environmental specifications leads to more and more complex design in terms of geometry and multi-layered microstructures for high temperature jet engine and power plant turbines. Conventional manufacturing processes, such as forging, casting and/or powder metallurgy can find limitations for highly complex geometries, integrated structures, miniaturized and/or small-volume production. Additive manufacturing (AM) techniques are nowadays particularly appropriate for manufacturing such structural components requiring complex design, high mechanical performance, and good surface reactivity [25]. Furthermore, these near-net-shape manufacturing processes tend to limit and even eliminate tooling operations, aiming at considerably reducing processing operations and lead time [26,27]. The powder bed fusion (PBF) AM technique consists in manufacturing parts layer-by-layer by selectively melting thin powder layers using a focused laser or electron source. Such a layered manufacturing strategy, also called “Selective Laser Melting” (SLM), aims to manufacture structural components with both internal and external complex geometries and with spatial resolutions and geometrical tolerances more and more compatible with industrial applications, especially in the field of aerospace. Due to its excellent weldability, SLM-processed Alloy 625 has been widely investigated in terms of solidified microstructure and metallurgical state, crystallographic texture, and mechanical performance in comparison with conventionally wrought Alloy 625 [28–35]. However, the high temperature oxidation resistance of SLM-processed Alloy 625 and coated Alloy 625 components was sparsely reported in the open literature. Fully SLM-processed NiCrAlY coated Alloy 625 was recently investigated in terms of manufacturing feasibility, microstructure, and interdiffusion [36]. A set of optimal processing parameters were identified to produce coatings with very low residual porosity ($\leq 0.1\%$). In addition, contrary to typical overlay NiCrAlY coatings deposited by plasma spray processes, SLM processed NiCrAlY coating exhibited substantial dilution into the Alloy 625 substrate in the as-deposited state, resulting in a progressive Al concentration distribution throughout the coating [36]. The capability of this novel manufacturing approach is promising, and additional microstructural, thermal stability, mechanical performance and surface reactivity characterizations are needed to validate this processing route.

In the present investigation, the high temperature oxidation behavior under isothermal conditions of fully SLM-processed NiCrAlY overlying Alloy 625 parts is investigated between 800 °C and 1000 °C by means of *ex-situ* thermogravimetric analyses (TGA) in order to document their oxidation kinetics. The oxidation behavior of the coated superalloy is compared to the one of bulk NiCrAlY and Alloy 625. Optical and scanning electron microscopy observations of the sample surface and cross-section, X-ray diffraction, energy dispersive

spectroscopy, and topographic analyses were also conducted to document local oxidation events related to the fabrication process.

2. Experimental procedures

2.1. Materials

Bulk Alloy 625, bulk NiCrAlY and NiCrAlY coated Alloy 625 samples were manufactured by SLM. The Alloy 625 and the NiCrAlY powders, obtained by gas-atomization, were supplied by SLM SOLUTIONS and DUCAL INTERNATIONAL, respectively. The chemical composition of both powders was measured by inductively coupled plasma optical emission spectrometry (ICP-OES) and are reported in Table 1. The average diameters of the powders were similar, i.e. 29 μm for the Alloy 625 powder and 35 μm for the NiCrAlY powder. The morphology, the size distribution, and the flow rate of both powders used are detailed in Ref. [36].

A SLM 125HL© machine from SLM SOLUTIONS was used to manufacture the different samples. It is equipped with a 400 W Yb laser (1075 nm) with a Gaussian-beam-focus diameter of 70–100 μm . The fabrication process was performed under a protective argon atmosphere to limit oxidation: the build chamber was initially flooded with argon, then the pressure was kept at 80 mbar during the process. The partial pressure of oxygen was kept below 0.1 atomic %. Furthermore, a constant flow of Ar was maintained above the powder bed to blow away the spatter. The building platform was held at 150 °C (for NiCrAlY) or 200 °C (for Alloy 625) during the whole process to reduce thermal stresses. The different processing conditions and sample geometries used to manufacture the three materials are reported in Table 2 and in Fig. 1. The scanning strategy included contours and used a stripes fill pattern type including stripes with length of 7.5 mm (for NiCrAlY coatings) or 10 mm (for Alloy 625 and bulk NiCrAlY) and a rotation angle of the scanning directions of 67° (for NiCrAlY coatings) or 33° (for Alloy 625 and bulk NiCrAlY) between consecutive layers. A hatch spacing h of 120 μm and a layer thickness t of 50 μm were selected for all the SLM processed materials. These parameters correspond to standard parameters recommended by SLM SOLUTIONS for Alloy 625, and optimized parameters determined in a previous work for NiCrAlY [36].

For bulk Alloy 625, 10 × 10 × 10 mm³ samples were manufactured on small pillar and block supports for easier sample removal from the substrate plate (Fig. 1(a)). Note that no stress release heat treatment was applied to the samples. 1-mm thick slices were then extracted from the cube with a precision cutting machine (Isomet5000 from

Table 2

Processing parameters used to manufacture the bulk Alloy 625, the bulk NiCrAlY and the NiCrAlY coated Alloy 625.

	Power P (W)	Scanning speed v (mm s ⁻¹)	Angle increment (°)	Stripe length (mm)
Bulk In625	275	760	33	10
Bulk NiCrAlY	250	800	33	10
In625 substrate	275	760	33	10
NiCrAlY coating	250	800	67	7.5



Fig. 1. Sample geometry for the three materials: (a) bulk Alloy 625, (b) bulk NiCrAlY, and (c) NiCrAlY coated Alloy 625 samples.

BUEHLER).

For bulk NiCrAlY, $15 \times 10 \text{ mm}^2$, 1-mm thick samples were directly fabricated onto the substrate plate (Fig. 1(b)) and samples were then sliced using electrodischarge machining (EDM). A preliminary study aimed to optimize the sample geometry for bulk NiCrAlY samples due to the highly brittle behavior of MCrAlY coating below 600–800 °C [37]. Therefore, bulk NiCrAlY samples had a design with larger dimensions than bulk Alloy 625 ones. Samples were manufactured with rounded corners to avoid severe cracking during the fabrication. Bulk NiCrAlY samples were polished using a precision Jig to gently remove the initial roughness of the sample as well as the potential dilution region affected by the substrate plate. The polishing procedure is detailed in Ref. [38].

For NiCrAlY coated Alloy 625, $5 \times 5 \times 5 \text{ mm}^3$ Alloy 625 samples were first manufactured on small pillar type supports (Fig. 1(c)). The SLM machine was subsequently cleaned to switch to NiCrAlY powder feed. Then, two layers of NiCrAlY powder (about 100 μm) were SLM processed on the top surface only of the small cubes without any further surface preparation. Based on the apparent density of the powder (around 60%), this would theoretically correspond to a coating layer of about 60–70 μm thick after solidification. Samples were removed from the substrate plate and sliced in the middle plane parallel to the coating surface, leaving a total thickness of about 1 mm, to limit contribution of the coating free side surfaces during oxidation tests. The bottom surface sliced was finally polished all together with the same precision Jig as for bulk NiCrAlY samples to ensure parallelism between the coating surface and the back face as well as repeatability in specimen thickness.

It is worth noting that bulk Alloy 625 and bulk NiCrAlY samples were polished on both faces (P2400 grit paper) while solely the Alloy 625 face for NiCrAlY coated Alloy 625 samples was polished, the coating surface remaining in the as-built (“AB”) state from SLM fabrication. Therefore, the true surface of the NiCrAlY coating is thus significantly larger. All the samples were finally subjected to two consecutive heat treatments under vacuum designed for promoting interdiffusion for standard NiCrAlY coated parts: 6 h at 1080 °C followed by 20 h at 870 °C [39]. This metallurgical state was hereafter labelled “as-heat-treated” (“AHT”) microstructure in the present paper and is the microstructure of interest in the present study.

It should also be noted that both bulk NiCrAlY and NiCrAlY coatings exhibited some cracks as what is assumed to be the result of delayed cracking caused by high levels of residual stress within the material, a typical feature of SLM processing [40]. Indeed, these cracks appear after some time if no heat treatment is performed quickly after manufacturing, in a time scale not yet determined. If the diffusion heat treatment is performed right after manufacturing by SLM, which is not the case in this study, little to no cracking is expected.

2.2. High temperature oxidation.

Isothermal oxidation tests were conducted under laboratory air at 800, 900, and 1000 °C for a maximum duration of 200 h.

Bulk Alloy 625 and NiCrAlY samples were oxidized for 48 h in a

SETSYS thermobalance from SETARAM to continuously monitor the mass evolution during the high temperature exposure (resolution of 10 μg). Samples were directly hung in the furnace using a platinum suspension. Samples with dimensions of $10 \times 10 \times 0.5$ and $15 \times 10 \times 0.5 \text{ mm}^3$ were used for bulk Alloy 625 and for bulk NiCrAlY, respectively. Based on the brittleness of NiCrAlY materials, a 1.5 mm-diameter hole was purposely included in the design produced by SLM. For bulk Alloy 625, the 1.5 mm-diameter hole to hung the sample with the Pt wire was drilled.

For NiCrAlY coated Alloy 625 samples, *ex-situ* thermogravimetric analyses were performed using a NABERTHERM N 11/H furnace, due to the size of samples judged too small for *in-situ* analysis. The temperature was recorded with a K-type thermocouple, and the mass evolution was measured using a precision balance (SARTORIUS MC5) with a resolution of $\pm 1 \mu\text{g}$. Samples were directly hung in an alumina crucible with platinum wires to expose all sample faces to the environment. Interruptions at definite exposure times were carried out, i.e. 5, 10, 20, 50, 100, and 200 h to document the evolution of the mass gain and the nature of the oxidation products.

Macrographs of the samples were acquired with a LEICA DMS 300 calibrated microscope in order to measure the projected surface of samples by image analysis, which was subsequently used for the calculation of specific mass gain.

Topographic measurements were conducted using an OLS 5000 LEXT laser scanning confocal microscope by OLYMPUS with a 405 nm monochromatic source and a MPLFLN10xLEXT lens. Height measurement maps of the NiCrAlY coated Alloy 625 samples were acquired with a z-resolution of 0.1 μm and x/y-resolution of 0.3 μm . Topographic measurements were necessary to assess the developed surface of the NiCrAlY coated Alloy 625 samples with their as-built roughness. Stitching reconstruction was used to cover the $5 \times 5 \text{ mm}^2$ sample surface. Prior to weighing and oxidation, all samples were cleaned for 15 min in acetone, followed by 15 min in ethanol using an ultrasonic bath.

2.3. Material characterizations

Surface and cross sectional observations were conducted using a field-emission gun scanning electron microscope (FEG-SEM) Nova NanoSEM 450 from THERMOFISHER SCIENTIFIC in a backscattered electron mode. The FEG-SEM was equipped with a GENESIS APEX 2i EDS detector from EDAX for chemical profiles and mapping. For cross-sectional characterizations, the samples were hot mounted without cutting to not alter the oxides at the surface of the oxidized samples. The mounted samples were then polished up to the mid-section plane of the specimen using standard automatic metallographic techniques and a surface finish of 0.05 μm alumina particles suspension. An XPRT PANALYTICAL X-Ray diffractometer from PHILIPS was used for the identification of crystallographic structures. X-ray scans were recorded using the Cu-K α radiation ($\lambda = 1.54\text{\AA}$), covering a range of angles (2θ) from 15° to 100° with a step size of 0.033° .

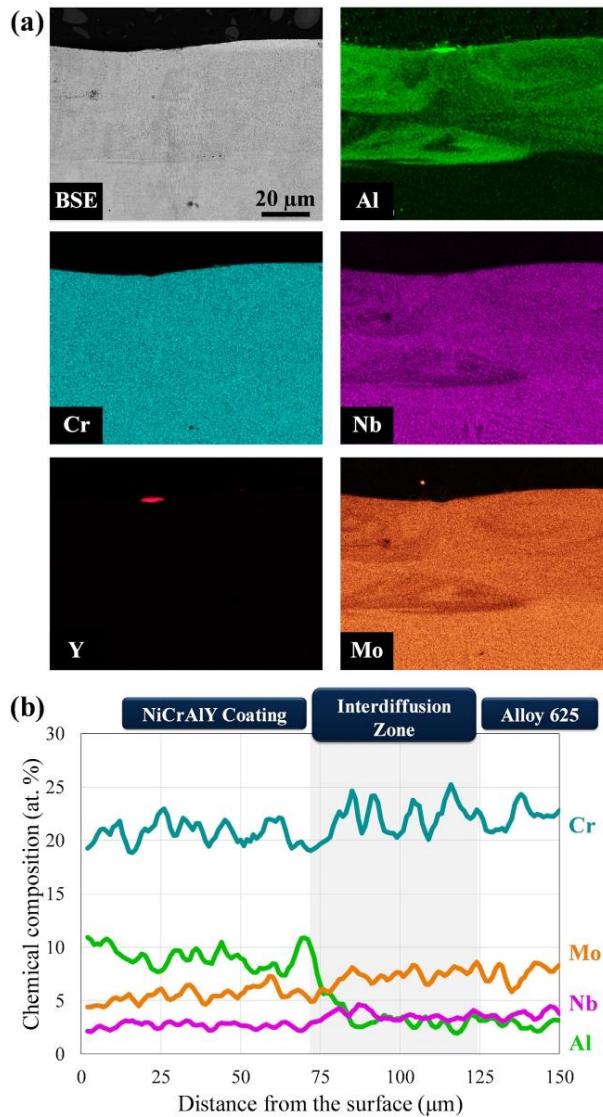


Fig. 2. Element distribution of the NiCrAlY coated Alloy 625 sample before heat treatment (as-built state) measured with EDS: (a) Micrograph in BSE mode and element maps for Al, Cr, Nb, Mo and Y, and (b) Chemical profiles showing the interdiffusion between the NiCrAlY coating and the Alloy 625 substrate.

3. Results

3.1. Chemical analysis of the as-built NiCrAlY coated Alloy 625

Cross-sectional analyses of as-built (AB) NiCrAlY coated Alloy 625 samples, *i.e.* just after the SLM process, were conducted to document the gradient of chemical composition within the coated system due to

dilution effects. EDS maps in Fig. 2(a) give a qualitative representation of the element distribution within the 60 μm thick coating in the as-built state (before heat treatment) and Alloy 625 substrate. It highlights the presence of substantial amount of Nb and Mo within the coating as a result of dilution of the coating into the substrate when processing the two layers of NiCrAlY powders by SLM, which typically involves the remelting of already solidified material across several layers. While the

chromium element map is particularly homogeneous along the whole cross-section, a layered/beam pattern is observed for Al, Nb and Mo elements, leading to strong variability in local chemical composition. As expected, the Al content is higher in the coating compared to the bulk Alloy 625, and the Nb and Mo content is slightly lower. The presence of significant amount of alloying elements from the Alloy 625 substrate explains the difference in microstructure with the bulk NiCrAlY variant, notably the precipitation of the Mo-rich σ phase after the heat treatment (Section 3.2). The chemical profiles in Fig. 2(b) aim to further evidence this dilution effect. Al content was found twice higher in the NiCrAlY coating compared to the bulk Alloy 625, showing the Al enrichment suitable for improvement in high temperature oxidation. However, the Al content in the NiCrAlY coating is nearly 40% lower than the one in the NiCrAlY powder and bulk NiCrAlY. Nb and Mo levels in the coating represent about 70% of the content in bulk Alloy 625. Interestingly, the coating region appeared to be almost devoid of Y, which was found to fully segregates on the top surface in the form of monoclinic $Y_4Al_2O_9$ oxide (YAM) as mentioned in Section 3.2 below. In addition, the chemical composition of the NiCrAlY coating was analyzed at different locations of the sample. Some variability in the chemical composition was observed and the composition range for each element was added in Table 1. The chemical composition of bulk Alloy 625 and bulk NiCrAlY materials were also reported in Table 1 for information. Both the bulk materials and their respective powders have a similar chemical composition. Hence, Al evaporation during SLM processing, which can be subjected to this issue, was considered as not significant with the set of parameters used.

Top surface observations of as-built NiCrAlY coated Alloy 625 evidenced regularly spaced oxide beads parallel to the scanning direction (Fig. 3(a)). These oxide beads were located at the inter-beads region, i.e. in the area between consecutive weld tracks from the NiCrAlY powder SLM processing. These oxides were identified as $Y_4Al_2O_9$ phase (see Supplementary note 1 in the Supplementary Information file). As on the Y EDS map in Fig. 2(a), a cross sectional observation of the $Y_4Al_2O_9$ bead is illustrated in Fig. 3(a). Bulk SLM processed NiCrAlY samples did not exhibit such a significant Y enrichment on the external surface (Fig. 3(b)). Top surface observations also revealed the presence of a local network of small cracks (yellow arrows in Fig. 3(a)) perpendicular to the scanning direction within the NiCrAlY coating, contrary to bulk NiCrAlY samples. It should yet be noted that few macroscopic cracks were observed in bulk NiCrAlY specimens, as mentioned in Section 2.1.

3.2. Microstructure of the “as-heat-treated” NiCrAlY coating versus bulk Alloy 625 and NiCrAlY

The as-heat-treated (AHT) microstructures of bulk Alloy 625, bulk NiCrAlY and NiCrAlY coated Alloy 625 were characterized using scanning electron microscopy in a backscattered electron mode and EDS analysis (Fig. 4). Punctual EDS analyses, EDS mapping, and XRD analyses were added as Supplementary Information to document phase identification for the three materials.

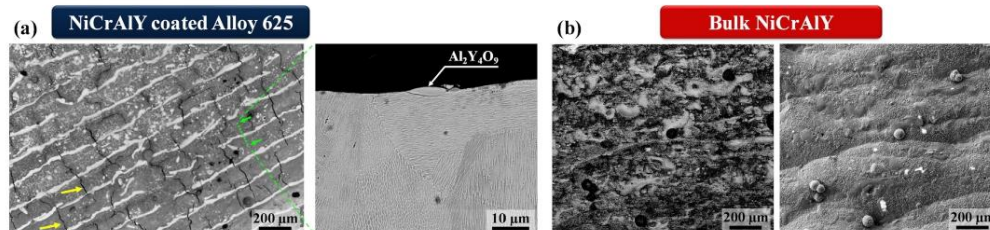


Fig. 3. Segregation in Y for both as-built NiCrAlY materials: (a) NiCrAlY coated Alloy 625, and (b) bulk NiCrAlY.

The microstructure of as-heat-treated Alloy 625 was found typical of SLMed Alloy 625 annealed and aged above 850 °C [35,41,42]. It consisted mainly of a FCC γ -Ni matrix with fine, globular Nb-rich MC primary carbides distributed at the grain boundaries and within grains (sub-micrometer in the latter case), as depicted in Fig. 4(c, f). Secondary phases formed during the 20 h dwell at 870 °C were also observed and include some intra- and intergranular δ -Ni₃Nb needle-like particles and bulky secondary carbides distributed along grain boundaries. Based on their chemical composition (Mo,Nb)-rich and Si-containing, the latter precipitates are expected to be M_6C rather than $M_{23}C_6$ type carbides, as reported in Refs. [42,44]. In addition, $M_{23}C_6$ becomes less stable than M_6C above 850 °C [45,46].

Cross-sectional micrographs of bulk NiCrAlY and NiCrAlY coatings in the heat-treated state were compared at different magnifications in Fig. 4. Significant differences in terms of phase occurrence and morphology were observed between the coating and the bulk variants (Fig. 4(a, d) versus Fig. 4(b, e)). A γ -Ni/ γ' -Ni₃Al matrix with well dispersed α -Cr precipitates (bulky and lamellar) and (Ni,Y)-rich intermetallic precipitates were identified in the bulk NiCrAlY variant (Fig. 4(b, e)), consistent with the expected phases for Ni-22Cr-10Al-1Y [47].

The NiCrAlY coating microstructure was composed of intragranular Nb-containing γ' -Ni₃Al precipitates and (Mo,Cr)-rich needle-like precipitates embedded in a γ -Ni matrix (Fig. 4(a, d)). The needle-like precipitates, showing specific orientation with the γ -Ni matrix and a composition rich in (Mo,Cr) and depleted in Ni, were identified as the topologically close packed (TCP) phase σ [42–44]. Grain boundaries were decorated with larger γ' -Ni₃Al precipitates, α -Cr precipitates and Mo-rich blocky precipitates having a similar composition to that of the (Mo,Cr)-rich needle-like precipitates, also identified as the TCP σ phase. At last, contrary to the bulk NiCrAlY variant, no (Ni,Y)-rich intermetallic precipitates were found within the coatings. Instead, yttrium was segregated on the top surface of the coating as $Y_4Al_2O_9$ oxide beads locally found at the boundary between NiCrAlY beads (see Section 3.1, Figs. 2(a) and 3(a)). Qualitative elemental analysis by EDS and XRD results indicated that those oxides were most likely the $Y_4Al_2O_9$ phase, often referred as YAM [48].

3.3. Oxidation behavior: mass gain evolution

Thermogravimetric analyses were conducted for the three AHT material variants at 800, 900, and 1000 °C: (i) *in-situ* TGA for bulk NiCrAlY and bulk Alloy 625, (ii) *ex-situ* TGA for NiCrAlY coated Alloy 625.

Regarding bulk NiCrAlY and bulk Alloy 625 specimens, continuous mass evolution was recorded during 48 h for each temperature, as delineated with solid lines in Fig. 5. Dashed lines continuing experimental measurements correspond to the extrapolation of the mass evolution for each material/temperature condition using a parabolic behavior of high temperature oxidation. The parabolic behavior of the oxidation kinetics was confirmed for both materials in the test time interval of 48 h, as

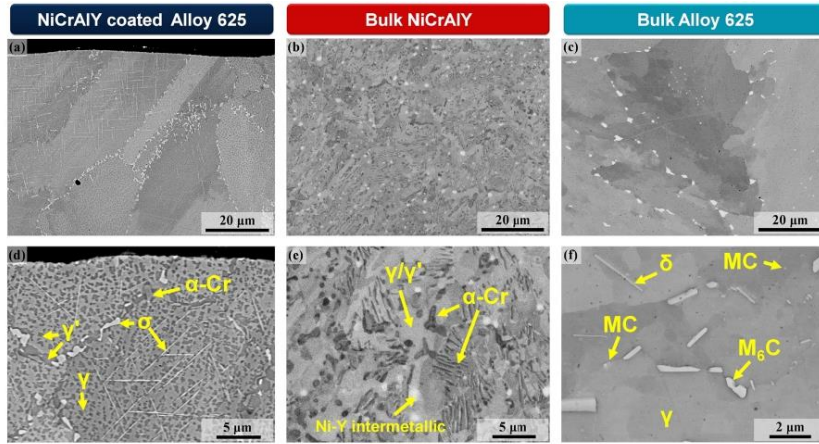


Fig. 4. Cross-sectional observations of the microstructure of the as-heat-treated "AHT" (a, d) NiCrAlY coated Alloy 625, (b, e) bulk NiCrAlY, and (c, f) bulk Alloy 625 samples.

illustrated by the linear trend of the square of the mass gain as a function of the oxidation time in Fig. 6. Parabolic constants k_p for the three temperatures are reported in Table 3 and plotted in an Arrhenius diagram (Fig. 7) with other constants found in the literature for the sake of comparison for bulk materials (different allotropic configurations of Al_2O_3 [22], Cr_2O_3 [49], NiO [50], Alloy 625 [5,9–12], and NiCrAlY alloys [22–24,51,52]). Colored domains in Figs. 5 and 6 correspond to the domain of the square mass gain vs. time comprised between the curve of bulk NiCrAlY (lower limit) and bulk Alloy 625 (upper limit) at a given temperature; bulk NiCrAlY exhibits lower kinetics of oxidation than Alloy 625 in the 800–1000 °C temperature window (2.3 times lower at 800 °C and 12.6 times lower at 1000 °C).

Regarding the oxidation behavior of the NiCrAlY coated Alloy 625, it is worth reminding that both bulk NiCrAlY and Alloy 625 specimens were polished then heat-treated under controlled atmosphere (see

Section 2.1) prior to oxidation characterization by *in-situ* TGA. In contrast, the topography of the NiCrAlY coatings characterized by *ex-situ* TGA remained in as-built conditions, and thus presented a significantly higher surface roughness compared to the five other polished surfaces of each sample (four lateral and one bottom surfaces). Topographic measurements of the NiCrAlY coatings top surface using laser scanning confocal microscopy were performed on ten specimens. The developed surface, *i.e.* the true surface of the samples, was found to be 1.60 ± 0.13 times larger in average than the projected surface. Therefore, mass gain evolution of the NiCrAlY coated specimens was reported as projected mass gain (Alloy625Coat-Proj) and developed/true mass gain (Alloy625Coat-Dev), *i.e.* taking into account the projected surface of the NiCrAlY coating and the developed/true surface of the NiCrAlY coating, respectively. As for bulk specimens, NiCrAlY coated Alloy 625 samples were heat-treated under a protective

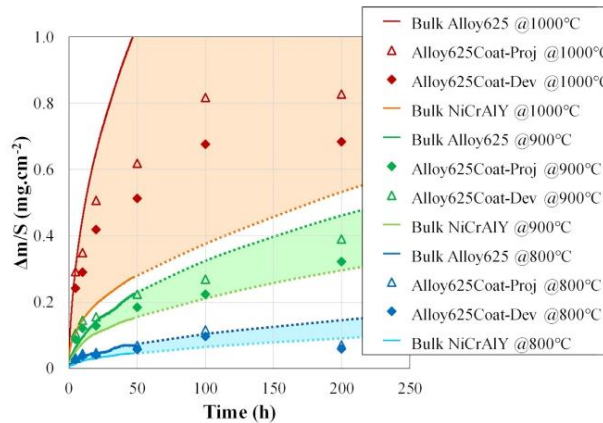


Fig. 5. Mass gain evolution for the three materials at 800 °C, 900 °C and 1000 °C. The measurements of the mass evolution for bulk Alloy 625 and bulk NiCrAlY samples (solid lines) were continuously recorded using a thermobalance and interrupted oxidation tests were conducted for NiCrAlY coated Alloy 625 (data points).

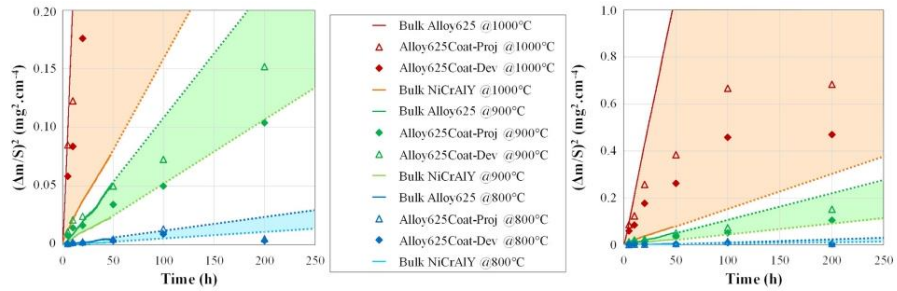


Fig. 6. Evolution of the square mass gain for the three materials at 800 °C, 900 °C and 1000 °C, showing deviation from a parabolic oxidation behavior for NiCrAlY coated Alloy 625 samples.

Table 3

Parabolic constant of oxidation for the bulk Alloy 625, the bulk NiCrAlY and the NiCrAlY coated Alloy 625 (in $\text{mg}^2\text{cm}^{-4}\text{s}^{-1}$).

k_p	Exposure (hours)	800 °C	900 °C	1000 °C
Bulk In625	0–48	$3.01 \cdot 10^{-8}$	$2.81 \cdot 10^{-7}$	$5.92 \cdot 10^{-6}$
Bulk NiCrAlY	0–48	$1.30 \cdot 10^{-8}$	$1.42 \cdot 10^{-7}$	$4.71 \cdot 10^{-7}$
NiCrAlY coated In625 (proj. surf.)	0–50	$2.9 \cdot 10^{-8}$	$2.98 \cdot 10^{-7}$	$2.38 \cdot 10^{-6}$
NiCrAlY coated In625 (proj. surf.)	0–200	$1.41 \cdot 10^{-8}$	$2.14 \cdot 10^{-7}$	$1.20 \cdot 10^{-6}$
NiCrAlY coated In625 (dev. surf.)	0–50	$1.98 \cdot 10^{-8}$	$2.04 \cdot 10^{-7}$	$1.63 \cdot 10^{-6}$
NiCrAlY coated In625 (dev. surf.)	0–200	$9.65 \cdot 10^{-9}$	$1.47 \cdot 10^{-7}$	$8.22 \cdot 10^{-7}$

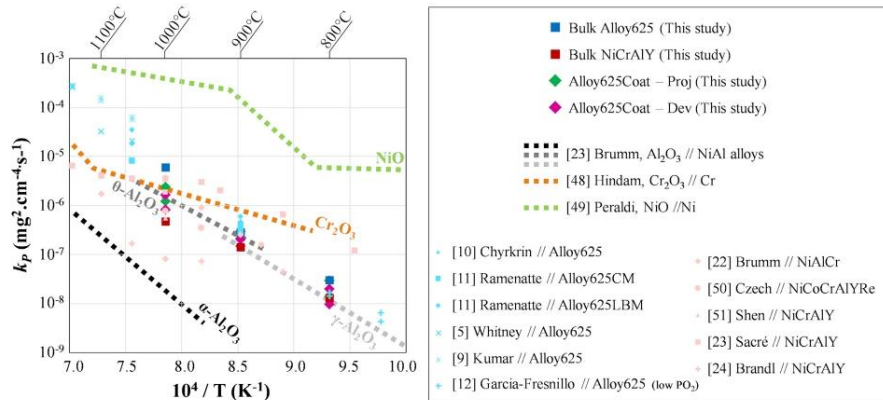


Fig. 7. Evolution of the parabolic constants of oxidation for the three materials as a function of the temperature in comparison with the literature. k_p reported for different allotropic configurations of Al_2O_3 [22], Cr_2O_3 [49], NiO [50], Alloy 625 [5,9–12], and NiCrAlY alloys [22–24, 51, 52]. While the oxidation behavior of both the bulk NiCrAlY and bulk Alloy 625 in the investigated temperature range, the k_p value for NiCrAlY coated Alloy 625 is shown for comparison since its oxidation behavior deviate from a parabolic oxidation behavior.

atmosphere (see Section 2.1), prior to oxidation characterization. Isothermal oxidation tests were conducted at 800, 900, and 1000 °C up to 200 h using one sample per temperature/time condition. Mass gain evolution was reported in Figs. 5 and 6. For most of the oxidation conditions, the oxidation behavior of NiCrAlY coated Alloy 625 is intermediate between that of bulk NiCrAlY and that of bulk Alloy 625 samples. For short time exposures, both the projected and developed mass gains of the bi-material are very similar and sometimes higher than that of the bulk Alloy 625, i.e. the upper limit of the corresponding colored oxidation domain. A pronounced mass gain is observed during the transient stage. After a few hours ($50 \text{ h} \leq t \leq 100 \text{ h}$), the oxidation

behavior of the NiCrAlY coated Alloy 625 deviates from the parabolic regime and tends to follow the behavior of the bulk NiCrAlY samples. In other words, the oxidation behavior of NiCrAlY coated Alloy 625 processed by SLM is not parabolic in this range of temperature (800–1000 °C) and the oxidation kinetics gradually decrease with exposure time. In order to discriminate the oxidation kinetics of the transient oxidation from the long-term oxidation of the NiCrAlY coated Alloy 625 specimens, k_p values between [0 – 50] hours and [0 – 200] hours were calculated and reported in Table 3 and in Fig. 7. k_p values are very close for the three materials at 800 °C but the difference in k_p values increases with the temperature.

3.4. Oxidation behavior: oxidation products

Oxidation products were investigated for the three materials using both EDS and XRD analyses on the top surface and cross-sections of the oxidized specimens (see Supplementary Information). As expected, bulk Alloy 625 developed a continuous, homogeneous and compact Cr_2O_3 external layer for all the temperatures, consistent with the k_p values derived from oxidation tests (Table 3 and Fig. 7). Internal oxidation of Al_2O_3 was observed at the different temperatures. Sparsely distributed NiO oxides and Cr-rich spinels were also observed. In addition, the Cr-depletion beneath the oxide scale promoted the formation of a δ -Ni₃Nb layer beneath the Cr_2O_3 scale, as reported by Chyrkin et al. and Ramenatte et al. [10,11].

For bulk NiCrAlY samples, an external oxide grew on top of the specimen surfaces, mainly constituted of Al_2O_3 . Cr_2O_3 was also observed within the external oxide scale, and its proportion, maximal at 800 °C, decreased as temperature increased.

For NiCrAlY coated Alloy 625 samples, the coating free Alloy 625 surfaces behaved similarly to bulk Alloy 625 samples. However, the SLM processed NiCrAlY coating behaved differently from the bulk NiCrAlY samples. Indeed, the oxide scale developing onto the NiCrAlY coating is heterogeneous at all temperatures and exposure times, as illustrated in Fig. 8 showing macrographs of the samples top surface. Most specimens exhibited a bright/medium gray central region surrounded by a darker gray region near the edges, identified by chemical analyses (EDS) on the oxidized surface as respectively constituted of external Al_2O_3 and external Cr_2O_3 oxide scales (Fig. 9). Intermediate gray regions are composed of a mixture of $\text{Cr}_2\text{O}_3/\text{Al}_2\text{O}_3$ external oxides. It is worth noting that the proportion of Cr_2O_3 and Al_2O_3 scale onto the NiCrAlY coating do not correlate to temperature and oxidation duration.

Interestingly, the Y-rich oxides, *i.e.* YAM, observed previously in Fig. 3(a) are intense and distributed continuously along weld tracks in Al_2O_3 -rich regions. Cr_2O_3 oxides developed at the cracks present normal to the weld track, as shown in the left Cr element map in Fig. 9. In Cr_2O_3 -rich regions, less Y-rich oxides, showing discontinuous distribution, were observed, and no crack within the weld tracks was noticed. Cross-sectional observations of the specimens aimed to identify the presence of internal oxidation (Al_2O_3) beneath the external Cr_2O_3 oxide layer. At 1000 °C–50 h, 15 to 20 μm deep internal oxidation was

observed, as illustrated in Fig. 10 showing the microstructure at the junction of bright and dark regions. It is worth noting that the extension of the internal oxidation-affected region increased with temperature and oxidation duration (Fig. 11). For oxidation duration of 100 h, the extension of the internal oxidation affected region was about 4 to 5 μm at 800 °C while the extension was about 18–23 μm at 1000 °C. The platelet-like morphology of the internal Al_2O_3 densified with the time/temperature increase. At 1000 °C, internal Al_2O_3 started coalescing at the internal oxidation front and Al_2O_3 -platelets were much thicker in the bulk than in the near-surface region.

3.5. Topography and chemical analyses of the SLM processed NiCrAlY coated specimens

As aforementioned, chemical segregation, heterogeneous crack distribution, and heterogeneous oxide formation were observed on NiCrAlY coated Alloy 625 samples. Large EDS maps were performed on four as-built and as-heat-treated samples to document the element distribution at the top surface of the SLM-processed NiCrAlY coatings. Crack distribution was also estimated from SEM images obtained in secondary electron mode.

Variability in chemical composition was evidenced for all specimens, as illustrated in Fig. 12 for a AHT sample. The back-scattered image of the surface in the AHT state at the upper-left corner clearly shows two regions with different chemical nature: (i) a dark gray central region but also to some extent near the edges, and (ii) a light gray contour in-between. The content of Al, Cr and Y, *i.e.* elements constitutive of the NiCrAlY powder, was higher in the dark gray region than in the bright regions, where elements constitutive of Alloy 625 like Nb and Mo were present in higher proportions (see element maps for the relationship).

Interestingly, cracks, mostly orthogonal to the laser beam direction (direction of the highest tensile residual stress in SLM samples [40]), were concentrated in the Al-rich/dark gray region.

This AHT NiCrAlY coated Alloy 625 was then subjected to 900 °C for 50 h. SEM micrographs obtained in a backscattered electron mode was depicted for the oxidized specimen in Fig. 12 (bottom-right corner). After oxidation, Al_2O_3 external oxide was found to develop solely in the Al- and Cr-rich central region while the periphery was mainly composed of Cr_2O_3 external/ Al_2O_3 internal oxides. Some Cr_2O_3 external

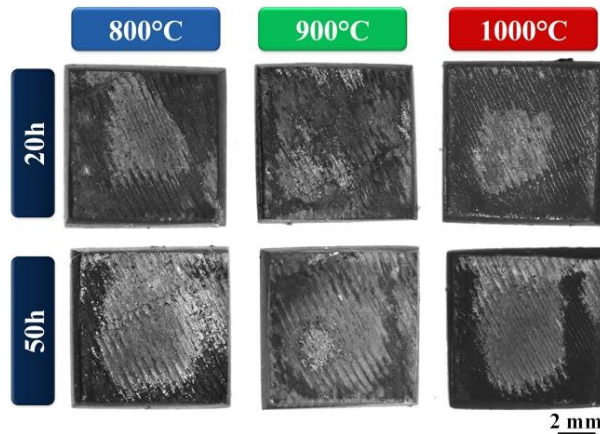


Fig. 8. Surface macrographs of samples oxidized between 800 °C and 1000 °C for 20 and 50 h showing different oxides growing at the surface of the NiCrAlY coated Alloy 625 samples.

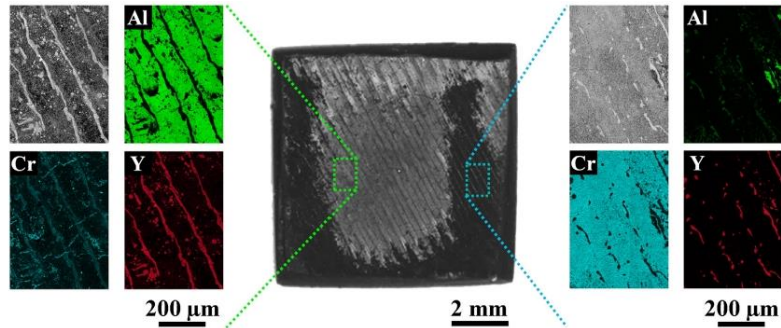


Fig. 9. Formation of Cr_2O_3 and Al_2O_3 external oxides after high temperature exposure ($1000\text{ }^\circ\text{C} - 50\text{ h}$) at the surface of the NiCrAlY coated Alloy 625 sample.

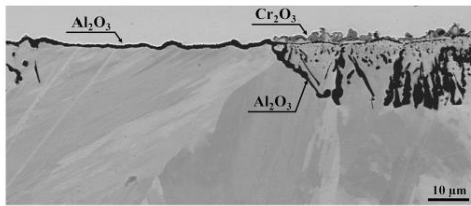


Fig. 10. Cross-section observations of oxidized NiCrAlY coated Alloy 625 samples exposed at $1000\text{ }^\circ\text{C}$ for 50 h showing regions with solely external oxidation of Al_2O_3 and regions with external oxidation of Cr_2O_3 and internal oxidation of Al_2O_3 .

oxide mixed with the Al_2O_3 external oxide was also found to develop in the Al- and Cr-rich central region but in a lower proportion.

Topographic measurements were performed on this sample to map the height characteristics of the SLM processed NiCrAlY sample (top right corner in Fig. 12). Black/dark violet and yellow/orange regions corresponded to lower altitude and higher altitude regions, denoted “valley” and “hill”, respectively. Interestingly, the valley regions appear to match particularly well with the Al-, Y- and Cr-rich regions, i.e. corresponding to a composition closer to that of the NiCrAlY powder.

Large field cross-sectional observation of NiCrAlY coated Alloy 625 sample in electron back-scattered mode in Fig. 13 provides a general view of the sub-surface microstructure as a function of the topography (as SLMed state, i.e. before heat treatment). The distinction between the substrate and the NiCrAlY coating microstructure was particularly difficult to assess in the hill regions (top left and top right (#2) regions in Fig. 13) as a result of a Mo and Nb content close to that of the Alloy 625

substrate combined with a low Al content compared to the nominal composition of the NiCrAlY powder (chemical profile in region #2). The effective coating thickness deduced from the chemical profile was approximately $40\text{ }\mu\text{m}$ on average. In the valley regions, i.e. the central region #1 in Fig. 13, the coating is significantly darker than the substrate due to a higher Al content (twice the content measured in region #2) and a difference in Mo and Nb content more significantly marked with the Alloy 625 substrate (chemical profile in region #2). The average thickness of the coating in the valley region was about $50\text{ }\mu\text{m}$, slightly larger than in the hill region. Therefore, while an aluminum enrichment is noticed in both regions, the coating in the valley region contained twice as much aluminum as compared to the hill region, extended slightly deeper within the bi-material and also had a thicker interdiffusion zone (light gray domains in chemical profiles). However, the maximum aluminum content measured within the NiCrAlY coating was only about 10 atomic % in the valley region, i.e. about half the content in the NiCrAlY powder due to dilution effect during the SLM process.

4. Discussion

The high temperature oxidation behavior of Alloy 625, bulk NiCrAlY and NiCrAlY coated Alloy 625, all produced by the SLM additive manufacturing process, was investigated in the present study. After a standard two-step heat treatment under vacuum designed for promoting interdiffusion (6 h at $1080\text{ }^\circ\text{C}$ followed by 20 h at $870\text{ }^\circ\text{C}$), AHT samples were subjected to isothermal oxidation tests at 800, 900, and $1000\text{ }^\circ\text{C}$ for a maximum duration of 200 h, during which mass gain was monitored.

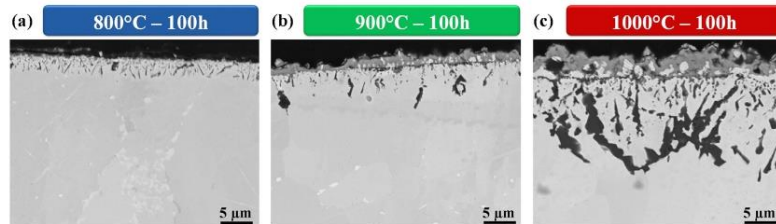


Fig. 11. Cross-section observations of NiCrAlY coated Alloy 625 samples exposed at temperatures between $800\text{ }^\circ\text{C}$ and $1000\text{ }^\circ\text{C}$ for 100 h showing the extension of the internal oxidation with the temperature.

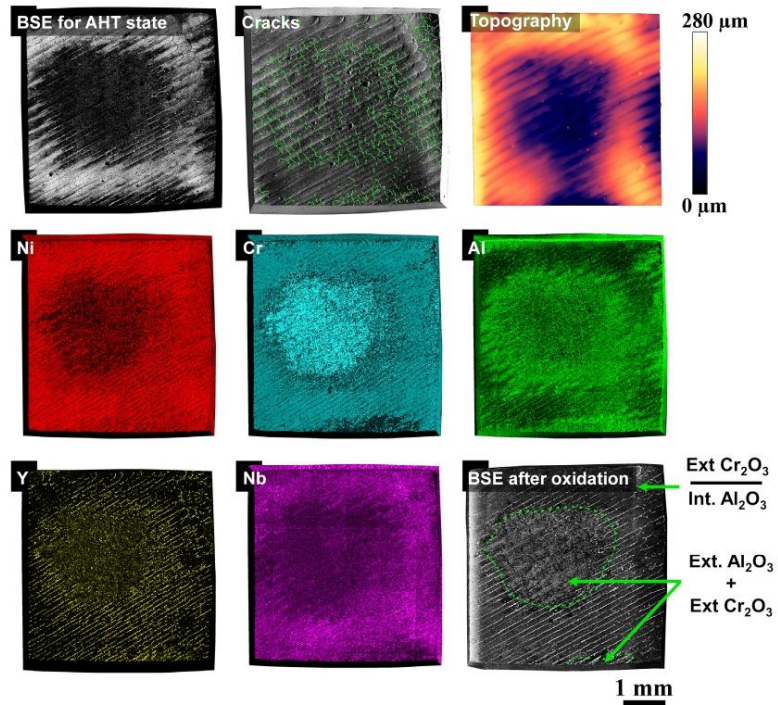


Fig. 12. Effect of the topography and the element distribution at the surface of the NiCrAlY coated Alloy 625 sample on the crack distribution within the coating and the formation of oxides after high temperature exposure. Upper-left corner image is a BSE macrograph of the AHT sample, prior to oxidation.

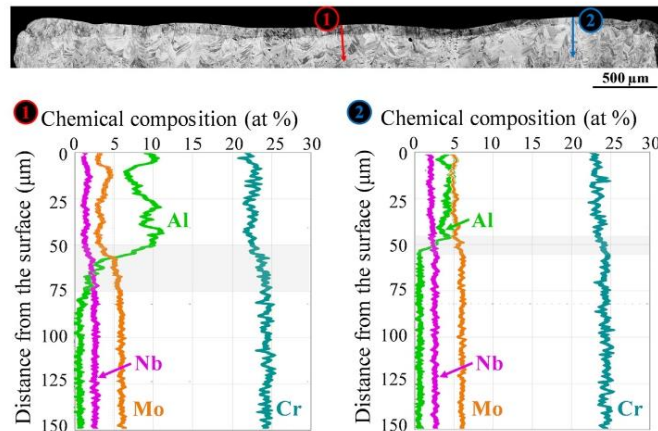


Fig. 13. Microstructure evolution of the as-built NiCrAlY coating, i.e. before heat treatment, as a function of the sample topography. Chemical profiles highlighting variability in the SLM processed coating chemistry in valley regions (#1) and hill regions (#2).

4.1. Process-dependant chemistry, microstructure, and oxidation response

While the microstructure and mechanical properties of superalloys produced by SLM have been extensively investigated in the open literature, little work has been done to assess their oxidation behavior at high temperature. As expected, the oxidation of SLMed Alloy 625 was characterized by the growth of a continuous, homogeneous and compact Cr_2O_3 external layer at all temperatures with oxidation kinetics following a parabolic law (Figs. 5 and 6). As shown in Fig. 6 and in Table 3, the derived values of the parabolic constants of oxidation, k_p , ranged from $3.01 \cdot 10^{-9} \text{ mg}^2 \cdot \text{cm}^{-4} \cdot \text{s}^{-1}$ at 800 °C to $5.92 \cdot 10^{-6} \text{ mg}^2 \cdot \text{cm}^{-4} \cdot \text{s}^{-1}$ at 1000 °C. These k_p values appear comparable and even slightly lower than k_p values for its cast and wrought counterparts [10–12]. However, SLM Alloy 625 demonstrates good performance in high temperature oxidation in the 700–1000 °C range. A frequency factor k_0 of $7.87 \cdot 10^6 \text{ mg}^2 \cdot \text{cm}^{-4} \cdot \text{s}^{-1}$ and $1.68 \cdot 10^8 \text{ mg}^2 \cdot \text{cm}^{-4} \cdot \text{s}^{-1}$ and an activation energy Q of $298 \text{ kJ} \cdot \text{mol}^{-1}$ and $324 \text{ kJ} \cdot \text{mol}^{-1}$ were calculated for the present SLM processed Alloy 625 and for all the oxidation results of Alloy 625 summarized in the Arrhenius plot given in Fig. 7, respectively. It should be noted that oxidation tests were performed on polished, then heat-treated SLMed specimens, which could explain the lower parabolic constants obtained as compared to other studies on additively manufactured Alloy 625. Indeed, a tens-to-hundred-of-nanometer oxide scale developed onto the Alloy 625 specimens during the standard two-step heat treatment despite the vacuum environment, thus slightly lowering the oxidation flux through the oxide scale. Chen et al. [53] reported that the parabolic constant at 1000 °C of heat treated SLMed Alloy 625 was slightly lower than that of as-built samples, possibly due to the fast outward diffusion channels for Cr atoms provided by the dendritic structure composing the microstructure of as-built samples. In addition, AM processes usually produce samples having high surface roughness, which can affect the area of the reactive surface and, therefore, the oxidation properties [11,54–56]. This significant roughness was also reported as a source of deviation from the parabolic oxidation behavior, the mass gain of rough specimens being greater in the early stages of oxidation. This would indeed explain that mass gain is more important at early stage of oxidation for NiCrAlY coated 625 (Figs. 5 and 6).

Standard diffusion heat treatment of the bulk NiCrAlY SLM processed with parameters optimized in a previous study [36] produced the expected $\gamma\text{-Ni}/\gamma'\text{-Ni}_3\text{Al}$ + $\alpha\text{-Cr}$ microstructure for the chosen composition range (Fig. 4(b, e)). With an aluminum content higher than 10 atomic percent, bulk NiCrAlY promoted the growth of a thin, continuous, slow-growing and adherent Al_2O_3 scale obeying a parabolic law. Cr_2O_3 external oxide mixed with the Al_2O_3 external oxide was also observed, especially at 800 °C. The growth kinetics of the Cr_2O_3 oxide is greater than the Al_2O_3 and participate in an apparent mass gain greater than purely alumina-forming materials. Calculated constants of oxidation k_p ranging from $1.30 \cdot 10^{-8} \text{ mg}^2 \cdot \text{cm}^{-4} \cdot \text{s}^{-1}$ at 800 °C to $4.71 \cdot 10^{-7} \text{ mg}^2 \cdot \text{cm}^{-4} \cdot \text{s}^{-1}$ at 1000 °C lie within the dispersed range of k_p values for MCrAlY coatings available in the literature [22–24,51,52] and reported in Fig. 7. Constant of oxidation domains for the allotropic variants of Al_2O_3 identified by Brumm et al. [22], i.e. $\alpha\text{-Al}_2\text{O}_3$, $\theta\text{-Al}_2\text{O}_3$, and $\gamma\text{-Al}_2\text{O}_3$, reported as dashed black-gray lines in Fig. 7, suggest that the oxide scale formed on the material could be the metastable γ/θ oxide variants, consistent with the relatively low temperature range investigated. However, $\alpha\text{-Al}_2\text{O}_3$ was identified with XRD analyses (see Supplementary Information), indicating that metastable alumina could participate in the oxide formation but could transform in $\alpha\text{-Al}_2\text{O}_3$ at high temperature exposure.

Fine (Ni,Y)-rich intermetallic precipitates were observed in the bulk NiCrAlY, well dispersed in the microstructure and in a fairly large quantity (Fig. 4(b, d)). Y addition in MCrAlY coatings aims to enhance resistance to oxidation by reactive-element effect [57]. Y is intended to segregate at oxide grain boundaries, to improve the adherence and the protective role of the Al_2O_3 scale by the combination of several

mechanisms. Indeed, the formation of Y-rich oxide pegs at the metal/oxide interface [58], the decrease in Al diffusion through Al_2O_3 , and the prevention from vacancies coalescence at the metal/oxide interface are highly beneficial in terms of high temperature surface reactivity, especially under thermal cycling [2]. Concentration of reactive element is critical if scale adhesion is to be optimal. Overdoping of the alloy (typically above 0.5% in weight for Y [2]) is known to impair the oxidation resistance of Ni-based alloys through precipitation of Y oxides from Ni-Y intermetallics. The nominal Y content measured within bulk NiCrAlY was close to that of the powder ($\approx 1 \text{ wt}\%$). The powder composition was purposely chosen in the present study based on typical composition for plasma spray applications, using powders with a relatively greater content of Y to compensate for significant oxidation during the process. This was not the case during SLM due to the low partial pressure of O_2 within the SLM chamber ($\leq 0.1 \text{ wt}\%$) and the protective Ar flow above the powder bed, hence resulting in high Y content within the material. Adjustment of the initial Y concentration in the initial powder would therefore be required to further ensure a more efficient alloy design.

In addition to melting powders, SLM involves the remelting of previously solidified material across several layers, ensuring excellent metallurgical bonding between layers and components with high-density [36]. As a result of manufacturing dissimilar material, and more particularly thin coating, substantial dilution occurs. Effects of this dilution can be observed as deep as hundreds of micrometres, corresponding to typically a thickness of 5 to 10 layers. As observed in the element distribution maps in Fig. 2, the SLM processed NiCrAlY coating onto Alloy 625 contained a significant amount of Mo and Nb. The presence of these two elements results from the remelting of the substrate and the subsequent dilution during the deposition of the two layers of NiCrAlY. Cross section observations showed that although coating thickness was limited to approximately 60 μm , remelted layers went locally as deep as $\approx 150 \mu\text{m}$. Despite good adhesion of the coating and a smoother composition transition at the interface (Figs. 2(b) and 13), the modification of the coated layer composition from the powder composition has three effects: (i) the formation of TCP phases and microstructures after heat treatment very different from that of bulk NiCrAlY (Fig. 4), (ii) the segregation of yttrium at the top surface of the coating as (Y,Al)-rich oxides (Figs. 2 and 3), and (iii) the decrease of the Al content due to dilution (maps of Mo, Nb and Al in Figs. 2 and 13). Regarding the microstructure, the presence of Mo led to the formation of the σ -TCP phase during the heat treatment as intragranular platelet-like precipitates and bulky precipitates at the grain boundaries. The needle-like TCP phases are deleterious in Ni-based superalloys and reported as a potential source for crack initiation and propagation, thus causing low-temperature brittle failure [44]. Nb atoms appeared to have preferentially diffused into γ' precipitates during the heat treatment, which has the capability to accommodate a small quantity of Nb as a substitute to Al [59].

(Ni-Y)-rich particles were found to precipitate within bulk NiCrAlY whereas YAM oxides ($\text{Y}_4\text{Al}_2\text{O}_9$) solely formed out of the coating, i.e. onto the coating top surface. Since bulk NiCrAlY is free of alien Alloy 625 elements, the mechanism leading to Y segregation onto the top surface of the NiCrAlY coating variant is assumed to be as follow: the substantial presence of elements from Alloy 625 within the melt pool, presumably both Mo and Nb, led to a significant drop in the solubility of Y in the alloy. Upon solidification, the liquid phase at the surface of the melt-pool got progressively enriched in Y. Its high reactivity potentially led to the formation of (Al,Y)-rich oxides from the remaining traces of O_2 within the chamber ($\leq 0.1\%$), identified as $\text{Y}_4\text{Al}_2\text{O}_9$. Upon remelting of the solidified material (adjacent line scan of the same layer or next layer), the less dense oxide remains at the surface of the melt pool as a slag. Surface tension rejects the slag to the side between weld tracks, forming the regularly spaced continuous oxide beads parallel to the scanning direction observed at the top surface of NiCrAlY coated Alloy 625 samples (Figs. 3(a) and 9). This scenario, if confirmed, would make

difficult the addition of reactive Y in SLM processed coatings with thickness smaller than the remelting depth (≈ 3 to 4 layers), as it would not be possible to avoid a large dilution of the coating powder within the underlying substrate.

Macrographs of oxidized specimens (Fig. 8), surface element distribution maps (Fig. 12), cross-section observations of the coating (Fig. 13) and surface topography (Fig. 12) evidenced a good correlation between the coating topography, the heterogeneous distribution of Al within the coating and the distribution of oxidation products after exposure to 800 °C, 900 °C and 1000 °C for up to 200 h. As illustrated in the topography map (top right corner in Fig. 12) and the cross-section microstructure in Fig. 13, the coating follows the topography inherited from the manufacturing of the Alloy 625 substrate, which exhibits large hill and valley regions with height difference as high as $180 \pm 20 \mu\text{m}$ on average. Additive manufactured components usually present edges with a higher altitude than the central region for various reasons including (i) the effect of contour scanning strategies in SLM process, (ii) the distortion at free edges, and (iii) the starting/ending points of beads. Given the small surface of the samples ($5 \times 5 \text{ mm}$), edge effects impact a significant portion of the whole surface. In the default strip scanning strategy used for SLM processing, the whole surface of the building area was divided into 7.5 mm wide stripes and specimens were laser one by one according to the global stripe pattern. When occasionally samples were located between two or more adjacent stripes, the junction would also lead to a visible local variation of the topography (e.g. top right sample in Fig. 8). Variations of the substrate topography caused valley regions (mainly central regions) to be covered by a thicker layer of NiCrAlY powder than hill regions (mainly near the edges) during SLM process. The quantity of Al in central regions remained sufficiently high ($\approx 10 \text{ at}\%$) to allow the formation a continuous, protective film of external Al_2O_3 (Type III oxidation), as expected from the NiCrAlY coating [19–21]. However, in regions of higher altitude, the thinner coating subject to a higher degree of dilution, led to lower Al content, below the required threshold for an external Al_2O_3 to form. Instead, Type II oxidation behavior typical of high Cr low Al alloys was observed [19–21], characterized by the growth of an external Cr_2O_3 scale and an internal oxidation of Al_2O_3 (Figs. 10 and 11).

The mass gain evolution of NiCrAlY coated Alloy 625, intermediate between those of Al_2O_3 -forming bulk NiCrAlY and Cr_2O_3 -forming bulk Alloy 625, confirmed that the coating provided some degree of protection towards high temperature oxidation to the substrate, despite the imperfect Al_2O_3 covering of the NiCrAlY coated surface. Contrary to bulk NiCrAlY specimens, the oxidation behavior after few hours of the NiCrAlY coated Alloy 625 deviates from the parabolic regime and tends to the behavior of the bulky NiCrAlY samples. In other words, the oxidation behavior of NiCrAlY coated Alloy 625 processed by SLM is not parabolic in the investigated range of temperature, the oxidation kinetics gradually decreasing with the time. Such deviation from the parabolic oxidation behavior was also observed for an In718 SLM processed oxidized at 850 °C [54–56]. Rough surfaces demonstrate a greater mass gain in the early stages of oxidation then decreasing down to kinetics of polished surface due to surface smoothing and local variation in oxide thickness, oxide in the valley regions being thicker compared to hill regions. It should also be noted that the fraction of Al_2O_3 and Cr_2O_3 growing regions differed from one sample to another (Fig. 8), which could also have contributed to a dispersion of the data (each one corresponding to a different sample).

4.2. Some keys for further improvements

The present study showed that improvement of the high temperature oxidation properties of Alloy 625 between 800 and 1000 °C is possible using a SLM processed NiCrAlY coating. Compared to standard plasma spray deposition, the remelting of the underlying solidified layers ensures a strong metallurgical bonding of the coating with the

substrate and liquid state dilution leads to a smooth composition transition at the interface. Both effects could favour a good adherence of the coating over the lifetime of coated parts. Due to the low pressure of O_2 and the argon shielding flow on top of the powder bed, the SLM process produced coatings devoid of embedded oxidation products. However, several process related issues were noted, which allowed to identify some keys for further improvement in terms of process, chemistry and microstructure. The most striking issue encountered was the heterogeneous distribution of Al element in the coating (in the x-y plane) due to the lack of flatness of the SLM Alloy 625 substrate, enhanced by the small surface area of the samples (edge effects) and the default non-optimized stripe scanning pattern. This issue can be possibly solved by surface preparation of substrates to correct roughness and flatness and/or a wiser selection of scanning strategies and process parameters. For instance, Mohammadian et al. [60] developed a chemical-abrasive flow polishing technical to improve surface finish control of additively-manufactured Alloy 625 components with complex geometries. Note that coating deposition onto flat surfaces only and with relatively small dimension remains a current limitation of the SLM process itself.

The substantial diffusion of Mo and Nb was found to cause heterogeneous segregation to the surface of most of the reactive Y as oxides, where its beneficial effect on the resistance to oxidation would be nullified. Process parameters used in the present study induced deep remelting of the substrate (100–150 μm) relative to the thickness of the NiCrAlY coating. Influence of the substrate in terms of composition alteration in SLM are typically of the order of 200–300 μm , depending on the energy density applied (P , V and hatch distance h). NiCrAlY coatings exceeding 300 μm in thickness are less likely to be completely affected by this issue. In the case of thin coatings, adjusting the process parameters for limiting the dilution effect, could be appropriated. At last, addition of reactive element in a different form, as dispersed oxide for example, could also be an alternative strategy.

The modification of coating composition led to changes in the phases present in the microstructure and their morphology, in particular the precipitation of platelet-like and undesirable TCP σ phases in Mo-rich regions after the heat treatment, known to embrittle Ni-based superalloys. The current results did not show evidence of detrimental effects of the σ phase or the modified microstructure other than the particular change in oxidation behavior when the amount of Al dropped below the critical level required for the formation of external Al_2O_3 . Strategies for reducing dilution of coatings within the surface such as presented in the previous paragraph, are expected to help promoting a microstructure closer to the one of bulk SLMed NiCrAlY.

Finally, SLM processed coatings presented, as soon as from the as-built stage, a surface network of fine, microscopic cracks within beads, normal to the scanning direction (Fig. 12) and propagating across the whole coatings. These cracks can be very detrimental to the oxidation resistance. The occurrence of high tensile stresses within beads is typical of SLMed materials, stress being maximum along the bead length [40]. Most of the cracks appeared in Al-rich areas of the coatings, where the composition was closer to that of the NiCrAlY composition. Not observed at this scale in bulk NiCrAlY samples, the crack network formed within the thin coating is believed to originate from the higher level of residual stresses within the coating caused by the presence of the underlying Alloy 625 (thermal expansion mismatch, high temperature mechanical performance, etc.). Compared to Alloy 625 substrate, NiCrAlY coating has a high amount of Al. Thus, during SLM of NiCrAlY coating onto Alloy 625, the coated NiCrAlY should tend to significantly shrink due to γ' prime precipitation. However, the Alloy 625 substrate constrained its shrinkage. Accordingly, the coated NiCrAlY is subjected to high degree of tensile stresses. However, it must be noted that the crack network in NiCrAlY coatings occurred as delayed cracking. Preliminary results demonstrated that heat-treating samples consecutively after manufacturing greatly reduces the extend of cracking. A stress relieving heat treatment is advised and often

carried out right after fabrication in typical applications. In the present work, samples were heat treated several weeks after being manufactured, i.e. after the occurrence of a large crack network.

5. Conclusions

The main conclusions drawn from this study on the high temperature oxidation in the temperature range of 800 to 1000 °C of a NiCrAlY coating Alloy 625 processed by SLM are given below:

- (i) Improvement in high temperature oxidation properties of SLM processed Alloy 625 between 800 and 1000 °C was found possible using a SLM processed NiCrAlY coating, i.e. a two-step SLM deposition process;
- (ii) Dilution effects due to some remelting of the substrate influence the chemistry and the microstructure of the coating. Using two deposition layers, the aluminum content within the coating was half the content of the NiCrAlY powder composition, and the coating was significantly enriched in elements from the Alloy 625 substrate (Mo and Nb), leading to the segregation of the reactive Y to the surface as $Y_4Al_2O_9$ oxides;
- (iii) Dilution effects during the NiCrAlY coating manufacturing was sensitive to the topography of the SLM processed Alloy 625 substrates: thicker powder layers before laser melting in valley region led to elements of the NiCrAlY being more concentrated in the valley regions;
- (iv) Variability in oxidation products at the surface of the SLM processed NiCrAlY coating was intimately related to topography-assisted chemical and microstructural heterogeneities;
- (v) SLM processed bulk Alloy 625 and bulk NiCrAlY followed a parabolic oxidation behavior in the present temperature range, which was not the case for the NiCrAlY coated Alloy 625 bi-material.

CRedit authorship contribution statement

Damien Texier: Conceptualization, Methodology, Data curation, Validation, Investigation, Writing - original draft, Writing - review & editing, Visualization. **Etienne Copin:** Conceptualization, Methodology, Data curation, Validation, Investigation, Funding acquisition, Writing - original draft, Writing - review & editing, Visualization. **Agustin Flores:** Methodology, Data curation, Investigation, Writing - original draft, Visualization. **Jiwon Lee:** Methodology, Investigation, Writing - review & editing, Visualization. **Mathieu Ternier:** Conceptualization, Methodology, Validation, Funding acquisition, Writing - original draft, Writing - review & editing, Visualization. **Hyun-Uk Hong:** Conceptualization, Supervision, Funding acquisition, Project administration, Writing - review & editing. **Philippe Lours:** Conceptualization, Supervision, Funding acquisition, Project administration, Writing - review & editing.

Declaration of competing interest

The authors declare that they have no known competing financial interests or personal relationships that could have appeared to influence the work reported in this paper.

Acknowledgements

The authors acknowledge the financial support of the National Research Foundation of Korea (NRF) grant funded by the Korean government (MSIP, NRF-2020R1A2C4002291 and NRF-2018R1A5A6075959). This work used the precision Jig for specimen preparation developed during the ANR-JCJC-COMPACT project

funded by the Agence Nationale de la Recherche (ANR) [ANR-18-CE08-0003]. The authors are grateful to the Raimond Castaing Microanalysis Centre (Mixed Services Unit 3623) for access to microscopy facilities.

Appendix A. Supplementary data

Supplementary data to this article can be found online at <https://doi.org/10.1016/j.surfcoat.2020.126041>.

References

- [1] T. Pollock, S. Tin, Nickel-based superalloys for advanced turbine engines: chemistry, microstructure, and properties, *J. Propuls. Power* 22 (2006) 361–374.
- [2] R. Reed, *The Superalloys: Fundamentals and Applications*, Cambridge University Press, 2008.
- [3] D.J. Young, *High Temperature Oxidation and Corrosion of Metals*, 2nd ed., Elsevier Science, 2016, <https://doi.org/10.1016/B978-0-08-100101-1.01001-3>.
- [4] C. Vernot-Loier, F. Cortial, Influence of heat treatments on microstructure, Mechanical Properties and Corrosion Behaviour of Alloy 625 Forged Rod (2012) 409–422.
- [5] E. Whitemy, G. Smikovich, J. Fink, High Temperature Oxidation of a Modified Alloy 625 (2012) 695–704.
- [6] H. Eiselstein, D. Tillack, The Invention and Definition of Alloy 625 (2012) 1–14.
- [7] L. Mataveli Suave, D. Bertheau, J. Cormier, P. Villechaise, A. Soula, Z. Hervier, F. Hamon, J. Laigo, Impact of thermomechanical aging on alloy 625 high temperature mechanical properties, 8th International Symposium on Superalloy 718 and Derivatives, 2014 2014, pp. 317–331.
- [8] L. Mataveli Suave, J. Cormier, D. Bertheau, P. Villechaise, A. Soula, Z. Hervier, F. Hamon, High temperature low cycle fatigue properties of alloy 625, *Mater. Sci. Eng. A* 650 (2016) 161–170.
- [9] L. Kumar, R. Venkataramani, M. Sundaraman, P. Mukhopadhyay, S.P. Garg, Studies on the oxidation behaviour of inconel 625 between 873 and 1523 K, *Oxid. Met.* 45 (1996) 221–244.
- [10] A. Chyrkin, P. Huczowski, V. Shemet, L. Singheiser, W.J. Quadakkers, Sub-scale depletion and enrichment processes during high temperature oxidation of the nickel base alloy 625 in the temperature range 900–1000°C, *Oxid. Met.* 75 (2011) 143–166.
- [11] N. Ramenatte, A. Vernouillet, S. Mathieu, A. Vande Put, M. Vilasi, D. Monceau, A comparison of the high-temperature oxidation behaviour of conventional wrought and laser beam melted Inconel 625, *Corros. Sci.* 164 (2020) 108347.
- [12] L. Garcia-Fresnillo, A. Chyrkin, C. Böhme, J. Barnikel, F. Schmitz, W. Quadakkers, Oxidation behaviour and microstructural stability of alloy 625 during long-term exposure in steam, *J. Mater. Sci.* 49 (2014) 6127–6142.
- [13] C.S. Tedmon, The effect of oxide volatilization on the oxidation kinetics of cr and fe-cr alloys, *J. Electrochem. Soc.* 113 (1966) 766.
- [14] D. Young, B. Pint, Chromium volatilization rates from Cr2O3 scales into flowing gases containing water vapor, *Oxid. Met.* 66 (2006) 137–153.
- [15] R. Mével, State of the art on high-temperature corrosion-resistant coatings, *Mater. Sci. Eng. A* 120–121 (1989) 13–24.
- [16] T. Rhys-Jones, *Coatings for Blade and Vane Applications in Gas Turbines*, (1989), [https://doi.org/10.1016/0010-938X\(89\)90104-2](https://doi.org/10.1016/0010-938X(89)90104-2).
- [17] S. Bose, *High Temperature Coatings*, 1st ed., 81 Butterworth-Heinemann, 2007, <https://doi.org/10.1007/s11085-013-9462-3>.
- [18] W. Leng, R. Pillai, P. Huczowski, D. Naumenko, W. Quadakkers, Microstructural evolution of an alumina coating on alloy 625 during wet air exposure at 900 °C and 1000 °C, *Surf. Coat. Technol.* 354 (2018) 268–280.
- [19] G. Wallwork, A. Hed, Some limiting factors in the use of alloys at high temperatures, *Oxid. Met.* 3 (1971) 171–184.
- [20] C. Giggins, F. Pettit, Oxidation of Ni-Cr-Al alloys between 1000° and 1200°C, *J. Electrochem. Soc.* 118 (1971) 1782–1790.
- [21] J. Smialek, N. Jacobson, Oxidation of high-temperature aerospace materials, in: Y. Bar-Cohen (Ed.), *High Temperature Materials and Mechanisms*, February, 2014, pp. 95–162, <https://doi.org/10.1201/b16545-6>.
- [22] M. Brumm, H. Grabke, The oxidation behaviour of NiAl-I. Phase transformations in the alumina scale during oxidation of NiAl and NiAl-Cr alloys, *Corros. Sci.* 33 (1992) 1677–1690.
- [23] S. Sacré, U. Wienstroth, H. Feller, L. Thomas, Influence of the phase compositions on the transient-stage high-temperature oxidation behaviour of a NiCoCrAlY coating material, *J. Mater. Sci.* 28 (1993) 1843–1848.
- [24] W. Brandt, D. Toma, H. Grabke, The characteristics of alumina scales formed on HVOF-sprayed MCrAlY coatings, *Surf. Coat. Technol.* 108–109 (1998) 10–15.
- [25] T. DebRoy, H. Wei, J. Zuback, T. Mukherjee, J. Elmer, J. Milewski, A. Beese, A. Wilson-Heid, Z.W. De A, Additive manufacturing of metallic components – process, structure and properties, *Prog. Mater. Sci.* 92 (2018) 112–224.
- [26] W.E. Frazier, Metal additive manufacturing: a review, *J. Mater. Eng. Perform.* 23 (2014) 1917–1928.
- [27] K. Wong, A. Hernandez, A review of additive manufacturing, *ISRN Mechanical Engineering* (2012) 1.
- [28] D. Ma, A.D. Stoica, Z. Wang, A.M. Beese, Crystallographic texture in an additively manufactured nickel-base superalloy, *Mater. Sci. Eng. A* 684 (2017) 47–53.
- [29] G. Lindwall, C.E. Campbell, E.A. Lass, F. Zhang, M.R. Stoudt, A.J. Allen, L.E. Levine, Simulation of TTT curves for additively manufactured inconel 625, *Metallurgical*

- and Materials Transactions A: Physical Metallurgy and Materials Science 50 (2019) 457–467.
- [30] A. Kreitzberg, V. Brailovski, S. Turenne, Elevated temperature mechanical behavior of IN625 alloy processed by laser powder-bed fusion, *Mater. Sci. Eng. A* 700 (2017) 540–553.
- [31] I. Koutiri, E. Pessard, P. Peyre, O. Amlou, T. De Terris, Influence of SLM process parameters on the surface finish, porosity rate and fatigue behavior of as-built Inconel 625 parts, *J. Mater. Process. Technol.* 255 (2018) 536–546.
- [32] S. Li, Q. Wei, Y. Shi, C.K. Chua, Z. Zhu, D. Zhang, Microstructure characteristics of Inconel 625 superalloy manufactured by selective laser melting, *J. Mater. Sci. Technol.* 31 (2015) 946–952.
- [33] M. Leary, M. Mazur, H. Williams, E. Yang, A. Alghamdi, B. Lozanovski, X. Zhang, D. Shidid, L. Farahbod-Sternahl, G. Witt, I. Kelbassa, P. Choong, M. Qian, M. Brandt, Inconel 625 lattice structures manufactured by selective laser melting (SLM): mechanical properties, deformation and failure modes, *Mater. Des.* 157 (2018) 179–199.
- [34] C. Li, R. White, X.Y. Fang, M. Weaver, Y.B. Guo, Microstructure evolution characteristics of Inconel 625 alloy from selective laser melting to heat treatment, *Mater. Sci. Eng. A* 705 (2017) 20–31.
- [35] G. Marchese, M. Lorusso, S. Parizia, E. Bassini, J.-W. Lee, F. Calignano, D. Manfredi, M. Terne, H.-U. Hong, D. Ugues, M. Lombardi, S. Biamino, Influence of heat treatments on microstructure evolution and mechanical properties of Inconel 625 processed by laser powder bed fusion, *Mater. Sci. Eng. A* 729 (2018) 64–75.
- [36] J. Lee, M. Termer, E. Copin, P. Lours, H.U. Hong, A novel approach to the production of NiCrAlY bond coat onto IN625 superalloy by selective laser melting, *Additive Manufacturing* 31 (2020) 100998.
- [37] D. Texier, D. Monceau, F. Grabos, E. Andrieu, Tensile properties of a non-line-of-sight processed $\beta - \gamma - \gamma'$ MCrAlY coating at high temperature, *Surf. Coat. Technol.* 326 (2017) 28–36.
- [38] D. Texier, D. Monceau, J.-C. Salabura, R. Mainguy, E. Andrieu, Micromechanical testing of ultrathin layered material specimens at elevated temperature, *Mater. High Temp.* 33 (2016) 325–337.
- [39] D. Texier, D. Monceau, Z. Hervier, E. Andrieu, Effect of interdiffusion on mechanical and thermal expansion properties at high temperature of a MCrAlY coated Ni-based superalloy, *Surf. Coat. Technol.* 307 (2016) 81–90.
- [40] S. Le Roux, M. Salem, A. Hor, Improvement of the bridge curvature method to assess residual stresses in selective laser melting, *Additive Manufacturing* 22 (2018) 320–329.
- [41] Z. Tian, C. Zhang, D. Wang, W. Liu, X. Fang, D. Wellmann, Y. Zhao, Y. Tian, A review on laser powder bed fusion of Inconel 625 nickel-based alloy, *Appl. Sci.* 10 (2020) 81.
- [42] L. Mataveli Suave, J. Cormier, P. Villechaise, A. Soula, Z. Hervier, D. Bertheau, J. Laigo, Microstructural evolutions during thermal aging of alloy 625: impact of temperature and forming process, *Metall. Mater. Trans. A* 45 (2014) 2963–2982.
- [43] J. Davis, *ASM Specialty Handbook: Nickel, Cobalt, and their Alloys*, ASM International, 2000.
- [44] C. Sims, N. Stoloff, W. Hagel, *Superalloys II: High-Temperature Materials for Aerospace and Industrial Power*, 2nd ed., Wiley, 1987.
- [45] N. Evans, P. Maziasz, J. Shingledecker, Y. Yamamoto, Microstructure evolution of alloy 625 foil and sheet during creep at 750 °C, *Mater. Sci. Eng. A* 498 (2008) 412–420.
- [46] M. Donachie, S. Donachie, *Superalloys: A Technical Guide*, 2nd ed., ASM International, 2002.
- [47] M.T. Pace, R.C. Thomson, J. Wells, Oxidation of MCrAlY coatings on Ni based superalloys, *Energy Materials* 2 (2007) 181–190.
- [48] O. Fabricznaya, H.J. Seifert, R. Weiland, T. Ludwig, F. Aldinger, A. Navrotsky, Phase equilibria and thermodynamics in the $Y_2O_3-Al_2O_3-SiO_2$ system, *Z. Met.* 92 (2001) 1083–1097.
- [49] H. Hindam, D. Whittle, Microstructure, adhesion and growth kinetics of protective scales on metals and alloys, *Oxid. Met.* 18 (1982) 245–284.
- [50] R. Peraldi, D. Monceau, B. Pieraggi, Evolution of scale microstructure as a function of scale oxide thickness during oxidation of nickel at 700 °C, *Mater. Sci. Forum* 369–372 (2001) 189–196.
- [51] N. Czech, M. Juez-Lorenzo, V. Kolarik, W. Stamm, Influence of the surface roughness on the oxide scale formation on MCrAlY coatings studied in situ by high temperature X-ray diffraction, *Surf. Coat. Technol.* 108–109 (1998) 36–42.
- [52] M. Shen, P. Zhao, Y. Gu, S. Zhu, F. Wang, High vacuum arc ion plating NiCrAlY coatings: microstructure and oxidation behavior, *Corros. Sci.* 94 (2015) 294–304.
- [53] L. Chen, Y. Sun, L. Li, X. Ren, Effect of heat treatment on the microstructure and high temperature oxidation behavior of TiC/Inconel 625 nanocomposites fabricated by selective laser melting, *Corros. Sci.* 169 (2020) 108606, <https://doi.org/10.1016/j.corsci.2020.108606> (In press).
- [54] T. Sanviemvongsak, D. Monceau, B. Macquaire, High temperature oxidation of IN 718 manufactured by laser beam melting and electron beam melting: effect of surface topography, *Corros. Sci.* 141 (2018) 127–145.
- [55] D. Seo, K. Ogawa, T. Shoji, S. Murata, High-temperature oxidation behavior and surface roughness evolution of VPS NiCrAlY coating, *J. Therm. Spray Technol.* 17 (2008) 136–143.
- [56] L.-y. Ni, Z.-l. Wu, C.-g. Zhou, Effects of surface modification on isothermal oxidation behavior of HVOF-sprayed NiCrAlY coatings, *Progress in Natural Science: Materials International* 21 (2011) 173–179.
- [57] D.P. Whittle, J. Stringer, Improvements in high-temperature oxidation resistance by additions of reactive elements or oxide dispersions, *Philos. Trans. R. Soc. Lond.* 295A (1980) 309–329.
- [58] H. Tawancy, N. Abbas, A. Bennett, Role of Y during high temperature oxidation of an M-Cr-Al-Y coating on a Ni-base superalloy, *Surf. Coat. Technol.* 68–69 (1994) 10–16.
- [59] W. Mankins, S. Lamb, *Nickel and Nickel Alloys*, ASM International, 1990, <https://doi.org/10.31399/asm.hb.v02.9781627081627>.
- [60] N. Mohammadian, S. Turenne, V. Brailovski, Surface finish control of additively-manufactured Inconel 625 components using combined chemical-abrasive flow polishing, *J. Mater. Process. Technol.* 252 (2018) 728–738.

Nouvelle fabrication de l'alliage 625 et du revêtement de liaison MCrAlY par la fusion laser sélective sur lit de poudre et contrôle des microstructures

Dans cette étude, l'alliage 625 a été élaboré par l'une des méthodes de fabrication additive (AM) les plus couramment utilisées, la fusion laser sélective sur lit de poudre (L-PBF), et ses propriétés mécaniques ont été évaluées à différentes températures. L'alliage 625 fabriqué par L-PBF a montré une résistance élevée et un allongement à la rupture médiocre. Ainsi, des traitements thermiques ont été appliqués pour améliorer ses performances. Un traitement thermique de mise en solution à une température supérieure à 1000 ° C a été appliquée à l'alliage L-PBF 625, ce qui a entraîné une recristallisation en raison de l'énergie stockée par le matériau attribuée à la forte densité de dislocations présentes dans l'alliage. Cette microstructure modifiée a montré une résistance satisfaisante lors des essais de traction à température ambiante (résistance plus élevée que l'alliage corroyé 625 et allongement supérieur à l'alliage L-PBF brut de fabrication). À l'étape suivante, l'alliage L-PBF 625 recristallisé a été soumis à un traitement thermique de *Grain Boundary Serration* (GBS, dentelure des joints de grains) pour améliorer ses propriétés mécaniques à haute température. Comme il s'agissait de la première tentative pour générer la GBS d'un alliage à haute teneur en Nb, il était d'abord important de comprendre le mécanisme GBS. Pour induire le GBS, il est nécessaire que les larges atomes de soluté se déplacent près des joints de grains (GB). Par conséquent, le traitement thermique GBS a été modifié pour être appliqué à l'alliage L-PBF 625. Le traitement thermique de GBS spécialement conçu a réussi à induire pour la première fois les motifs en zigzag des GB dentelés. Cet alliage GB-L-PBF dentelé 625 a montré des propriétés mécaniques améliorées à haute température en termes de ductilité accrue et d'élimination de l'effet de vieillissement dynamique (DSA). Pour améliorer davantage les propriétés à haute température de l'alliage L-PBF 625, un revêtement de liaison NiCrAlY a été nouvellement appliqué au substrat en alliage 625 par la même méthode (L-PBF) pour améliorer l'efficacité du processus de production et augmenter la résistance à l'oxydation/corrosion à haute température. Bien que leurs différentes propriétés thermiques aient conduit à de nombreux essais et erreurs dans la fabrication du matériau, les paramètres optimaux ont été définis et vérifiés pour évaluer le potentiel de commercialisation du procédé. La caractéristique de refusion du L-PBF a induit une bonne liaison entre le substrat et le revêtement, ce qui indique une bonne stabilité. Le comportement à l'oxydation de l'alliage 625 revêtu de NiCrAlY a été caractérisé par analyse thermo-gravimétrique (TGA) et des tests de chocs thermiques ; les résultats ont indiqué que le nouveau matériau avait une résistance à l'oxydation plus élevée que l'alliage 625 brut de fabrication. Par conséquent, le traitement thermique de GBS associé à un revêtement NiCrAlY efficace peut améliorer considérablement les propriétés mécaniques à haute température de l'alliage 625 fabriqué par L-PBF.

Keywords

L-PBF, Alliage 625, Traitement thermique, NiCrAlY, Oxydation, Propriétés mécaniques

Novel Fabrication of Alloy 625 and MCrAlY Bond Coat by Laser Powder Bed Fusion and Microstructure Control

In this study, Alloy 625 was fabricated by one of the most commonly used additive manufacturing (AM) methods, laser powder bed fusion (L-PBF), and its mechanical properties were evaluated at various temperatures. The L-PBF fabricated Alloy 625 showed high strength and relatively poor elongation. Thus, some heat treatments were applied to improve its performance. A solid-solution heat treatment with a temperature of more than 1000 °C was applied to the L-PBF Alloy 625, resulting in recrystallization because of high energy stored within the alloy attributed by high density of dislocations. This modified microstructure of the L-PBF Alloy 625 sample showed the required strength under tensile testing at room temperature (higher strength than wrought Alloy 625 and greater elongation than L-PBF as-built alloy). In view of enhancing mechanical properties at high temperature, a grain boundary serration (GBS) heat treatment was specifically designed for L-PBF Alloy 625. Because this was the first attempt to produce GBS in a high-Nb-content alloy, it was necessary to understand its mechanism first. To induce GBS, it is necessary for large solute atoms to move near the grain boundaries (GBs). Therefore, the GBS heat treatment was modified for application to the L-PBF Alloy 625. The specially designed GBS heat treatment successfully induced the zigzag patterns of serrated GBs for the first time. This GBS L-PBF Alloy 625 showed improved high-temperature mechanical properties in terms of increased ductility and elimination of the dynamic strain aging (DSA) effect at elevated temperatures. To further improve the high-temperature property of the L-PBF Alloy 625, NiCrAlY bond coat was applied to the Alloy 625 substrate by the same method (L-PBF) for the first time to improve the efficiency of the production process and increase the resistance to oxidation. Although their different thermal properties led to many trials and errors in the manufacturing of the material, the optimal parameters for applying NiCrAlY bond coat deposition by L-PBF were set and verified to assess the potential for the process to be commercialized. The remelting characteristic of L-PBF induced good metallurgical bonding between the substrate and coating, which indicates good stability. The oxidation behavior of the NiCrAlY-coated Alloy 625 was characterized by thermal gravimetric analysis (TGA) and thermal shock testing; the results indicated that the novel coated material had higher resistance to oxidation than bulk Alloy 625. Therefore, the GBS heat treatment together with efficient NiCrAlY coating can greatly improve the high-temperature mechanical properties of L-PBF manufactured Alloy 625.

Keywords

Laser Powder Bed Fusion, Alloy 625, Heat treatment, NiCrAlY, Oxidation, Mechanical properties